Impedance Analysis of Epithelial Barrier Function:

New Devices and Assays

DISSERTATION

zur Erlangung des Doktorgrades der

Naturwissenschaften (Dr. rer. nat.)

der Fakultät für Chemie und Pharmazie

der Universität Regensburg

vorgelegt von **Kathrin Hajek** aus Mitterfelden, 2016

Diese Doktorarbeit entstand in der Zeit von Januar 2013 bis August 2016 am Institut für Analytische Chemie, Chemo- und Biosensorik der Fakultät Chemie und Pharmazie der Universität Regensburg.

Die Arbeit wurde angeleitet von Prof. Dr. Joachim Wegener.

Promotionsgesuch eingereicht am: 18. Oktober 2016

Kolloquiumstermin: 02. Dezember 2016

Prüfungsausschuss:

Vorsitzender:	Prof. Dr. Antje J. Baeumner
Erstgutachter:	Prof. Dr. Joachim Wegener
Zweitgutachter:	Prof. Dr. Günther Bernhardt
Drittprüfer:	PD Dr. Miriam Breunig

In loving memory of Eduard Hajek.

Contents

1 Introduction 1

1.1 Epithelial barriers ... 2

1.1.1 Architecture of epithelial cell-cell and cell-substrate contacts ... 2

1.1.2 Transport routes across epithelial barriers ... 4

1.2 Quantification of epithelial barrier function ... 5

1.2.1 Water permeability ... 5

1.2.2 Molecular permeability ... 7

1.2.3 Ionic permeability ... 10

2 Objectives 13

3 Theoretical background 15

3.1 Impedance spectroscopy ... 15

3.1.1 Equivalent circuit modeling ... 17

3.1.2 Data presentation ... 18

3.1.3 Transfilter measurements ... 20

3.1.4 Electric cell-substrate impedance sensing (ECIS) ... 24

3.1.5 Impedance spectroscopy in presence of a redox couple ... 26

3.2 Permeability assays ... 28

3.2.1 Permeability coefficient P_E ... 29

3.2.2 Calculation protocol ... 31

4 Materials and methods 35

4.1 Cell culture techniques ... 35

4.1.1 Cell lines ... 35

4.1.2 General cell culture conditions ... 35

4.1.3 Subcultivation ... 36

4.1.4 Particular inoculation protocols ... 37

4.1.5 Cryopreservation ... 39

4.1.6 Solution osmolarity 40
4.1.7 Buffers and solutions 40
4.2 Electrode preparation 42
4.2.1 Planar electrodes 42
4.2.1.1 Indium tin oxide electrodes 44
4.2.1.2 Gold electrodes 45
4.2.2 Stainless steel electrodes 46
4.2.3 Porous gold electrodes 47
4.3 Impedance measurements 48
4.3.1 Experimental set-up 48
4.3.2 Specific assay conditions 48
4.3.2.1 Transfilter measurements using stainless steel electrodes 49
4.3.2.2 Transfilter measurements including the porous backside electrode 49
4.3.2.3 Combined electrochemical determination of substrate permeability and TEER 50
4.3.2.4 Transcellular permeability monitoring via whole-cell impedance-based biosensors 51
4.3.2.5 ECIS measurements in a 96-well array format 52
4.3.3 Equivalent circuit modeling 52
4.4 Diffusion assays 53
4.4.1 Permeability assay using isotopic tracer molecules 54
4.4.2 Optical permeability assays 54

5 Porous electrodes as transducer for cell-based assays 57

5.1 Preliminary remarks: Resistance contribution of the subepithelial adhesion zone 57
5.2 Characterization of porous electrodes and the measurement chamber 63
5.2.1 Characterization of the measurement set-up 63
5.2.2 Parasitic impedance contributions: correction methods 68
5.2.3 Electrochemical properties of porous electrodes 71
5.3 Impedance analysis of barrier forming cell types in mono- or co-cultures 74

5.3.1 Homogeneous co-cultures 75
5.3.1.1 MDCK-Ir co-culture 75
5.3.1.2 MDCK-hr co-culture 84
5.3.2 Heterogeneous co-cultures 88
5.3.3 Independent access and readout of both compartments 91
5.3.4 Barrier manipulation: Influence of cytochalasin D on co-cultured cell layers 94
5.4 Porous gold electrodes in combination with the ECIS-technique 97
5.5 Summary and conclusion 100

6 Combined electrochemical determination of substrate permeability and TEER 103

6.1 Influence of $[Fe(CN)_6]^{3-/4-}$ on epithelial barrier function 104
6.1.1 Electric cell-substrate impedance sensing (ECIS) 104
6.1.2 Transepithelial electrical resistance in presence of $[Fe(CN)_6]^{3-/4-}$ 106
6.2 Impedance based permeability studies 107
6.2.1 Electrode characterization and set-up calibration 107
6.2.2 Detecting defects within confluent cell layers 112
6.2.3 Impedimetric monitoring of $[Fe(CN)_6]^{3-/4-}$ permeation across cell monolayers 114
6.2.4 Permeability coefficients 119
6.3 Optical analysis of $[Fe(CN)_6]^{3-/4-}$ permeation 122
6.4 Summary and outlook 124

7 Monitoring the permeation of endogenous molecules via whole-cell impedance-based biosensors 125

7.1 U-373 MG cells as sensory element 126
7.1.1 Impact of histamine on epithelial barrier function 126
7.1.2 Monitoring histamine diffusion across barrier forming cell layers 128
7.1.3 Permeability coefficients of H_1R ligands 132
7.2 BAECs as sensory element 136

7.3 Summary, conclusion and outlook 138

8 Impedimetric monitoring of epithelial barrier function: relevance and perspectives 141

9 Summary 143

10 Zusammenfassung 147

11 References 151

12 Appendix 159

12.1 Supplementary information 159

12.2 Abbreviations and symbols 175

Curriculum vitae 179

Danksagung 181

1 Introduction

Four basic types of tissues are found in mammalian organisms - nervous, muscle, connective and epithelial tissue. They differ in both structure and function (Patton 2015). The latter is often subdivided into two parts, the membranous (or surface) epithelium and glandular epithelium. Furthermore, surface epithelium is classified by its cell shape and the number of cell layers (simple or stratified structures). Simple, one layered epithelial tissue can be found as blood or lymphatic vessel linings. In this case, the squamous epithelium is called endothelium. Simple cuboidal or columnar epithelial tissue is lining glands and their ducts (e.g. in the kidney) or parts of the digestive system. Depending on the physiological location and the tissue structure, epithelial cell layers execute various functions. Sensory functions, secretory activities as well as the absorption of nutrients or the excretion of metabolic products is rendered by epithelial tissues. In order to allow directional transport processes, epithelial cell sheets exhibit tight cell-cell contacts and an apical/basal membrane polarity. The molecular composition of lipids and proteins in the apical (luminal) membrane domain differs from the basolateral membrane domain (Balcarova-Staender et al. 1984). This asymmetric distribution and activity of transport proteins, ion channels or pumps is in combination with a tight sealing of the intercellular gaps essential for a directed transcellular substance transport. The connection of neighboring cells via cell-cell contacts prevents the uncontrolled paracellular diffusion of most hydrophilic molecules as well as the lateral diffusion of membrane components, thereby also maintaining the apical/basal polarity. Additionally, the membrane area of epithelial tissue, which is involved in absorption processes, is often increased due to the formation of microvilli in the apical membrane domain. An increased apical surface area is favorable for rapid and effective transport or absorption processes. Arranged as a sheet of densely packed cells with adjustable intercellular junctions, each cell also exhibits contacts to a basement membrane (cell-substrate junctions). This membrane is a network of extracellular matrix proteins onto which the cells can adhere. The basement membrane allows a mechanical stabilization of the epithelium and separates it from the connective tissue below (Wang et al. 1990).

Epithelial cell layers form tight diffusion barriers to separate two physiologically neighboring compartments (e.g. organs) from each other mainly via tight junctions. These intercellular barriers control the diffusion of proteins, metabolites or ions and allow the formation and preservation of chemical and electrochemical gradients. Hence, epithelial barrier integrity is

essential to maintain a constant chemical milieu (homeostasis) within an organ. Physiologically important examples for the significance of intact epithelial barriers are the blood-brain-barrier and the blood-cerebrospinal fluid-barrier (Abbott et al. 2006, Weiss et al. 2009). Both barrier systems separate the brain from the circulating blood stream and thereby ensure the homeostasis in brain tissue, which is necessary for neuronal activity and unaffected signal transfer.

The following paragraphs describe the architecture of epithelial cell-cell and cell-matrix contacts. Furthermore, transport pathways across cellular barriers as well as the most common experimental techniques are discussed.

1.1 Epithelial barriers

1.1.1 Architecture of epithelial cell-cell and cell-substrate contacts

Epithelial cells exhibit various connections between adjacent cells and to the basement membrane (Alberts et al. 2015). Besides almost impermeable intercellular contacts (tight junctions), epithelial cell layers are mechanically stabilized by anchoring junctions to the neighboring cells (adherens junctions, desmosomes) and to the basement membrane (actin-linked cell-matrix junctions, hemidesmosomes). Communicating cell junctions are also found in epithelial tissue (gap junctions). These specialized intercellular channels connect the cytosol of two adjacent cells and allow a rapid signal transfer within the epithelium.

Tight junctions are located close to the apical surface of the plasma membrane. By encircling the apical end of the lateral membrane, these junctions seal the intercellular cleft between two neighboring cells (Shin et al. 2006). Thereby, these connections prevent an uncontrolled paracellular diffusion of molecules across the epithelial cell sheet (barrier function) and the lateral diffusion of membrane components from apical to basolateral or vice versa (fence function). Tight junctions consist of transmembrane proteins and peripheral membrane proteins. Transmembrane proteins (occludin, claudins, tricellulin and junctional adhesion molecules) connect the membranes of adjacent cells and seal the intercellular cleft tightly (Staehelin 1973, Furuse et al. 1993, Furuse et al. 1998, Mandell and Parkos 2005, Krug et al. 2014). Several studies indicate that the combination of claudin subtypes determines the tightness of the barrier since they form size and ion selective channels within the tight junctions of cultured epithelial tissue (Van Itallie and Anderson 2006, Furuse 2010). The

intracellular domain of transmembrane proteins is connected via peripheral membrane (scaffold) proteins like *zonula occludens* proteins (Stevenson et al. 1986, González-Mariscal et al. 2000, Fanning and Anderson 2009), the cingulin protein (Citi et al. 1988) or rab13 (Zahraoui et al. 1994) to the cytoskeleton. Hence, also the cytoskeletons of adjacent cells are connected via tight junctions. The tight junctional network is located apical to adherens and desmosome junctions on the lateral membrane. The assembly of these three parts is called the junctional complex. Cadherin-mediated adhesion molecules are the major components of adherens junctions. Cadherins are homophilic, Ca^{2+}-dependent transmembrane proteins that connect neighboring cells in a clustered, zipper-like structure (Shapiro et al. 1995, Gumbiner 1996, Alpha et al. 1997). The cytoplasmic part of cadherin proteins is connected to the actin cytoskeleton via diverse mediator proteins like catenins (Niessen 2007). Hence, adherens junctions are linked to the contractile bundles of belt-like actin filaments (Harris and Tepass 2010). Desmosomes are located underneath adherens junctions and are also cadherin-based structures. However, desmosomal cadherins are packed more densely (Al-Amoudi et al. 2007). In contrast to adherens junctions, desmosomes are coupled to intermediate filaments via adaptor proteins and desmoplakin (Gallicano et al. 1998).
Additional anchoring junctions connect the basolateral cell membrane to the basement membrane (Alberts et al. 2015). Chiefly, proteins of the integrin superfamily mediate the attachment of epithelial cells to the extracellular matrix (ECM). Integrin molecules are composed of two non-covalently associated glycoprotein subunits (called α and β). Heterodimers of different combinations span the cell membrane (Burridge et al. 1988). The extracellular domains of integrins bind directly to specific amino acid sequences in extracellular matrix proteins like fibronectin or laminin (Hynes 2002). Within the cytosol, the β-subunit of an active integrin is connected to actin filaments via several mediator proteins (e.g. talin, Zaidel-Bar et al. 2007). Besides actin-linked cell-matrix junctions (focal contacts), integrin or highly specialized transmembrane proteoglycans can also be connected to intermediate filaments (hemidesmosomes). The β-subunit of integrin $\alpha_4\beta_6$ is thereby linked to intracellular keratin filaments via plectin and BP230 as mediator proteins (Borradori and Sonnenberg 1996, Koster et al. 2003, Litjens et al. 2006).

Unlike tight junctions and anchoring junctions, gap junctions do not contribute to the barrier function or mechanical stabilization of epithelial tissue. Gap junctions are adjustable channel-like structures between two adjacent cells, which allow an electrical and metabolic

coupling. The cytoplasm of an epithelial cell is linked to the neighboring cell by channel-forming transmembrane connexin proteins (Beyer et al. 1990). Six connexin proteins form a hemichannel, called connexon. Two connexons can be assembled to a water filled intercellular channel. Among others, intracellular Ca^{2+} concentration and pH value regulate the permeability of connexons. These pores, with an inner diameter of 1.4 nm, can be opened or closed immediately to adjust the exchange of water, small inorganic ions and other molecules with a molecular mass below 1000 Da like amino acids, glucose or second messengers (Maeda et al. 2009, Nakagawa et al. 2010).

The complex architecture of cell-cell and cell-matrix contacts within an epithelial cell sheet offers several pathways for transepithelial transport or substance diffusion.

1.1.2 Transport routes across epithelial barriers

Compounds can migrate across an epithelial cell layer either on transcellular pathways across the plasma membrane or on the paracellular route between two neighboring cells (Hillgren et al. 1995, Anderson 2001, Wise 2002, Balimane et al. 2006, Komarova and Malik 2010). Thereby, the physicochemical properties of a compound (e.g. solubility, pKa, molecular weight, lipophilicity) determine the transport pathway. Several transport ways are illustrated in Fig. 1.1. Passive diffusion of a molecule is driven by a concentration (or electrochemical) gradient and can either take place on the transcellular pathway mainly for hydrophobic molecules (Fig. 1.1, (1)) or on the paracellular route across the tight junctions for small hydrophilic molecules and ions (Fig. 1.1, (4)). Transcellular diffusion can be facilitated by specialized membrane channels or transport proteins (Fig. 1.1, (2)). Transport processes can also be performed against a given gradient. In this case, the process requires energy which is provided by a coupled reaction (Fig. 1.1, (3)). Primary active transport is based on an ATP-consuming step, whereas secondary active transport (symport or antiport) needs energy from an electrochemical potential difference. For large, hydrophilic molecules active transport is enabled by transcytosis (Fig. 1.1, (6)). In some cases, the absorbed molecule serves as metabolic substrate, which leads to a reduced transcellular transport process (Fig. 1.1, (5)). Reduced absorption is also caused by the presence of efflux transporters either on the apical or basolateral membrane domain (Fig. 1.1, (7)).

Transport processes across intact epithelial cell layers are strictly regulated under physiological conditions in order to maintain organ specific functions and homeostasis.

Alterations within the cellular junctions and the resulting effects on the barrier properties of epithelial tissue can induce pathological conditions. In principle, epithelial barrier integrity is essential to maintain the physiological functions of several organs like lung, kidney, liver and the intestine (Fink and Delude 2005). Epithelial or endothelial dysfunction can contribute to respiratory inflammations (Holgate 2007), edema formation (Abbott et al. 2006) or the development of atherosclerotic lesions (Davignon and Ganz 2004). Hence, the investigation of epithelial or endothelial barrier integrity is of wide scientific interest. In order to gain detailed structural of functional information, scientists utilize *in vitro* assays. Several technical approaches which are commonly used to characterize the regulation and dynamics of epithelial barrier function are discussed in the following section.

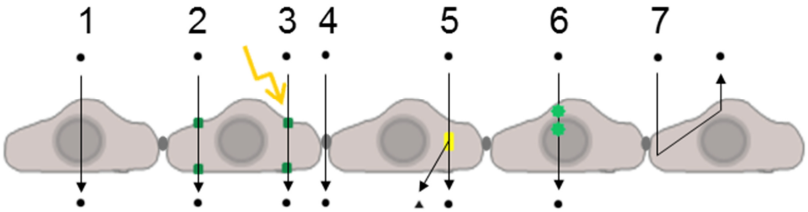

Fig. 1.1: Transport routes across epithelial cell layers: **1** passive transcellular diffusion; **2** facilitated diffusion; **3** primary active or secondary active transport; **4** passive paracellular diffusion; **5** metabolic conversion; **6** receptor-mediated transport/transcytosis; **7** absorption limited by efflux transporters.

1.2 Quantification of epithelial barrier function

In vitro assays are commonly performed to quantify epithelial barrier function. Three main aspects are of interest: (i) The permeability of water through epithelial cells is characterized by its hydraulic permeability coefficient P_f. (ii) The permeability of small inorganic ions gives rise to the transepithelial electrical resistance (TEER). (iii) The third parameter is calculated from the permeability of uncharged (macro)-molecular probes across the epithelial barrier which results in the molecular permeability coefficient P_E. The following chapter describes the basic concepts and experimental strategies to characterize epithelial permeability.

1.2.1 Water permeability

Water can pass biological barriers either via simple diffusion across the lipid bilayer or through membrane channels (or pores). In absence of any pressure gradient and under steady-state conditions, Fick's first and second law give rise to the diffusive water flux J_w across a membrane and to the diffusional permeability coefficient of water P_d [cm/s]:

$$J_w = - D_w \left(\frac{\Delta c_w}{\delta}\right) = - P_d \, \Delta c_w \qquad (1.1)$$

including the diffusion coefficient of water D_w, the water concentration difference Δc_w and the membrane thickness δ. The diffusional water permeability is commonly measured by radiolabeled water flux (^{3}HHO, ^2H_2O, $H_2{}^{18}O$) or via NMR-techniques (Solomon 1989, Ye and Verkman 1989, Verkman 1995).

Physiologically important water flux across a biological cell membrane is driven by the differences in hydrostatic pressure (ΔP) and/or osmotic pressure ($\Delta\pi$). The volume flux J_{volume} across a membrane can be described as:

$$J_{volume} = L_p \, (\Delta P - \sigma_s \Delta\pi) \qquad (1.2)$$

where L_p is the hydraulic permeability (in cm·s^{-1}atm^{-1}). The solute reflection coefficient σ_s displays the membrane selectivity for a solute in comparison to water. The coefficient σ_s can range between 0 (solute permeability is equal to water permeability) and 1 (no solute permeability). Only if σ_s = 1, the volume flux across a cell membrane is equal to the water flux. The term ($\sigma_s\Delta\pi$) is often referred to as effective osmotic pressure difference (Schafer et al. 1978, Curry 1985, Maurel 1997, Baumgarten and Feher 2001, Wills et al. 2012, Hamilton and Devor 2016). The proportionality constant L_p (hydraulic permeability, hydraulic conductivity or filtration coefficient) is relating volume flux to hydrostatic pressure as well as to osmotic pressure.

A quantitative description of transmembrane water transport requires the quantification of the hydraulic permeability coefficient L_p and the ratio of osmotic permeability coefficient P_f to diffusional water permeability coefficient P_d (Verkman et al. 1996). Equation 1.2 can be used to measure the hydraulic permeability L_p in absence of a hydrostatic pressure difference ($\Delta P = 0$). Therefore, an osmotic pressure difference ($\Delta\pi$) is applied by adding an impermeable solute (σ_s = 1) to one side of the epithelial cell sheet. The change in cell water volume over time (dV_{cell}/dt) can be used to calculate L_p in response to the imposed osmotic pressure difference, with A_{mem} as the membrane area (Kleinhans 1998).

$$L_p = \frac{\mathrm{d}V_{cell}}{\mathrm{dt}} \left(\frac{1}{A_{mem} \, (\sigma_s \Delta\pi)}\right) \qquad (1.3)$$

Several methods are common to study cell volume changes of adherently growing cells, e.g. via light scattering techniques, total internal reflection or confocal microscopy (Verkman

2000). In addition, cell volume changes can be detected with impedance-based techniques (Kimelberg et al. 1992, Hua and Pennell 2009) or via surface plasmon resonance spectroscopy (Robelek and Wegener 2010). The hydraulic permeability L_p can be converted into the osmotic water permeability coefficient P_f [cm/s] according to:

$$P_f = L_p \left(\frac{RT}{V_w}\right) \tag{1.4}$$

with V_w as the partial molar volume of water, R as the gas constant and T as the absolute temperature. The ratio of osmotic to diffusional water permeability is often used as an indicator for a predominantly diffusional or non-diffusional water transport. For a purely diffusional process the ratio P_f/P_d equals unity. In biological membranes, especially in epithelial tissue, high P_f/P_d ratios are reported, giving evidence to the presence of water transporting proteins called AQPs (aquaporins, Preston and Agre 1991, Murata et al. 2000, Verkman and Mitra 2000). Techniques to quantify the diffusional and osmotic permeability coefficients are experimentally very challenging and error prone (e.g. due to unstirred water layers, Korjamo et al. 2009, Whittembury and Reuss 1992, Günzel et al. 2010). Additionally, a differentiation between transcellular, aquaporin-mediated and paracellular water flux across the tight junctional complex is only indirectly accessible (Carpi-Medina and Whittembury 1988, Rosenthal et al. 2010). Blocking the transcellular pathway by inhibition of aquaporin channels with mercury, the only potent AQP blocker, is often not an option since its effective concentration causes cytotoxic effects in many cells and tissues (Knepper 1994). On the other hand, blocking the paracellular pathway with inhibitors such as protamine was unsuccessful due to possible transcellular side effects (Poler and Reuss 1987, Loeschke and Bentzel 1994). Hence, determination of epithelial permeability to ionic species and uncharged molecular probes became the methods of choice to quantify epithelial barrier function.

1.2.2 Molecular permeability

Solute flux across cellular barriers is often studied via simple permeation assays. For these widely used and well-established assays, the cells are cultured on highly permeable filter supports which are needed for mechanical support. The commercially available filter membranes differ in membrane material as well as pore size and density. To avoid any additional restrictive effect of the membrane, pore size and density should be at a maximum. Cell-covered filter inserts are placed into a standard two-chamber set-up. Thereby, the

epithelial cell sheet acts as diffusion barrier between both fluid filled compartments. The set-up provides independent access to the apical cell surface as well as to the basolateral side and, hence, mimics the physiological conditions of an epithelium. To analyze the barrier function of epithelial cells, a tracer compound is added to one of both compartments (donor side). If the tracer molecule can pass the cellular barrier, its accumulation is detected over time in the receiver compartment. In order to prevent an additional diffusive contribution due to the presence of unstirred water layers (Youdim et al. 2003) the assay should be performed under mild agitation. Furthermore, a strict control of temperature and buffer pH value is necessary. The time-dependent increase in tracer concentration is used to calculate the molecular permeability coefficient P_E (denoted in cm/s). A derivation of the equation for P_E as well as a detailed calculation protocol is given within the theoretical section (chapter 3.2). The molecular tracer compound should meet several requirements. Highly water-soluble compounds are used if transcellular diffusion via the plasma membrane has to be excluded. Additionally, information about compound-specific transcellular diffusion pathways via cellular transport systems (active transport or facilitated diffusion) is needed. Typical tracer molecules for these standard *in vitro* assays are sucrose, mannitol, inulin or high molecular weight probes like dextrans or polyethylene glycols (Sanders et al. 1995, Ghandehari et al. 1997). These tracer molecules can pass epithelial cell layers only by the paracellular pathway. Depending on the size of the compound, diffusion across the junctional complex is mediated by two different pathways (Spring 1998, Cohen et al. 1999, Watson et al. 2001, Neuhaus et al. 2006, Van Itallie et al. 2008, Krug et al. 2009a). Diffusion across the tight junctions is mainly mediated by a high number of small pores (diameter ~ 8 Å) located at the bicellular junctions. Larger pores (diameter ~ 100 Å, Staehelin 1973) are supposed to be located at the contact zone of three adjacent cells (tricellular tube, Ikenouchi et al. 2005) and enable the paracellular diffusion of macromolecules (> 20 kDa). Since the number of tricellular tubes is relatively low, their contribution to the overall paracellular diffusion capacity is of around 1 % (Krug et al. 2009a).

The detection of a molecular probe in the receiver compartment depends on the labeling type. Most often, the tracer compound is linked to a small fluorescent dye (e.g. fluorescein isothiocyanate, FITC) or the molecule is radiolabeled at a specific position. Coupled detection techniques like liquid chromatography are used for unlabeled compounds. At preset time points after addition of the tracer compound, samples of the fluid in the receiver compartment are analyzed. Besides this time and cost consuming step, the coupling of a fluorescent label

can alter the physicochemical properties of a tracer compound significantly. In addition, real-time information of the junctional constitution cannot be provided using a static two-chamber set-up, since the accumulation of the tracer in the receiver compartment usually takes time (Matter and Balda 2003). These permeation assays are performed extensively to monitor and quantify cellular barrier function, but the specific permeability coefficient is an integrated parameter which reflects the permeability of the entire cellular surface area. Small defects within the confluent cell layer (e.g. due to apoptosis) might cause a short-cut to tracer flux and thereby lead to a misinterpretation of cellular barrier function. A lateral resolution of tracer permeability can illustrate the heterogeneities in paracellular barrier function (Sill et al. 1992). Phelps and DePaola used agarose gels instead of a liquid receiver compartment in order to visualize spatial variations in transendothelial macromolecular transport (2000). The labeled tracer compound diffuses across the cell layer directly into the gel underneath the filter membrane. The agarose gel hinders the tracer diffusion and thereby enables a spatial mapping of the macromolecular permeability at a given time point. However, the lateral resolution remained low with this approach. It could be optimized by the use of affinity interactions. For this purpose, the tracer compound is additionally conjugated to e.g. avidin and the cells are cultured on a biotinylated adhesive matrix (gelatin or collagen networks) instead of using permeable membranes (Dubrovskyi et al. 2013). An elegant method to enhance the lateral resolution below cellular dimensions was published by Michaelis et al. in 2012. Instead of using permeable filter membranes as mechanical support, the authors cultured epithelial cells directly on macroporous substrates. The small pores in the substrate are densely packed and only open to the side which is facing the cell layer. A penetrating fluorescent tracer compound accumulates in these femtoliter cavities at the site of permeation and can be visualized by using an upright confocal laser scanning microscope. This set-up can additionally be used to image local defect areas in the cell layer and to discriminate between trans- and paracellular diffusion. Furthermore, Michaelis and colleagues combined the lateral permeability assay with an impedimetric monitoring of the cell layer. But not only fluorescent tracer molecules can be used to image spatially resolved permeation profiles. The diffusion of redox-active compounds (e.g. ferrocene methanol or ruthenium hexamine chloride) across an epithelium has been visualized by means of scanning electrochemical microscopy (SECM) in a non-invasive and time-resolved way. Passive transport of these redox mediators was recorded by using ultramicroelectrodes with sub-cellular resolution (Bergner et al. 2012).

1.2.3 Ionic permeability

The most common measure of epithelial permeability to small inorganic ions is the transepithelial electrical resistance (TEER). The TEER mainly expresses the permeability to Na^+, Cl^-, K^+ and HCO_3^- ions for a non-selective epithelium (Günzel et al. 2010). The electrical resistance of an epithelium is often measured routinely during *in vitro* cell culture periods to reflect the state of confluency. For this purpose, the cells are again cultured on permeable filter supports as described previously. Two sets of electrodes are placed into both compartments. One set of electrodes is needed to apply a direct current (DC) across the cell layer. The resulting voltage drop is detected with the second electrode pair. The described arrangement is referred to as 'chopstick'-electrode set-up. According to Ohm's law, the resistance can be calculated as the ratio of voltage to current. However, the resistance of a cell-free filter insert (including the buffer resistivity / bulk resistance) must be determined separately and subtracted. Denoted in Ωcm^2, TEER is an integral and area-specific measure for ionic permeability of the entire cell layer. Due to its integral nature, TEER is prone to misinterpretation in analogy to the permeability coefficient P_E mentioned above. Short-cuts to current flow result in a highly decreased resistance value. Since the permeable inserts are often not optically transparent, the absence of single cells within an otherwise confluent cell layer is difficult to detect in advance. Additionally, TEER determined with these handheld devices is strongly dependent on the position of the probing electrodes (Jovov et al. 1991). Reliable results can be obtained by using Ussing chambers, where the four electrodes are fixed in position (Ussing 1949, Kottra et al. 1989). Modern devices no longer work under DC conditions. In order to avoid polarization effects to the electrodes or the cell layer, low-frequency AC (alternating current) conditions are used (± 10 μA, 12.5 Hz).

However, the content of information remains low by using DC or 'near DC' conditions. The transepithelial electrical resistance can be calculated via reciprocal addition of transcellular (due to the resistance of open ion channels) and paracellular resistance (Powell 1981). Most state-of-the-art approaches enable a more detailed analysis of the epithelial cell layer by applying an alternating current or voltage. The cell-covered filter insert is therefore placed in between two electrodes which are fixed in position to guarantee homogeneous electric field conditions (Wegener et al. 2004). Instead of analyzing the signal at a single fixed frequency, impedance spectroscopy (IS, chapter 3.1) can be carried out in an automated manner and over a broad frequency range (typically 1 – 10^6 Hz). The amplitude and the phase of an AC

current are measured while the frequency of the applied voltage is swept. The resulting total AC impedance contains information about the transepithelial electrical resistance. Additionally, IS allows a reliable determination of both, the TEER and the bulk resistance in one experiment. Information about the cell membrane capacitance is also available as the dielectric core of the lipid bilayer acts as electrical capacitor. All three parameters (TEER, bulk resistance, membrane capacitance) can be extracted at any time point from the complex impedance spectra by means of equivalent circuit modeling. However, this approach does not allow a differentiation between trans- and paracellular resistance. Krug et al. published a technique based on impedance spectroscopy, that allows to differentiate between paracellular and transcellular ion transport pathways (2009). Krug and colleagues combined IS and flux measurements of paracellular marker compounds. Provided that the marker is exclusively transported across the cell layer on the paracellular pathway and that the resistance of this pathway can be modulated without affecting transcellular resistance, the contribution of the transcellular resistance to the overall TEER can be calculated. As trans- and paracellular pathways get analyzed, the authors entitled this technique as two-path impedance spectroscopy (2PI, Günzel et al. 2010, Günzel et al. 2012). Even if the integral transepithelial electrical resistance can be broken down into its trans- and paracellular contributions, paracellular resistance does not reflect the resistance due to the tight junctional complex only. The paracellular resistance determined via impedance spectroscopy still includes the lateral intercellular resistance and the resistive contribution due to the cell-substrate adhesion zone (Lo et al. 1999). The latter can be quantified by another impedance-based technique referred to as electric cell-substrate impedance sensing (ECIS). Instead of using porous filter membranes, the cells are directly cultured on the measurement electrodes. The lack of a basolateral compartment excludes the application for transport studies. However, the ECIS technique offers the possibility to determine the resistance contribution arising from the cell-substrate contacts (Giaever and Keese 1984, Giaever and Keese 1991, Giaever and Keese 1993). Both techniques, impedance spectroscopy for filter grown cells and the ECIS method are discussed in detail in the theoretical section (chapter 3.1.3 and 3.1.4). Electrical resistance measurements are valuable tools to study and quantify cellular barrier properties. These non-invasive techniques can be used to monitor epithelial or endothelial barrier function in an automated set-up. However, a combination of at least two of the above mentioned techniques is required in order to determine all cell-specific parameters (Tab. 1.1). Neither impedance recordings of filter grown cells nor ECIS measurements take account for

local heterogeneities in cellular barrier function. In 1997 Gitter et al. used impedance measurements in standard Ussing chambers and combined the technique with mobile-scanning microelectrodes to image local differences in transepithelial resistance (Gitter et al. 1997, Gitter et al. 2001). The microelectrodes are adjusted directly above the cell surface. A heterogeneous clamp current is applied across the epithelium while the microelectrodes are detecting the local and confined potential. These conductance or voltage scanning techniques provide distinct local conductivity data. Conductance scanning can be used to detect local defects within the cell layer and the lateral resolution can be enhanced such that differentiation between para- and transcellular resistance becomes possible.

Besides the resistance measurements summarized above, various other methods are performed to determine epithelial ion permeabilities. Among other techniques, ion flux measurements are used to study the permeability of radioactive isotopes (Bijvelds et al. 1997) similar to the molecular permeability measurements described above (chapter 1.2.2). Dilution potential or bionic potential experiments can also be performed to determine the relative permeability of chloride ions to sodium ions or other monovalent cations (Sugiharto et al. 2008, Günzel et al. 2010). In order to discriminate between trans- and paracellular ion movement, permeability measurements are often performed at low temperature. Active membrane-mediated transport mechanisms are temperature-dependent, whereas passive paracellular diffusion is much less affected. Furthermore, the paracellular permeability of ions should be independent of the direction, so that diffusion studies can be carried out in both directions (apical ↔ basolateral) to provide further insights.

Tab. 1.1: Resistance measurements and the accessible cell-related parameter (DC: direct current, AC: alternating current, 1PI: conventional impedance spectroscopy IS, 2PI: two-path impedance spectroscopy, ECIS: electric cell-substrate impedance sensing, TEER: transepithelial electrical resistance, R_{para}: paracellular resistance, R_{trans}: transcellular resistance, R_{sub}: resistance contribution due to cell-substrate adhesion, C_{mem}: membrane capacitance).

	DC technique	**AC techniques**		
parameter	**'chopstick' electrodes**	**1PI**	**2PI**	**ECIS**
TEER	+	+	+	+
R_{para}			+	
R_{trans}			+	
R_{sub}				+
C_{mem}		+	+	+

2 Objectives

Epithelial or endothelial barrier dysfunction is significantly involved in various diseases (Fink and Delude 2005, Holgate 2007, Weiss et al. 2009, Komarova and Malik 2010). Great efforts have been made to investigate the dynamics and alterations of epithelial barriers under physiological and pathological conditions. *In vitro* models are designed to mimic *in vivo* like conditions and to study changes in response to certain stimuli. The transepithelial or -endothelial electrical resistance (TEER) serves as a measure for barrier function of filter grown cell layers. TEER can be recorded routinely in a non-invasive way under physiological conditions. However, TEER is not only determined for single cell layers but also for co-culture systems where cells are cultured on either side of a porous filter device. When physiologically neighboring cell types are probed, the measured overall transcellular resistance is influenced by both cell layers to an unknown extend. It was the aim of this thesis to develop a device that can be used to monitor the integrated overall transcellular resistance of co-cultured cell layers together with the individual monolayer contributions. The new device should fit into the standard transfilter measurement systems and it should be compatible with other impedance-based assay formats like the ECIS system. Furthermore, the new device should be evaluated in studies regarding cell attachment and spreading as well as barrier disintegration.

Due to the non-invasive nature of TEER measurements and their outstanding temporal resolution, the transcellular resistance is often favored over permeability assays to ensure barrier integrity. *In vitro* permeability assays are highly relevant to study the permeation of certain endogenous compounds or novel drug candidates across intact interfacial tissues. The permeation of the target compound across the barrier is commonly followed via a fluorescence or radio-labeling. So far, the compound detection is generally performed discontinuously and both assay types, TEER measurement and permeability assay, are executed consecutively. Thus, the second project in this thesis addressed an impedance-based device for a combined TEER and permeation assay. A simultaneous and automated permeability monitoring should be enabled by using a redox active tracer compound which provides a concentration-dependent impedance readout. After having confirmed no cytotoxic or barrier altering effects of the redox tracer, the device should be used to determine the compound and cell specific permeability coefficients. Additionally, several sensing electrodes at different sites underneath the filter should enable a spatially

resolved permeability determination to detect existing barrier heterogeneities within the confluent cell layer.

Most standardized *in vitro* permeability assays are based on labeled tracer molecule. Since the technical effort is a lot smaller, fluorescent probes are often preferred over radiolabeled marker compounds. However, the covalent coupling of fluorophores to the tracer compound consequently alters the physicochemical properties of the tracer. Thus, *in vitro* results must be interpreted with caution regarding its transfer to *in vivo* like conditions. The situation is even more pronounced when the permeation of endogenous molecules, like neurotransmitters (like dopamine, histamine or glutamate) or inflammatory mediators, across the blood brain barrier are under investigation (Abbott 2000, Abbott et al. 2006). Until now, the detection of unlabeled compounds is only possible by using a subsequent detection technique like liquid chromatography.

Hence, the aim of the third project within this thesis was to overcome this limitation. Integrated into the receiver compartment, a whole-cell impedance based biosensor should enable a fast and continuous detection of unlabeled, endogenous compounds (ligand) of interest via a specific ligand-receptor-interaction in the sensory cells. The set-up should be evaluated by proof-of-concept studies. Furthermore, the permeability of a specific ligand across an intact epithelial barrier as returned by the response of the biosensor-based assay should be compared to standard permeability measurements using isotopic tracer compounds.

3 Theoretical background

The theoretical section provides basic information about all methods and assay techniques important for this thesis. The chapter is mainly focused on the field of impedance spectroscopy (IS). This method is a highly versatile tool to investigate electric properties of a variety of solid materials and electrochemical systems (Macdonald 1992, Lasia 2002). The complex impedance Z of a system depends on the frequency of a sinusoidal alternating current signal which is used for excitation and provides detailed information about resistive and capacitive components of the studied system. Since applying small amplitudes of exciting alternating current (AC) or voltage enables a damage-free investigation, IS became a very appropriate method to analyze biological samples in a non-invasive way.

Besides this electrochemical method, the second part of this chapter describes a special assay technique which is used to quantify endothelial or epithelial barrier function. In addition to the permeability of water or small inorganic ions, the permeability of molecular probes across a cell layer is a widely studied parameter to describe barrier function efficiency (Wegener and Seebach 2014). Permeability assays are performed to determine the specific permeability coefficient P_E of a tracer molecule. The theoretical section about permeability assays addresses the fundamental equations and boundary conditions for the calculation of P_E.

3.1 Impedance spectroscopy

According to Ohm's law, the resistance R of an electric system in a DC (direct current) circuit is defined as the ratio of applied voltage U to resulting current I.

$$R = \frac{U}{I} \tag{3.1}$$

However, IS applies a sinusoidal AC voltage as excitation signal. Thus, the AC voltage $U(t)$ is described as a function of frequency w and time t:

$$U(t) = U_0 \sin(wt) \tag{3.2}$$

where $w = 2\pi f$ is the angular frequency and f is the AC frequency. The resulting current $I(t)$

has a sinusoidal form of the same frequency as the exciting voltage with the amplitude I_0 and is shifted in phase φ if the studied system is not perfectly resistive. $I(t)$ can be mathematically expressed as:

$$I(t) = I_o \sin(wt - \varphi) \tag{3.3}$$

Euler's formula is used to express AC voltage and current as complex quantities:

$$U(t) = U_0 e^{i(wt)} \tag{3.4}$$

and

$$I(t) = I_0 e^{i(wt-\varphi)} \tag{3.5}$$

where $i = \sqrt{-1}$.

According to Ohm's law, the complex impedance Z of an AC circuit is given by the ratio of complex voltage (eq. 3.4) to complex current (eq. 3.5):

$$Z = \frac{U(t)}{I(t)} = \frac{U_0 e^{i(wt)}}{I_0 e^{i(wt-\varphi)}} = \frac{U_0}{I_0} e^{i\varphi} = |Z| e^{i\varphi} \tag{3.6}$$

In the complex Gaussian plane (imaginary part plotted as a function of the real part) the complex impedance is displayed as a vector (Fig. 3.1). The length of this vector corresponds to the impedance magnitude $|Z|$. The angle between $|Z|$ and the real axis determines the phase shift φ between voltage and current. The real part R of the complex impedance Z arises from current which is in-phase with the applied alternating voltage. Besides the resistance R, capacitive and inductive impedance contributions induce a phase shift between voltage and current and are represented by the imaginary part reactance X.

Using Cartesian coordinates, Z can be expressed as the sum of its real and imaginary part:

$$Z = Re(Z) + i\, Im(Z) = R + i\, X = |Z| \cos\varphi + i\, |Z| \sin\varphi \tag{3.7}$$

Resistance R and reactance X can be converted into the polar coordinates impedance magnitude $|Z|$ and phase angle φ:

$$|Z| = \sqrt{R^2 + X^2} \tag{3.8}$$

and

$$\varphi = \arctan\left(\frac{X}{R}\right) \tag{3.9}$$

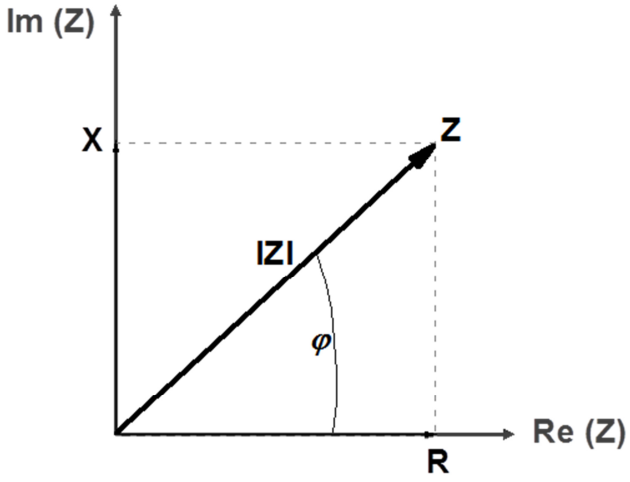

Fig. 3.1: Representation of the impedance Z in the complex Gaussian plane. The x-axis is the real part of the complex impedance $Re(Z)$, whereas the ordinate displays the imaginary part $Im(Z)$. Z can be described in polar coordinates by the vector length $|Z|$ (impedance magnitude) and the angle φ (phase shift between voltage and current).

3.1.1 Equivalent circuit modeling

In order to identify the impedance contribution of different electrochemical components in a given system, electric equivalent circuits with a similar frequency-dependent response are constructed. Therefore, several electric elements are commonly arranged to a network. Besides ideal electric elements (resistor *R*, capacitor *C* and inductor *L*), non-ideal empirical elements (e.g. constant phase element, CPE) can be introduced (Tab. 3.1), since ideal elements are not always suited for the description of electrochemical systems. Empirical circuit elements are used to characterize systems where charge transporting ions show a different behavior in comparison to electrons in common electric elements (Lasia 2002). The CPE represents the non-ideal capacitive behavior of solid electrodes which are in contact to an electrolyte. While the observed phase angle is constant, the double-layer capacitance of the electrodes is frequency-dependent. The CPE can be described by the two parameters A_{CPE} and n_{CPE}. With n_{CPE} = 1, the element behaves like an ideal capacitor (A_{CPE} = C). When n_{CPE} equals a value of 0, the CPE acts as a pure resistor (A_{CPE}^{-1} = R). Any value for n_{CPE} between 0 and 1 leads to resistive and capacitive properties of this empirical circuit element. The frequency-dependence of the electrodes' capacitance is often explained as a consequence of surface roughness (inhomogeneities) and ion adsorption (Raistrick and

Macdonald 2005). Thus, CPE is used to describe the impedance contribution of an electrode-electrolyte interface, with its' double layer exhibiting non-ideal capacitive behavior (Pajkossy 1994). °

Tab. 3.1: Impedance contribution and phase shift of equivalent circuit elements.

equivalent circuit element	parameter	impedance Z	phase shift φ
Ohmic resistor	R	R	0
capacitor	C	$(iwC)^{-1}$	- π/2
inductor	L	iwL	+ π/2
constant phase element CPE	A, n ($0<n<1$)	$(iw)^{-n}A^{-1}$	-nπ/2

The parameters *R*, *L*, *C* and CPE are sufficient for the description of an electrochemical system. However, in the presence of redox species in solution, an electrochemical process involving the transfer of electrons across the electrode interface may occur. A detailed discussion for an electric circuit containing a faradaic reaction is presented in chapter 3.1.5.
Complex circuit models must be correctly simplified in order to avoid an over-parameterized (redundant) system. Since the same data may be exactly described by different equivalent circuit models, additional information is often necessary to decide which circuit fits best to the electrochemical system. Once an adequate equivalent circuit is constructed, the corresponding transfer function can be calculated according to Ohm's and Kirchhoff's laws. The transfer function is the mathematical expression of the equivalent circuit. To identify the impedance contribution of the individual elements involved in a system under study, the calculated impedance of the equivalent circuit is compared to the experimental data (chapter 4.3.3).

3.1.2 Data presentation

There are two ways to present impedance data in a graphical manner. Complex plane plots (Argand diagrams or Nyquist plots) visualize impedance data by plotting the imaginary part of the impedance against the real part. Since the imaginary part is usually negative, - *Im(Z)* is plotted versus *Re(Z)*. However, these complex plane plots do not contain information about the frequency domain. Therefore, some frequencies are often added to better visualize the frequency domain. Bode plots represent the second graphical impedance plot. The logarithm of the impedance magnitude (log $|Z|$) and the phase angle (φ) are plotted against the logarithm of the frequency (log f). The following paragraph demonstrates the interpretation of

a Bode plot for a simple electric circuit.

The equivalent circuit describing an electrode, which is in contact to an electrolyte, is shown in Fig. 3.2. Herein, the electrical circuit is represented by a serial combination of a resistor (R_{bulk}, electrolyte resistance) and a constant phase element (CPE).

The CPE combines the sum of the capacitance of the working electrode (CPE_{WE}) and the counter electrode (CPE_{CE}) when the impedance is measured in a two-electrode-cell.

$$\frac{1}{CPE_{system}} = \frac{1}{CPE_{WE}} + \frac{1}{CPE_{CE}} \tag{3.10}$$

If only the impedance of the working electrode is of interest, the surface area of the counter electrode must be increased so that the second term in equation 3.10 can be neglected.

According to Ohm's and Kirchhoff's laws (chapter 3.1.1), the transfer function of the R_{bulk}-CPE circuit is:

$$Z\,(w) = R_{bulk} + \frac{1}{(iw)^n A} \tag{3.11}$$

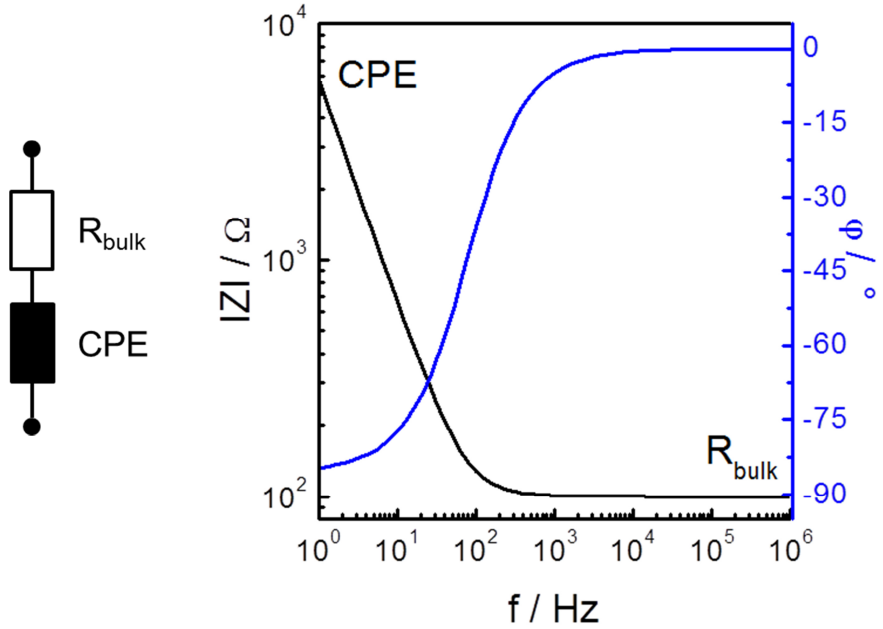

Fig. 3.2: Equivalent circuit and calculated Bode plot for an R_{bulk}-CPE connection in series. The Bode plot includes information about the impedance magnitude $|Z|$ and the phase angle φ. Parameters: R_{bulk} = 100 Ω, A_{CPE} = 30 μFs$^{(n-1)}$/cm^2, n_{CPE} = 0.95.

The Bode plot in Fig. 3.2 clearly shows that the Ohmic resistance of the electrolyte dominates the impedance in the high frequency range (horizontal line). This frequency-independent behavior is represented by a horizontal line of the impedance magnitude running parallel to the x-axis in the Bode plot. The phase shift in this frequency range is 0° (horizontal line). With decreasing frequency, the capacitance characteristics of the constant phase element influence the impedance signal progressively. The impedance magnitude increases while the phase angle decreases from 0° to a minimum of around - 85° when n_{CPE} is 0.95.

3.1.3 Transfilter measurements

Impedance spectroscopy is applied heavily to investigate biological systems like mammalian cell layers or even tissue. Therefore, permeable filter supports are often used as culture substrates for endothelial or epithelial cells to mimic the physiological situation of interfacial tissues between two compartments. The cell layer resistance is measured by placing two measurement electrodes on either side of the cell-covered filter membrane. Resistance measurements are performed by two slightly different techniques, regarding the electrode arrangement and measurement conditions. As afore mentioned (chapter 1.2.3), chop-stick electrodes can be placed on each side of the filter membrane. With this set-up the measured cell layer resistance is determined at a specific frequency and the result is strongly dependent on the electrode positioning. An inherent inhomogenous electric field across the cell layer often leads to an overestimation of the measured resistance (Jovov et al. 1991). In order to increase accuracy, information content and throughput of transfilter measurements, a device published by Wegener et al. (2004) is often preferred. Instead of placing the cell-covered filter membrane in between error-prone chop-stick electrodes, two disk shaped stainless steel electrodes are used. One of these electrodes is integrated in the bottom of the measurement chamber underneath the cell layer, whereas the second stamp-like electrode is dipping into the upper filter compartment. The filter support is fixed in its position. Since the cell layer is sandwiched between these two disk electrodes, a homogeneous electric field across the entire surface of the cell layer is guaranteed. Transcellular resistance measurements can be performed accurately and automated in a standard cell culture incubator. Moreover, the device records the impedance not at a single fixed frequency but over a broad frequency range. The cell layer resistance R_{cl} (or transepithelial /-endothelial electrical resistance, TEER) is then extracted from the impedance spectra by means of equivalent circuit modelling (chapter 3.1.1).

To describe the dielectric properties of the transfilter measurement set-up, the equivalent electrical circuit shown in Fig. 3.2 needs to be expanded by a parallel combination of a resistor and a capacitor ($R_{cl}||C_{cl}$), expressing the electrical properties of the cell layer. Herein, R_{cl} is equivalent to the transcellular resistance (TEER). The parameter C_{cl} describes the dielectric properties of the cellular plasma membrane and C_{cl} includes the serial combination of the apical and basolateral membrane capacitance. The transfer function of this R_{bulk}-($R_{cl}||C_{cl}$)-CPE circuit according to Wegener et al. (2000) is presented in Fig. 3.3 and can be expressed as:

$$Z\,(w) = R_{bulk} + \frac{1}{\frac{1}{R_{cl}} + iwC_{cl}} + \frac{1}{(iw)^n A} \qquad (3.12)$$

As described in chapter 3.1.2 (Fig. 3.2), the impedance magnitude is again dominated by the Ohmic resistance of the electrolyte R_{bulk} in the high frequency range (phase angle = 0°). The electrode-electrolyte interface for both electrodes is represented by the empirical impedance element CPE, which dominates the impedance magnitude in the low frequency range (phase angle - 85° for n_{CPE} = 0.95). In the mid frequency range, impedance magnitude and phase

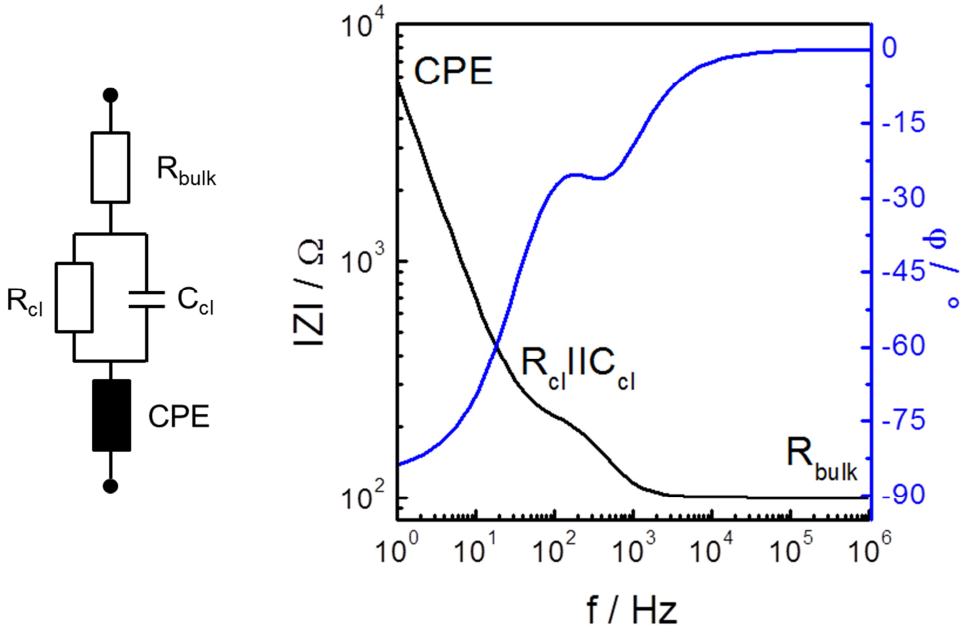

Fig. 3.3: Equivalent circuit and calculated Bode plot for an R_{bulk}-($R_{cl}||C_{cl}$)-CPE circuit. The impedance contribution of the cell layer is affecting $|Z|$ and φ in the mid frequency range. Parameters: R_{bulk} = 100 Ω, R_{cl} = 100 Ωcm^2, C_{cl} = 5 µF/cm^2, A_{CPE} = 30 µFs$^{(n-1)}$/cm^2, n_{CPE} = 0.95.

shift are influenced by the impedance contribution of the cell layer, resulting in a plateau region. The height of this plateau depends on the resistance of the cell layer, whereas the width is influenced by its capacitance. In this particular frequency range, the current is forced to flow through the pores of the filter support, into the narrow gap between filter and basolateral cell membrane and around the cell bodies in between two neighboring cells to escape in the bulk electrolyte. For this paracellular pathway, cell-cell-contacts display a restriction (R_{cl}, TEER).

Fitting this equivalent circuit to the recorded experimental data offers the possibility to determine two specific, but integrated, cell related parameters. The parameter R_{cl} quantifies the cellular barrier function and is usually calculated with respect to the cell covered area (expressed in Ωcm^2). C_{cl} represents the cell layer capacitance for a given area as the reciprocal of the sum of the reciprocals of basolateral and apical membrane capacitance (denoted in $\mu F/cm^2$). However, the calculated resistance (TEER or R_{cl}) reflects the resistance of the paracellular pathway only for moderately tight epithelial or -endothelial cell layers. In case extremely tight or very leaky cell layers are probed, the calculated TEER is affected by other resistive contributions. When impedance measurements on very tight cell layers are performed, a distribution of current flow can occur. If the resistance of the paracellular pathway is similar to the cell membrane resistance, the current can either follow the paracellular pathway across the cell junctions or the transcellular pathway through the cell membranes. Both contributions are then included in the measured resistance. With the parallel connection of both resistance elements, a differentiation is not possible without further experiments (e.g. two-path impedance spectroscopy, chapter 1.2.3). Lo et al. mentioned a second resistive parameter which must be considered when TEER measurements are discussed (1999). The width of the narrow cleft between the filter surface and the lower cell membrane is only 50 to 200 nm. The length of this cleft depends on the filter porosity (pore diameter, pore density) and on the specific cell diameter. Paracellular current has to flow from the pores underneath the cell layer through the cell-substrate adhesion region before it reaches the cell periphery. This resistive contribution (R_{sub}) due to the cell-substrate adhesion zone increases with the cellular diameter and the reduction of the cleft height. Since this additional resistive element is arranged in series to the junctional resistance, an independent determination of both parameters is not possible. However, Lo et al. modeled the impact of this resistance contribution. Depending on the filter insert porosity, they introduced two

models which can be used to estimate the (maximum or minimum) contribution of this resistive element to the measured transcellular resistance. Model 1 uses the assumption, that there is only one large pore underneath the center of a cell. The pore size is calculated as the sum of all pores which are covered by a single cell. The resistance contribution arising from the cell adhesion zone can be calculated as a function of cell-substrate distance (d_{sub}), cell radius (r_c) as well as pore radius (r_{pore}) and solution resistivity (ρ_{sub}):

$$R_{sub} = \pi r_c^2 \frac{\rho_{sub}}{2\pi d_{sub}} \ln\left(\frac{r_c}{r_{pore}}\right) \tag{3.13}$$

Since a cell covers in fact more than one pore located underneath the center of the cell, the calculated resistance will be clearly overestimated. Hence, the authors introduced a second model, which can be used to estimate the minimal resistive effect. Model 2 assumes that the resistance of the pores of the filter membrane is evenly distributed underneath the cells. The calculation is based on the ECIS model (chapter 3.1.4). Another model to calculate the seal resistance between cell and substrate was introduced by Weis and Fromherz in 1997. The authors described a calculation model for the junctional resistance of a neuron transistor which is based on the assumption that the contact between cell and the solid substrate is concentrated in a ring of a defined radius (point-contact model). The radius of this contact ring is the averaged radius obtained for all possible cell-substrate contacts. The point-contact model was adopted form Wegener et al. (1999) to estimate R_{sub} underneath a cell according to:

$$R_{sub} \approx \pi r_c^2 \frac{\rho_{sub}}{5\pi d_{sub}} \tag{3.14}$$

with the specific resistivity of the electrolyte in the subcellular cleft ρ_{sub}, the cell-substrate distance d_{sub}, and the cell radius r_c.

This model can be adapted to the situation of cells cultured on permeable membranes (adapted point-contact model). Therefore, the area of all filter membrane pores is addeded and this area is evenly distributed around the junctional contact ring. Hence, the averaged radius of the contact ring is enlarged by the area of the filter pores.

The value of the cell-substrate resistance, according to the various models, depends on the cell type and the filter properties and can only serve as a rough estimation. The resistance contribution of the adhesion zone might be neglected if the paracellular resistance of (moderately) tight cell layers is investigated. But it influences the integrated parameter R_{cl} for

cell types which are highly leaky diffusion barriers. Keeping all this limitations in mind, TEER/R_{cl} still represents the integral resistance of a cell layer as a measure of its ionic permeability. But with the absence of one or several single cells (e.g. due to apoptosis) a short-cut to current flow can occur, causing a general misinterpretation of the cellular barrier function.

3.1.4 Electric cell-substrate impedance sensing (ECIS)

Barrier function of endothelial or epithelial cells is commonly analyzed by transfilter measurements. The two-chamber set-up mimics the physiological situation of barrier forming cell layers and the transport or permeation of solutes across the cell layer can be studied. However, impedance analysis can also be performed when cells are directly cultivated on the surface of solid electrodes instead of using permeable filter supports. The dielectric properties of a cell layer are determined by measuring the impedance of cell-covered electrodes over a broad frequency range followed by a detailed analysis using an appropriate equivalent circuit model. This technique was first described by Giaever and Keese (1984, 1991, 1993) and is referred to as electric cell-substrate impedance sensing (ECIS). ECIS uses cytocompatible gold electrodes, which are thin enough to be optically transparent. Two electrodes are integrated into the bottom of a cell culture well, which can be closed by a lid to ensure sterile conditions during cell culture and measurement periods. By making the circular working electrode more than 100 times smaller than the counter electrode, the impedance of the entire system is dominated by the impedance contribution of the cell-covered working electrode (see chapter 3.1.2). Additionally, the small circular electrode diameter of typically 250 μm offers a highly sensitive measurement of a small cell population. The electrical connection between both coplanar electrodes in an AC measurement is provided by the culture medium serving as electrolyte. Although the use of solid electrodes as culture substrate does not mimic *in vivo* like conditions for barrier forming cell types, the technique became a well-established method for barrier analysis. Among other advantages, ECIS electrodes can be miniaturized and integrated into 8-well, 96-well or even 384-well formats to perform automated high-throughput studies. Due to the application of gold electrodes, the combination with other electrochemical (Janshoff et al. 1996, Keese et al. 2004, Stolwijk et al. 2011) or even optical techniques (Michaelis et al. 2013) is possible.

Impedance raw data can be analyzed with the equivalent circuit derived for transfilter measurements (chapter 3.1.3, Fig. 3.3). Again, the frequency-dependent impedance of the

system is dominated by the impedance contribution of the cell layer in the mid frequency range. However, impedance spectra recorded for adherent cell layers on gold film electrodes contain more information than the paracellular resistance (R_{cl}) and the cell layer capacitance (C_{cl}). Giaever and Keese described a corresponding model, which can be used to break down R_{cl} to three subcellular components C_m, R_b and α (1991, 1993). The membrane capacitance is described by the parameter C_m. The Ohmic resistance of the cell layer due to cell-cell contacts is displayed in the parameter R_b. The frequency-dependent impedance contribution of the cell substrate zone (with a distance d between electrode surface and basolateral membrane) is described by the parameter α. The parameter α is calculated by equation 3.15, where ρ is the specific resistance of the electrolyte.

$$\alpha = r_c \sqrt{\left(\frac{\rho}{d}\right)} \tag{3.15}$$

In the model of Giaever and Keese, cells are considered as cylindrical or disk-shaped objects with a radius r_c. Since current flow between the electrode surface and the lower cell membrane is position-depended the model cannot be expressed by a simple equivalent circuit model. Instead, the transfer function which describes the impedance of the system is derived from a set of differential equations and can be mathematically expressed as:

$$Z = R_{bulk} + \left[\frac{1}{Z_{CPE}} + \left(\frac{Z_{CPE}}{Z_{CPE} + Z_M} + \frac{\frac{Z_M}{Z_{CPE} + Z_M}}{\frac{1}{2}\gamma r_c \frac{I_0(\gamma r_c)}{I_1(\gamma r_c)} + R_b\left(\frac{1}{Z_{CPE}} + \frac{1}{Z_M}\right)}\right)\right]^{-1} \tag{3.16}$$

with the impedance elements Z_{CPE} (representing the constant phase element), Z_M (membrane impedance, $Z_M = -i/(2\pi f C_m)$) and the electrolyte resistance R_{bulk} (chapter 3.1.1). I_0 and I_1 are modified Bessel functions of the first kind of order 0 and 1 and the term γr_c is expressed as:

$$\gamma r_c = r_c \sqrt{\frac{\rho}{d}\left(\frac{1}{Z_{CPE}} + \frac{1}{Z_M}\right)} = \alpha \sqrt{\left(\frac{1}{Z_{CPE}} + \frac{1}{Z_M}\right)} \tag{3.17}$$

ECIS data, analyzed by fitting the parameters of the transfer function (eq. 3.16) to the measured impedance of the system under study, provide the quantification of the cell specific parameters R_b, α and C_m (Tab. 3.2).

Tab. 3.2: Cell-related parameters of the ECIS model according to Giaever and Keese.

parameter	unit	interpretation
R_b	Ωcm^2	resistance of cell-cell junctions
α	$\Omega^{0.5}cm$	impedance contribution of cell-substrate zone
C_m	$\mu F cm^{-2}$	average capacitance of the cell membrane

Impedance contributions arising from the cellular junctions and the cell-substrate zone can be quantified independently by ECIS based measurements without any further experimental effort.

3.1.5 Impedance spectroscopy in presence of a redox couple

As mentioned in chapter 3.1.1, the presence of a redox active species in an AC circuit can lead to an electron transfer from the electrode to the species in solution at a decent potential. In this case, the electric equivalent circuit for the electrode-electrolyte interface contains the empirical faradaic impedance element (Z_f) in parallel to the electrode capacitance (or in parallel to the constant phase element CPE, which is commonly used to describe the non-ideal impedance contribution of an electrode-electrolyte interface). More detailed information about equivalent circuits containing faradaic elements is described by Bard and Faulkner (2001) or Lasia (2002).

In brief, the faradaic impedance consists of a two parts. The real part of Z_f is called the charge-transfer resistance R_{ct}. Besides this kinetically controlled parameter, the second part of the faradaic impedance is called mass transfer impedance or Warburg impedance Z_W (in case of semi-infinite linear diffusion). The Warburg impedance consists of a real and an imaginary part of the same magnitude and can be expressed as (Macdonald and Johnson 2005):

$$Z\,(w) = \frac{(1-i)\sigma}{\sqrt{w}} \tag{3.18}$$

with the Warburg coefficient σ as:

$$\sigma = \frac{\mathrm{RT}}{n^2 F^2 \mathrm{A}\sqrt{2}} \left(\frac{1}{D_O^{1/2} c_O^*} + \frac{1}{D_R^{1/2} c_R^*} \right) \tag{3.19}$$

This coefficient is a function of several parameters, listed in Tab. 3.3:

Tab. 3.3: Parameters included in the Warburg coefficient.

symbol	parameter
R	ideal gas constant
T	absolute temperature
n	stoichiometric number of electrons involved
F	Faraday constant
A	electrode area
c_R^* / c_O^*	bulk concentration of the reduced (R) / oxidized (O) species
D_R / D_O	diffusion coefficient of the reduced (R) / oxidized (O) species

The equivalent circuit differs from the well-known Randles circuit only by the use of a constant phase element instead of an ideal capacitor (Randles 1947). A R_{bulk}-(CPE||(R_{ct}-Z_W)) circuit diagram is depicted in Fig. 3.4 and the corresponding transfer function is:

$$Z\,(w) = R_{bulk} + \frac{1}{(iw)^n A + \dfrac{1}{R_{ct} + \dfrac{(1-i)\sigma}{\sqrt{w}}}} \tag{3.20}$$

The frequency-dependent influence of the Warburg element on the total impedance magnitude of the system is strongly affected by the concentration of the redox active species.

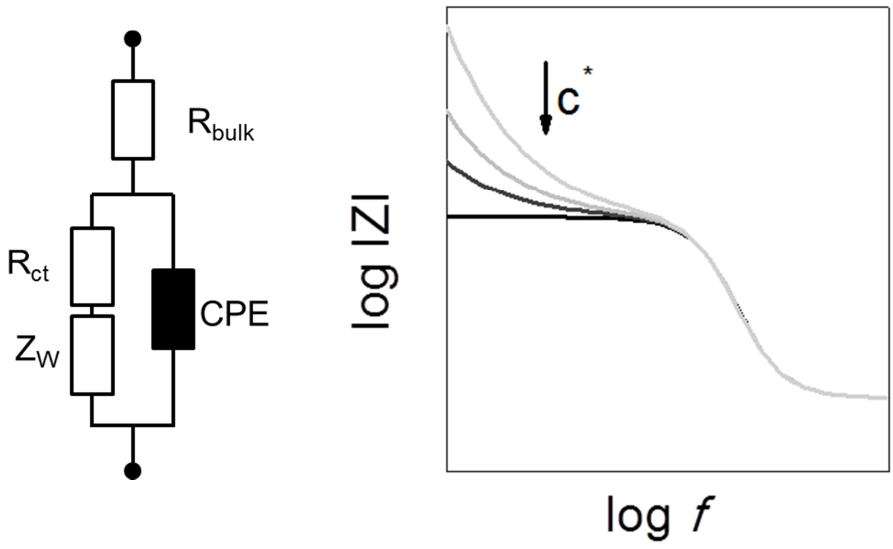

Fig. 3.4: Equivalent circuit and schematic, simplified impedance spectra for an R_{bulk}-(CPE||(R_{ct}-Z_W)) circuit. The spectrum includes information about changes in the impedance magnitude $|Z|$ when the Warburg coefficient decreases due to an increase in the bulk concentration of the redox species c^*. Concentration-dependent variations of R_{ct} are neglected.

The schematic spectra in Fig. 3.4 presents the influence of c^* (bulk concentration of the redox active species) on the total impedance magnitude, when all other parameter are kept constant. An increased bulk concentration c^* of the redox species leads to a decreased Warburg coefficient σ (eq. 3.19) and thus to a decreased impedance contribution of the Warburg element (eq. 3.20). This reflects the fact, that the Warburg impedance is a diffusion controlled parameter. If the concentration of the redox species in the electrolyte is high enough, the resistive contribution due to diffusion can be neglected. Therefore, the equivalent circuit is often simplified to a serial combination of R_{bulk} and CPE with R_{ct} in parallel to CPE. In this case, the R_{ct} element leads to a second frequency-independent impedance contribution in the lower frequency domain.

3.2 Permeability assays

Besides the above described techniques to determine the permeability of an intact cell layer for small inorganic ions (chapter 3.1.3, transcellular resistance TEER), the permeability for molecular probes is often determined to quantify endothelial or epithelial barrier function (chapter 1.2.2). Therefore, cells are also grown on highly permeable membranes of commercial filter inserts. The cell-covered membrane is placed between two fluid filled compartments and thus, acts as diffusion barrier. A tracer compound is added to one of both compartments (donor compartment) and the permeation of the marker molecule across the cell layer into the other compartment (acceptor or receiver compartment) is followed over time. The time-dependent increase of the marker concentration in the receiver compartment allows calculating the permeability coefficient P_E (chapter 3.2.1), which is specific for the cell type and the marker molecule. To correlate the calculated value P_E to the functional properties of junctional cell-cell contacts, the tracer molecule should be selected carefully. Permeation across the cell membranes via cellular transport mechanisms must be excluded. Since P_E reflects the permeability of a marker molecule across a cell-covered filter membrane, the permeability of the cell-free filter insert must be determined separately and taken into account. However, this correction does not include the additional diffusion contribution, which is caused by the narrow gap between the filter membrane and the cell layer. The diffusion pathway of the tracer molecule within the adhesion zone is extended with decreasing pore size and pore density, similar to the situation discussed for transfilter measurements (chapter 3.1.3). Similarly to the transcellular resistance, the permeability coefficient P_E is an integral

parameter. Small defects in the cell layer can influence the marker flux which might lead to overestimation of molecular permeability.

The following sections provide a derivation of all equations necessary for the calculation of P_E, as well as a detailed description of the calculation protocol used in this thesis, according to C. Wise (2002).

3.2.1 Permeability coefficient P_E

The diffusive flow of the tracer molecule depends on the concentration gradient between the donor compartment and the receiver compartment, as well as on the diffusion coefficient in the medium. Within any barrier, the concentration gradient is dependent on the chemical composition of the barrier and its morphology. To simplify the calculation of the permeability coefficient P_E, the cellular barrier is seen as a flat disk with a homogeneous chemical composition.

Fick's first law relates the flow J of a substance from the donor to the receiver side to its concentration profile in the barrier to:

$$J = \mathrm{D}\ \frac{dc(x)}{dx} \tag{3.21}$$

where D is the diffusion coefficient in the barrier and $c(x)$ is the concentration in the barrier at the coordinate x. The parameter K displays the distribution coefficient between the medium in the barrier and the aqueous donor and receiver side. The concentration in the barrier equals $K \times c_D$ at the donor side, where c_D is the concentration in the donor compartment. At the receiver side, the concentration in the barrier is $K \times c_R$ (concentration in the receiver compartment c_R). Hence, the gradient $dc(x)/dx$ can be expressed as:

$$\frac{dc(x)}{dx} = K\ \frac{(c_R - c_D)}{h} \tag{3.22}$$

with the thickness of the barrier h. Moreover, the flow must be equal to the rate of substance occurrence dn/dt in the receiver compartment divided by the cross-sectional area of the barrier A. This leads to the following expression for J:

$$J = \frac{dn_R}{dt}\frac{1}{A} = -D\frac{dc}{dx} = -D\,K\,\frac{c_R - c_D}{h} \quad (3.23)$$

Equation 3.23 can be transferred into eq. 3.24 with n_R as the amount of substance in the receiver compartment:

$$\frac{dn_R(t)}{dt} = \frac{K\,D}{h} A\,(c_D - c_R) \quad (3.24)$$

The apparent permeability coefficient P_{app} is equal to the quantity ($K \times D/h$) and reflects the rate by which the substance passes the barrier. Hence, equation 3.24 can be written as:

$$\frac{dn_R(t)}{dt} = P_{app}\,A\,(c_D(t) - c_R(t)) \quad (3.25)$$

with the time-dependent parameters $c_D(t)$, $c_R(t)$ and $n_R(t)$. If the transport rate is very small, the concentration in both compartments will not change significantly with time. If this is the case, the receiver concentration is approximated as zero and the experiment is performed under so-called *sink conditions*. Under these conditions, a receiver concentration of less than 10 % of c_D is accepted and no diffusion back to the donor compartment is expected. By regarding the concentration in the donor compartment as constant ($c_{D,0}$), eq. 3.25 is simplified to:

$$\frac{dn_R(t)}{dt} = P_{app}\,A\,c_{D,0} \quad (3.26)$$

Equation 3.26 shows the mathematical expression to calculate the apparent permeability coefficient P_{app}. The unit of P_{app} is [cm/s].

$$P_{app} = \frac{1}{A\,c_{D,0}}\frac{dn_R(t)}{dt} = \frac{V_{D,0}}{A\,n_{D,0}}\frac{dn_R(t)}{dt} \quad (3.27)$$

It has to be mentioned, that any loss of tracer substance due adsorption to the cell membrane, plastics or the filter insert is neglected in eq. 3.27. In order to quantify the loss of retarded tracer ($n_{ret.}$), the total amount of tracer in the donor compartment at the end of the experiment has to be determined separately. Hence, eq. 3.27 can be written as:

$$P_{app} = \frac{V_{D,0}}{A(n_{D,0} - n_{ret.})} \frac{dn_R(t)}{dt} \quad (3.28)$$

As mentioned before, the apparent permeability coefficient P_{app} reflects the permeability of a marker molecule for a cell-covered filter insert. The permeability coefficient for a cell-covered filter insert ($P_{app,exp}$) needs to be corrected by the value for a cell-free filter insert ($P_{app,filter}$) according to eq.3.29 in order to calculate the permeability coefficient P_E.

$$\frac{1}{P_E} = \frac{1}{P_{app,exp}} - \frac{1}{P_{app,filter}} \quad (3.29)$$

3.2.2 Calculation protocol

The following calculation protocol was used to determine the permeability coefficient P_E for all experiments shown in this thesis. After the addition of the labeled molecular probe to the donor compartment, its concentration in the receiver compartment was followed over time. In order to calculate P_E according to eq. 3.28, sink-conditions are mandatory. Therefore, the ratio of the tracer concentration in the receiver compartment to its concentration in the donor compartment must be below 10 % for each sampling occasion. The donor concentration at a specific time point *i* ($c_D(t_i)$) is calculated from the donor concentration at the previous time point ($c_D(t_{i-1})$) and the amount detected in the receiver compartment during this time interval by eq. 3.30.

$$c_D(t_i) = c_D(t_{i-1}) - \frac{[c_R(t) - F c_R(t_{i-1})]V_R}{V_D} \quad (3.30)$$

In this equation, V_R is the volume of the receiver compartment and V_D displays the volume of the donor compartment. The dilution factor F considers the sample replacement in the receiver compartment, with V_s as the sample volume.

$$F = 1 - \frac{V_s}{V_R} \quad (3.31)$$

If the calculated ratio of $c_R(t_i)$ to $c_D(t_i)$ is less than 0.1, *sink-conditions* apply. Ratios above 10 % indicate that eq. 3.27 and eq. 3.28 are no longer applicable to calculate the permeability coefficient P_E.

In case of passive cellular transport, the concentration of the tracer in the receiver compartment should increase linearly with time as long as the experiment is performed under sink-conditions. However, when the concentration of the probe in the receiver compartment is plotted against time, derivations from this ideal behavior might be observed. Fig. 3.5 shows a schematic concentration profile, which is often observed in transport studies. The time-dependent increase is subdivided into three periods, starting with a lag phase. Within this lag phase, probe transported into the receiver compartment is yet below the steady state transport rate in the first sampling interval. Poor temperature control at the beginning of the experiment might be the reason. Other than that, initial accumulation of the tracer substance in the cell membrane or the filter pores might be the rate-limiting step until saturation is achieved. The lag phase is followed by the linear phase. Only within this interval, sink-conditions apply and the concentration of the tracer substance in the receiver compartment increases linearly with time. When the concentration gradient decreases with time, the transport rate will be reduced, providing a stationary concentration in both compartments.

In order to calculate the permeability coefficient P_E with eq. 3.29 under *sink-conditions*, only the linear phase in the time-dependent concentration profile is used. The experimental data within this period (either concentration against time or the amount of substance against time) are analyzed by a linear regression to obtain the parameter dc/dt or dn/dt.

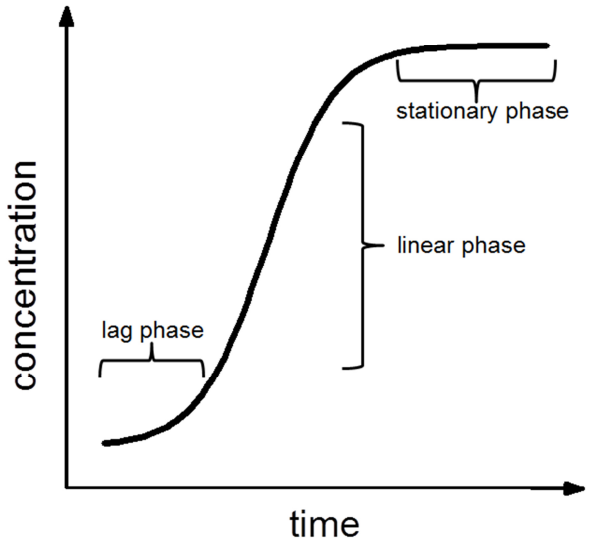

Fig. 3.5: Schematic drawing of the time-dependent concentration increase in the receiver compartment.

The obtained parameters were only used, if the adjusted coefficient of determination (adj. R^2) of the linear regression was equal or bigger than 0.9.

Whenever possible, the loss of mass due to cellular retention, plastics or the filter membrane adsorption was determined in order to calculate the permeability coefficient according to eq. 3.27. Therefore, the amount of substance in the both compartments was determined at the end of the experiment to quantify the loss of mass. Additionally, the determined permeability coefficient was corrected for the value of a cell-free filter insert (eq. 3.29).

4 Materials and methods

4.1 Cell culture techniques

4.1.1 Cell lines

Experiments included in this thesis were carried out using the adherently growing epithelial cell lines MDCK-I and MDCK-II (Madin Darby canine kidney, strain I and II), epithelial-like cell line NRK (normal rat kidney, clone 52E), astrocytic cell line U-373 MG (human glioma cell line) and endothelial cell line BAEC (bovine aortic endothelial cells). MDCK cells and NRK cells were obtained from the *Deutsche Sammlung von Mikroorganismen und Zellkulturen* (DSMZ). U-373 MG cells were provided by Prof. Buschauer (University of Regensburg, Germany) whereas BAEC cells were kindly provided by Dr. Zink and Prof. Rösen (*Deutsches Diabetes-Zentrum* DDZ, Düsseldorf, Germany). Information about all cell lines involved in this thesis is listed in Tab. 4.1.

Tab. 4.1: Cell lines used in this thesis.

cell line	origin	morphology	literature	supplier
MDCK-hr* & MDCK-lr*	Madin Darby canine kidney	epithelial	Richardson et al. 1981, Balcarova-Staender et al. 1984	DSMZ, Germany
NRK-52E	normal rat kidney (clone 52E)	epithelial-like	Delarco and Todaro 1978	DSMZ, Germany
U-373 MG	human glioma cell line	pleomorphic/ astrocytoid	Bigner et al. 1981	Prof. Buschauer
BAEC	bovine aortic endothelial cells	endothelial	Zink et al. 1993	DDZ, Germany

4.1.2 General cell culture conditions

General cell culture work was performed under sterile conditions using a laminar flow hood (Thermo Fisher Scientific Inc, Waltham, USA). Buffers, media and other solutions were autoclaved (20 min, 120 °C) or passed through a sterile filter with a pore diameter of 0.2 μm (TPP®, Sigma Aldrich, Munich, Germany). All cell lines were cultured on the bottom of sterile culture flaks with a growth area of 25 cm^2 (Greiner, Kremsmünster, Austria) and kept in cell

*

Several MDCK cell types are known (Gekle et al. 1994, Dukes et al. 2011). However, the nomination is often inconsequent. For better comparison with other results obtained for MDCK cells, the nomination is adapted to the specific phenotypes (transepithelial electrical resistance). MDCK-I (strain I) as well as MDCK-C7 cells are high resistance subtypes denoted as MDCK-hr (hr: high resistance). MDCK-II (strain II) and MDCK-C11 cells are grouped into MDCK-lr (lr: low resistance).

culture incubators (Thermo Fisher Scientific Inc, Waltham, USA) at 37 °C in an atmosphere with 5 % CO_2 and 95 % relative humidity. Cell culture medium (Tab. 4.2) was exchanged every third day.

Tab. 4.2: Cell culture media composition.

medium	composition
MDCK culture medium	Minimum Essential Medium Eagle (MEM-Eagle) incl. 1g/L glucose 5 % (v/v) fetal bovine serum (FBS) 100 µg/mL penicillin 100 µg/mL streptomycin 4 mM L-glutamine
U-373 MG culture medium	MEM-Eagle incl. 1 g/L glucose 5 % (v/v) FBS 100 µg/mL penicillin 100 µg/mL streptomycin 2 mM L-glutamine
NRK-52E culture medium	Dulbecco´s Modified Eagle's Medium (DMEM) incl. 4.5 g/L glucose 5 % (v/v) FBS 100 µg/mL penicillin 100 µg/mL streptomycin 2 mM L-glutamine
BAEC culture medium	DMEM incl. 1g/L glucose 10 % (v/v) FBS 100 µg/mL penicillin 100 µg/mL streptomycin 4 mM L-Glutamin

4.1.3 Subcultivation

All cell lines were subcultured once a week. A standard protocol was used to transfer the cells into new culture flaks (Tab. 4.3, Tab. 4.4). All buffer solutions and media were pre-warmed to 37 °C in a water bath (Julabo, type TW12, Seelbach, Germany). Cells were washed with phosphate buffered saline solution without calcium or magnesium ions (PBS^{--}, Sigma Aldrich, Munich, Germany). Subsequently, cells were incubated with EDTA solution (ethylenediamintetraacetic acid, Merck KGaA, Darmstadt, Germany) at 37 °C followed by an

enzymatic digestion with trypsin (Sigma Aldrich, Munich, Germany). Enzymatic activity was stopped by addition of culture medium (10-fold excess). Suspended cells were transferred into a centrifugation tube (Cellstar® centrifuge tubes, Greiner Bio-One, Kremsmünster, Austria) and spun down at 110 x g for 10 min at room temperature (RT) (Heraeus 1-SR, Thermo Fisher Scientific Inc., Waltham, USA). The supernatant was discarded and the cell pellet was resuspended in fresh culture medium. Cells were diluted and seeded into new culture flasks.

Tab. 4.3: Incubation times at 37 °C for individual subcultivation steps and dilution ratios for the cell lines under study.

cell line	PBS^{--}	EDTA	trypsin
MDCK-hr	3 × 5 min	2 × 10 min	10 – 15 min
MDCK-lr	2 × wash	7 – 10 min	7 – 10 min
NRK-52E	2 × wash	7 – 10 min	7 – 10 min
U-373 MG	1 × wash	-	2 - 3 min
BAEC	1 × wash	-	2 - 4 min

Tab. 4.4: Subculturing buffers.

solution	composition
Dulbecco's Phosphate Buffered Saline (PBS^{--})	0.2 g/L KCl 0.2 g/L KH_2PO_4 8.0 g/L NaCl 1.15 g/L Na_2HPO_4
EDTA solution	1 mM EDTA in PBS^{--}
trypsin solution	0.025 % (w/v) trypsin in EDTA solution (0.25 % (w/v) trypsin for MDCK-hr)

4.1.4 Particular inoculation protocols

In the course of subcultivation (chapter 4.1.3), cells were seeded in defined cell numbers onto culture substrates with integrated electrodes or on porous growth substrates (chapter 4.2). Therefore, a hemocytometer (Bürker, Marienfeld-Superior, Lauda Königshofen, Germany) was used to count the number of suspended cells.

Subsequently, the suspension was diluted to the desired cell density (Tab. 4.5) before the cells were seeded onto sterilized substrates (argon plasma for 15 s., Plasma cleaner, Harrick Plasma Inc., Ithaca, USA).

Tab. 4.5: Area-specific inoculation to provide confluent cell monolayers within 24 hours.

cell line	inoculation
MDCK-hr & lr	450.000 cells/cm^2
NRK-52E	450.000 cells/cm^2
U-373 MG	100.000 cells/cm^2
BAEC	90.000 cells/cm^2

When cells were directly cultured on planar electrodes (chapter 4.2.1), the suspension was pipetted into the culture well (V = 2 mL). In case of BAEC cells, the substrate was coated with 0.5 % gelatin (Sigma Aldrich, Munich, Germany) in water (30 min, RT) and washed with culture medium before cells were seeded.

In case of cell seeding on permeable growth substrates like standard Transwell® filter inserts (growth area: 1.12 cm^2, polycarbonate membrane, pore diameter: 400 nm, pore density: 10^8 pores/cm^2, Corning, NY, USA) or modified gold coated filter membranes (chapter 4.2.2), the inserts were placed into an ordinary 12-well culture plate (Costar Corning, LMS Consult, Brigachtal, Germany). The lower compartment was filled with 1.5 mL culture medium, the upper compartment with 0.5 mL cell suspension (Fig. 4.1).

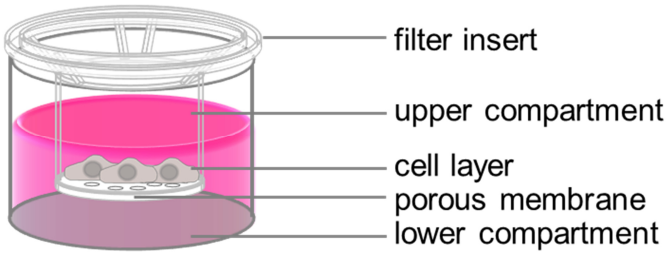

Fig. 4.1: Cell culture set-up for permeable filter inserts.

Defined defect areas within a confluent cell layer cultured on these porous filters were introduced by placing small silicon spacers on the membrane. Therefore, commercially available culture inserts (for self insertion, ibidi®, Munich, Germany) were cut into 1 mm^2 pieces, exposed to argon plasma for 20 s (plasma cleaner, Harrick Plasma Inc., Ithaca, USA) and attached to the membrane prior to cell seeding.

Whenever cells were cultured on both sides of the permeable filter insert, cell inoculation on the bottom side of the membrane was performed first. Therefore PDMS (polydimethylsiloxane, Sylgard® 182, Dow Corning, Midland, USA) rings were prepared. Base elastomer and curing agent were mixed (10:1, v/v) and cured at 60 °C for 24 h. The insert

was flipped and the PDMS ring was placed over the insert to form a temporary culture well around the filter area (V = 1mL). Subsequently, the filter insert was placed into a polycarbonate vessel (30 mL volume, Carl Roth, Karlsruhe, Germany) and the vessel was filled with 13 mL culture medium (Fig. 4.2).

1 mL cell suspension was added into the PDMS well before the vessel was closed and kept at 37 °C for 4 h (Fig. 4.2 step 1). After formation of a confluent cell monolayer with stable cell-substrate contacts, the PDMS ring was stripped and the insert was placed into a standard medium-filled culture plate (Fig. 4.2 step 2). Cells were seeded onto the upper side of the membrane (Fig. 4.2 step 3).

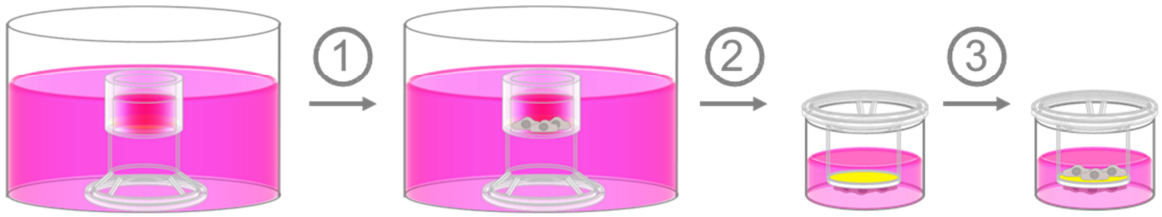

Fig. 4.2: Seeding sequence for co-cultured cell layers on permeable filter supports.

4.1.5 Cryopreservation

Adherently growing cells were detached from standard culture flaks according to the subcultivation protocol (chapter 4.1.3). After centrifugation, the cell pellet was resuspended in cryopreservation medium consisting of 10 % (v/v) DMSO (dimethyl sulfoxide, Carl Roth, Karlsruhe, Germany) in FBS (Sigma Aldrich, Munich, Germany). The cell suspension was then transferred into cryovials (TPP®, Sigma Aldrich, Munich, Germany) and cooled to – 70 °C using an isopropanol bath (Nalgene® CryoBox™, Sigma Aldrich, Munich, Germany). This first phase of slow cooling (1 °C/min) was followed by a final transfer into a liquid nitrogen tank (German Cryo GC-BR2150 M, german-cryo® GmbH, Jüchen, Germany) for long term storage. For recultivation of frozen cells, cryovials were removed from the liquid nitrogen tank and kept at – 20 °C for 1 – 2 h. Subsequently, the cell containing vials were thawed using a 37 °C warm water bath (Julabo, type TW12, Seelbach, Germany). The cell suspension was transferred into a centrifugation tube (Cellstar® centrifuge tubes, Greiner Bio-One, Kremsmünster, Austria) and diluted by a dropwise addition of 10 mL pre-warmed culture medium. After centrifugation (110 x g for 10 min at RT, Heraeus 1-SR, Hanau, Germany), the

cell pellet was resuspended in standard culture medium. Cells were seeded in culture flasks at different ratios with respect to their former growth area. 24 h after cell thawing, the culture medium was exchanged. Cells were kept under general culture conditions according to chapter 4.1.2.

4.1.6 Solution osmolarity

Buffer osmolarity (in mOsmol/kg) was determined by using a cyroscopic osmometer (Osmomat 030, Gonotec, Berlin, Germany). The instrument compares the freezing point of pure water to the freezing point of the solutions of interest. The measured freezing point depression is then used to calculate the osmolarity of the sample.

Physiological osmolarities are necessary to maintain the osmotic balance between the cellular cytosol and the surrounding buffer to avoid cell swelling or cell shrinking. A range of 260 - 320 mOsmol/kg is regarded as acceptable for most cell lines (Freshney 2005).

4.1.7 Buffers and solutions

Physiological buffers (referred to as buffer 1 and buffer 2) with individual electric conductivities were prepared according to Tab. 4.6. The buffer composition was adopted from C. Rommel's PhD thesis (2007) with the exception that D-mannitol was used instead of D-glucose.

Tab. 4.6: Composition of physiological buffers with varying conductivities.

salt	buffer 1	buffer 2	supplier
KCl	5.4 mM	5.4 mM	Merck KGaA, Darmstadt, Germany
NaCl	135 mM	-	VWR International GmbH, Ismaning, Germany
$CaCl_2 \bullet 2H_2O$	2.0 mM	2.0 mM	Sigma Aldrich, Munich, Germany
$MgCl_2 \bullet 6H_2O$	1.0 mM	1.0 mM	Merck KGaA, Darmstadt, Germany
HEPES	5.0 mM	5.0 mM	Carl Roth, Karlsruhe, Germany
D-mannitol	10 mM	240 mM	Serva GmbH, Heidelberg, Germany

After all components had been dissolved in pure water, both buffers were tested for their specific conductivity (inoLab® Cond 720, cell constant: 0.478 cm^{-1}, WTW GmbH, Weilheim, Germany) and osmolarity (chapter 4.1.6). The characteristics of both buffers are listed in Tab. 4.7.

Tab. 4.7: Properties of physiological buffers with different conductivities.

buffer	conductivity (at 23.5°C)	osmolarity
1	14.65 mS/cm	282 mOsmol/kg
2	1.28 mS/cm	274 mOsmol/kg

The buffers were passed through a sterile filter with a pore diameter of 0.2 μm (TPP®, Sigma Aldrich, Munich, Germany) and stored at 4 °C.

Cytochalasin D was purchased from Sigma Aldrich (Munich, Germany), diluted to a concentration of 9.85 mM (5 mg/mL) in DMSO (dimethyl sulfoxide, Carl Roth, Karlsruhe, Germany) and stored at - 18 °C. The stock solution was further diluted to a final concentration of 3 μM in culture medium directly before use (incl. 0.03 % DMSO).

Cell lysis buffers were prepared in pure water according to Hartmann et al. (2007). A list of all components is displayed in Tab. 4.8. Triton-X-100 and sodium deoxycholate were purchased from Sigma Aldrich (Munich, Germany). Both buffers were passed through a sterile filter (0.2 μm, TPP®, Sigma Aldrich, Munich, Germany) and stored at 4 °C.

Tab. 4.8: Lysis buffer components.

lysis buffer	Triton-X-100	sodium deoxycholate
1	1 % (v/v)	-
2	1 % (v/v)	1 % (w/v)

A FITC-dextran solution (10 kDa fluorescein isothiocyanate labeled dextran, Sigma Aldrich, Munich, Germany) was solubilized in PBS^{++} buffer to a concentration of 2 mg/mL (w/v).

Potassium ferrocyanide ($K_4[Fe(CN)_6]\bullet 3H_2O$) and potassium ferricyanide ($K_3[Fe(CN)_6]$) were purchased from Merck KGaA (Darmstadt, Germany) and dissolved in PBS^{++} buffer containing 1 g/L glucose (Sigma Aldrich, Munich, Germany). Mixtures including both cyanides in the same concentration were prepared. All solutions were passed through a sterile filter with a pore diameter of 0.2 μm (TPP®, Sigma Aldrich, Munich, Germany) and stored at 4 °C.

Solutions for the activation of G protein-coupled receptors (GPCRs) were always directly prepared before use in diverse serum-free cell culture media (Tab. 4.9). Histamine dihydrochloride and isoprenaline hydrochloride were dissolved to a final concentration of 100 μM and mepyramine maleate to 5 μM.

Tab. 4.9: Receptor agonists and antagonists used in this thesis.

substance	formula	classification	supplier
histamine dihydrochloride	$C_5H_9N_3$ •2HCl	endogenous H_1-receptor agonist	Carl Roth, Karlsruhe, Germany
mepyramine maleate	$C_{17}H_{23}N_3O$ •$C_4H_4O_4$	H_1-receptor antagonist	Sigma Aldrich, Munich, Germany
isoprenaline hydrochloride	$C_{11}H_{17}NO_3$ •HCl	β-adrenergic receptor agonist	Sigma Aldrich, Munich, Germany

Carbol fuchsin solution (according to Ziehl-Neelson, Sigma Aldrich, Munich, Germany) was used to visualize cells, which were cultivated on porous filter inserts. Prior to the unspecific staining, cells were washed twice with PBS^{++} buffer (Sigma Aldrich, Munich, Germany) followed by a fixation step using a solution of 4 % (w/v) paraformaldehyde (Sigma Aldrich, Munich, Germany) in PBS^{++} (10 min, RT). The filter inserts were washed again two times with buffer before 100 µL Carbol fuchsin solution were added to the cell-covered membrane (5 min, RT). The dye excess was washed out several times and the filter insert was dried under nitrogen flow. Microscopic images were taken at a Nikon SMZ1500 stereomicroscope or a Nikon Diaphot phasecontrast microscope (Nikon Instruments Europe, Amstelveen, Netherlands) with attached digital camera.

4.2 Electrode preparation

4.2.1 Planar electrodes

Electrodes were prepared using a standard photolithography protocol (Fig. 4.3). The substrates were either indium tin oxide (ITO) continuously coated on a polyethylene foil (PET), or gold sputtered on Lexan® plates (GE, Munich, Germany). The ITO/PET foils (sheet resistance: 60 Ω/cm) were purchased from Sigma Aldrich (Munich, Germany), whereas a 100 nm thick gold film was deposited on Lexan® plates using a sputter device (Bal-Tec sputter coater, Capovani Brothers Inc., Scotia, USA) with gravimetric thickness monitoring.

For lithography the substrates were coated with a layer of AZ®-ECI3027 positive photoresist (Microchemicals, Ulm, Germany) using a spin coater (model WS-650-23B, Laurell Technologies Corporation, North Wales, USA, parameters: 3000 rpm, 1 min, Fig. 4.3 step 1). After a soft bake step (100 °C, 30 min, heating oven type 500, Memmert, Schwabach, Germany), the photopolymer film was covered with a layout mask which defined all

conductive structures and exposed to UV light (2 min, isel® UV illumination device nr. 2, Elterfeld, Germany, Fig. 4.3 step 2). The masks were printed in black on a transparent foil with a HP Officejet 6300 printer. The light exposed areas of the polymer were then developed with a solution of 7 g/L sodium hydroxide in water (20 s, Fig. 4.3 step 3). All metal areas, which were no longer protected by the photopolymer were removed using an etch solution (Fig. 4.3 step 4). In case of ITO/PET the substrate was rinsed with a solution of $H_2O/HCl_{conc.}/HNO_{3\ conc.}$ (v/v: 47/47/6) for 30 s. Gold was removed using an aqueous solution of KI (0.265 mmol/L) and I_2 (0.499 mmol/L) for 1 min. The etching process was stopped by a washing step in water. Subsequently, the photoresist was removed (Fig. 4.3 step 5). Therefore acetone was used for ITO/PET substrates. Since Lexan® is not stable in acetone, the Au-Lexan® substrates were again exposed to UV light without any mask and the photoresist was removed with NaOH solution (Fig. 4.3 step 2 & 3). The structured metal surfaces were again covered by a layer of photoresist followed by a soft bake step (Fig. 4.3 step 6). A second photolithographic mask, which defines the final conductive parts of the electrode layout, was used for the following UV light exposure (Fig. 4.3 step 7). The exposed polymer areas were removed with NaOH solution (Fig. 4.3 step 8) and the remaining photopolymer (insulating layer) was stabilized by a hard bake step (2 h, 118 °C, Fig. 4.3 step 9).

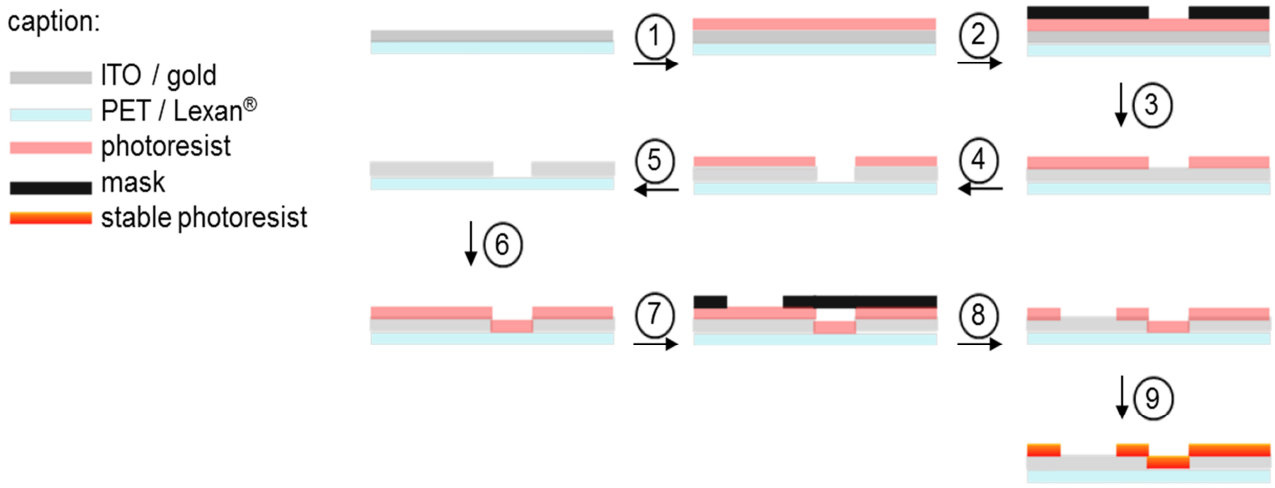

Fig. 4.3: Schematic description of the photolithographic process.

4.2.1.1 Indium tin oxide electrodes

ITO/PET foils (56 mm × 26 mm, ITO: 130 nm) were fabricated using the above-mentioned photolithography protocol (chapter 4.2.1). Fig. 4.4 shows the illumination masks. Mask 1 separates two conductive areas (gap size: 500 μm). The second mask is needed to define a small working electrode (Ø = 500 μm) within the photoresist layer which insulates the remaining part of the electrode.

Fig. 4.4: Schematic photolithographic masks for ITO/PET foils. Red circles indicate the borders of the measurement chamber.

This layout was chosen in order to prevent a high lead resistance, since the height of the ITO layer is only 130 nm. The dashed red ring indicated the position of a glass ring, which was glued on the final electrode layout to define a cell culture well and measurement chamber. Therefore, a 20 mm high glass ring (Ø = 2.4 cm) was mounted on the substrate using non-cytotoxic silicone glue (Master fix Aquarium Silikon, Warenimport und Handels GmbH, Vienna, Austria). Fig. 4.5 shows an example of the transparent cell culture wells.

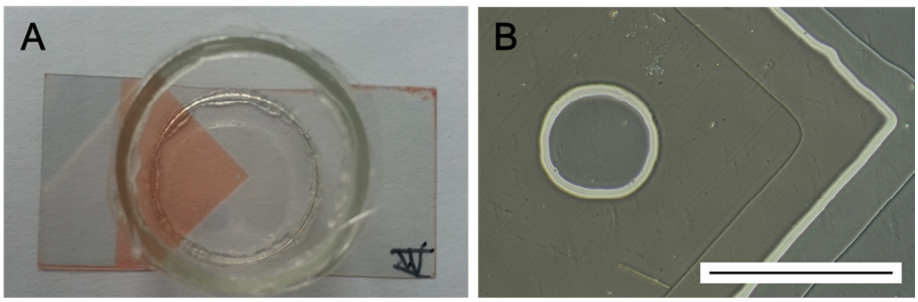

Fig. 4.5: A Photographic image of the cell culture well with integrated ITO electrodes on the bottom of the substrate. **B** Microscopic image of the working electrode (A = 2E-03 cm^2, Ø = 500 μm, scale bar: 1 mm).

4.2.1.2 Gold electrodes

Gold/Lexan® sheets (76 mm × 26 mm, Au: 100 nm) were prepared and processed according to chapter 4.2.1. The thin gold layer was structured with the help of the photolithographic mask shown in Fig. 4.6 A. The thin connection between the working electrode (1 mm Ø) and the contact area was insulated with a non-cytotoxic silicone glue (Master fix Aquarium Silikon, Warenimport und Handels GmbH, Vienna, Austria). A 20 mm high glass ring with an inner diameter of 24 mm was mounted on the substrate to create a cell culture well (Fig. 4.6 B).

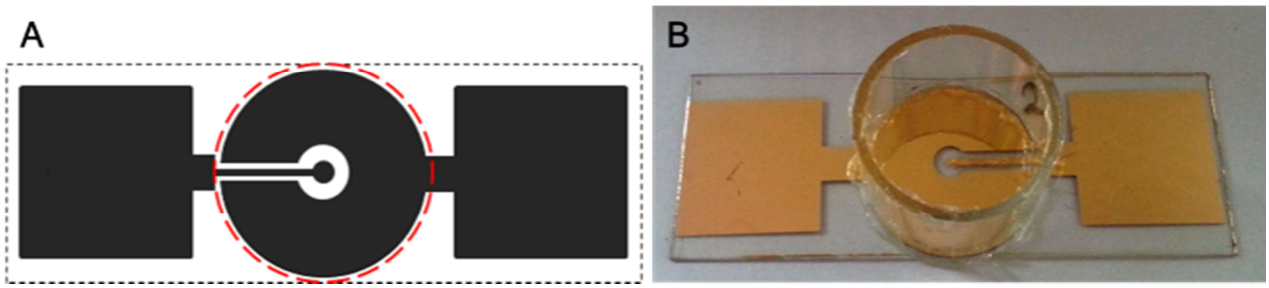

Fig. 4.6: A Schematic of the photolithographic mask used for the coplanar gold layout. **B** Photographic image of the cell culture well with integrated gold electrodes on the bottom of the substrate.

A second gold electrode was fabricated as custom array 2W6x1E (Fig. 4.7) by Applied BioPhysics (Troy, USA). The contact pads are arranged to fit into a commercially available ECIS array station (Applied BioPhysics, Troy, USA). Each substrate (PET foil) includes two sets of 6 small individually addressable working electrodes (Ø = 1 mm) which are surrounded by a circular counter electrode (A = 3.8 cm^2). The size of the counter electrode was reduced to an area of 0.9 cm^2 by insulating the gold surface with a thin layer of silicon glue. Around the counter electrode a 10 mm high glass ring was glued (24 mm inner diameter) to serve as buffer reservoir.

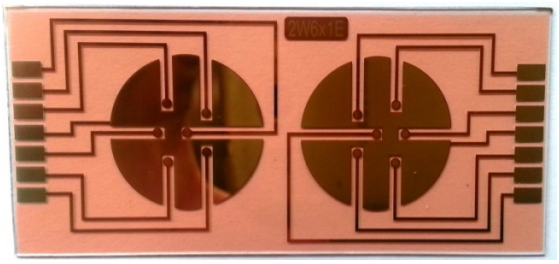

Fig. 4.7: Photographic image of the 2W6x1E electrode layout fabricated by Applied BioPhysics.

For cytotoxicity studies, a 96-well ECIS array was purchased from Applied BioPhysics (Troy, USA). Each well of the 96W1E+ PET array contained two circular gold electrodes (Ø = 350 μm) on a PET substrate (Fig. 4.8). In addition, 8W10E arrays were also purchased from Applied BioPhysics. Each of the eight wells (A = 0.75 cm^2) included a set of 10 working electrodes (Ø = 250 μm, A = 0.49 mm^2) and a common counter electrode.

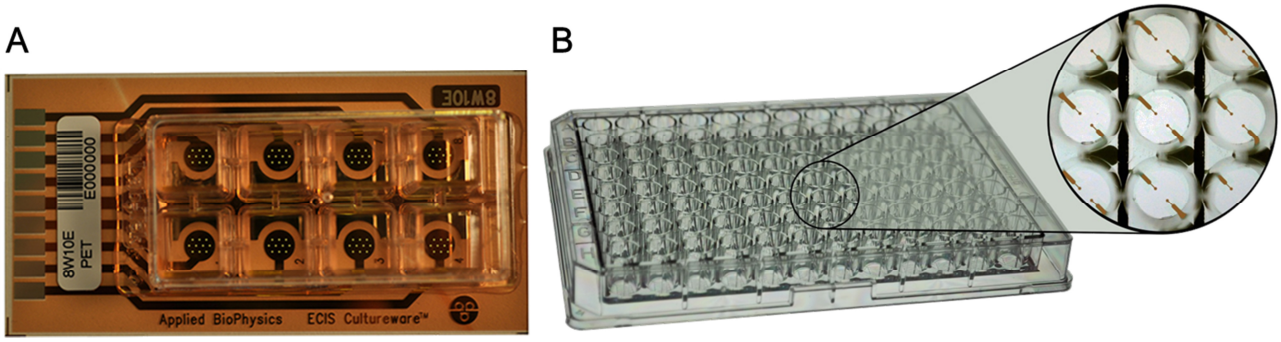

Fig. 4.8: Commercially available 8W10E array (**A**) and 96W1E+ PET array (**B**, pictures: www.biophysics.com/cultureware).

4.2.2 Stainless steel electrodes

A 2 mm thick stainless steel plate was glued on a Lexan® plate (GE, Munich, Germany). A glass ring (height: 20 mm, inner diameter: 24 mm) was then mounted on the steel plate to serve as buffer reservoir and to mechanically fix a standard filter insert (chapter 4.1.4) above the bottom electrode.

A stainless steel dipping electrode was used as counter electrode. A 4 mm thick rod is flattened at one end to a circular disk with a diameter of 10 mm and a height of 1 mm. This dipping electrode was either used unmodified or covered with a thin gold layer (100 nm). In the latter case, gold was deposited using a Bal-Tec sputter coater (Capovani Brothers Inc., Scotia, USA).

The dipping electrode was integrated into a standard petri dish lid (Ø = 40 mm, TPP®, Sigma Aldrich, Munich, Germany). The lid fixed the electrode 2 mm above the permeable membrane and was needed to close the measurement chamber (Fig. 4.9). The electrode-electrolyte interface was calculated to an area of 1.85 cm^2.

The design of the fabricated measurement chamber was adopted from a device published by Wegener et. al (2004).

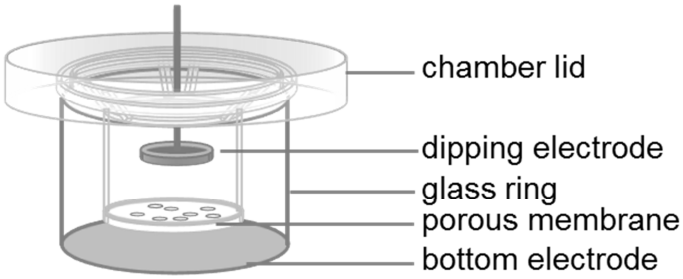

Fig. 4.9: Schematic drawing of the measurement chamber with integrated stainless steel electrodes.

4.2.3 Porous gold electrodes

Standard permeable filter inserts were used to prepare porous gold electrodes (Fig. 4.10). Therefore, Corning Transwell® permeable supports (polycarbonate membrane, growth area: 1.12 cm^2, pore diameter: 400 nm, pore density: $10^8/cm^2$) were received from LMS Consult (Brigachtal, Germany). A 100 nm thick gold film was deposited on the bottom side of the porous membrane using a Bal-Tec sputter coater (Capovani Brothers Inc., Scotia, USA). The modified membrane was electrically connected to a copper wire using a silver conductive adhesive (Conrad, Regensburg, Germany). Contact paths were insulted against culture medium by the use of non-cytotoxic silicone glue (Master fix Aquarium Silikon, Warenimport und Handels GmbH, Vienna, Austria).

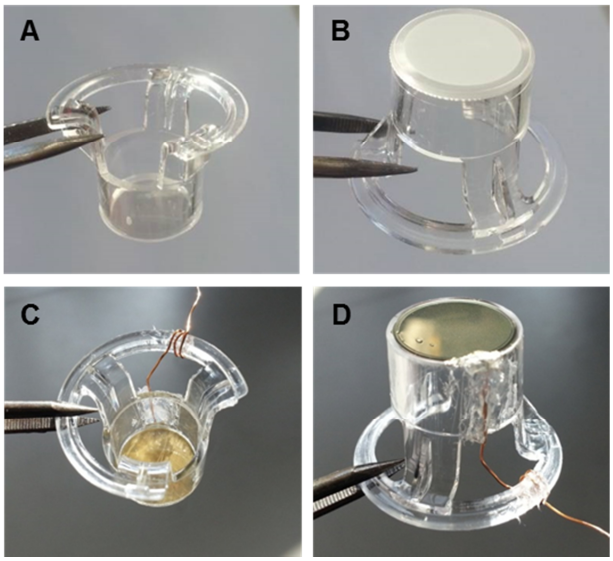

Fig. 4.10: Photographic images of Transwell® permeable cell culture supports with a membrane area of 1.12 cm^2 (**A**,**B**). The inserts were used to prepare porous gold electrodes (**C**,**D**).

4.3 Impedance measurements

4.3.1 Experimental set-up

All non-invasive impedance measurements were carried out under standard cell culture conditions. The measurement chambers were placed into an incubator (type: Ultima® II, Revco®) and kept at 37 °C and 95 % relative humidity. The electrodes were connected to a relay. The relay is needed to switch between the different electrode combinations. Impedance analyzer (type: SI-1260, Solartron Instruments, Farnborough, UK) and relay were connected to an ordinary PC (Fig. 4.11). The oscillator, integrated in the impedance analyzer, applied a sinusoidal alternating voltage of a preset frequency and amplitude to the electrodes and measured the resulting current. The impedance magnitude and the associated phase angle between voltage and current were recorded within a frequency range from 1 - 10^6 Hz. In total, 61 individual frequencies were measured, equally spaced on a logarithmic scale. The measurement was controlled by a PC using a LabVIEW™ based software (National Instruments, Austin, USA) written by Prof. Wegener (University of Regensburg).
Details regarding the individual experimental conditions for each assay are discussed in the following paragraphs.

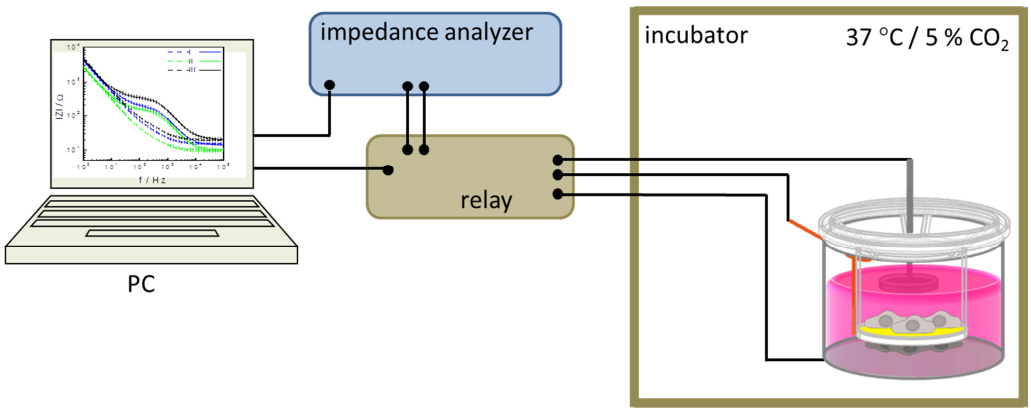

Fig. 4.11: Schematic set-up for impedance measurements.

4.3.2 Specific assay conditions

All electrodes were sterilized using an argon plasma cleaner (15 s, Harrick plasma, Ithaca, USA) prior to the experiments. Cells were cultured on permeable supports or directly on the measurement electrodes (gold or ITO) according to chapters 4.1.3 and 4.1.4.

4.3.2.1 Transfilter measurements using stainless steel electrodes

The measurement chamber (chapter 4.2.2) was filled with 2 mL of cell culture medium or buffer solution. Depending on the type of electrolyte solution, the CO_2 content in the incubator was adjusted to 0 % or 5 % (v/v). The cell-covered filter insert was placed above the stainless steel bottom electrode. The dipping electrode was placed into the apical compartment (V = 0.5 mL) of the filter insert (Fig. 4.12). Both electrodes were connected to the measurement set-up described in chapter 4.3.1. The frequency range was set to 1 - 10^6 Hz. A non-invasive voltage amplitude of 10 mV (rms) was applied. All liquid handling (e.g. cell suspensions for attachment studies, drug solutions or other buffers) was performed by a total liquid replacement in one or both compartments. Continuous recording of impedance spectra resulted in a time resolution of 1.5 min per filter device.

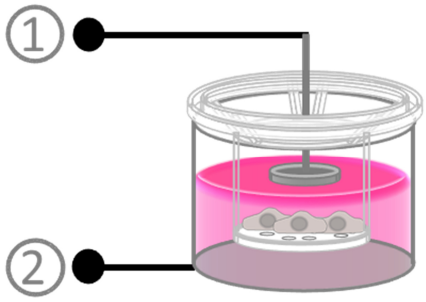

Fig. 4.12: Experimental set-up for transfilter measurements. The filter insert was placed between the steel bottom electrode (2) and the steel dipping electrode (1).

4.3.2.2 Transfilter measurements including the porous backside electrode

All parameters described in chapter 4.3.2.1 were kept constant for transfilter measurements that included the porous gold electrode (chapter 4.2.3). The standard integrated transfilter measurement was performed by readings between the dipping electrode (Fig. 4.13 A: electrode 1) and the bottom electrode (Fig. 4.13 A: electrode 3). The porous gold electrode (Fig. 4.13 A: electrode 2) served as common counter electrode when both compartments were measured successively. Stainless steel and gold electrodes were combined here. To avoid any battery effect between the two different metals used as electrodes, the DC potential was clamped to zero during the measurement of a given electrode pair. The overall impedance of a co-culture was recorded in the transfilter mode 1 – 3. The impedance of the cells growing on the upper side of the filter device was measured in mode 1 – 2 whereas the

impedance of the cells grown on the backside of the filter membrane was measured by readings between electrode 2 and 3 in mode 2 – 3.

For this set-up, continuous recording of impedance spectra led to a time resolution of about 4 min.

The set-up was further expanded to additionally apply the ECIS principle (Fig. 4.13 B). Hence, the stainless steel electrode at the bottom of the measurement chamber was substituted by a co-planar gold electrode layout (chapter 4.2.1.2, Fig. 4.6). The non-invasive impedance monitoring of cells, cultivated directly on the planar gold electrodes, was achieved when the circular working electrode (Fig. 4.13 B: electrode 4, Ø = 1 mm) was electrically connected to the large horse-show like counter electrode (Fig. 4.13 B: electrode 3). Additionally, the stainless steel dipping electrode (Fig. 4.13 B: electrode 1) was covered by a layer of gold (chapter 4.2.2). The combination of four gold electrodes for simultaneous investigation of three individual cell layers resulted in a time resolution of 5.5 min.

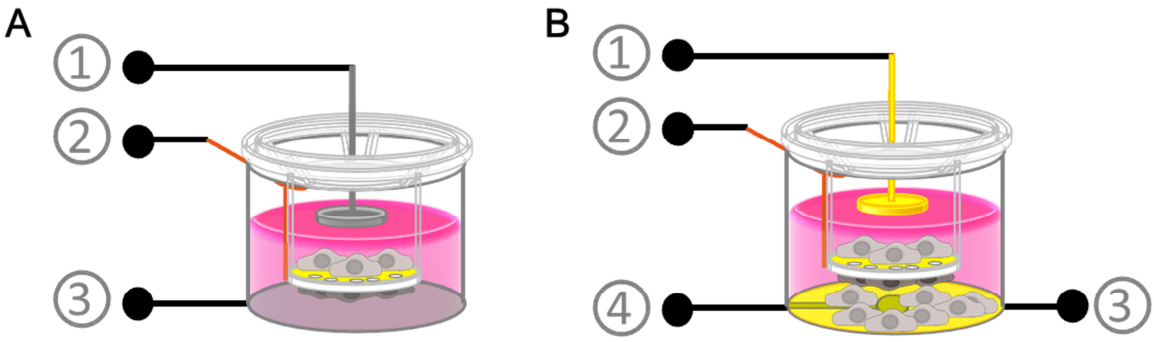

Fig. 4.13: Experimental set-up for transfilter measurements with an integrated porous gold electrode (**A**). The modified version, including only gold as electrode material is shown in (**B**). The former uniform bottom electrode was divided into a small working electrode (4) and a large horse-shoe like counter electrode (3).

4.3.2.3 Combined electrochemical determination of substrate permeability and TEER

All impedimetric permeability measurements were carried out at 37 °C in a humidified atmosphere with no additional CO_2 content. The 2W6x1E arrays (chapter 4.2.1.2, Fig. 4.7) were used to study the local substrate permeability of the redox couple $[Fe(CN)_6]^{3-/4-}$ across a confluent cell layer (NRK, MDCK-lr, MDCK-hr) by an impedimetric readout. Therefore, the lower reservoir was filled with 700 µL of PBS^{++} buffer (containing 1 g/L glucose). The cell-covered filter inserts were placed directly on top of the co-planar electrodes on the bottom. A dipping gold electrode (chapter 4.2.2) was connected to a copper wire and placed

into the upper filter compartment (V = 0.5 mL, Fig. 4.14). The array and the copper wire of the dipping electrode were assembled into a commercially available ECIS array station (Applied BioPhysics, Troy, USA) for the connection to the impedance analyzer. The addition of $[Fe(CN)_6]^{3-/4-}$ was performed by replacing 250 µL of the apical compartment volume by 250 µL of double concentrated redox couple solution.

The set-up combined the continuous determination of the transepithelial electrical resistance (Fig. 4.14: electrode 1 vs. electrode 3) and the substrate permeation of a redox couple (Fig. 4.14: electrode 2 vs. electrode 3) for an individual cell layer. The applied voltage amplitude was set to 70 mV (rms) and the complex impedance was recorded at 61 individual frequencies, equally spaced on a logarithmic scale in a range of 1 – 10^6 Hz. Impedance spectra for all electrodes were recorded within 8 min.

In case a better time resolution was requested, the dipping gold electrode was neglected, the frequency range was reduced and the impedance was recorded at a frequency of 1 Hz and 10 Hz, improving the time resolution to 1.2 min.

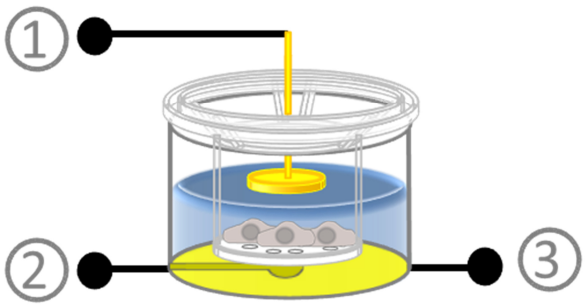

Fig. 4.14: Experimental set-up for impedimetric monitoring of $[Fe(CN)_6]^{3-/4-}$permeation across a confluent cell layer. For better clarity, the scheme displays only one of six individual working electrodes (2). The filter insert was placed directly on the electrodes at the bottom (2,3) of the measurement chamber. The dipping electrode (1) was placed into the apical filter compartment.

4.3.2.4 Transcellular permeability monitoring via whole-cell impedance-based biosensors

U-373 MG cells or BAECs were cultured on ITO/PET electrodes (chapter 4.2.1.1). MDCK or NRK cells were cultured on the membrane of porous filter inserts. Prior to the measurement, the cell culture media were replaced by serum-free culture media (V_{well} = 2 mL, V_{insert} = 0.5 mL). The distance between the filter membrane and the cell-covered ITO electrodes on the bottom of the chamber was adjusted to 2 mm in the assembled device (Fig.

4.15). The AC voltage amplitude was set to 50 mV (rms) and the resulting impedance signal was recorded at distinct frequencies. The frequency range was preset to 10 – 10^6 Hz with 51 discrete frequencies equally spaced on a logarithmic scale. Two experiments were carried out simultaneously, which provided a time resolution of approx. 2.5 min. Additions of GPCR agonits in serum-free media were performed by a complete exchange of the liquid in the upper filter compartment.

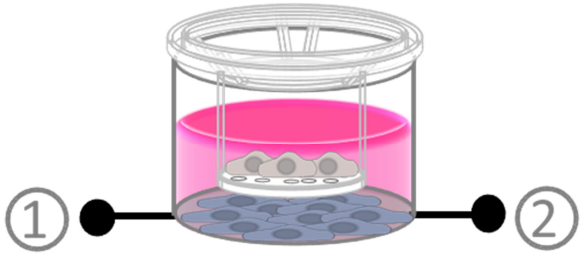

Fig. 4.15: Experimental set-up for molecular permeability measurements of different GPCR agonists across confluent cell layers. A cell-covered filter insert was mounted 2 mm above a cell layer, which was directly cultivated on the integrated ITO electrodes on the bottom (1,2).

4.3.2.5 ECIS measurements in a 96-well array format

A 96W1E+ PET array (chapter 4.2.1.2, Fig. 4.7) was used to detect a potential cytotoxic effect of the redox couple $[Fe(CN)_6]^{3-/4-}$ on confluent monolayers of NRK, MDCK-lr and MDCK-hr cells. Measurements were performed in PBS^{++} buffer (containing 1 g/L glucose) at 37 °C in a humidified cell culture incubator (type: RH M48S-230, MMM Medcenter Einrichtungen, Munich, Germany). The array was connected via a 96-well station to a ECIS Z instrument (both purchased from Applied BioPhysics, Troy, USA). The impedance magnitude was followed at a fixed frequency of 8 kHz over several hours after addition of $[Fe(CN)_6]^{3-/4-}$ in various concentrations.

4.3.3 Equivalent circuit modeling

Parameters to describe the electrical properties of a cell layer were received by fitting the elements of a non-redundant equivalent circuit to the recorded impedance data (chapter 3.1.3). For this purpose LabVIEW® and MATLAB-based programs, written by Prof. Wegener (University of Regensburg), were used. The weighted sum of squares S of the differences between experimental data (Z_i) and calculated impedances of the transfer function ($Z_{i,calc}$)

were minimized by finding the best values of the adjustable circuit parameters (Bevington and Robinson 1969, Lasia 2002) according to equation 4.1. Thereby, the summation runs over all N frequencies. The minimization of the weighted sum of squares S was either carried out by using a complex non-linear least-square method according to the iterative Levenberg-Marquardt algorithm or by a numerical approach. For both programs, an appropriate estimation of the starting parameters is needed. Time-resolved data analysis was performed by using dynamic start values. Starting values for spectrum (*i+1*) were the best fit results for spectrum *i*.

$$S = \sum_{i=1}^{N} \left\{ \omega_i \left[Z_i - Z_{i,calc} \right]^2 \right\} \tag{4.1}$$

ω_i displays the data proportional weighting factor which is necessary to avoid an overestimation of high impedance values. Every measured impedance value Z_i is multiplied by a relative error p. The weighting factor is defined as:

$$\omega_i = \frac{1}{(pZ_i)^2} \tag{4.2}$$

The relative error p which was used in the proportional weighting was set to $p = 0.01$ in dependence on the experimental data. Since the fit errors of the calculated parameters depend on the choice of the value p, SD is often not mentioned. The quantitative analysis provided all parameters of the circuit elements. The resistance of the cell layer (TEER in Ωcm^2) and the cell layer capacitance (C_{cl} in $\mu F/cm^2$) were calculated with respect to the investigated filter membrane area. The frequency-independent TEER values of cell-free filter inserts were either subtracted from the results obtained for the cell-covered filter measurements or the parameters of the filter membrane were included into the fitting routine.

4.4 Diffusion assays

Determination of substrate permeability across barrier forming cell layers was carried out using Transwell® permeable cell culture supports in 12 well plates (chapter 4.1.4). Cells (NRK, MDCK-hr, MDCK-lr) were grown to confluence on these porous membranes and diffusion of a specific molecule was followed over time by either radioanalytical or optical

measurements. The permeability coefficient P_E or the apparent permeability P_{app} was calculated according to the protocol described in chapter 3.2.2.

4.4.1 Permeability assay using isotopic tracer molecules

The measurements described in this section were performed by M. Beer-Krön under supervision of Prof. Bernhardt in the laboratory of Prof. Buschauer (Department of Pharmaceutical/Medicinal Chemistry II, University of Regensburg).

The cell-covered filter inserts were incubated with L-15 medium (Leibovitz, Sigma Aldrich, Munich, Germany) in a standard 12-well filter plate (V_{well} = 2 mL, V_{insert} = 0.5 mL). The plates were kept at 37 °C and agitated at 250 rpm (Thermo-Shaker, type: PHMP, Grant-bio Instruments Ltd., Cambridgeshire, England). The L-15 medium in the apical filter compartment (donor compartment) was replaced by L-15 medium containing defined concentrations of histamine dihyrdrochloride (100 μM) or mepyramine (5 μM) including a portion of the radiolabeled molecule (Tab. 4.10). The concentration of the radiolabeled marker component (in mol/mL) was calculated by the ratio of the given concentration (in both cases: 1 mCi/mL) to the specific activity (Ci/mmol). After the addition of the solution, 100 μL samples were collected at different time points from the receiver compartment. The samples were added to 6 mL mini-vials (Sarstedt, Nümbrecht, Germany) containing 2 mL of Rotiszint® Eco plus (Carl Roth, Karlsruhe, Germany). Radioactivity was determined by liquid scintillation counting using a LS 6500 Liquid Scintillation Counter (Beckman Coulter, Krefeld, Germany).

Tab. 4.10: Tritium-labeled substances used for time dependent concentration analysis.

substance	[^{3}H] position	spec. activity	supplier
histamine dihyrdochloride	[ring, methylene-3H]	25 Ci/mmol	Hartmann Analytik, Braunschweig, Germany
mepyramine (or pyrilamine)	[pyridinyl 5-3H]	20 Ci/mmol	

4.4.2 Optical permeability assays

Optical permeability assays were performed with a mixture of ferro- and ferricyanide ($[Fe(CN)_6]^{3-/4-}$) as permeation marker molecules. Cell-covered filter inserts (NRK, MDCK-lr, MDCK-hr) were incubated with PBS^{++} buffer (+ 1g/L glucose) in standard 12-well plates at 37 °C in a humidified atmosphere. The inserts were agitated at 120 rpm (KM 2 Akku, Edmund

Bühler GmbH, Hechingen, Germany) to reduce effects of unstirred water layers. 250 µL of the apical volume was replaced by 250 µL of a 8 mM $[Fe(CN)_6]^{3-/4-}$ solution. At defined time points after addition, 100 µL samples were collected from the receiver compartment and pipetted into a 96-well plate (TPP®, Sigma Aldrich, Munich, Germany). This was performed without removing the filter inserts from the culture plate. The samples were measured together with samples of defined concentrations of the marker molecule mixture $[Fe(CN)_6]^{3-/4-}$ at a wavelength of 405 nm using a UV-VIS photometer (Tecan Sunrise, Maennedorf, Switzerland).

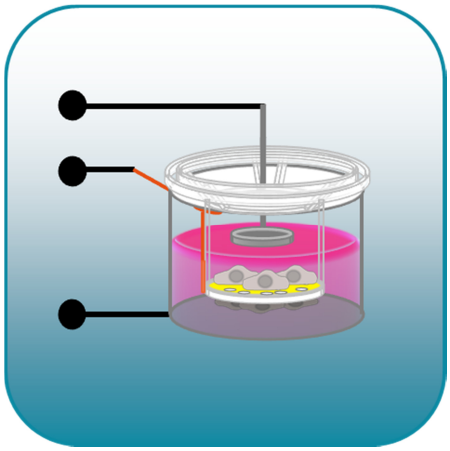

5 Porous electrodes as transducer for cell-based assays

The aim of this project was to develop a device which can be used to monitor the individual dynamics of epithelial barrier function of co-cultured cells in a non-invasive and time-resolved manner. Commercially available filter inserts were modified to serve as growth substrate and porous electrode in between two confluent cell layers. The measurement chambers as well as the fabricated electrodes were thoroughly characterized in their cell-free and cell-covered state. For proof-of-concept studies, different cell types were seeded to confluence on both sides of the permeable membrane and time-resolved attachment and spreading experiments were performed using impedance spectroscopy as monitoring readout. Furthermore, the device was used to report on changes in epithelial barrier function upon addition of a barrier disrupting drug. The new device was also combined with the ECIS technique to determine the electrical properties of three barrier-forming cell layers in parallel.

5.1 Preliminary remarks: Resistance contribution of the subepithelial adhesion zone

Cell-related parameters are obtained from impedance measurements, performed on cell-covered filter inserts, by means of equivalent circuit modelling. However, TEER (transepithelial electrical resistance) values include the resistive contribution arising from the

cell-substrate adhesion zone (R_{sub}) and the resistance due to the intercellular space between adjacent cells. Hence, TEER cannot be solely attributed to the junctional resistance of cell-cell contacts as often denoted. The resistive contribution R_{sub} is dependent on the nature of the used filter inserts (material, porosity) and the cell type under study. In 1999 Lo et al. pointed out, that the additional serial resistance R_{sub} can be a large part of the measured TEER for cells with close cell-substrate contacts. In order to relate TEER values to the true barrier function of a cell layer, R_{sub} needs to be quantified or at least estimated. R_{sub} cannot be measured directly. Lo et al. introduced two models which can be used for a rough estimation of R_{sub} (chapter 3.1.3). The first model is assuming that there is only one large filter pore underneath the cell center (big pore model). The area of the pore is calculated as the sum of all existing pores underneath a single cell. R_{sub} is then dependent on the cell-substrate distance, cell radius as well as the diameter of the big pore and the solution resistivity (eq. 3.13, Tab. 5.1). The second model calculates R_{sub} by assuming that the resistivity of the pores is uniformly distributed underneath the cells (smeared pores model). The calculation is based on a general formula (Giaever and Keese 1993) developed for ECIS measurements (chapter 3.1.4). The smeared pore model relies on the filter resistance. This parameter can be calculated when the pore diameter and thickness of the filter membrane are known. The filter resistance is calculated to less than 1 Ωcm^2 for filter inserts used in this thesis. However, Lo and coworkers used the same insert type but used a measured filter resistance of 10 Ωcm^2 for the calculation. Another prominent model to calculate the seal resistance between cell and substrate was introduced by Weis and Fromherz in 1997 for neuron-silicon junctions and adopted by Wegener et al. (1999) to calculate the subepithelial resistance contribution of confluent cell layers cultured on impermeable electrodes (chapter 3.1.3, eq. 3.14). This 'point-contact' model can be transferred to the situation of filter grown cells. The area of all filter membrane pores is added and this total area is modeled as a conductive ring underneath the cells. The center radius of this ring corresponds to the average radius of pores (point-contact model) whereas its width is given by the total area of pores.

Tab. 5.1: Cell radii and cell-substrate distances for different cell types according to Reiß (2004; low resistance cell type (lr): MDCK-II, high resistance cell type (hr): MDCK-C7). The numbers of pores per cell is calculated from the specific cell radius and the filter properties (A = 1.12 cm^2, pore density: 10^8 pores/cm^2, pore-Ø: 400 nm).

parameter	NRK	MDCK-lr	MDCK-hr
cell radius/ μm	9.2 ± 0.3	8.6 ± 0.2	17.4 ± 0.6
cell-substrate distance / nm	73 ± 3	27 ± 1	60 ± 6
pores per cell	266 ± 17	232 ± 11	952 ± 66

The additional serial resistance arising from the cell-substrate adhesion zone, which is included in the measured TEER values, was calculated according to the different models. The above-mentioned models were integrated into a MATLAB and LabVIEW®-based simulation software written by Prof. Wegener (2016). The results for three different cell types (see Tab. 5.1) are given in Tab. 5.2. The calculated subepithelial resistance R_{sub} for NRK cells varies between 1.2 Ωcm^2 and 10.9 Ωcm^2 depending on the model. Results obtained for MDCK-lr (low resistance type) cells are in a range of 2.8 Ωcm^2 to 11.9 Ωcm^2 and between 5.1 Ωcm^2 and 15.7 Ωcm^2 for MDCK-hr (high resistance type) cells.

Tab. 5.2: Subepithelial resistance (in Ωcm^2) calculated for different cell types (NRK, MDCK-lr, MDCK-hr) cultured on permeable filter supports (A = 1.12 cm^2, pore density: 10^8 pores/cm^2, pore-Ø: 400 nm, membrane thickness: 10 μm, specific electrolyte resistance: 60 Ωcm) according to Lo et al. (1999) and Weis and Fromherz (1997). Cell radii and cell-substrate distances were adopted from Reiß (2004, Tab. 5.1). The filter resistance was preset to 10 Ωcm^2 for the smeared pore model.

model	NRK	MDCK-lr	MDCK-hr
big pore	3.6	8.5	15.7
smeared pores	10.9	11.9	13.4
point-contact (adopted)	1.2	2.8	5.1

The big pore model is not appropriate to calculate R_{sub} for filter membranes used in this thesis. Since polycarbonate membranes with a pore diameter of 400 nm and a density of $10^8/cm^2$ were utilized in all measurements, the assumption of only one big pore being present underneath a single cell is not realistic. With cellular radii of at least 8 μm, more than 200 pores per cell are found underneath a single cell (Tab. 5.1). Hence, results calculated with the big pore model might lead to a misinterpretation of the subepithelial resistance contribution for permeable substrates of defined porosity. Furthermore, R_{sub} calculated for MDCK-lr cells (8.5 Ωcm^2) differs significantly from the values obtained by Lo et al. (152 Ωcm^2). The authors assumed a very narrow and underestimated cell-substrate distance of 1 nm (instead of 27 nm, Tab. 5.1) for the calculation of R_{sub}.

The assumption of a uniform distribution of the filter pores resistances underneath the cellular bodies is more reasonable (smeared pores model). Using this model, the calculated subepithelial resistance for NRK cells cultured on polycarbonate membranes of this type is 10.9 Ωcm^2. NRK cells are described as highly permeable epithelium with TEER values of (13 ±1) Ωcm^2 (Prozialeck et al. 2006, Limonciel et al. 2012). Compared to the TEER of NRK cells, the calculated subepithelial resistance contributes more than 83 % to the overall

measured resistance although there is a considerable distance of 73 nm between the confluent cell layer and the substrate. R_{sub} calculated with the smeared pores model for moderately tight MDCK-lr cell layers is 11.9 Ωcm^2. Reported TEER values of cells of this type are in a range of 50 Ωcm^2 to more than 300 Ωcm^2 (Stevenson et al. 1988, Gekle et al. 1994, Furuse et al. 2001, Reichel et al. 2003). It has to be mentioned that reported transepithelial resistance values for a given cell type often differ significantly. TEER depends on several factors like temperature, buffer pH value and constitution, culture period and cell density as well as membrane type and porosity (Butor and Davoust 1992). Additionally, the measurement system can have an significant influence on the result (Jovov et al. 1991). Assuming a mean value of 100 Ωcm^2 for the transepithelial electrical resistance for MDCK-lr cell layers, the resistance contribution of the narrow cell-substrate adhesion zone is almost 12 %. Hence, the influence of R_{sub} to the integrated TEER needs to be considered for highly permeable NRK cells and moderately tight (leaky) MDCK-lr cells, especially when the results are compared to impedance measurements for cells grown on solid culture substrates (Lo et al. 1999). Alterations in the cell-substrate separation distance as well as in the tight junctional permeability to ions may affect the obtained overall resistance TEER. The situation is different for tight MDCK-hr cells. The calculated subepithelial resistance is 13.4 Ωcm^2 (smeared pores model). Since TEER values reported for MDCK-hr cells are in between 2500 Ωcm^2 and > 5000 Ωcm^2 (Fuller et al. 1984, Stevenson et al. 1988, Gekle et al. 1994), the contribution of R_{sub} to the overall resistance is less than 1 % and can be neglected for this cell type. The expected increase in R_{sub} due to the increased cellular diameter (17.4 μm) is probably compensated by the width of the cell-substrate adhesion zone (60 nm). Although the resistive contribution of R_{sub} to the overall measured resistance is insignificant for tight cellular barriers, TEER still does not display the specific tight junctional resistance in this case. Since the resistance within the paracellular cleft is in the same order of magnitude as the specific membrane resistance (1000 Ωcm^2, Lo et al. 1995), the transcellular current pathway contributes almost equally to the integral resistance. Hence, the integral cellular resistance (TEER) differs significantly from the junctional resistance.

In contrast to the smeared pores model, R_{sub} values obtained with the adopted point-contact model are significantly smaller for all three cell types (Tab. 5.2). According to this model, the subepithelial resistance contribution is less than 10 % for NRK cells, 2.8 % for MDCK-lr cells and again less than 1 % for MDCK-hr cell layers. Moreover, the obtained results are

decreased by a factor of 3 compared to the calculated values for the big pore model. This trend can be explained by the almost identical equations (eq. 3.13 and eq. 3.14). Both calculations differ only in a geometric factor resulting from the location of the big pore or the conducting ring underneath the cells.

Results obtained when applying the smeared pores model are comparable and show the same trend as data modeled by J. Wegener (1998) for the situation of different cell layers on conducting solid substrates. Wegener calculated the cell layer resistance as a function of cell-substrate distance and showed that R_{sub} increases with decreasing cleft width. Furthermore, Wegener's simulated results show that the subcellular resistance contribution to the integral cell layer resistance is negligible for tight epithelia and for moderately tight cell layers with cell-substrate distances above 10 nm. In addition, the monolayer resistance of highly permeable cell layers (e.g. NRK cells) is exclusively defined by the paracellular resistance (dominated by the intercellular cleft width) and significantly increases with decreasing cell-substrate distance (increasing R_{sub}).

In summary, the smeared pore model is considered as most reliable to estimate the subepithelial resistance contribution of cell layers discussed in this thesis since at least 200 pores are located underneath a single cell. However, this model is based on the assumption, that disk shaped cellular bodies are hovering above an impermeable electrode (ECIS model, chapter 3.1.4). The ECIS technique is often applied to study the junctional resistance R_b between cells similar to TEER measurements. Since the ECIS technique allows R_b to be distinguished from the impedance contribution of the subepithelial adhesion zone, R_b is regarded as the true paracellular resistance. Discrepancies between TEER and R_b in comparative studies are often attributed to R_{sub} (included in TEER, Lo et al. 1999).

A comparable experiment was performed here in order to investigate whether R_{sub} is the only factor which causes a discrepancy in epithelial barrier determinations for cells cultured on porous and solid substrates. Low resistance MDCK cells were seeded under identical conditions on permeable filter inserts as well as on commercially available solid ECIS electrode arrays (type 8W10E). Cell attachment and spreading was followed for 24 h and the impedance data were analyzed with the equivalent circuit displayed in Fig. 3.3. This method is reasonable since the used circuit is non-redundant and applicable for impedance measurements of confluent cell layers on porous as well as on solid surfaces. Fig. 5.1 illustrates the obtained results for the transepithelial electrical resistance of MDCK-Ir cells on permeable inserts and solid devices. TEER starts to increase above base line levels within

two hours for both conditions and is almost identical until t = 7.5 h. However, TEER observed for cells on solid supports reaches a maximum value of (122 ± 12) Ωcm^2 at t = 9 h and decreases afterwards to final resistance values of (80 ± 4) Ωcm^2. MDCK-lr cells cultured on permeable membranes show a divergent time course. TEER increases rapidly within 14 h to values of (375 ± 26) Ωcm^2. The transepithelial resistance decreases in the following 10 h by around 50 % to final values of (202 ± 28) Ωcm^2. Both time courses show a transient maximum though its appearance is delayed for filter grown cells. In addition, final TEER values are more than doubled for cell layers which are cultured on permeable substrates. The question arises, whether these differences in TEER progression can be attributed to the additional subepithelial electrical resistance only. Three parameters influence the resistance contribution of the adhesion zone: (i) the specific resistance of the electrolyte underneath the cell layer, (ii) the cell-substrate distance and (iii) the cellular radius.

(i) Since the pores of a filter insert provide a homogeneous distribution of all buffer components, the specific resistance in the adhesion cleft is equal to the specific bulk resistance of the buffer. Furthermore, it was shown that the specific resistance in the adhesion zone is increased by a factor > 10 for this cell type when cultured on impermeable substrates (Reiß 2004). A higher intrinsic resistance should therefore lead to higher TEER values for cells grown on impermeable supports and hence, differences in TEER arising from the resistance of the buffer in the adhesion zone are unlikely.

(ii) The cell-substrate distance was determined to (27 ± 1) nm for MDCK cells cultured on solid supports (Reiß 2004). The distance of the cell layer to a permeable membrane has not been determined so far. Nevertheless, Butor and Davoust showed that MDCK cells form processes at the basal membrane domain which extend into the filter pores (Butor and Davoust 1992). These processes are limited to porous substrates and can increase the subepithelial resistance contribution to the integral TEER significantly. However, a resistance increase by 100 % due to these membrane processes is unlikely.

(iii) Decreasing cellular radii (smaller cells) would result in a decrease of TEER since the linear amount of paracellular elements (junctions) per unit area (length of cell borders between neighboring cells per area, Claude 1978) is increased. This assumption holds true as long as the specific resistance per micrometer of junction remains constant. In fact, it was shown that around 25 % lower cell densities are found for filter grown MDCK cells (Butor and Davoust 1992). Hence, TEER values for MDCK cells spread on permeable substrates show

indeed an increased radius in comparison to cells grown on solid ECIS substrates. However, the question arises why cells exhibit different properties depending on the nature of the growth substrate. Under physiological conditions, epithelial tissue acts as diffusion barrier between two compartments. Permeable inserts mimic these *in vivo* conditions and are more appropriate to study epithelial differentiation and barrier function *in vitro*. Thus it is likely that epithelial differentiation is affected by the nature of the substrate.

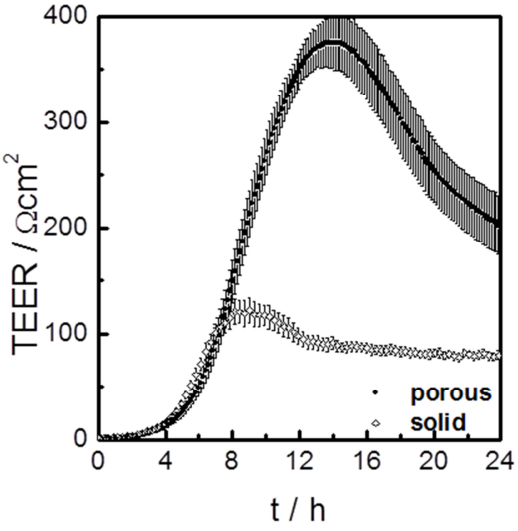

Fig. 5.1: Transepithelial electrical resistance (TEER) of MDCK-Ir cells on porous filter inserts compared to resistance measurements on solid ECIS electrode array type 8W10E (mean ± SE, n = 4). Cells were seeded to confluence on the substrate surface at time zero.

5.2 Characterization of porous electrodes and the measurement chamber

For complex impedance recordings, a measurement chamber for filter inserts was fabricated as published by Wegener et al. in 2004 (chapter 4.2.2). Commercially available filter inserts were modified to serve as porous electrode by depositing a 100 nm thick gold layer on the back side of the polycarbonate membrane (chapter 4.2.3). Impedance spectra of the device were recorded along a frequency window from 1 Hz to 10^6 Hz in complete culture medium at 37 °C with 5 % CO_2 in a humidified incubator (chapter 4.3.1).

5.2.1 Characterization of the measurement set-up

Cell-free polycarbonate filter inserts were placed in between the two electrodes of a

measurement chamber. Stainless steel (Fig. 5.2 A - C) or gold (Fig. 5.2 D - F) was used as material for the dipping (upper filter compartment) and the bottom electrode (lower filter compartment). The complex impedance *Z* was recorded in the transfilter measurement mode. Frequency-dependent impedance magnitude *IZI,* real and imaginary components of the complex impedance presented as resistance *R* and capacitance *C* are analyzed. The influence of the filter insert (plastic scaffold with attached membrane) and the membrane-free scaffold on the measured signal are shown for both measurement chambers in Fig. 5.2 (stainless steel and gold). All quantities are influenced by the capacitive properties of the electrode/electrolyte interface in the low frequency range and by the resistive contribution of the electrolyte in the higher frequency range. Data recorded with both chambers show that the filter insert influences the impedance magnitude in the mid and high frequency range (Fig. 5.2 A, D: f > 50 Hz). The impedance contribution of the filter insert does not depend on the presence of the polycarbonate membrane but also on the plastic scaffold and the electrode material. The effect is even more pronounced when the resistance *R* is plotted against the measured frequencies (Fig. 5.2 B, E). In both cases, the bulk resistance in the high frequency range is decreased when the insert is removed from the measurement chambers. The resistive properties of the filter insert are apparent when stainless steel is used as electrode material (Fig. 5.2 B). In addition to the resistive contributions of the filter insert, capacitive properties are detectable. Capacitance spectra illustrate that the plastic insert reduces *C* for frequencies ≥ 100 Hz (Fig. 5.2 C, F). The scattered capacitance signal for frequencies above 10^4 Hz are due to parasitic contributions of the set-up.

In order to quantify the parasitic resistive and capacitive properties of the device ($R_{paras.}$, $C_{paras.}$), the elements of the equivalent circuit presented in Fig. 3.3 were fitted to the raw data. Parameters of all circuit elements are presented in Tab. 5.3. The elements of the constant phase element (A_{CPE}, n_{CPE}) remain almost unchanged for both measurement chambers after removing the polycarbonate membrane and successively the plastic scaffold. For stainless steel electrodes A_{CPE} is determined to values between 29.7 $\mu Fs^{(n-1)}/cm^2$ and 31.1 $\mu Fs^{(n-1)}/cm^2$ with n_{CPE} between 0.891 and 0.901. For gold as electrode material, A_{CPE} is in between 53.5 $\mu Fs^{(n-1)}/cm^2$ and 58.5 $\mu Fs^{(n-1)}/cm^2$ with n_{CPE} between 0.929 and 0.949. The bulk resistance is reduced from more than 18 Ω to around 8 Ω for the stainless steel set-up and from more than 30 Ω to almost 20 Ω for the set-up including gold electrodes when the plastics are removed from the chambers. Parasitic resistive and capacitive contributions of the device

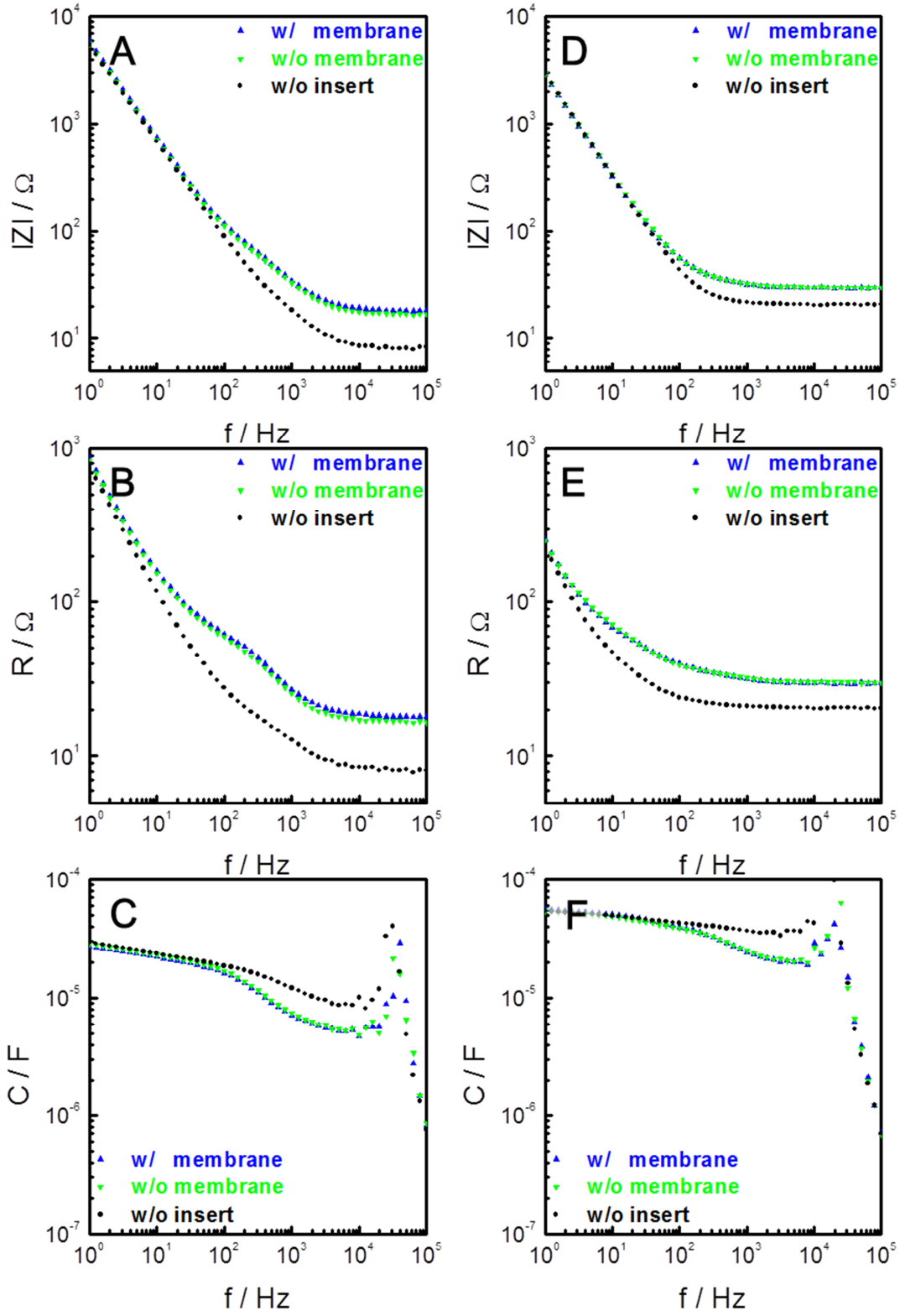

Fig. 5.2: Frequency-dependent impedance, resistance and capacitance spectra of cell-free filter systems in two different measurement chambers (**A** - **C**: stainless steel electrodes, **D** - **F**: gold electrodes). Impedance magnitude *IZI*, resistance *R* and capacitance *C* are plotted against the frequency *f*. Data are shown with the intact insert (**w/ membrane**) placed between both electrodes, the plastic insert scaffold without the attached polycarbonate membrane (**w/o membrane**) and without any insert (**w/o insert**).

remain almost constant independent of the presence of the polycarbonate membrane. Only the removal of the plastic scaffold leads to significant changes of the circuit elements $R_{paras.}$ and $C_{paras.}$ in both set-ups. The resistance contribution ($R_{paras.}$) of the device is decreased from more than 30 Ωcm^2 to 6 Ωcm^2 for the stainless steel electrode arrangement accompanied by a change in the capacitance element ($C_{paras.}$) from 9.30 $\mu F/cm^2$ to 25.5 $\mu F/cm^2$. For the set-up including gold electrodes, this parameter is reduced to about 90 % to a value of 0.7 Ωcm^2 after the plastic insert has been removed. $C_{paras.}$ is calculated to 51.3 $\mu F/cm^2$ in presence of the filter insert and to 432 $\mu F/cm^2$ after removal of the plastics. The bulk resistance (R_{bulk}) is reduced to around 33 % in the set-up containing gold as electrode material and to more than 55 % for the stainless steel device after the insert has been removed.

Tab. 5.3: Parameters for all elements of the electric equivalent circuit are presented for transfilter measurements of polycarbonate filter inserts in measurement chambers with stainless steel electrodes or gold electrodes (w/ mem: intact insert; w/o mem: plastic holder without membrane; w/o insert: chamber without filter insert).

steel	R_{bulk} / Ω	$R_{paras.}$ / Ωcm^2	$C_{paras.}$ / $\mu F/cm^2$	A_{CPE} / $\mu Fs^{(n-1)}/cm^2$	n_{CPE}
w/ mem	18.3	30.6	9.30	29.7	0.895
w/o mem	18.5	28.7	9.13	30.7	0.891
w/o insert	8.4	6.0	25.5	31.1	0.901
gold	R_{bulk} / Ω	$R_{paras.}$ / Ωcm^2	$C_{paras.}$ / $\mu F/cm^2$	A_{CPE} / $\mu Fs^{(n-1)}/cm^2$	n_{CPE}
w/ mem	30.6	7.5	51.3	58.5	0.931
w/o mem	30.5	5.4	56.4	56.8	0.929
w/o insert	20.4	0.7	432	53.5	0.949

The two-electrode set-up was preferred over ‘chopstick’ electrodes in order to enable a homogeneous electric field across the filter membrane (Jovov et al. 1991). Stainless steel as well as gold is suitable as electrode material for transfilter impedance measurements. However, stainless steel is preferable since the electrodes are very stable and chamber fabrication is less expensive. Differences in the bulk resistance are due to the thickness of the electrodes. Whereas the stainless steel plates are 2 mm thick, the thickness of the gold layer is only 100 nm. This very thin metal layer leads to a higher lead resistance and hence, an increase in R_{bulk}. The high lead and bulk resistance of the thin gold electrodes masks the parasitic effect of the filter insert and the measurement chamber (Fig. 5.2 E). Equivalent circuit modeling shows that the parameter of the constant phase element A_{CPE} (chapter 3.1.1) depends on the electrode material and the geometry (active electrode area) which is equal in both measurement chambers. Since the measurement chamber was adopted from Wegener

et al. (2004) A_{CPE} is in good agreement with the published values for stainless steel electrodes (31.5 $\mu Fs^{(n-1)}/cm^2$). Deviations due to the electrode sizes (A_{el}) and distances result in a changed capacitance *C* of the non-ideal circuit element CPE according to:

$$C = \frac{\varepsilon_0 \varepsilon_r A_{el}}{d} \tag{5.1}$$

where C is the capacitance, ε_0 is the electric field constant, ε_r is the dielectric constant and d is the separation between both electrodes. Parameters obtained for n_{CPE} are in between the typical range of 0.85 - 1 (Daniels and Pourmand 2007, Heiskanen and Emnéus 2011). Gold electrodes form very smooth surfaces in general, thus n_{CPE} is higher compared to stainless steel used as electrode material. With n_{CPE} of around 0.9, the constant phase element of both devices indicate highly capacitive properties. The calculated parameters for the parasitic, capacitive properties of the device ($C_{paras.}$) show that the polycarbonate filter membrane as well as the polystyrene scaffold of an intact filter insert can be discussed as two dielectrics in series. The capacitance is stepwise increased by removing the membrane and the scaffold subsequently. The inverse is observed for the parasitic resistance ($R_{paras.}$). The effect of the porous insert to transfilter measurements is well-known. However, it was assumed that its influence is mainly due to the porous polycarbonate membrane and TEER values are often corrected with respect to the resistance of the cell-free membrane/insert (Günzel et al. 2010, Wegener and Seebach 2014). The results shown in Tab. 5.3 prove that no significant effect is observed when the filter membrane is removed. The scaffold plastics and the electrodes express resistive and capacitive properties which need to be considered when the cell-related parameters are calculated from transfilter measurements.

Parameters which are calculated for the insert-free set-up might lead to misinterpretation. Since both electrodes are only in contact to the electrolyte, the equivalent circuit is redundant. The system should be described as a serial connection of resistor (bulk resistance) and a constant phase element (electrode/electrolyte interface, see Fig. 3.2). However, the experimental data (w/o insert, Fig. 5.2 A-C) do not fit to such a simple circuit. Resistive and capacitive contributions are present even in absence of the filter insert. This effect is not explainable so far but might arise due to the composition of the stainless steel electrodes. Since the complex equivalent circuit (Fig. 3.3) is most suited to describe the experimental data, all measurements are evaluated by fitting the elements of this circuit to the raw data.

5.2.2 Parasitic impedance contributions: correction methods

Cell-specific parameters can be determined from transfilter measurements by means of equivalent circuit modeling (chapter 3.1.1). As detailed in the previous section, the cell-related parameters transepithelial electrical resistance (TEER) and cell layer capacitance (C_{cl}) include the parasitic contributions of the cell-free device (membrane, scaffold, electrodes). The corresponding equivalent circuit is presented in Fig. 5.3 A. The total impedance of the system must be corrected for the contribution of the cell-free device. The impedance contribution of the cell-free device is measured separately and the parasitic parameters are quantified. Two correction methods are possible. (i) The parasitic resistance of the device ($R_{paras.}$) is subtracted from the TEER determined for the cell-covered device. Additionally, the capacitance of the cell-covered device is corrected for the parasitic capacitance of the device ($C_{paras.}$). (ii) The parasitic parameters are determined separately and are then integrated into the fitting program according to the equivalent circuit presented in Fig. 5.3 B. These parameters are kept constant during the fitting procedure.

Both methods can be used to correct for the impedance contribution of the cell-free device and provide the cell-related parameters. Tab. 5.4 summarizes results which are calculated with both methods for three different cell types cultured on polycarbonate filter inserts.

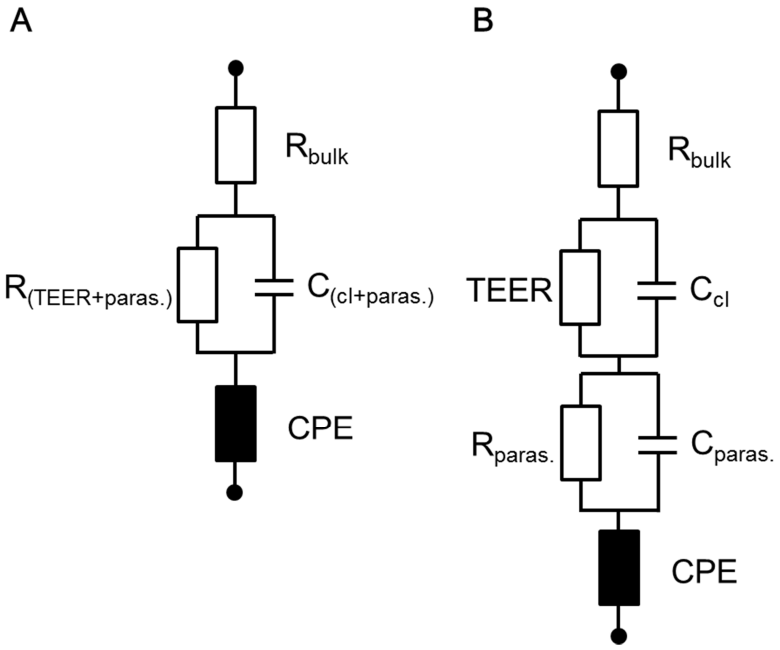

Fig. 5.3: Equivalent circuits used to determine cell-related parameters from transfilter measurements. **A** Parasitic resistive and capacitive contribution of the cell-free device ($R_{paras.}$, $C_{paras.}$) and the cell layer (TEER, C_{cl}) are combined in a non-redundant circuit. **B** The circuit discriminates between the impedance contributions of the cell-free device and the cell layer.

The results for TEER of NRK cells layers differ for both correction methods. The values received by the subtraction method (i) are determined to (-5 ± 5) Ωcm^2 whereas the values obtained by the correction method (ii) are (12 ± 1) Ωcm^2. No significant difference in TEER is observed for both correction methods applied to MDCK cell experiments (hr: high resistance type and lr: low resistance type). No significant deviation is detectable for both correction methods regarding the capacitances of MDCK cells, except for increased standard errors calculated according to method (i). However, results calculated for confluent NRK cells again differ by a factor of four from each other.

Tab. 5.4: Transepithelial electrical resistance (TEER) and cell layer capacitance (C_{cl}) determined NRK cells, MDCK-lr cells and MDCK-hr cells (mean ± SE, n = 3). The experimental values are corrected with two different methods (i: parasitic parameters are subtracted: $R_{paras.}$ = (25 ± 2) Ωcm^2, $C_{paras.}$ = (11.6 ± 1.3) $\mu F/cm^2$; ii: parasitic parameters are integrated and set constant during equivalent circuit modeling: $R_{paras.}$ = (25 ± 2) Ωcm^2, $C_{paras.}$ = (9.80 ± 1.07) $\mu F/cm^2$).

TEER / Ωcm^2	**no correction**	**method (i)**	**method (ii)**
NRK	20 ± 2	-5 ± 5	12 ± 1
MDCK-lr	108 ± 1	83 ± 4	83 ± 1
MDCK-hr	3083 ± 222	3060 ± 130	2975 ± 129
C_{cl} / $\mu F/cm^2$	**no correction**	**method (i)**	**method (ii)**
NRK	3.39 ± 0.50	4.79 ± 1.43	1.01 ± 0.04
MDCK-lr	2.11 ± 0.06	2.57 ± 1.34	2.19 ± 0.08
MDCK-hr	1.95 ± 0.01	2.34 ± 1.34	2.07 ± 0.02

Electric parameters for different confluent cell layers often vary since they strongly depend on the specific culture conditions. Hence, these parameters can not be regarded as specific for a given cell type. However, cell-related parameters determined for MDCK cells (both types) are in good agreement with published data (Tab. 5.5). Both correction methods are appropriate to determine transepithelial resistances and cell layer capacitances. In general, the specific capacitance of an unfolded cell membrane, arising from the insulating and hydrophobic part of the lipid bilayer, is in the order of 1 $\mu F/cm^2$ (Cole 1972). Since the apical and basal cell membranes act as two capacitors connected in series to each other the minimal cell layer capacitance is 0.5 $\mu F/cm^2$. Any increase in cell surface area (e.g. due to membrane invaginations, protrusions or microvilli formation) leads to increased values. MDCK cells are known to exhibit a large amount of microvilli on the apical cell surface accompanied by large basolateral membrane enfolding (Madsen and Tisher 1986, Butor and Davoust 1992). Thus, cell layer capacitance values of ~ 2 $\mu F/cm^2$ are reasonable.

The situation is different for highly permeable NRK cells. The transcellular resistance cannot be discriminated from cell-free filter value by applying correction method (i). Only by integrating the parasitic cell-free parameters into the fitting routine (method ii), the electrical properties of NRK cells can be determined in a reproducible and reliable manner. This observation can be explained by comparing the fitted values, derived with both methods, to the experimental data (Fig. 5.4). The best parameters obtained by fitting the elements of the simplified equivalent circuit (Fig. 5.3 A) to the impedance data do not fit the experimental data properly for frequencies above 200 Hz (Fig. 5.4 A). The parasitic impedance contribution of the device (mid frequency range) is not considered in the equivalent circuit used in the fit routine. Highly permeable cell types, like NRK cells, influence the total impedance of the system in the high frequency range. Hence, the fitted NRK parameters are in between the values for the cell-related and the parasitic parameters of the device before the correction method (i) is applied. Thus, correction method (i) results in negative TEER values. Correction method (ii) is favorable for the impedance analysis of highly permeable cell types (Fig. 5.4 B). Data analyzed by applying the equivalent circuit presented in Fig. 5.3 B are similar to the electrical properties reported for NRK cells (Tab. 5.5), especially the calculated transepithelial resistance of (12 ± 1) Ωcm^2.

In summary, both correction methods are appropriate to determine the passive electrical properties of (leaky or moderately) tight MDCK cell layers cultured on permeable supports.

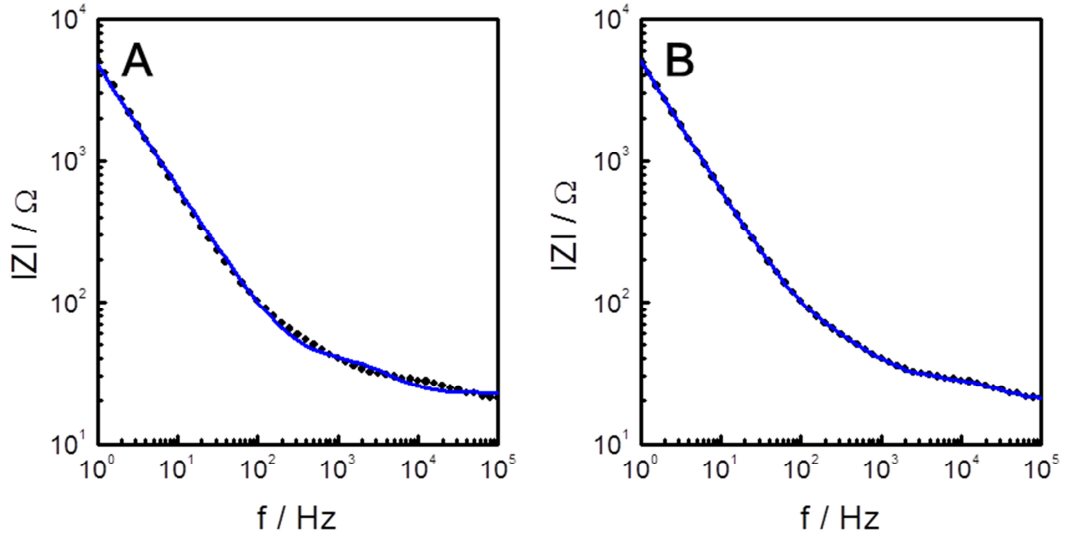

Fig. 5.4: Equivalent circuit modeling: Frequency-dependent impedance magnitude of a confluent NRK cell layer cultured on permeable filter inserts. The same typical data set is analyzed with two different equivalent circuits (● recorded data, ▬ fitted data). **A** The equivalent circuit shown in Fig. 5.3 A is used. Fit parameters: R_{bulk} = 23 Ω, TEER = 15 Ωcm^2, C_{cl} = 2.81 $\mu F/cm^2$, A_{CPE} = 37.8 $\mu Fs^{(n-1)}/cm^2$, n_{CPE} = 0.870. **B** The equivalent circuit which includes the cell-free device parameters is used for data analysis (Fig. 5.3 B). Fit parameters: R_{bulk} = 21 Ω, TEER = 11 Ωcm^2, C_{cl} = 0.93 $\mu F/cm^2$, $R_{paras.}$ = 25 Ωcm^2, $C_{paras.}$ = 9.80 $\mu F/cm^2$, A_{CPE} = 33.5 $\mu Fs^{(n-1)}/cm^2$, n_{CPE} = 0.905.

However, method (ii) is superior regarding the accuracy of the determined parameters. Therefore, all data are analyzed via the extended equivalent circuit which includes the correction for the parasitic parameters of the cell-free device (Fig. 5.3 B).

Tab. 5.5: Electrical properties of different cell monolayers cultured on permeable substrates.

cell type	TEER / Ωcm^2	C_{cl} / $\mu F/cm^2$	reference
NRK	13 ± 1		Prozialeck et al. 2006
	12		Limonciel et al. 2012
	9.3 ± 0.8	0.60 ± 0.04	Reiß and Wegener 2015
	12 ± 1	1.01 ± 0.04	this work
MDCK-lr	52 ± 34		Stevenson et al. 1988
	82 ± 2.4		Carr et al. 2010
	136 ± 17		Lo et al. 1999
	330 ± 20		Gekle et al. 1994
	73.2 ± 1.8	2.29 ± 0.01	Rommel 2007
	25	3.40	Günzel et al. 2012
	~100	~ 1.30	Krug et al. 2009b
	83 ± 1	2.19 ± 0.08	this work
MDCK-hr	4940 ± 859		Stevenson et al. 1988
	4301 ± 674		Butor and Davoust 1992
	2870 ± 240	0.96 ± 0.04	Reiß 2004
	1750 ± 250	1.00 – 1.80	Wegener 1998
	1543 ± 252	1.46 ± 0.06	Janshoff et al. 1996
	1600	1.30	Günzel et al. 2012
	2975 ± 129	2.07 ± 0.02	this work

5.2.3 Electrochemical properties of porous electrodes

Commercially available filter inserts were compared to the fabricated porous electrodes. Therefore, the inserts were placed in between two stainless steel electrodes of the measurement chamber and the complex impedance of the system was measured. Fig. 5.5 shows the impact of the filter membrane modification (including the electrical connections) to the impedance magnitude *IZI* (A), resistance *R* (B) and capacitance *C* (C) of the set-up recorded in the transfilter measurement mode (dipping electrode vs. bottom electrode, porous electrode remains unconnected on floating potential, Fig. 5.5 A - C). The frequency spectra show the double layer capacitance of the electrode/electrolyte interface in the lower frequency range and the resistance of the bulk in the higher frequency range. The impedance contribution of the filter inserts is visible for frequencies between 10 Hz and 10^2 Hz for *IZI* and *R* and from 10^2 Hz to $3 \cdot 10^4$ Hz in the capacitance spectra. All three parameters show no detectable difference between the Transwell® filter inserts (TW) and the gold-modified filter

inserts (AuTW). By including the porous gold electrode to the set-up, two additional measurement modes are accessible. Fig. 5.5 D - F displays the common transfilter measurement mode (● **1-3**, dipping electrode no. 1 vs. bottom electrode no. 3) and two new additional recording modes. The impedance of the upper filter compartment can be recorded by measureing the porous electrode (no. 2) against the dipping electrode (no. 1) which is placed in the apical filter compartment (mode ▲ **1-2**). The complex impedance of the lower compartment can be recorded when the porous electrode is measured against the bottom electrode no. 3 (mode ▼ **2-3**). For better comparison of the measured data, the elements of an equivalent electric circuit (Fig. 3.3) were fitted to the raw data displayed in Fig. 5.5. Tab. 5.6 lists the best fit determined values for all elements of the equivalent circuit. Minor variations are determined for standard filter inserts (TW) compared to the set-up including a porous electrode (AuTW) in the transfilter measurement mode (**1-3**). The additional measurement modes of the set-up, which include the porous electrode (**1-2**, **2-3**) differ significantly from the transfilter measurement mode (**1-3**) in all parameters except for n_{CPE}. The calculated bulk resistance (R_{bulk}) is reduced from (18.9 ± 0.3) Ω in mode **1-3** to (14.3 ± 0.5) Ω in mode **1-2** and to (8.4 ± 0.5) Ω in measurement mode **2-3**. The determined parasitic resistance ($R_{paras.}$) decreases in the same sequence from (32 ± 2) Ωcm^2 to (11 ± 1) Ωcm^2 whereas the parasitic capacitance ($C_{paras.}$) of the device increases from (11.00 ± 0.02) μF/cm^2 to a value of (26.52 ± 0.01) μF/cm^2. Additionally, the parameter A_{CPE} is significantly different for all measurement modes. A_{CPE} is (38.8 ± 0.2) μFs$^{(n-1)}$/cm^2 for mode **1-2**, (64.9 ± 0.5) μFs$^{(n-1)}$/cm^2 for the lower filter compartment (**2-3**) and (34.68 ± 0.03) μFs$^{(n-1)}$/cm^2 for the transfilter measurement (**1-3**).

Within the standard deviation, similar mean values are obtained for all set-up related parameters in the transfilter measurement mode (**1-3**). Hence, the membrane modification does not have any significant influence on the electrochemical measurement. The modified filter membranes display highly reproducible electric properties in all three measurement modes. Due to the positioning of the permeable electrode in between the dipping and the bottom electrode, the bulk resistance is reduced for both new measurement modes (**1-2**, **2-3**). Since the distances between the electrodes are not equal, the measured values differ from each other. Furthermore, the parameter A_{CPE} of the constant phase element is different for all three measurement modes. According to eq. 5.1, A_{CPE} is directly proportional to the active

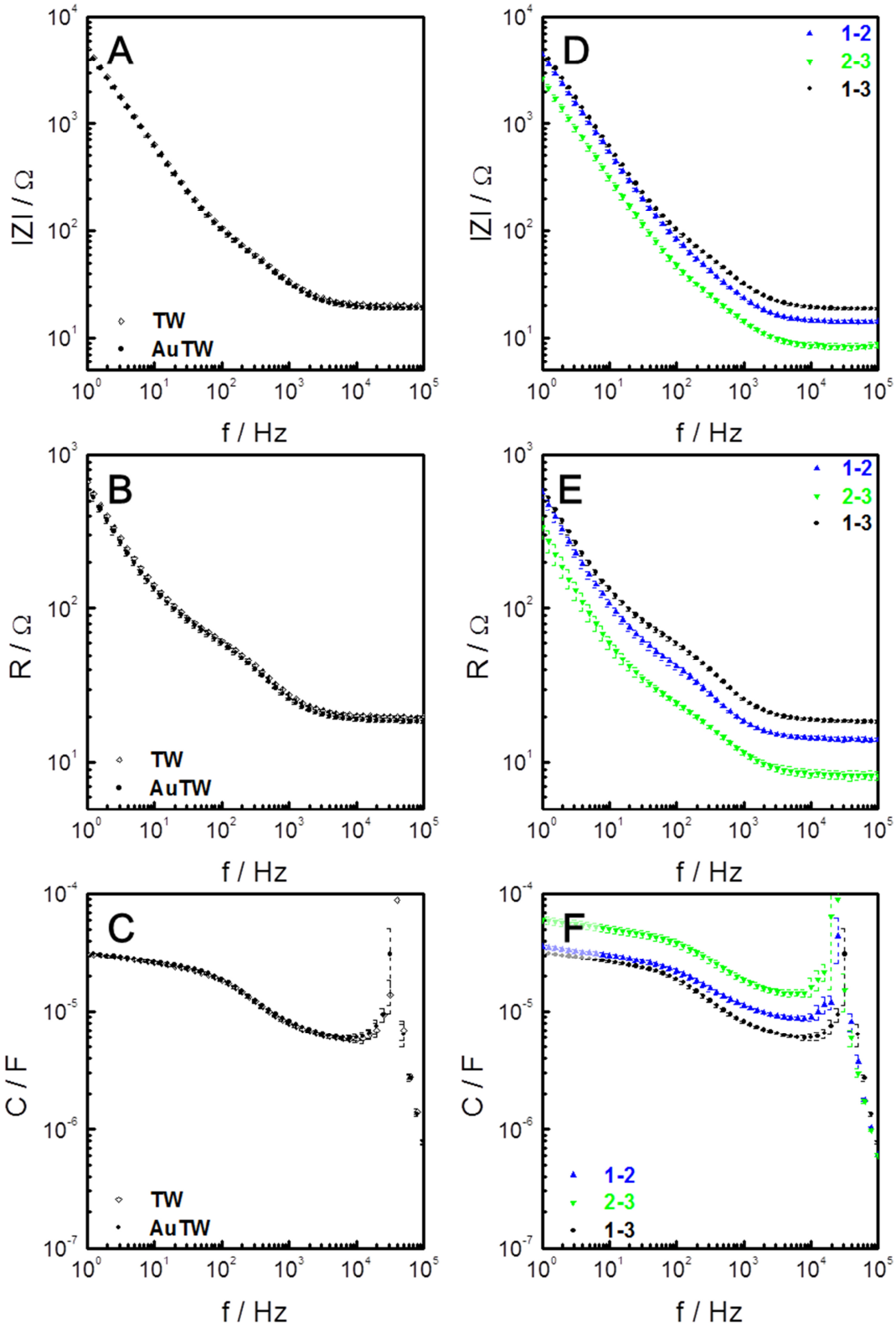

Fig. 5.5: Frequency spectra of impedance magnitude *IZI*, resistance *R* and capacitance *C* for cell-free filter inserts (mean ± SDM, n ≥ 9). **A - C**: Standard filter inserts (**TW**) are compared to gold-modified inserts (**AuTW**) in the transfilter measurement mode. **D – F**: Individual measurement modes accessible with porous electrodes (upper filter compartment (▲ **1-2**), lower compartment (▼ **2-3**), both compartments in the integrative transfilter measurement mode (● **1-3**).

electrode area. The diameter of the porous electrode is increased compared to the dipping electrode in the upper filter compartment. Hence, highest values of A_{CPE} are calculated for measurement mode **2-3**. The parasitic contributions of the device ($R_{paras.}$, $C_{paras.}$) to the total impedance of the system are reduced in mode **1-2** compared to the transfilter measurement mode (**1-3**). The gold layer is deposited on the back side of the filter membrane. Thus, the portion of the plastic scaffold which influences the electric field is reduced. The additional resistive and capacitive elements are also obtained by fitting the elements of the equivalent circuit to the data recorded in measurement mode **2-3**. Since the porous electrode is electrically connected to the bottom electrode by the electrolyte only, the situation should be described by a simple R-CPE connection. However, the extended equivalent circuit is suited much better to calculate cell-related parameters for all experiments shown in this thesis and, thus, all values are corrected for parameters of the cell-free device (Tab. 5.6).

Tab. 5.6: Parameters for all elements of the equivalent electric circuit (mean ± SDM, n ≥ 9) as determined for polycarbonate filter inserts (TW) and porous electrodes (AuTW) in all possible measurement modes (**1-3**: transfilter mode; **1-2**: upper filter compartment; **2-3**: lower filter compartment).

parameter / unit	TW (1-3)	AuTW (1-3)	AuTW (1-2)	AuTW (2-3)
R_{bulk} / Ω	20.1 ± 0.3	18.9 ± 0.3	14.2 ± 0.5	8.4 ± 0.5
$R_{paras.}$ / Ωcm^2	32 ± 2	32 ± 2	20 ± 2	11 ± 1
$C_{paras.}$ / μF/cm^2	10.49 ± 0.01	11.00 ± 0.02	19.15 ± 0.05	26.52 ± 0.01
A_{CPE} / μFs$^{(n-1)}$/cm^2	34.37 ± 0.02	34.68 ± 0.03	38.8 ± 0.2	64.9 ± 0.5
n_{CPE}	0.898 ±0.002	0.902 ±0.003	0.904 ±0.005	0.909 ±0.009

5.3 Impedance analysis of barrier forming cell types in mono- or co-cultures

Confluent cell layers were cultured on one or both sides of modified filter inserts. Co-cultures were prepared with the same or different MDCK cell types. Cells were seeded to the back side of the filter membrane first and allowed to attach and spread for 4 h. The inserts were flipped, placed into the measurement chamber and cells of the same (homogeneous co-culture) or a different cell type (heterogeneous co-culture) were seeded to the upper filter membrane side (chapter 4.1.4). Measurements were started immediately afterwards and the complex impedance was recorded over an extended frequency window in complete culture medium and under physiological conditions (chapter 4.3.2.2).

5.3.1 Homogeneous co-cultures

5.3.1.1 MDCK-Ir co-culture

The scheme in Fig. 5.6 A illustrates the experimental set-up for co-cultured MDCK-Ir cell layers. The electrodes involved are numbered. The dipping electrode (no. 1) is placed in the upper filter compartment. The porous electrode (no. 2) is located on the back side of the filter membrane which separates both fluid filled compartments. A third electrode (no. 3) is placed on the bottom of the measurement chamber. Impedance magnitude *IZI*, resistance *R* and capacitance *C* of the system are shown in Fig. 5.6 B - D for all three possible measurement

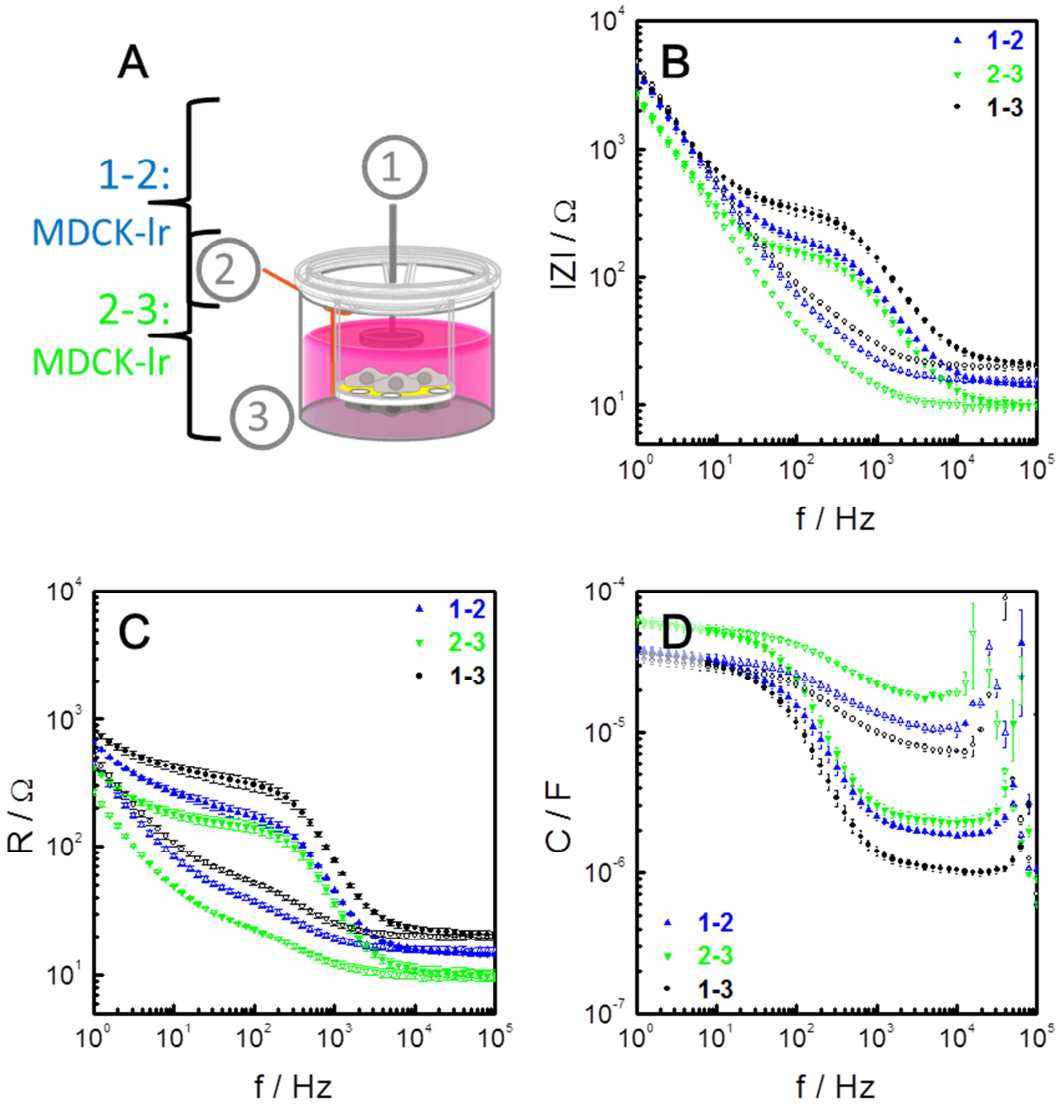

Fig. 5.6: A Schematic illustration of the experimental set-up. Frequency-dependent impedance magnitude *IZI* (**B**), resistance *R* (**C**) and capacitance *C* (**D**) are shown for MDCK-Ir cells, cultured on both sides of the filter insert (mean ± SE, n = 3). Empty symbols represent the cell-free devices. Filled symbols indicate the results for cell-covered membranes. The upper filter compartment is marked in blue (**1-2**), the lower filter compartment in green (**2-3**) and the transfilter measurement mode in black (**1-3**).

modes. Empty symbols represent the cell-free set-up whereas filled symbols are recorded for the cell-covered device 24 h after cell seeding when the cell layers are fully established. For all measurement modes, the impedance magnitude *IZI* is dominated by the double layer capacitance of the electrodes in a frequency window from 1 - 10 Hz and by the resistance of the bulk electrolyte in the high frequency range ($f > 2 \cdot 10^4$ Hz). The impedance of the system is significantly increased in the mid frequency range when confluent cell-layers are present on the filter membrane. Due to the impedance increase, a plateau region is detectable from 20 Hz to around 400 Hz. The impedance magnitude within this region reaches values of around 200 Ω for measurement mode **1-2** and **2-3**. Around 400 Ω are detected for the transfilter measurement mode (**1-3**). The frequency regions in which the cell layers affect the signal are shifted to $1 – 10^4$ Hz for the resistance spectra (Fig. 5.6 C) and to $20 - 4 \cdot 10^4$ Hz in the capacitance spectra (Fig. 5.6 D). In the plateau region, absolute resistance values of around 200 Ω for the cells located on the top side of the filter membrane (**1-2**) are obtained. MDCK-Ir cells attached on the back side of the filter show resistance values of around 150 Ω (**2-3**) in this frequency region. Almost 350 Ω are obtained for the integrated transfilter measurement mode (**1-3**). At a frequency of 10^4 Hz, the cell-covered system shows capacitance values of ~ 1 μF for the integrated signal (**1-3**) and ~ 2 μF for measurement mode **1-2** and mode **2-3** (Fig. 5.6 D). Capacitance spectra are scattered above this frequency due to parasitic contributions of the measurement set-up (electrical connections, relay).

For better comparison of the cell-related parameters, the recoded data were analyzed by means of equivalent circuit modeling. Tab. 5.7 lists the parameters obtained for the transepithelial electrical resistance (TEER) and cell layer capacitance (C_{cl}) after correction for the cell-free values. TEER values for the upper cell layer (**1-2**) are determined to (164 ± 22) Ωcm^2 and to (139 ± 16) Ωcm^2 for the cell layer located on the back side of the membrane (**2-3**). (305 ± 39) Ωcm^2 are obtained for the integrated signal measured over both cell layers (**1-3**). The cell layer capacitances (C_{cl}) are (1.98 ± 0.06) μF/cm^2 for the upper cell layer (**1-2**) and (2.30 ± 0.20) μF/cm^2 for the second MDCK-Ir cell layer (**2-3**). Integration over both cell layers measured in the transfilter mode (**1-3**) results in a value of (1.05 ± 0.06) μF/cm^2.

The cell-related parameters are in good agreement to published values (see Tab. 5.5). The resistances recorded for both separately measured MDCK-Ir cell layers (**1-2**, **2-3**) correspond to the reported mean values of 50 Ωcm^2 to 300 Ωcm^2.

Tab. 5.7: Parameters derived by means of equivalent circuit modelling for co-cultured MDCK-Ir cells 24 h after seeding (mean ± SE, n = 3).

mode	TEER / Ωcm^2	C_{cl} / µF/cm^2
1-2 (top side)	164 ± 22	1.98 ± 0.06
2-3 (back side)	139 ± 16	2.30 ± 0.20
1-3 (transfilter mode)	305 ± 39	1.05 ± 0.06

No significant difference in TEER is detectable for cells located on the upper or lower membrane side (substrate material top side: polycarbonate; back side: gold). The integrated resistance as well as the co-culture capacitance, measured over both cell layers (**1-3**), confirms the additivity of both resistive and capacitive contributions arranged in series. With an integral co-culture resistance of (305 ± 39) Ωcm^2, TEER measured in the standard transfilter mode represents exactly the sum of both separately measured cell layer resistances. The same holds true for the total co-culture capacitance (1.05 ± 0.06) µF/cm^2) which can be calculated according to:

$$\frac{1}{C_{co-culture}} = \frac{1}{C_{cell\ layer\ 1}} + \frac{1}{C_{cell\ layer\ 2}} \qquad (5.2)$$

Continuous impedance recordings with the new device provide detailed information about the kinetics of epithelial barrier formation in MDCK-Ir co-cultures. Time-resolved raw data (appendix: Fig. 12.1) were analyzed via equivalent circuit modeling. Cell-related parameters (TEER, C_{cl}) were calculated for all three measurement modes and are displayed in Fig. 5.7. TEER of the lower cell layer (**2-3**) starts to increase after 2 h (Fig. 5.7 A). The transepithelial electrical resistance of the cell layer peaks at t = 8.3 h at a value of (456 ± 50) Ωcm^2 and decreases thereafter to a final value of (139 ± 16) Ωcm^2 at t = 24 h r. Cells which were seeded directly on top of the filter membrane before the measurement started were followed in mode **1-2**. TEER starts to increase after around 6 h and reaches a maximum of (249 ± 36) Ωcm^2 at t = 14.3 h. At the end of the measurement the resistance of the cell layer is determined to a final value of (164 ± 22) Ωcm^2. A pronounced resistance peak as determined for the MDCK cell layer on the bottom membrane side is not observed. The integral transepithelial resistance of both cell layers, determined in the transfilter mode (**1-3**), is identical to the time-course for the lower MDCK cell layer within the first 5 h. A maximum of (458 ± 84) Ωcm^2 is reached at t = 8.7 h followed by a stationary phase between t = 11 h to t = 15 h after cell seeding ((523 ± 29) Ωcm^2). The transepithelial electrical resistance of the

entire co-culture decreases in the next 10 h to a final value of (305 ± 39) Ωcm^2.

Fig. 5.7 B shows the associated cell layer capacitances. The capacitance detected in the lower measurement chamber (**2-3**) decreases within the first 4 h from (12 ± 1) $\mu F/cm^2$ to a minimum value of (1.59 ± 0.04) $\mu F/cm^2$ at t = 4 h. Thereafter, capacitance values increase slightly in the next 16 h to a final value of (2.3 ± 0.2) $\mu F/cm^2$. The capacitance detected in the upper compartment (**1-2**) decreases very rapidly from (32 ± 2) $\mu F/cm^2$ at the beginning of the measurement to values of (1.66 ± 0.15) $\mu F/cm^2$ after 8 h. The cell layer capacitance increases slightly afterwards until final values of (1.98 ± 0.06) $\mu F/cm^2$ are reached. After a fast decrease from (9.4 ± 0.8) $\mu F/cm^2$, the integrated capacitance measured over both cell layers (**1-3**) reaches a minimum at t = 4 h of (1.29 ± 0.07) $\mu F/cm^2$. This first minimum is followed by a second minimum, detectable after 12 h ((0.90 ± 0.06) $\mu F/cm^2$)). The capacitance stays almost stable until the end of the measurement ((1.05 ± 0.06) $\mu F/cm^2$). Similar to the described TEER recordings, the integrated capacitance of the co-culture shows that the capacitive contributions of both cell layers are arranged in series.

Cell attachment and spreading on solid conducting surfaces can be followed in a time-resolved manner by monitoring the progress (decrease) of the total capacitance (Wegener et al. 2000, Benson et al. 2013). The capacitance is decreased due to the formation of a confluent layer of insulting cell membranes on top of the measurement

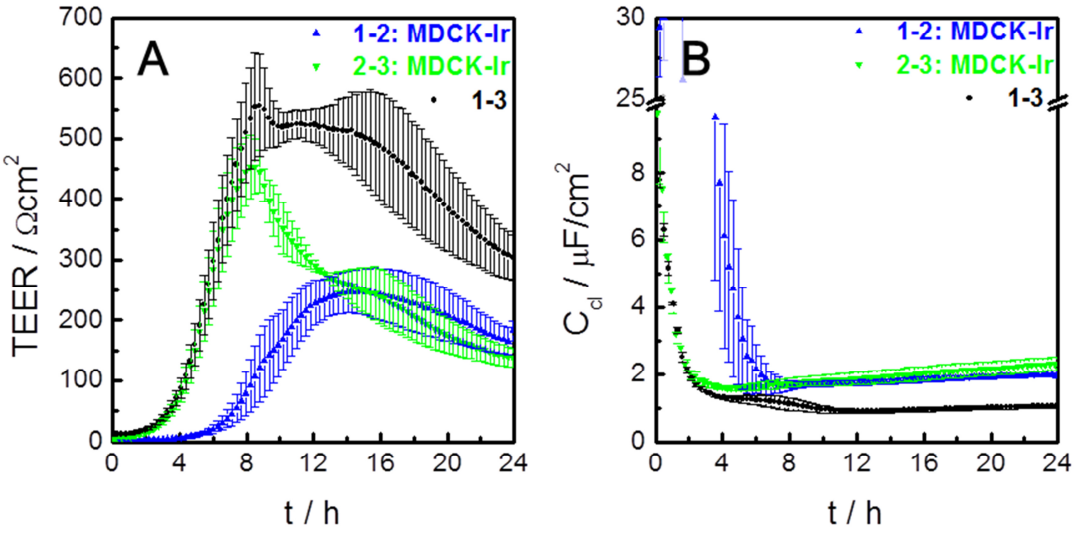

Fig. 5.7: Time course of the transepithelial electrical resistance TEER (**A**) and the cell layer capacitance C_{cl} (**B**) for all three possible measurement modes (mean ± SE, n = 3). Co-cultured MDCK-Ir cells are located on both sides of the membrane (▲ **1-2**, ▼ **2-3**). Values for the entire system are shown in black (● **1-3**).

electrode. In an analogous way, the system's capacitance can be used to follow the formation of a confluent cell layer on (macro-) porous substrates (Michaelis et al. 2012).

The capacitance progression observed here for both monolayers results in final values of around 2 $\mu F/cm^2$ after confluent cell layers are formed. This indicated a (apical and basolateral) membrane capacitance of ~ 4 $\mu F/cm^2$ and is similar to reported values (Cole 1972). It has to be mentioned, that high capacitance values obtained for subconfluent cell layers at the beginning of the experiment ($t < 4$ h) are clearly overestimated by means of equivalent circuit modeling. The bulk resistance masks the cell-based impedance when filter inserts with growth areas of more than 0.5 cm^2 are used. Hence, very high and unphysiological cell layer capacitance values are observed.

However, the new device offers the possibility to record time-resolved capacitance values of two cell layers in a co-culture separately. These capacitance recordings can provide additional information regarding cell attachment kinetics as well as cell membrane morphology. The two additional measurement modes resolve the integrated signal which is detected in the transfilter measurement (**1-3**). The integral capacitance measured over both cell layers shows two separate local minima. By analyzing measurement mode **1-2** and **2-3** it is obvious that each minimum represents the formation of a confluent cell layer on opposite sides of the filter.

The transepithelial resistance of both cell layers starts to increase above baseline levels 6 h after inoculation at $t = 2$ h (lower cell layer was seeded 4 h prior to the measurement). In addition, TEER reaches similar values at the end of the measurement period (Tab. 5.5). The characteristic TEER progression determined for the co-culture (**1-3**) can be explained by adding the resistance contributions of either cell layer. However, only the cell layer on the back side of the filter membrane shows a pronounced maximum in TEER during cell attachment and spreading studies (**2-3**). This TEER peak is not detectable for the cell layer which is seeded subsequently on the upper side.

Control experiments performed on the fabricated porous electrodes show, that the peak appearance does not depend on the position of the cell layer since the same time course can be observed when MDCK-Ir cells are cultured on the upper (polycarbonate) filter membrane side only (Fig. 5.8 A). However, the appearance of the peak is slightly delayed and less pronounced. In addition, the inoculation time is not crucial for the transient TEER maximum of the second cell layer. Only the cell layer which is present on the filter membrane first shows the remarkable resistance time course even for co-cultures with a delayed inoculation of the second cell layer (24 h instead of 4 h, Fig. 5.8 B - D). Hence, the absence of a pronounced

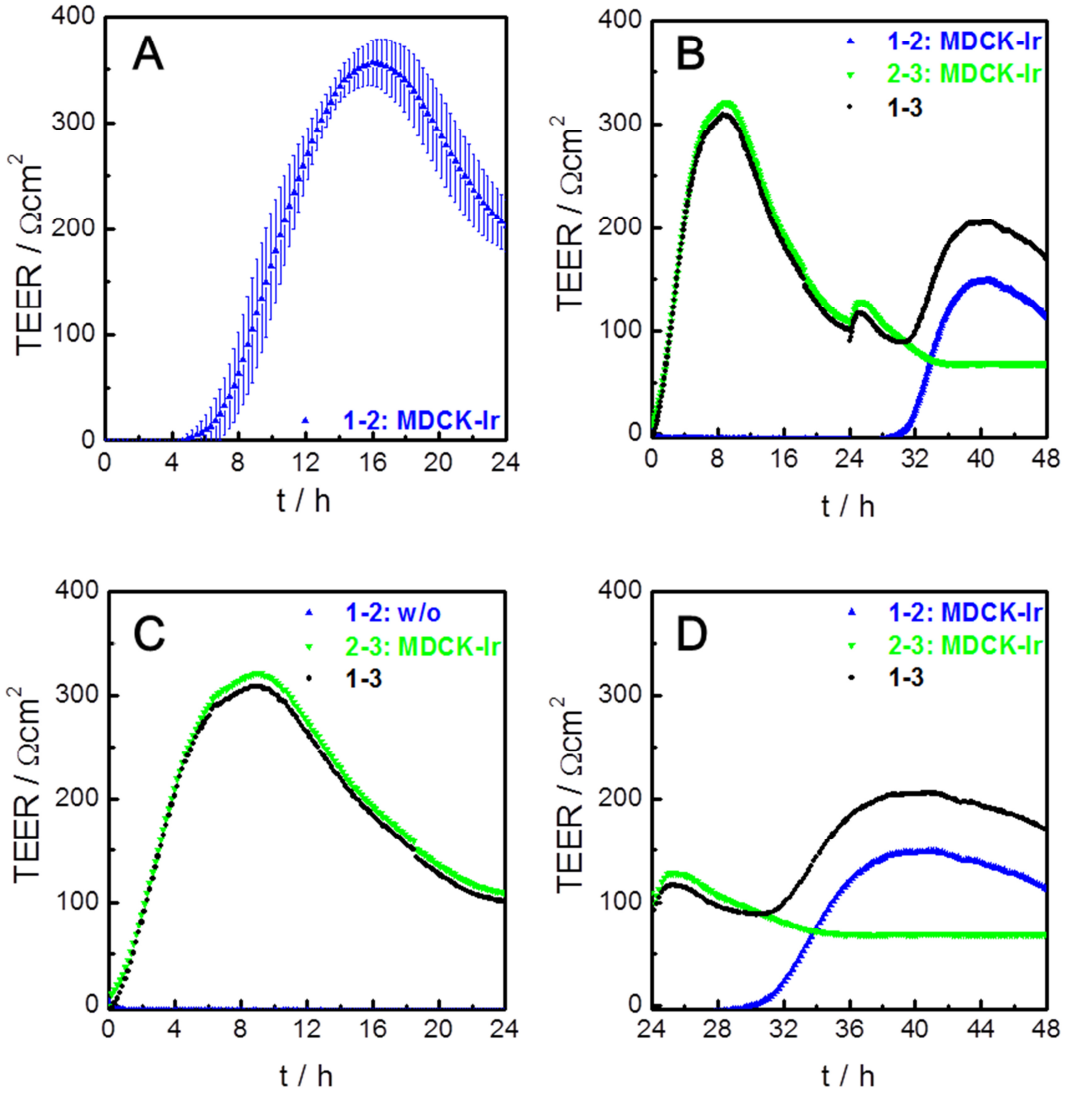

Fig. 5.8: Time course of the transepithelial electrical resistance for all three possible measurement modes (upper compartment ▲ **1-2,** lower compartment ▼ **2-3**, transfilter mode ● **1-3**). **A** MDCK-Ir cell are seeded on the top side of the membrane at t = 0 h (▲ **1-2,** mean ± SE, n = 3). **B** A first MDCK-Ir cell layer is cultured on the lower membrane side (▼ **2-3**). At t = 24 h, MDCK-Ir cells are also seeded on the top side (▲ **1-2**). **C** and **D** represent zoom-in parts of the measurement, displayed in **B**.

TEER peak in the cell layer seeded second could be caused by the presence of cell-derived extracellular matrix (ECM) proteins. Contacts of the basal cell membrane to proteins of the ECM are highly relevant for epithelial barrier function. ECM components influence the apical-basal cell polarization (Gumbiner 1996, Roignot et al. 2013) as well as the kinetics of cell attachment and spreading or tight cell-cell junction formation (Wegener et al. 2000, Hartmann et al. 2007). Therefore, the impact of an extracellular matrix on the barrier formation of MDCK-Ir cells was studied. Cells were allowed to attach and spread on the top side of permeable filter membranes as well as on solid gold electrodes of an ECIS arrays for 24 h. Endogenous extracellular matrix proteins were expressed and secreted during this

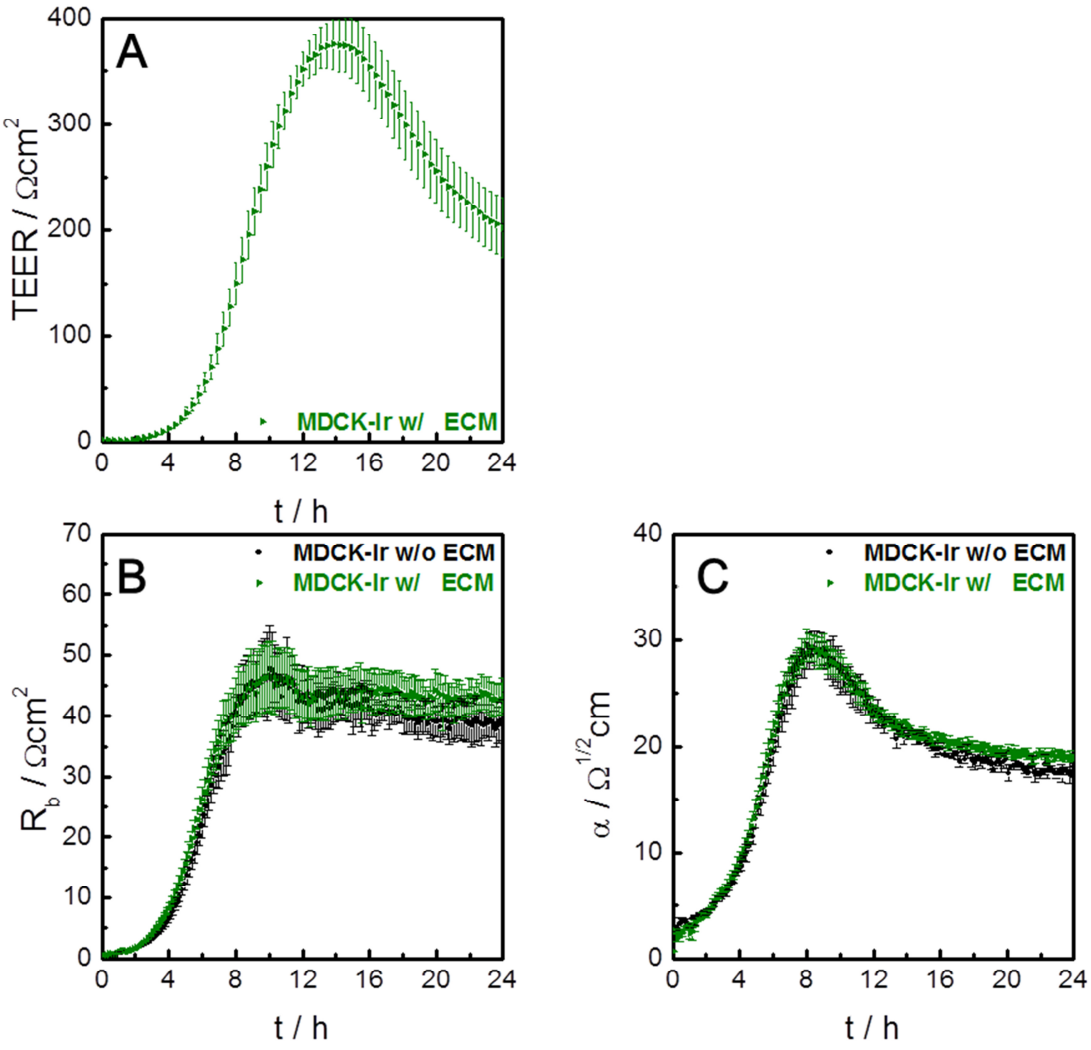

Fig. 5.9: Time course of the transepithelial electrical resistance (transfilter mode) for MDCK-Ir cells cultured on the upper side of porous filter inserts (mean ± SE, n = 4, **A**) is compared to MDCK-Ir cells cultured on solid gold film electrodes (8W10E ECIS array, mean ± SE, n = 4; **B**, **C**) with (► **w/**) or without (● **w/o**) a substrate coating with extracellular matrix proteins (ECM).

period. Subsequently, the cells were gently removed from the substrates (filters and ECIS array) leaving the surfaces coated with intact and native ECM components. Protein coated filter membranes were used for plating MDCK-Ir cells again on the upper filter membrane side. Fig. 5.9 shows the effect of ECM components to the typical time course of MDCK-Ir barrier formation. The time course observed in presence of a cell-derived ECM coating on the porous growth substrate (Fig. 5.9 A) is almost identical to control measurements (Fig. 5.8 A). No significant difference is seen for the time point or maximum values of the resistance peak. Furthermore, final TEER values are identical with or without ECM substrate coatings. In addition, epithelial barrier formation of MDCK-Ir cells from the same cell passage was observed via ECIS measurements under identical conditions (Fig. 5.9 B, C). The recorded data were analyzed with the ECIS model discribed in chapter 3.1.4 (software written by J. Wegener) to gain additional information about the impedance contribution of the cell-substrate adhesion zone. The junctional resistance R_b of MDCK-Ir cells seeded on impermeable gold surfaces shows no significant alteration of kinetics or final resistance values due to the influence of ECM components. The maxmimum values are reached at t = 10 h (● w/o ECM: (48 ± 7) Ωcm^2; ► w/ ECM: (47 ± 6) Ωcm^2) and remain almost constant for the rest of the observation time. Furthermore, the parameter α which discribes the resistance contribution of the cell-substrate adhesion zone is not altered by the presence of an ECM coating (Fig. 5.9 C). Interestingly and in contrast to the junctional resistance R_b, the time course of the parameter α shows a pronounced maximum at t = 8 h after cell seeding (~ 30 $\Omega^{1/2}$cm) and decreses to around 20 $\Omega^{1/2}$cm at the end of the measurement. Parameters which influence α are the cellular radius, the specific resistance of the electrolyte in the narrow adhesion cleft as well as the cell-substrate distance (eq. 3.15). Since the cell density was adjusted to form a confluent monolayer directly after seeding, the changes in cellular morphology are not likely to change at this stage. Furthermore, the junctional resistance already reaches stable values at t = 8 h which indicates completed maturation of cellular contacts. Hence, the characteristic pattern in the time course of the parameter α could result from both, the temporary close approach of the cell layer to the sensing electrode or the transient variation in the electrolyte composition underneath the cell sheet. Published ECIS data for the attachment of cells onto the measuring electrodes are not known. This is not surprising since the ECIS model is only accurate for already confluent cell layers and the commercially available software is not capable to determine values for subconfluent situations. Values determined here 24 h after

cell seeding are similar to published data for this cell type (Lo et al. 1999, Wegener et al. 2000, Rommel 2007). However, as described above, the situation for filter grown cell layers is different to MDCK-Ir cells cultured on impermeable devices. A direct correlation between both measurement principles is therefore difficult.

In summary, the characteristic peak can be observed in the time course of TEER with or without cell-derived ECM components on the growth substrate. In addition, neither the filter membrane side nor the growth substrate material influences the time course of TEER for MDCK-Ir cells. The absence of this transient resistance maximum in the second monolayer of the MDCK-Ir co-culture (Fig. 5.7 A) could be attributed to the already present cell layer on the back side of the filter membrane. The nature of the potential cell to cell signaling in a forced stratified cell layer arrangement is not clear so far.

Transient TEER maxima are well-known for MDCK cell monolayers during tight junction maturation (Butor and Davoust 1992, Gao et al. 2002). Several studies tried to clarify the reasons for this characteristic resistance peak. For example, Yu et al. showed that the peak height can be reduced from 400 Ωcm^2 to less than 200 Ωcm^2 via occludin suppression (Yu et al. 2005). These studies were performed for freshly plated cells and compared to results found in calcium-switch assays. For this assay, confluent monolayers (already attached to secreted extracellular matrix proteins) were incubated under calcium-free conditions which open up intercellular junctions. Switching back to Ca^{2+}-containing medium leads to a rapid junction resealing (Gumbiner and Simons 1986). Obviously, kinetics in barrier formation during calcium-switch assays are not comparable to those observed for *de novo* tight junction maturation. But Yu and coworkers found the characteristic resistance peaks in both assay types which also indicates the minor impact of ECM proteins on the transient TEER maximum. Other authors reported that silencing the *ZO-1* protein expression eliminates the initial peak appearance without any effect on the final transepithelial resistance values (McNeil et al. 2006). Furthermore, the appearance of the peak was found to be delayed and less pronounced in *Par*-3-knockdown cells (Chen and Macara 2005). *Par* proteins are generally involved in cell polarization and are localized in the apical and lateral membrane domains (Goldstein 2007). *Par-3* protein participation in tight junction assembly is strongly dependent on its correct location. Hence, dislocation of *Par-3* due to associated but unfunctional *JAM-A* (junctional adhesion molecule-A) also led to a reduced TEER peak development (Rehder et al. 2006). Since proteins of the *claudin* family are known to have significant influence on the development of tight epithelial cell sheets, changes in their

individual expression levels during barrier formation could also induce the characteristic TEER peak appearance (Furuse et al. 2001, Lipschutz et al. 2005, Furuse 2010, Krug et al. 2014). However, the complete mechanism underlying the generation of this initial TEER peak in cultured MDCK-lr cells remains unidentified so far.

5.3.1.2 MDCK-hr co-culture

Similar experiments as described above were performed with MDCK-hr cells which are reported to form tight cellular barriers with high transepithelial electrical resistance values

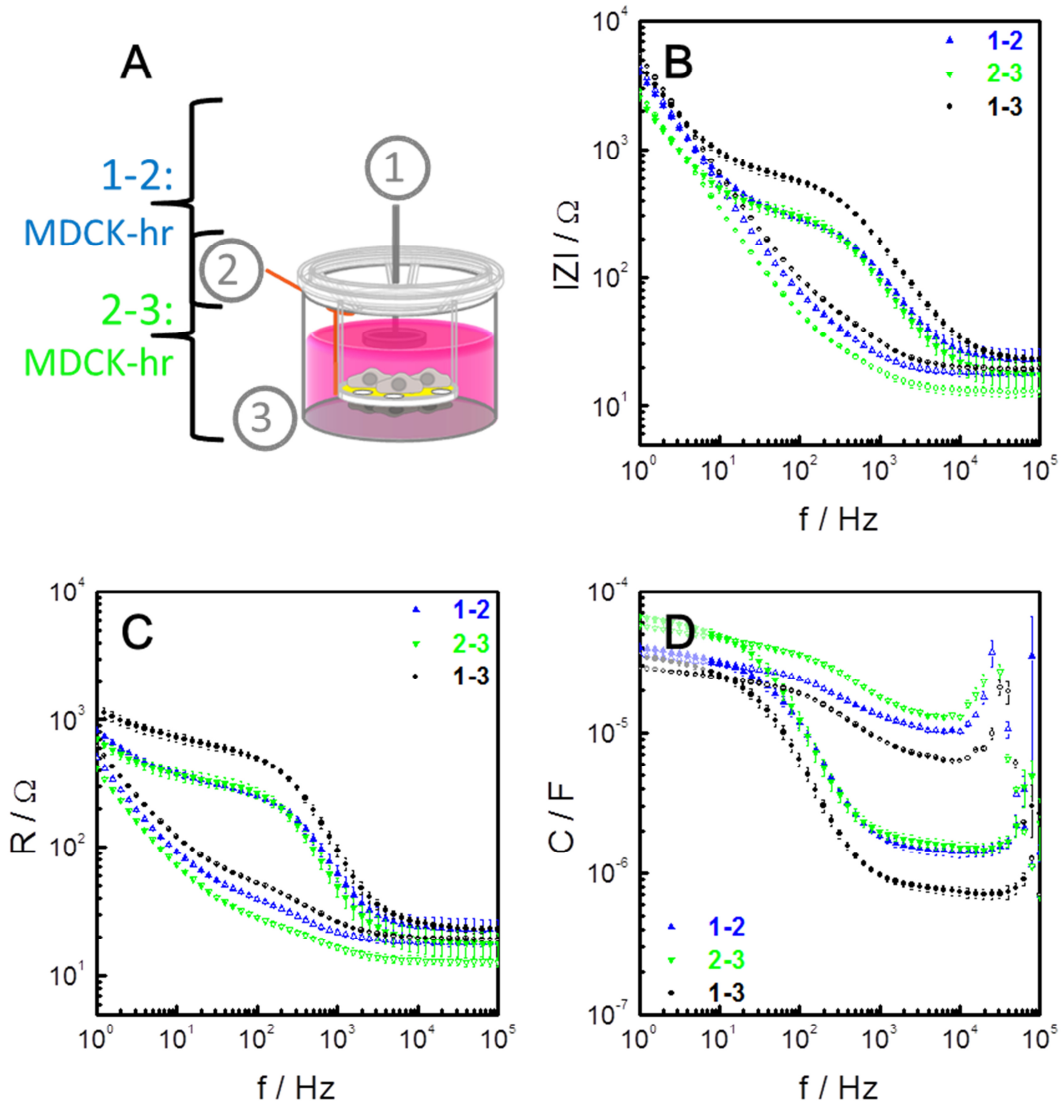

Fig. 5.10: Schematic illustration of the experimental set-up for a MDCK-hr co-culture (**A**). Frequency-dependent impedance magnitude *IZI* (**B**), resistance *R* (**C**) and capacitance *C* (**D**) are presented (mean ± SE, n = 3). Empty symbols represent the cell-free measurements. Filled symbols indicate the results for cell-covered membranes. The upper filter compartment is marked in blue (**1-2**), the lower filter compartment in green (**2-3**) and the transfilter measurement mode in black (**1-3**).

(MDCK-hr). Fig. 5.10 A illustrates the measurement set-up. MDCK-hr cells were located between electrode no. 1 and no. 2 on the upper filter membrane and between electrode no. 2 and no. 3 on the back side of the filter insert. Graphs displayed in Fig. 5.10 B - D show impedance magnitude *IZI*, resistance *R* and capacitance *C* for all three measurement modes. Empty symbols represent the cell-free set-up, filled symbols are used for the cell-covered device. The impedance magnitude *IZI* is again dominated by the double layer capacitance of the electrodes in a range of 1 - 10 Hz and by the resistance of the bulk electrolyte in the high frequency range (> 10^4 Hz). A significantly increased impedance is observed when confluent MDCK-hr cell layers are present on the filter membrane (10 – 10^4 Hz). The impedance increase is detectable in a plateau region from 20 Hz to around 500 Hz. *IZI* reaches values of around 300 Ω for each cell layer measured separately (mode **1-2** and **2-3**) and about 600 Ω in the transfilter measurement mode (**1-3**). The situation is similar for the resistance *R* (Fig. 5.10 C) of the cell-covered system. The frequency region in which the confluent MDCK-hr cell layer affects the signal is between 1 – 10^4 Hz. In this plateau region absolute resistance values of around 350 Ω are obtained for both individual cell layers (**1-2**, **2-3**). Almost 700 Ω are measured in the integrated transfilter measurement mode (**1-3**). The system's capacitance *C* (Fig. 5.10 D) is affected by the cell layer in a frequency range from 20 - $5 \cdot 10^4$ Hz. At a frequency of $2 \cdot 10^4$ Hz, the capacitance reaches values of around 1.5 μF for the measurement modes **1-2** and **2-3** and 0.7 μF in the transfilter mode (**1-3**).

The recorded data were analyzed by means of equivalent circuit modeling. Tab. 5.8 lists the parameters obtained for the transepithelial electrical resistance (TEER) and the cell layer capacitance (C_{cl}) 24 h after cell seeding. TEER values for the upper cell layer are determined to (258 ± 15) Ωcm^2 (**1-2**) and to (301 ± 40) Ωcm^2 for the cell layer located on the back side of the membrane (**2-3**). (566 ± 45) Ωcm^2 are obtained for the integrated TEER measured across both cell layers (**1-3**). The cell layer capacitances (C_{cl}) are (1.53 ± 0.15) μF/cm^2 for the upper MDCK-hr cell layer (**1-2**) and (1.66 ± 0.13) μF/cm^2 for the second MDCK-hr cell layer (**2-3**). Integration over both cell layers measured in the transfilter mode (**1-3**) provides C_{cl} values of (0.77 ± 0.05) μF/cm^2.

The results obtained for co-cultured MDCK-hr cell layers prove again that the integral measurement mode (**1-3**) can be broken down into two contributions arising from both compartments of the new device. Each MDCK-hr cell layer contributes almost equally to the integrated transfilter measurement. However, unlike the cell layer capacitance values, the

obtained resistance parameters for MDCK-hr cell layers are in a range of 300 Ωcm^2 and hence, do not agree with published values (Tab. 5.5). TEER of both separately measured MDCK-hr cell layers of the co-culture (**1-2**, **2-3**) are more than ten fold below the reported mean values for monolayers of this cell type when cultured on permeable supports.

Tab. 5.8: Parameter obtained by means of equivalent circuit modelling for co-cultured MDCK-hr cells 24 h after seeding (mean ± SE. n = 3).

mode	TEER / Ωcm^2	C_{cl} / $\mu F/cm^2$
1-2 (top side)	258 ± 15	1.53 ± 0.15
2-3 (back side)	301 ± 40	1.66 ± 0.13
1-3 (transfilter mode)	566 ± 45	0.77 ± 0.05

Deeper insights into these atypical barrier characteristics can be provided by the associated time-resolved data plotted in Fig. 5.11. As seen for the final capacitance values listed above, time-resolved data do not show any unexpected behavior (Fig. 5.11 B). Cell layer capacitances decrease within the first 6 h after plating to almost final values (**1-2**, **2-3**). The integral co-culture capacitance already reaches final values of around 0.7 $\mu F/cm^2$ at t = 3.5 h. A two-step decrease as seen in MDCK-lr experiments is not observed here since the capacitance of MDCK-hr cells layers is significantly smaller.

The situation is different for resistance recordings displayed in Fig. 5.11 A. TEER increase above baseline levels starts for both monolayers around 6 h after cell seeding. Transepithelial

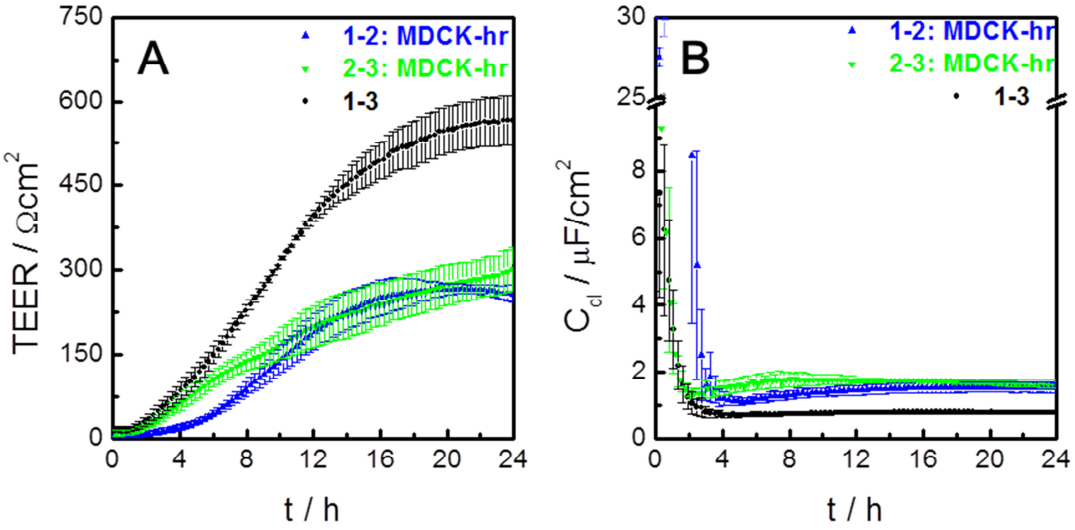

Fig. 5.11: Time course of the transepithelial electrical resistance (**A**) and the cell layer capacitance (**B**) for all three possible measurement modes (mean ± SE, n = 3). MDCK-hr cells are located on both sides of the membrane (▲ **1-2**, ▼ **2-3**). Values for the entire system are shown in black (● **1-3**).

electrical resistance of the lower cell layer increases rapidly to (138 ± 17) Ωcm^2 at t = 8 h and is then followed by a slow but continuous TEER increase to final values of (301 ± 40) Ωcm^2 (**2-3**). A similar time course can be seen for the second cell layer on top of the filter device (**1-2**) within the first 12 h of the experiment. TEER increases continuously from (44 ± 6) Ωcm^2 at t = 6 h, passes a maximum of (266 ± 9) Ωcm^2 at t = 20.8 h and decreases slowly to final values of (258 ± 15) Ωcm^2. The integral resistance of the co-culture measured in mode (**1-3**) increases rapidly from the beginning of the measurement to (149 ± 15) Ωcm^2 at t = 6 h and is then slightly slowed down before a plateau region appears at the end of the measurement period ((566 ± 45) Ωcm^2).

To explain the unexpected and weak barrier formation of co-cultured MDCK-hr cells, control experiments were performed with MDCK-hr monolayers. Cells were seeded to confluency on standard, unmodified filter inserts and the TEER progression was followed over time. As illustrated in Fig. 5.12, the increase in barrier tightness is accelerated drastically compared to the co-culture set-up. The resistance increases in a three-step process to final values of more than 2000 Ωcm^2. The observed transepithelial resistance is similar to values reported in literature (Tab. 5.5). Hence, the resistance of MDCK-hr cell layers is reduced by a factor of ~10 in a homogeneous co-culture in comparison to single monolayer conditions.

However, the transepithelial resistances for co-cultured MDCK-hr cell layers are close to values reported for the leaky subtype MDCK-lr (Tab. 5.5). Differences between leaky (MDCK-lr) and tight (MDCK-hr) MDCK cell layers in ionic permeability and, hence,

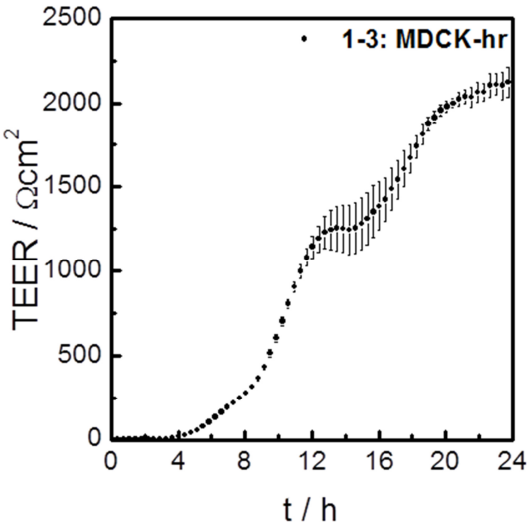

Fig. 5.12: Time course of the corrected transepithelial electrical resistance for the transfilter measurement mode (● **1-3**) after MDCK-hr cells are seeded on the top side of the membrane at t = 0 h (mean ± SE, n = 4).

transepithelial electrical resistance are attributed to the individual level of *claudin-2* expression. *Claudin-2* is not detectable in MDCK-hr monolayers. Furuse and coworkers reported that TEER values of MDCK-hr clones which stably express *claudin-2* decrease drastically to the resistance level of MDCK-lr cell layers (Furuse et al. 2001). However, transfection with other claudin types had no influence on the transepithelial resistance. MDCK cells are generally not studied in homogeneous co-cultures. Hence, the effects of a stratified arrangement of MDCK-hr cell layers on the expression leven of *claudin-2* or the entire differentiation of both epithelial cell sheets is unexplored so far.

5.3.2 Heterogeneous co-cultures

Heterogeneous co-cultures were prepared by seeding MDCK-lr cells on the back side of the porous filter device. MDCK-hr cells were allowed to attach and spread on the top side of the membrane. A scheme of the experimental set-up is illustrated in Fig. 5.13 A. Frequency-dependent impedance magnitude *IZI*, resistance *R* and capacitance *C*, extracted from the imaginary component, are shown in Fig. 5.13 B – C. In these graphs, data for the cell-free set-up is represented by empty symbols, the cell-covered device by filled symbols. In Fig. 5.13 B, *IZI* is dominated by the double layer capacitance of the electrodes in the lower frequency range for the cell-free device in measurement mode **2-3** (MDCK-lr cells). The impedance of the electrode-electrolyte interface is masked by the impedance contribution of the MDCK-hr cells for the measurement of the upper filter compartment (**1-2**) and the transfilter mode (**1-3**). The cellular impedance contribution is detectable up to frequencies of around $4 \cdot 10^4$ Hz in all three measurement modes. *IZI* is subsequently dominated by the bulk resistance of the electrolyte. The plateau regions observed for *IZI* in presence of a confluent cell layer are in a frequency range from 2 - 50 Hz in mode **1-2** and **1-3** (both ~ 2000 Ω) and in between 100 – 500 Hz in mode **2-3** (~ 100 Ω). The situation is similar for the system's resistance *R* (Fig. 5.13 C). The frequency regions in which the confluent MDCK cells alter the signal are in between 1 - $3 \cdot 10^4$ Hz measured in all modes. Mode **1-2** reports the highest resistance alteration due to the cell layer in a frequency window of 1 - 20 Hz. For this plateau region, absolute resistance values of around 2300 Ω are obtained. The same trend is observed for the integrated transfilter measurement mode (**1-3**). The resistive plateau region of the lower filter compartment (**2-3**) is present in a frequency range of 10 – 100 Hz with values for *R* of around 100 Ω. The system's capacitance *C* (Fig. 5.13 D, 2-3) is affected by

the MDCK-lr cell layer in between 40 Hz and $2 \cdot 10^4$ Hz. For mode **1-2** and **1-3**, the capacitance is altered in presence of confluent cell layers in a frequency range of $5 - 4 \cdot 10^4$ Hz. At a frequency of $2 \cdot 10^4$ Hz, *C* amounts to around 1.5 μF in measurement mode **1-2**, 0.25 μF in mode **2-3** and 0.8 μF in the transfilter mode (**1-3**).

A quantitative data analysis by means of equivalent circuit modeling was performed. Tab. 5.9 lists the transepithelial electrical resistance (TEER) and the cell layer capacitance (C_{cl}). TEER values for MDCK-hr cells are determined to (2091 ± 319) Ωcm^2 (**1-2**). For MDCK-lr cells a TEER of (87 ± 7) Ωcm^2 is observed (**2-3**). (2103 ± 332) Ωcm^2 are obtained for the integrated

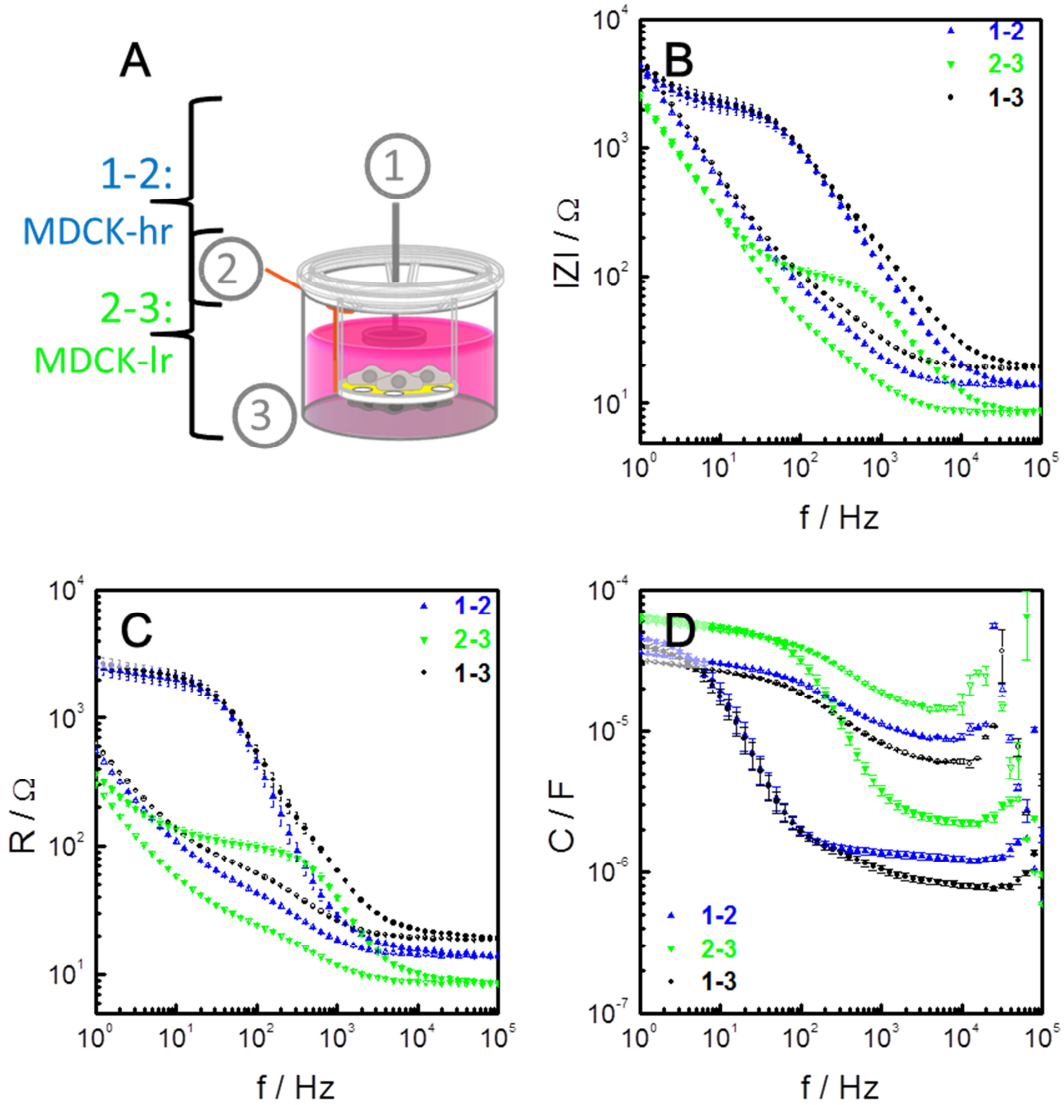

Fig. 5.13: A Schematic illustration of the experimental set-up for mixed co-cultures. Frequency-dependent impedance magnitude *IZI* (B), resistance *R* (C) and capacitance *C* (D) are shown for MDCK-lr cells cultured on the back side (**2-3**) and MDCK-hr cells located on the top side (**1-2**) of the filter insert (mean ± SE, n = 3). The transfilter measurement mode is displayed in black (**1-3**). Empty symbols represent the cell-free measurements. Filled symbols indicate the results for cell-covered membranes.

TEER measured across both cell layers (1-3). The cell layer capacitances (C_{cl}) are calculated to (1.34 ± 0.09) μF/cm^2 for the upper MDCK-hr cell layer (**1-2**) and (2.24 ± 0.15) μF/cm^2 for MDCK-lr cell layer (**2-3**). Integration over both cell layers measured in the transfilter mode (**1-3**) results in values of (1.04 ± 0.09) μF/cm^2.

Tab. 5.9: Dielectric parameter derived by means of equivalent circuit modelling of impedance spectra for co-cultured MDCK-lr (**2-3**) and MDCK-hr (**1-2**) cells and the transfilter results (**1-3**) 24 h after seeding (mean ± SE, n = 3).

mode	TEER / Ωcm^2	C_{cl} / μF/cm^2
1-2 (top side)	2091 ± 319	1.34 ± 0.09
2-3 (back side)	87 ± 7	2.24 ± 0.15
1-3 (transfilter mode)	2103 ± 332	1.04 ± 0.09

The cell-related parameters are matching values reported in literature (Tab. 5.5). In addition to these endpoint data, time-resolved measurements prove that both cell types exhibit regular developments of their individual transepithelial resistance with time (Fig. 5.14 A). The characteristic resistance peak of MDCK-lr (**2-3**) is reached at t = 6 h ((292 ± 25)Ωcm^2) and declines thereafter to final values (Tab. 5.9). TEER of the MDCK-hr cell layer starts to increase above base line levels within 4 h and increases continuously to final values of more than 2000 Ωcm^2 (**1-2**). Transepithelial electrical resistance measured across both filter

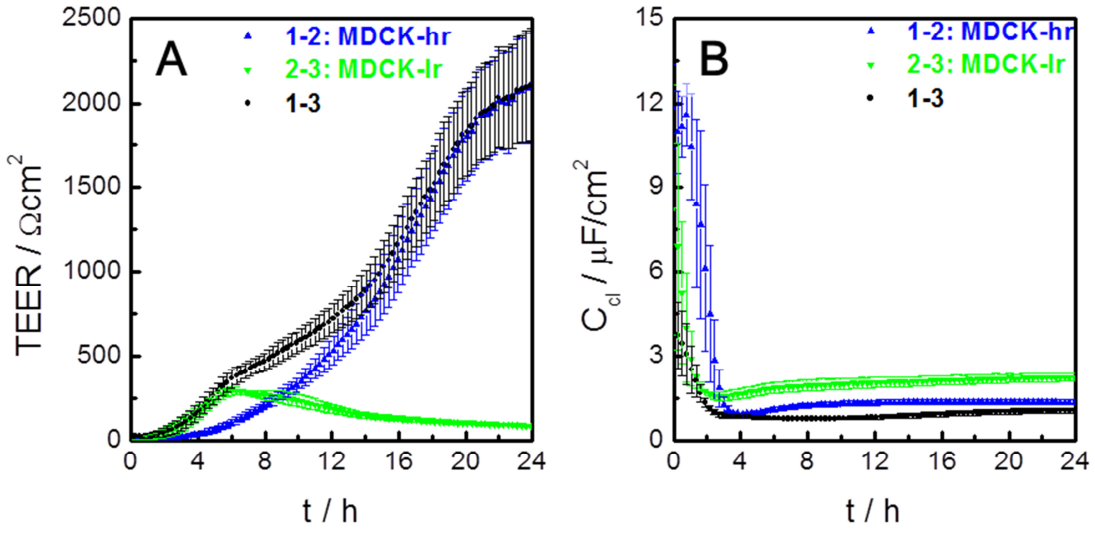

Fig. 5.14: Time course of the transepithelial electrical resistance (**A**) and the cell layer capacitance (**B**) for all three possible measurement modes (mean ± SE, n = 3). MDCK-lr cells are located on the back side of the membrane (▼ **2-3**). MDCK-hr cells are located on the top side of the membrane (▲ **1-2**). Values for the entire system are shown in black (● **1-3**).

compartments (**1-3**) is clearly dominated by the contribution of the MDCK-lr cell layer within the first 4 h. However, the contribution of the leaky MDCK strain to the entire resistance of the co-culture is almost neligible after the onset of MDCK-hr TEER. Furthermore, the cell layer capacitances remain almost constant 6 h after cell seeding (Fig. 5.14 B). Capacitance recordings show a parallel time course differ by approximately ~ 1 $\mu F/cm^2$ at the end of the observation time in between both MDCK cell layers.

These results show that both MDCK cell types express normal resistance and cell layer capacitance values when cultured together. Compared to co-cultured MDCK-lr cell layers, the obtained TEER is slighly decreased. However, the characteristic TEER peak is observed and final values are in good agreement with published values. MDCK-hr cell layers do not show a TEER increase as seen for monolayer experiments when grown in co-culture (Fig. 5.12) but express regular resistance values 24 h after cell seeding.

Comparing data recorded in each of the three measurement modes cleary shows, that the new device is a powerful tool to study TEER alterations of co-cultured cell layers. Changes in electrical properties of the low resistance cell type (MDCK-lr) are not detectable in the common transfilter measurement mode (**1-3**) since the high resistant cell type dominates the integral signal already 8 h after inocculation. Therefore, the content of information can be significantly enhanced by using porous electrodes as transducer elements for impedimetric measurements of filter-grown cell layers.

5.3.3 Independent access and readout of both compartments

By the use of permeable electrodes as transducer for impedance-based assays with filter-grown cell layers, an independent readout of both compartments is possible. Transfilter systems provide independent access to both fluid filled compartments. Hence, cell layers cultured on permeable membranes can be independently exposed to different buffer compositions in order to mimic physiological conditions. Confluent cell layers (MDCK-lr) were cultured on both sides of the membrane and physiological buffers with different conductivities (Tab. 4.7) were added successively to one of both fluid compartments. The scheme in Fig. 5.15 A represents the buffer replacement sequence. Both compartments were filled with the same buffer (σ = 14.65 mS/cm) at the beginning of the experiment (Fig. 5.15 A step a). In the following step (Fig. 5.15 A step b), the buffer in the lower compartment was replaced by a second buffer with decreased conductivity (σ = 1.28 mS/cm). After a short incubation time

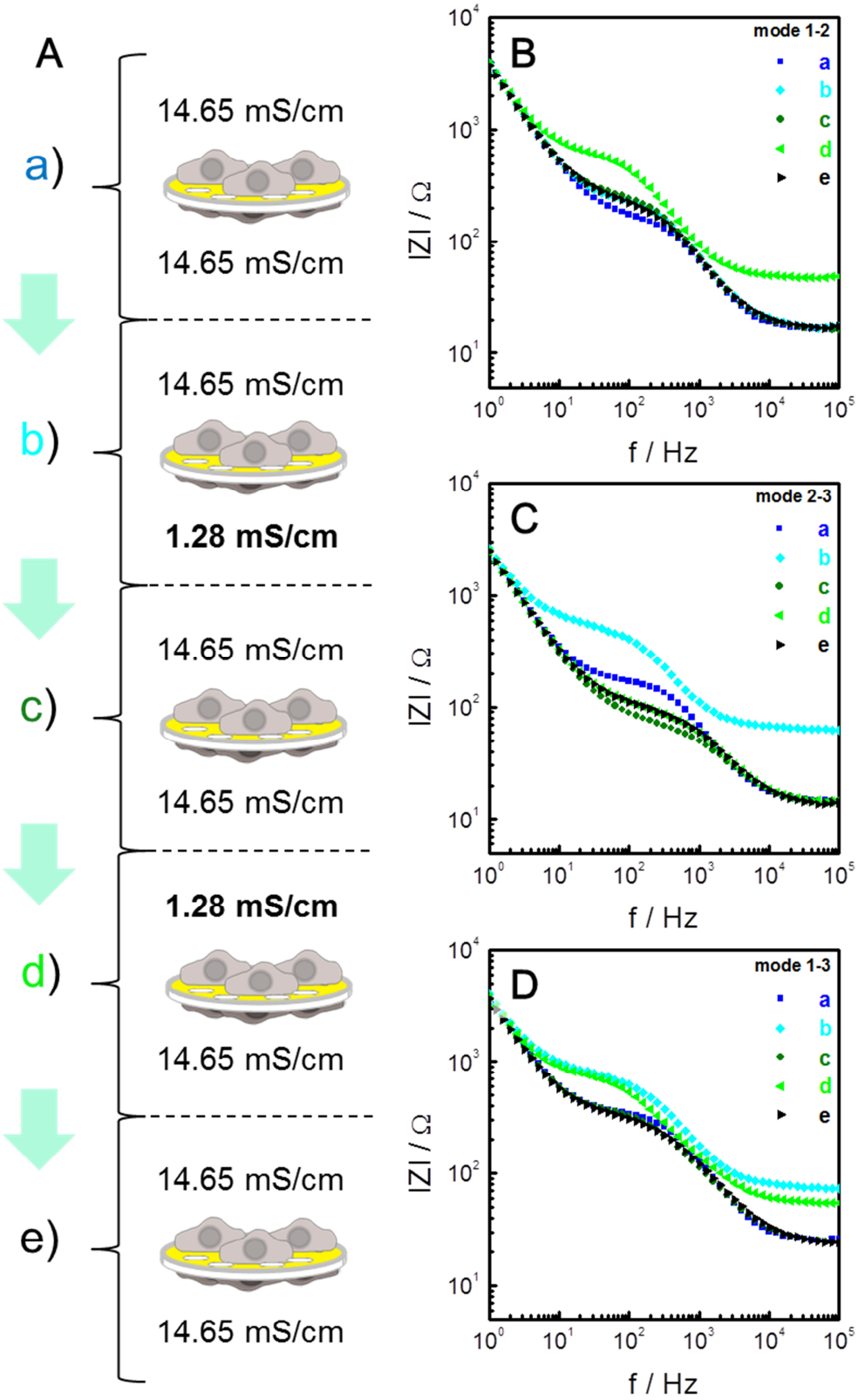

Fig. 5.15: A Scheme of the performed experimental procedure of well-defined conductivity changes in the upper and lower compartment. MDCK-Ir cells were seeded on both sides of the membrane. Typical frequency-dependent impedance magnitude *IZI* is plotted for all measurement modes. Buffer conductivity (in mS/cm) was adjusted successively in one of both compartments. **B** represents the upper compartment, **C** the lower compartment and **D** the integrated signal.

the buffer in the lower compartment was replaced by the initial buffer and its conductivity level (Fig. 5.15 A step c). The same sequence was repeated for the upper filter compartment. Fig. 5.15 A step d illustrates the situation when the buffer conductivity was adjusted from 14.65 mS/cm to 1.28 mS/cm. In the last step (Fig. 5.15 A step e) the cells were again exposed to a homogeneous buffer composition on both membrane sides.

The graphs in the right panel of Fig. 5.15 illustrate the recorded impedance magnitude spectra (MDCK-lr on both filter sides) for the upper filter compartment (Fig. 5.15 B), the lower filter compartment (Fig. 5.15 C) and the integrated signal, measured across both compartments (Fig. 5.15 D). The impedance, measured in the upper filter compartment (Fig. 5.15 B) shows a slight increase in the mid-frequency range upon buffer replacement. A significant increase in the plateau region (10 Hz < f < 10^3 Hz) is detectable when the buffer conductivity is decreased (step d) in the upper compartment. Additionally, the impedance in the high frequency range is increased from ~ 20 Ω to ~ 70 Ω for this buffer combination. The frequency-dependent impedance magnitude in the lower compartment (Fig. 5.15 C) shows that a decreased conductivity in this compartment leads to a strong impedance increase in a frequency window of 10 Hz – 10^3 Hz (cellular plateau region) and in the bulk resistance region above 10^3 Hz (Fig. 5.15 C, step b). The impedance, measured in the high frequency range is constant for all other experimental steps. However, *IZI* in the plateau region is decreased for low conductivity buffer compared to starting values. Results measured across both compartments are illustrated in Fig. 5.15 D. Increased impedance values are observed in the cellular plateau region as well as in the high frequency range for step b and step d in Fig. 5.15 D. In both cases, the buffer conductivity of one compartment is decreased. The buffer conductivity is equal for both compartments in step a, step c and step e which results in almost identical impedance spectra.

Alterations in the cellular plateau region and hence, the TEER of both MDCK-lr cell layers, are listed in Tab. 5.10. The transepithelial electrical resistance of the cell layer located on the back side of the filter membrane is increased significantly after the buffer conductivity on the apical side of the cell layer is decreased (mode **2-3** step b: 436 Ωcm^2). Thereafter, TEER drops down to a value of 51 Ωcm^2 (step c) before a recovery of the cell layer resistance is observed. TEER of the cell layer on the top side of the filter membrane (mode **1-2**) increases from 133 Ωcm^2 (step a) to 194 Ωcm^2 (step b). Since no buffer exchange was performed in this filter compartment, the TEER increase is probably caused by a limited mixture of the different

buffers on both sides of the filter membrane. This effect is enduring in step c although the initial buffer conductivity is present in both compartments. Thus, the adhesion region is shielded by both cell layers. As seen for the first cell layer, TEER is increased drastically only after the buffer conductivity on the apical side of this cell layer is decreased (mode **1-2** step d: 474 Ωcm^2). Hence, the junctional conductivity of the cell layers is influenced by the reduced buffer conductivity predominantly in the apical region. These results prove that independent access to both filter compartments is guaranteed due to the barrier properties of both cell layers and changes in the total impedance of the entire system can be analyzed with respect to the individual contributions of both filter compartments.

Tab. 5.10: Exemplary TEER values in Ωcm^2 for co-cultured MDCK-Ir cell layers after conductivity changes in one or both filter compartments (see Fig. 5.7: upper compartment **mode 1-2**, lower compartment **mode 2-3**, transfilter measurement **mode 1-3**).

step	mode 1-2	mode 2-3	mode 1-3
a	133	152	308
b	194	**436**	**649**
c	222	51	284
d	**474**	77	**616**
e	194	77	261

5.3.4 Barrier manipulation: Influence of cytochalasin D on co-cultured cell layers

The response of epithelial barrier function to different drugs is of major scientific interest. *In vitro* experiments on co-cultured cells are often preferred over monolayers set-ups in order to mimic physiological conditions. Until now, TEER can be determined only for the entire co-culture. Effects of different drugs or other compounds cannot be attributed to a specific cell type of the co-culture. In this thesis, porous electrodes were used to study the individual effects of a specific drug to either cell layer within a co-culture of MDCK-Ir cells. The well-known fungal toxin cytochalasin D (cD) was used to affect a cell layer's barrier integrity. cD is membrane-permeable and inhibits g-actin polymerization into growing filaments while depolymerization of actin filaments remains unaffected, finally causing actin monomer aggregation. Since barrier formation of confluent cell layers depends on the interlinkage of tight junction proteins to the functional cytoskeleton (Ballard et al. 1995), the transepithelial electrical resistance is reduced upon addition of cD. Furthermore, the TEER decreasing effect of cD is concentration-dependent and reversible for MDCK-Ir monolayers (Stevenson and Begg 1994). Due to the independent access to both filter compartments, the drug can be

added either to the upper or the lower filter compartment and the impact of cD on either cell layer can be monitored individually. To enable a better time resolution, the transfilter measurement mode (**1-3**) was neglected in the following experiments. After stable impedance values were reached, either the medium in the upper or in the lower compartment was replaced by cD-containing medium and washed out two hours after addition. The relative change in TEER (compared to initial TEER prior to addition) was determined and plotted against time (Fig. 5.16).

Fig. 5.16 A displays the time course of the relative change in TEER upon addition of 3 μM cD to the upper filter compartment. Instantly after cD exposure, a rapid loss of the TEER of around 90 % to a final value of (9 ± 3) % is detected within two hours for the cell layer facing the cD stimulation (**1-2**). The MDCK-Ir cell layer on the opposite side of the filter remains unaffected for more than 10 min before a retarded and less drastic decrease to a TEER value of (57 ± 4) % is detected (**2-3**). The reversibility of cD treatment on TEER can be detected immediately after the drug is washed out via fresh medium replacement (t = 2 h). The epithelial resistances of both cell layers increase rapidly, reaches baseline levels in less than 90 min and increase until constant values are detected at the end of the experiment. The time profile of the individual TEER readings are inverted when cD is added to the lower compartment of the device (Fig. 5.16 B). The addition of cD to the bottom compartment leads to a rapid decrease of barrier resistance for the MDCK-Ir cell layer facing the lower compartment to a value of (20 ± 6) % two hours after addition (**2-3**). The TEER of the cell layer on the opposite side of the filter shows a similarly retarded time course as seen in Fig. 5.16 A. Again, TEER remains stable for 10 min after cD addition before any impact on the upper cell layer is detectable (**1-2**) resulting in a final TEER value of (58 ± 10) %. After cD washout, the TEER of the cell layer facing the exposure side recovers to similar values as displayed in Fig. 5.16 A. However, the TEER recovery observed for the cell layer in the upper filter compartment (**1-2**) is attenuated. In addition, baseline levels are not passed as seen for the cell layer on the back side of the filter membrane.

As discussed for the attachment and spreading studies, the results show that the new device allows a simultaneous monitoring of individual dynamics in epithelial barrier function of co-cultured cell layers. The TEER decrease upon addition of cD to confluent layers of MDCK-Ir cells is similar to results reported by Stevenson and Begg (1994).

Here, the cell layer on the opposite side of the cD stimulation remains unaffected for several minutes until the barrier function of the facing cell layer is reduced to around 50 %. Once the

cell-cell contacts of the cell layer on the exposure side are disrupted, cD can diffuse into the second compartment and influence the cell layer on the opposite side. Due to the different volumes of both compartments, the final cD concentration is 0.5 μM when the drug is added to the upper filter insert side (0.5 mL) and 2.5 μM for the addition to the lower filter compartment (2.25 mL). Although the dilution of the drug is less when cD is added to the lower compartment, the effective concentration which influences the cell layer on the opposite side remains the same since both cell layers are only separated by the 10 μm thin filter membrane. Hence, the time course of TEER decrease is identical for the monolayers on the opposite sides of drug exposure. Stevenson and Begg also described that the effects of cD induced actin cytoskeleton disassembly is reversible after two washing steps. MDCK-Ir monolayers which were incubated with low concentrations of cD (4 μM) reestablished normal TEER values within two hours after washout and passed baseline levels to around 140 % of the initial TEER. The reason for the reported resistance overshoot is unknown so far. In contrast, higher concentrations (40 μM) only caused a delayed reestablishment of initial TEER within five hours. The time courses of TEER displayed in Fig. 5.16 are similar to the published results.

The new device based on porous electrodes offers the possibility to investigate all kinds of epithelial or endothelial barrier alterations due to a certain stimulus for both cell layers of a co-culture set-up separately and with a high time resolution.

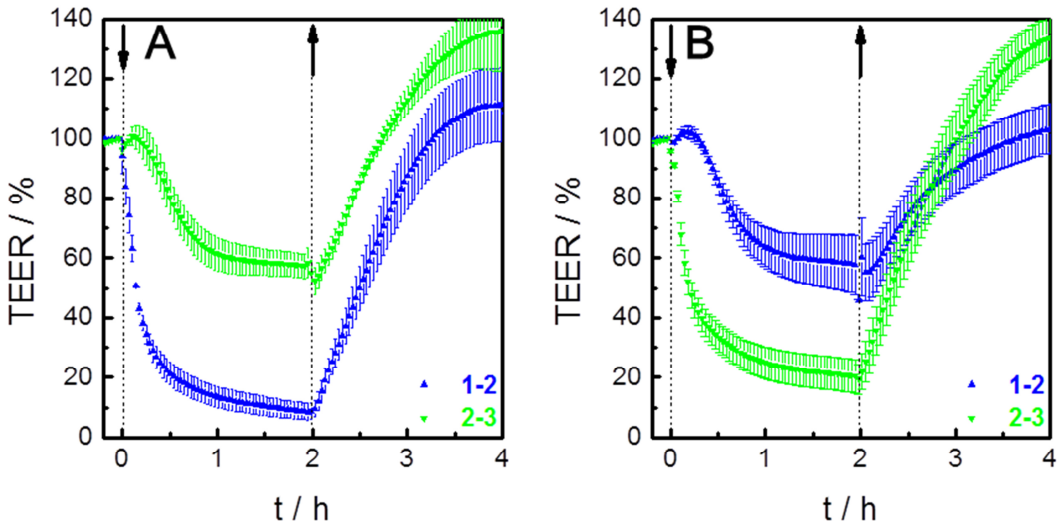

Fig. 5.16: Time course of the relative TEER of MDCK-Ir cells cultured on both sides of the membrane (▲ 1-2: top side, ▼ 2-3: back side) during exposure (↓) and after washout (↑) of 3 μM cytochalasin D (cD, mean ± SE, n = 3). cD is added to the upper filter compartment (**A**) or to the lower compartment (**B**).

5.4 Porous gold electrodes in combination with the ECIS-technique

Porous electrodes are a useful tool to analyze the individual dynamics in epithelial barrier function of two co-cultured cell layers *in vitro*. Since the observation of the co-culture is based on a non-invasive impedimetric readout, a combination with the ECIS technique is possible and offers the possibility to monitor three individual cell layers within one single experiment. The ECIS technique uses small circular electrodes which are integrated in the bottom of a

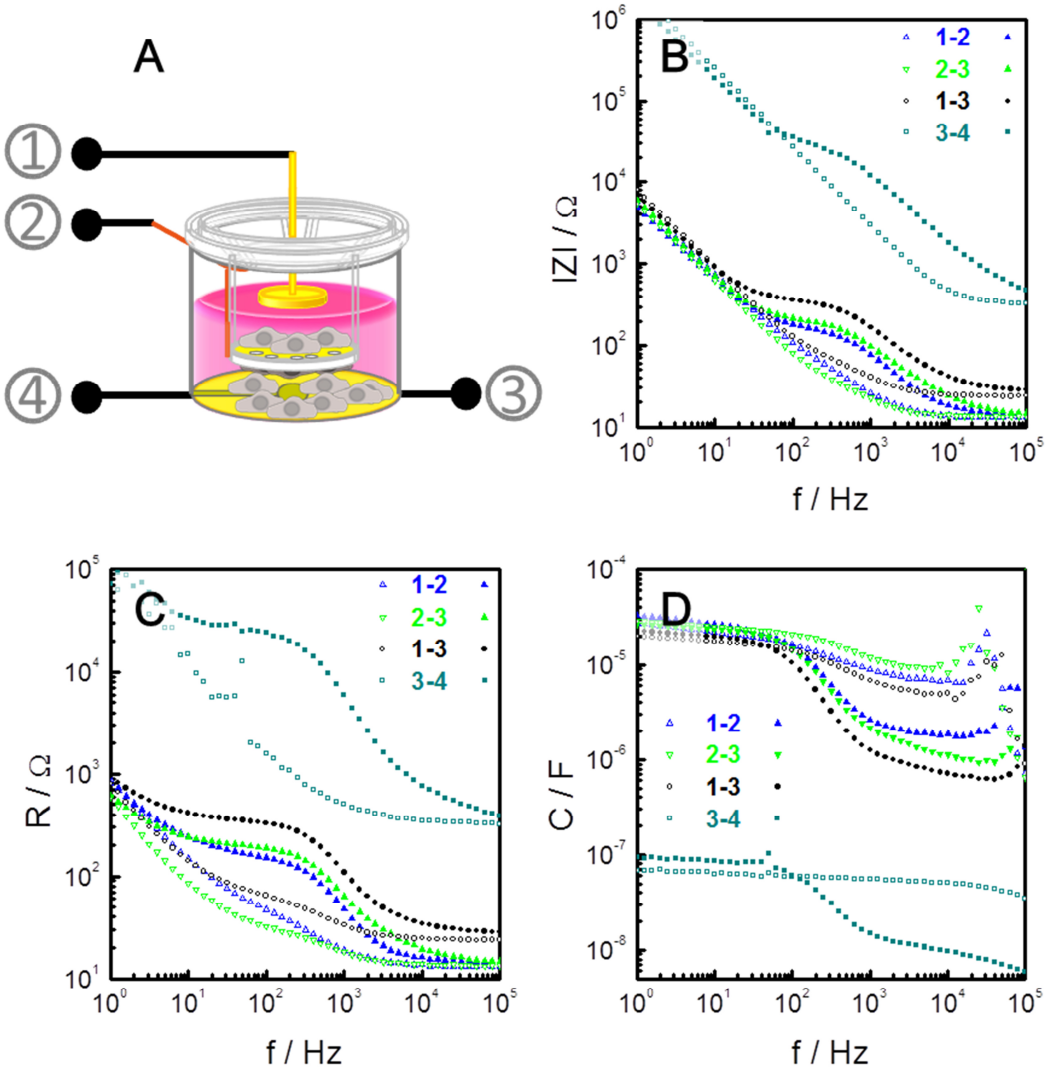

Fig. 5.17: A Schematic illustration of the experimental set-up. Typical spectra of the frequency-dependent impedance magnitude *IZI* (**B**), resistance *R* (**C**) and capacitance *C* (**D**) are shown for three layers of co-cultured MDCK-Ir cells. Open symbols represent the cell-free measurements. Fuilled symbols indicate the results for the cell-covered device. The upper filter compartment is marked in blue (▲ **1-2**), the lower filter compartment in green (▼ **2-3**) and the transfilter measurement mode in black (● **1-3**). The ECIS measurement mode is illustrated in cyan (♦ **3-4**).

growth substrate to measure the cellular impedance (chapter 3.1.4). In order to combine transfilter measurements with the ECIS principle, the bottom electrode of the transfilter measurement chamber was modified. Fig. 5.17 A illustrates the adapted set-up. The disk shaped electrode in the bottom compartment was divided into a small circular working electrode (Fig. 5.17 A, electrode no. 4, A = 8.0E-03 cm^2) and a horse-shoe like counter electrode (Fig. 5.17 A, electrode no. 3). Stainless steel as electrode material was replaced by gold to manufacture the electrode layout by photolithography techniques (chapter 4.2.1.2). The stainless steel dipping electrode was also covered with a thin gold layer (Fig. 5.17 A, electrode no. 1) whereas the porous filter electrode (Fig. 5.17 A, electrode no. 2) was used without any further modification. The bottom electrode layout offers the possibility to monitor an additional cell monolayer cultured directly on the measurement electrodes by applying the ECIS technique while the two co-cultured cell layers on both sides of the filter membrane can be monitored simultaneously via transfilter measurements. Hence, the electrical properties of three co-cultured cell layers of the same or different type can be determined in a single experiment in a time-resolved and label-free manner. All three cell layers are in close proximity which enables cellular communication and mimics *in vivo* like conditions far better.

As proof-of-concept study, MDCK-Ir cells were seeded to confluency on both sides of the permeable electrode and on the bottom electrodes of the measurement well. The electrical impedance of the set-up was recorded over a broad frequency window and impedance magnitude *IZI*, resistance *R* and capacitance *C* of each measurement mode were plotted in Fig. 5.17 B-D. Empty symbols represent the cell-free set-up, filled symbols are recorded for the cell-covered device. The impedance magnitude *IZI* is dominated by the double layer capacitance of the electrodes in a frequency window from 1 - 10 Hz and by the resistance of the bulk electrolyte in the high frequency range ($f > 10^5$ Hz) in all measurement modes. The impedance spectra determined in the ECIS mode (**3-4**) are clearly shifted to higher values since the size of electrode no. 4 is only 8.0E-03 cm^2. Impedance magnitude of all measurement modes is significantly increased in the mid frequency range in presence of confluent cell layers. The increase is detectable as a plateau region from 20 Hz to around 300 Hz in the transfilter modes (**1-2**, **2-3**, **1-3**). The impedance magnitude within this region reaches values of around 150 Ω - 200 Ω for recorded in mode **1-2** and **2-3**. Around 350 Ω are detected for the transfilter measurement mode (**1-3**). The cellular plateau region is less pronounced in the ECIS mode (**3-4**, 100 - 300 Hz, ~ 2.7 kΩ). The frequency regions in which

the cell layers affect the signal are shifted to 5 - 4·10^4 Hz for the resistance spectra (Fig. 5.17 C) and >10^5 Hz in the capacitance spectra (Fig. 5.17 C).

The recorded data were analyzed by means of equivalent circuit modeling. Parameters determined for the cell-free device are listed in Tab. 5.11 and can be compared to the set-ups based on stainless steel electrodes above (Tab. 5.6). Due to the different electrode material (here: gold) the parameters of the constant phase element are different. The parameter A_{CPE} is reduced due to the reduced surface area of the common counter electrode (no. 3), whereas parameter n_{CPE} is slightly increased in all three filter measurement modes since gold is used as electrode material. Parameters of the constant phase element determined in the ECIS mode (**3-4**) are in good agreement to values published by Wegener et al. (1999) for pure ECIS measurements. The bulk resistance stays almost constant for mode **1-2** compared to the value for the stainless steel device but is increased for mode **2-3** and mode **1-3**. The results are appropriate since the 2 mm thick stainless steel electrodes are replaced by a 100 nm thin gold film electrode. Hence, the lead resistance is increased. The parasitic resistive and capacitive contributions of the device are less pronounced due to the use of gold as electrode material (see Tab. 5.3) and not detectable in the ECIS measurement (**3-4**).

Tab. 5.11: Exemplary parameters for all possible measurement modes (**1-2**: upper filter compartment; **2-3**: lower filter compartment, **1-3**: transfilter mode, **3-4** ECIS mode).

parameter / unit	**1-2**	**2-3**	**1-3**	**3-4**
R_{bulk} / Ω	14.5	19.4	29.2	295
$R_{paras.}$ / Ωcm^2	18.9	7.9	33.8	0
$C_{paras.}$ μF/cm^2	7.62	28.73	6.49	0
A_{CPE} / μFs$^{(n-1)}$/cm^2	28.0	27.9	22.8	16.5
n_{CPE}	0.924	0.960	0.941	0.954

Monolayer resistance (TEER) and cell layer capacitance (C_{cl}) were determined for every MDCK-Ir monolayer after correction for the cell-free values (Tab. 5.12). TEER values for the upper cell layer (**1-2**) are determined to 149 Ωcm^2 and to 160 Ωcm^2 for the cell layer located on the back side of the membrane (**2-3**). 314 Ωcm^2 are obtained for the integrated signal measured across both cell layers (**1-3**). The resistance of MDCK-Ir cells, cultured on impermeable gold electrodes, is approx. 35 % lower than for cell layers cultured on the filter membrane (**3-4**, 100 Ωcm^2). The cell layer capacitances (C_{cl}) are determined to values between 1.74 μF/cm^2 and 2.44 μF/cm^2. Integration over both cell layers cultured on the filter

membrane (**1-3**) results in 0.95 μF/cm^2. The cell layer capacitance of MDCK-Ir cells determined in the ECIS mode is determined to in 2.44 μF/cm^2.

The electrical properties of confluent MDCK-Ir cell layers cultured on permeable substrates are in good agreement to values known from literature (Tab. 5.5) as well as those presented in this thesis (Tab. 5.7). The TEER of MDCK-Ir cells which are cultivated on impermeable gold electrodes (mode **3-4**) is decreased due to the nature of the growth substrate (chapter 5.1) but similar to published values recorded in ECIS-like arrangements (Wegener et al. 1996b).

Tab. 5.12: Exemplary parameter derived by means of equivalent circuit modelling for three layers of co-cultured MDCK-Ir cells 48 h after seeding (**1-2**, **2-3**, **3-4**). In addition, results determined for the transfilter mode (**1-3**) are listed.

mode	TEER / Ωcm^2	C_{cl} / μF/cm^2
1-2 (top side)	149	2.04
2-3 (bottom side)	160	1.74
1-3 (transfilter mode)	314	0.95
3-4 (ECIS mode)[1]	100	2.44

The new device is also capable of monitoring the dynamics in epithelial barrier function in a time-resolved manner. However, first experiments showed data scattering in ECIS mode (appendix: Fig. 12.2). Until now, the measurement software is limited to the application of a common alternating voltage of low amplitude for all electrode combinations. The value of 10 mV is sufficient for transfilter measurements where large electrodes are used. The small electrode area of the working electrode in the ECIS mode causes higher load impedances. Hence, the applied voltage leads to a very noisy impedance signal which could mask minor changes in the dynamics of epithelial resistance.

5.5 Summary and conclusion

The transepithelial or -endothelial electrical resistance (TEER) is commonly measured to quantify the barrier function of cell monolayers. For this purpose, barrier-forming cell monolayers are cultured on permeable membranes. The frequency-dependent impedance of the cell layer is recorded and the TEER is determined by means of equivalent circuit modeling of the raw data. However, only the integrated TEER can be measured for co-cultured cell layers on either side of the filter membrane. It is not possible to distinguish between both cell

[1] ECIS parameter: R_b = 60.2 Ωcm^2; α = 20.0 Ω$^{1/2}$cm; C_{cl} = 2.26 μF/cm^2

layers and their individual response to a certain stimulus. This chapter described the modification of common filter inserts in order to serve as a permeable electrode between co-cultured cell layers. The modification offered the possibility to investigate the electrical properties of both cell layers separately while the integrated impedance signal of the entire co-culture could still be monitored. The device was electrically characterized and the measurement concept was evidenced by cell attachment and spreading experiments for homogeneous as well as heterogeneous co-cultures. Additionally, time-resolved alteration of the transepithelial electrical resistance upon treatment with cytoskeleton disrupting drug were shown for both cell layers in a co-culture as proof of concept studies. The new device simplifies kinetic studies significantly since the barrier function of both cell layers can be monitored individually in a label-free and time-resolved manner. Furthermore, the device was combined with the ECIS technique to study three co-cultured barrier-forming cell layers in a single experiment under physiological and non-invasive conditions. Hence, the new devices represents a versatile tool for a detailed impedance analysis of two or even three co-cultured cell layers in parallel. Detailed impedance analysis of complex biological barrier systems, where the interactions between cell populations of different types are of interest, can now be performed with the new device *in vitro*. Experiments addressing the permeation of drugs or nanomaterials across biological barrier systems might benefit from this new technical approach. By modifying the electrode layout on the back side of the porous filter membrane, the concept will be applicable to adherent cells of any type and broaden the experimental opportunities in the future.

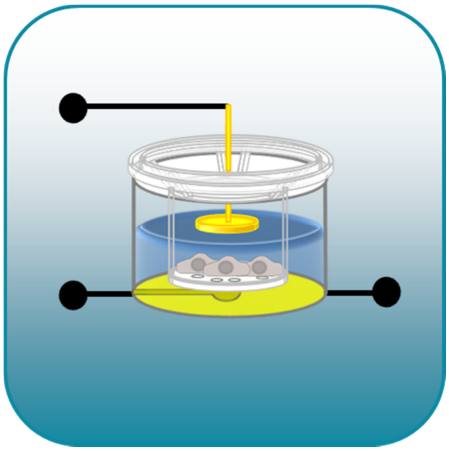

6 Combined electrochemical determination of substrate permeability and TEER

Non-invasive TEER measurements are generally performed prior to *in vitro* permeability assays to ensure cellular barrier integrity. Both assay techniques are of integral nature and executed consecutively. Local barrier function heterogeneities or small defects within the cell layer cannot be determined and, hence, might lead to misinterpretations.

The second project presented here describes a device for combined TEER and spatially resolved tracer permeation recordings based on impedance measurements in presence of a redox active compound. Therefore, a cell-covered filter membrane is placed in between two electrodes which monitor the transepithelial electrical resistance. The same cell layer is simultaneously incubated with a redox active substance which is added in the apical filter compartment. Its permeation across the cell layer is detected *in situ* via several small electrodes deposited on the bottom of the basal compartment without taking samples. Possible cytotoxic or barrier modulating effects of the used redox tracer $[Fe(CN)_6]^{3-/4-}$ have been probed in advance. The electrode layout of the new device is electrically characterized before proof-of-concept studies for the detection of defect areas are performed. Furthermore, tracer compound and cell type specific permeability coefficients (P_{app}) are determined for each electrode separately to quantify local heterogeneities of barrier function. The results are compared to optically determined permeability coefficients.

6.1 Influence of $[Fe(CN)_6]^{3-/4-}$ on epithelial barrier function

Electroactive compounds (e.g. ferrocene, $[Fe(CN)_6]^{3-/4-}$ or $[Ru(bpy)_3]^{3+/2+}$) are commonly used for the detection of (bio)chemical reactions at solid electrodes (K'Owino and Sadik 2005, Zhang et al. 2005, Sadik et al. 2009, Primiceri et al. 2011). These redox mediators can also be used in cell-based assays (Zhao et al. 2012, Sperber 2016). Mixtures of ferrocyanide and ferricyanide ions ($[Fe(CN)_6]^{3-/4-}$) in concentrations up to 10 mM are used very frequently as electroactive tracer substance. No cytotoxic effect is reported and, hence, $[Fe(CN)_6]^{3-/4-}$ is regarded as an optimal redox mediator in cell-based assays. Viability tests confirmed a minor impact of $[Fe(CN)_6]^{3-/4-}$ on the vitality of adherently growing cell types used in this thesis (appendix: Fig. 12.3). However, barrier integrity in presence of $[Fe(CN)_6]^{3-/4-}$ needs to be considered for the assay developed here. Therefore, ECIS and transfilter resistance measurements were performed.

6.1.1 Electric cell-substrate impedance sensing (ECIS)

Electric cell-substrate impedance sensing measurements were performed in a 96-well array format with three different cell types in presence of increasing concentrations of $[Fe(CN)_6]^{3-/4-}$ (appendix: Fig. 12.5). Data for three different concentrations were normalized to the values prior to addition of the redox couple (Fig. 6.1). The normalized impedance magnitude is plotted at a frequency of 8 kHz since no significant influence of the cyanide solutions to the total impedance of the cell-free system was detectable here (appendix: Fig. 12.4). The normalized impedance measured for NRK-covered electrodes, increases about 8 % after pure buffer (PBS^{++} incl. 1 g/L glucose) addition and stays constant thereafter (Fig. 6.1 A). The addition of $[Fe(CN)_6]^{3-/4-}$ to the buffer causes a concentration-dependent decrease of the impedance signal which starts after around 1 h of incubation and reaches (81 ± 2) % at t = 2 h for 0.4 mM and (75 ± 5) % for a concentration of 1 mM of the redox mediator. Control experiments performed with MDCK-lr cell layers show similar time courses (Fig. 6.1 B). A slight impedance decrease can be detected upon addition of $[Fe(CN)_6]^{3-/4-}$ to the buffer which is followed by an increase to control levels within 90 min incubation time. Then, a fast decrease in the impedance signal to final values of (86 ± 2) % can be monitored for a concentration of 1 mM. The impedance signal of MDCK-hr-covered electrodes shows no significant changes upon addition of the redox couple compared to control measurements

(Fig. 6.1 C). ECIS measurements are sensitive to morphological changes of cells in a confluent monolayer. Since viability assays showed no significant impact for $[Fe(CN)_6]^{3-/4-}$ concentrations studied here (appendix: Fig. 12.3), the observed effects of $[Fe(CN)_6]^{3-/4-}$ might be attributed to morphological changes and/or alterations in epithelial barrier function. From these data it is obvious that at least NRK and MDCK-lr cells react after around 90 min to higher concentrations of $[Fe(CN)_6]^{3-/4-}$ when cultured on solid substrates. Comparable data from literature are not available so far. To guarantee an insignificant effect of the permeation marker to the cells, all further experiments were performed with a redox couple concentration of 1 mM and a limited incubation time of 1 h.

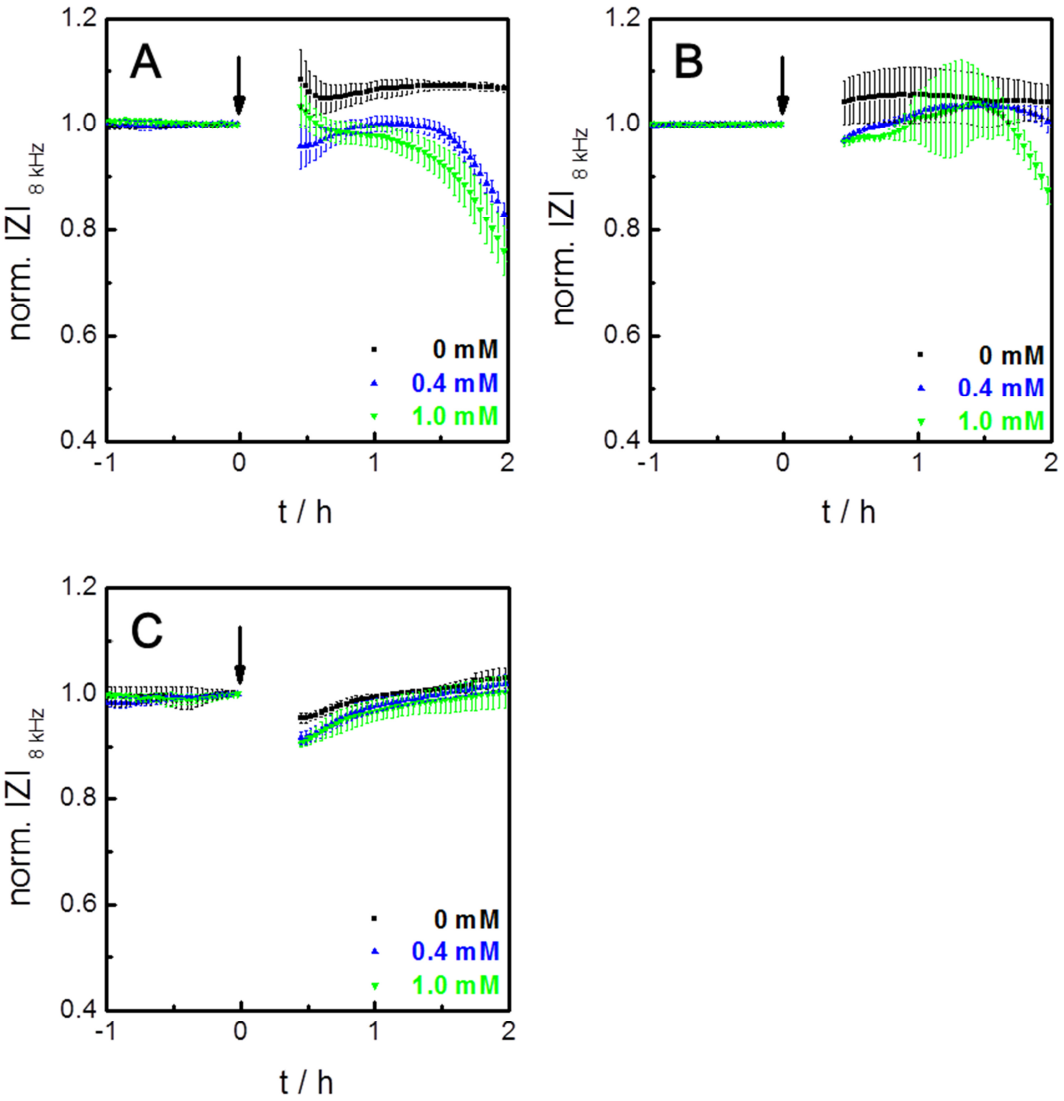

Fig. 6.1: 96-well ECIS measurements on confluent cell layers of NRK cells (**A**), MDCK-lr cells (**B**) and MDCK-hr cells (**C**). Time course of the normalized impedance magnitude *IZI* at a frequency of 8 kHz in presence of different concentrations of $[Fe(CN)_6]^{3-/4-}$ (addition at t = 0 h, mean ± SDM, n = 3).

6.1.2 Transepithelial electrical resistance in presence of $[Fe(CN)_6]^{3-/4-}$

TEER measurements were performed in order to determine a possible modulation of the transepithelial resistance due to addition of $[Fe(CN)_6]^{3-/4-}$. Standard TEER devices feature a big fluid filled basal compartment which is reduced in volume for the new assay format. Therefore, the new device shown in Fig. 4.14 was used directly for TEER determinations to avoid effects due to dilution. Different cell types were seeded to confluency on commercially available filter inserts and placed into the measurement chamber. After stable impedance values were recorded, the redox couple was added to the apical filter compartment. TEER time courses are shown in Fig. 6.2. TEER of highly permeable NRK monolayers increases about 15 % from $(8.9 \pm 0.9)\ \Omega cm^2$ to $(10.3 \pm 1.1)\ \Omega cm^2$ after the addition of 1 mM $[Fe(CN)_6]^{3-/4-}$. A minor resistance decrease from $(53.7 \pm 2.7)\ \Omega cm^2$ to $(49.3 \pm 2.8)\ \Omega cm^2$ is observed for MDCK-lr cells. Tight epithelial barriers (MDCK-hr) show a transient increase in resistance from $(643 \pm 237)\ \Omega cm^2$ to a maximum of $(1102 \pm 151)\ \Omega cm^2$ at t = 34 min after redox couple addition. At t = 1 h after addition the TEER monitored for MDCK-hr cell layers reaches values of $(922 \pm 178)\ \Omega cm^2$.

The TEER determined for all cell layers is similar to data known from literature (Tab. 5.5). Together with the results obtained via ECIS measurements, TEER values of cellular monolayers show that neither a cytotoxic effect nor a significant alteration in epithelial barrier function is caused by a 1 mM solution of the redox couple $[Fe(CN)_6]^{3-/4-}$ within an incubation

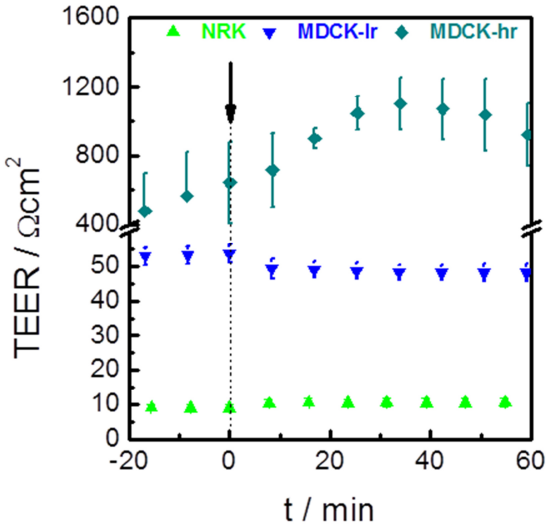

Fig. 6.2: Time course of the transepithelial electrical resistance (TEER) after addition of 1 mM $[Fe(CN)_6]^{3-/4-}$ to confluent monolayers of different cell types (▲ NRK, ▼ MDCK-lr, ● MDCK-hr, mean ± SE, n = 3).

time of less than 60 min for NRK- and MDCK-lr cells. The increase of TEER for MDCK-hr cell layers is significant but within the reported resistance values summarized in Tab. 5.5. Significant changes in the cell layer capacitances have not been observed. In addition, a cellular transport system to facilitate the active transport of this redox tracer across cell membranes is not known. Hence, this electroactive compound is suitable to serve as passive permeation marker across cellular monolayers.

6.2 Impedance based permeability studies

The device presented here aims to combine TEER and P_{app} quantification. The electrode layout established at the bottom of the measurement chamber is used to overcome the integral nature of transfilter substrate permeability assays. Several small electrodes (A_{el} = 7.5E-03 cm^2) are located on the bottom of the chamber to enable a spatially resolved detection of redox couple diffusion across the cell layer (Fig. 4.7 and Fig. 4.14). Variations in the kinetics of the tracer diffusion can then be attributed to barrier heterogeneities or small defect areas within the otherwise confluent cell monolayer. The individual and time-dependent appearance of the tracer in the receiver compartment is used to calculate the apparent permeability coefficient P_{app} for each detection spot underneath the cell layer.

6.2.1 Electrode characterization and set-up calibration

Cell-free filter inserts were placed directly on the co-planar gold electrodes which are integrated in the bottom of the measurement chamber. A gold-coated dipping electrode was placed in the upper filter compartment (Fig. 6.3 A). The complex impedance of the device was recorded in the transfilter mode through the filter insert (● **1-2**) and in the co-planar mode (▲ **2-3**) for the electrodes underneath the filter membrane over a broad frequency window. Impedance magnitude *IZI*, resistance *R* and capacitance *C* of both modes are shown in Fig. 6.3 B-D. In absence of the redox couple, all frequency spectra are influenced by the double layer capacitance of the electrode/electrolyte interface in the lower frequency range and the resistance of the bulk in the higher frequency range.

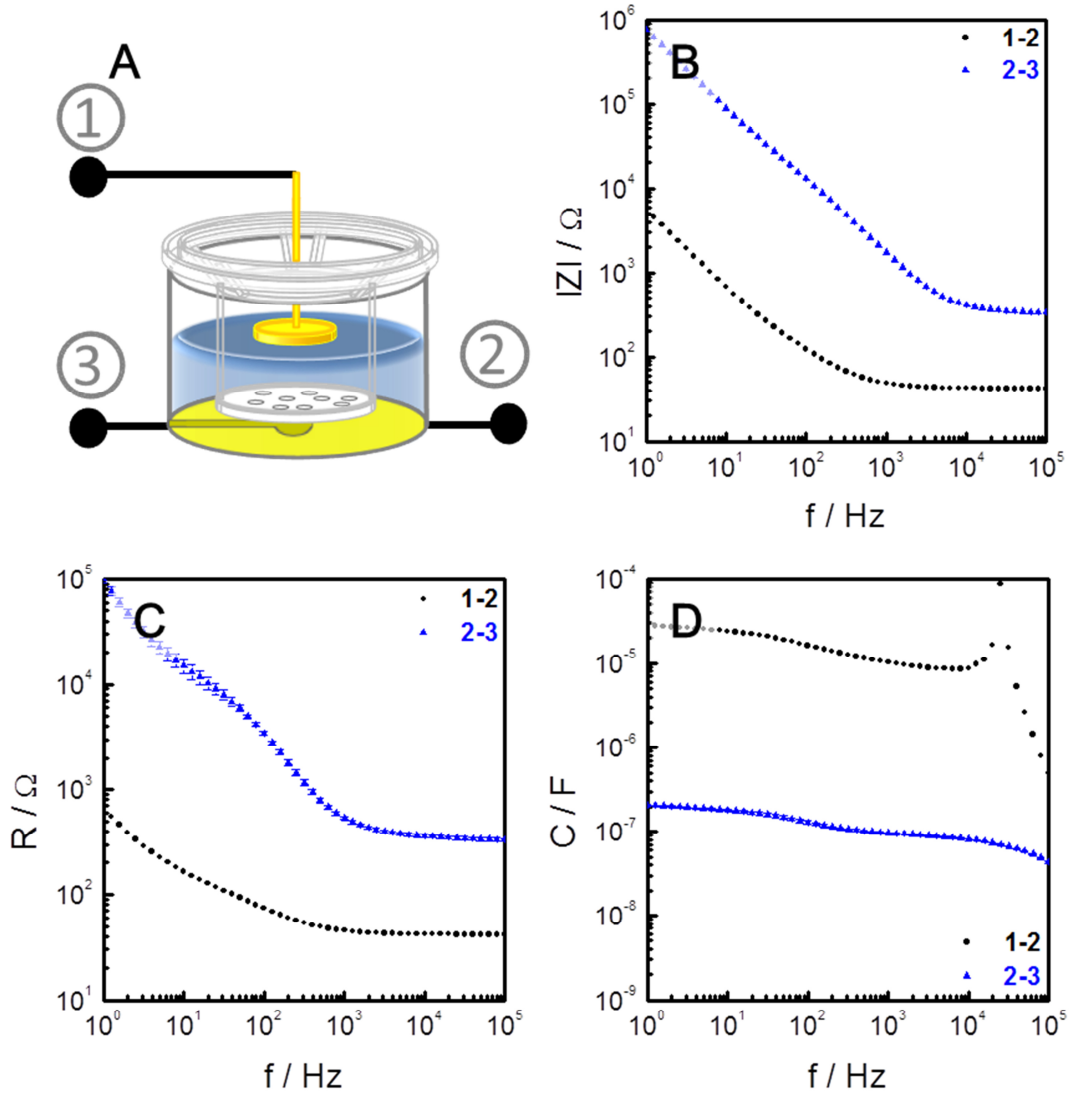

Fig. 6.3: A Schematic illustration of the experimental set-up: The electrical connetion of electrode nr. 1 to electrode nr. 2 is used for transfilter measurements (**1-2**). Six individual small electrodes (nr. 3) are surrounded by a big counter electrode (nr. 2) on the bottom of the device (**2-3**). Frequency spectra of the cell-free device are displayed as impedance magnitude *IZI* (**B**), resistance *R* (real part of *Z,* **C**) and capacitance *C* (**D**) for the transfilter measurement mode (● **1-2** TEER mode) and the co-planar electrode arrangement (▲ **2-3** co-planar mode, mean ± SE, n = 6).

Tab. 6.1: Parameters for all elements of the equivalent electric circuit used for analysis are presented for the transfilter TEER mode (**1-2**, mean ± SE, n = 3) and the co-planar measurement mode (**2-3**, mean ± SE, n = 6).

parameter / unit	**1-2**	**2-3**
R_{bulk} / Ω	49 ± 7	339 ± 11
$R_{paras.}$ / Ωcm^2	48 ± 1	18 ± 2
$C_{paras.}$ / μF/cm^2	40.5 ± 1.1	37.5 ± 1.5
A_{CPE} / μFs$^{(n-1)}$/cm^2	23.1 ± 5.1	31.5 ± 0.4
n_{CPE}	0.949 ±0.012	0.936 ±0.003

Since both modes differ in electrode size and separation, the measurement modes are clearly separated from each other in the impedance spectra. The parasitic impedance contributions of the cell-free device (filter inserts and measurement chamber) influence both measurement modes and are most pronounced in the resistance spectra (Fig. 6.3 C).

The elements of the equivalent circuit presented in Fig. 3.3 are fitted to these data and listed in Tab. 6.1. The calculated bulk resistance R_{bulk} is determined to a value of (49 ± 7) Ω in the TEER mode and to (339 ± 11) Ω in the co-planar measurement mode (**2-3**). Differences detected for R_{bulk} are mainly due to the higher lead and constriction resistance for the small electrodes on the bottom of the measurement chamber. The parasitic resistive and capacitive contributions of the device are less pronounced in mode **2-3** since the electric field crosses only a portion of the insert. Hence, $R_{paras.}$ is reduced to more than 60 % from (48 ± 1) Ωcm^2 in mode **1-2** to (18 ± 2) Ωcm^2 in mode **2-3**. $C_{paras.}$ is reduced from (40.5 ± 1.1) μF/cm^2 to (37.5 ± 1.5) μF/cm^2. Variations regarding the parameter A_{CPE} are due to different sizes of the active electrode areas. Since gold is used for all electrodes, n_{CPE} is overlapping for both modes. TEER calculations based on measurements performed in mode **1-2** need to be corrected for the parasitic parameters ($R_{paras.}$ / $C_{paras.}$) of the cell-free device (Tab. 6.1). The contribution of the filter insert is insignificant for the co-planar measurement mode (**2-3**) since impedance raw data in the low frequency range will be used to monitor the permeation of the redox active tracer compound across the cell layer.

The diffusion of the redox couple across a cellular barrier can be detected at six individual positions in the basal filter compartment (mode **2-3**). These individual sites are formed when the filter membrane is placed directly on top of the electrodes at the bottom of the chamber and they are confined laterally by the thin layer of insulting photoresist (h = 360 μm). Assuming a tight seal around the electrodes for simple calculation, the volume of each basal compartment is calculated to V = 2.55E-04 cm^3 (appendix: Fig. 12.6).

Changes in impedance magnitude of mode **2-3** upon redox tracer addition depend on the specific diffusion coefficient and the concentration of the redox couple (chapter 3.1.5) and, hence, need to be analyzed. Impedance measurements with increasing concentrations of $[Fe(CN)_6]^{3-/4-}$ were performed and the obtained impedance spectra are displayed in Fig. 6.4 A - B. $|Z|$ decreases in a concentration-dependent manner in the low-frequency region (1 - 10 Hz). The effect is stronger for decreasing frequencies and reaches a maximum at f = 1 Hz. The values of $|Z|$ at this most sensitive frequency are listed in Tab. 6.2.

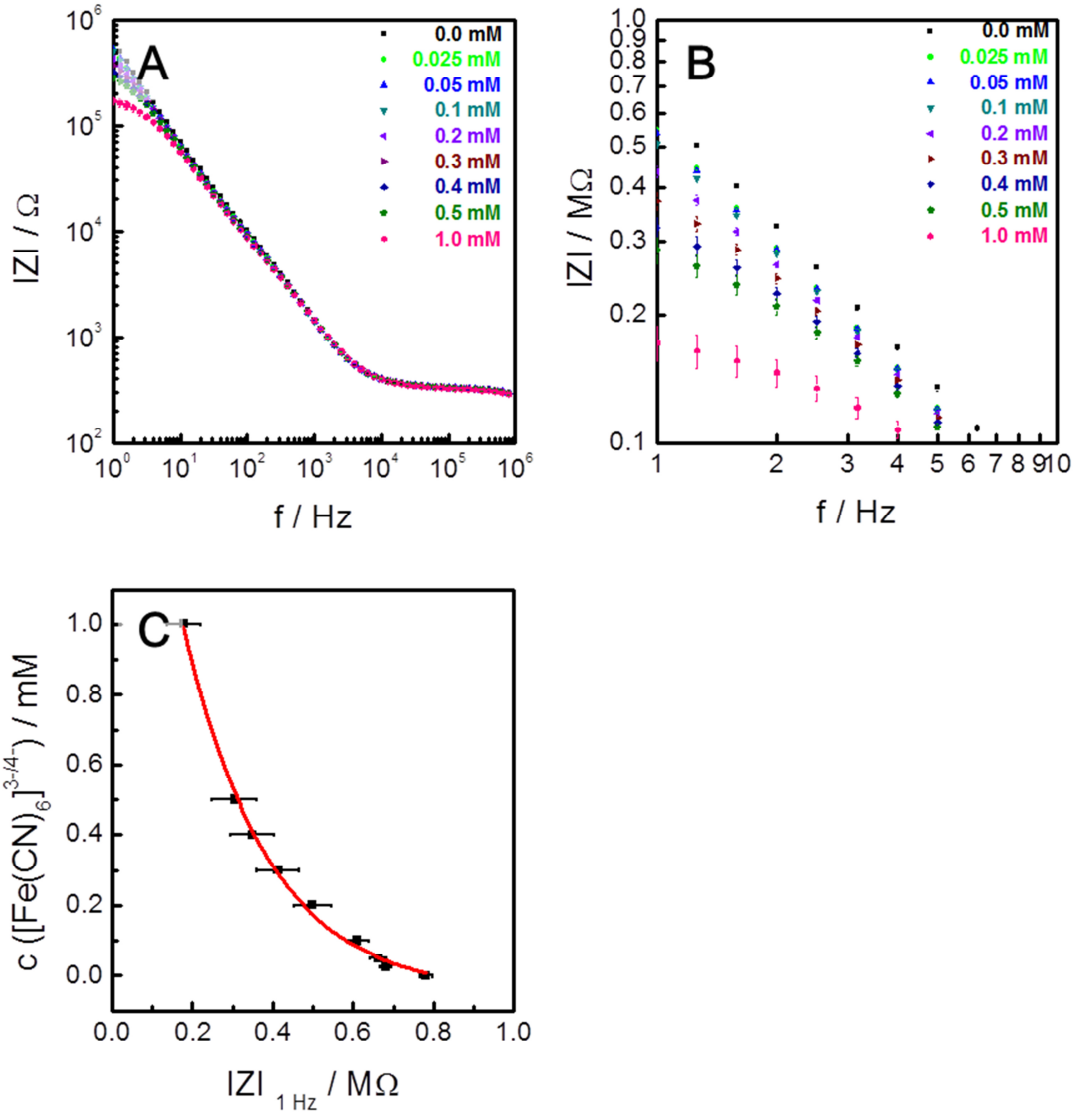

Fig. 6.4: Frequency spectra of impedance magnitude *IZI* (mode **2-3**) in presence of variable concentrations of redox couple $[Fe(CN)_6]^{3-/4-}$ (**A**, **B**). **C** Exponential decay (first order fit function, solid red line) between *IZI* at 1 Hz (mean ± SE, n =6) and $c([Fe(CN)_6]^{3-/4-})$ (parameters listed in Tab. 6.3).

Tab. 6.2: Impedance magnitude *IZI* (in MΩ) at a frequency of 1 Hz in response to different concentrations of the redox tracer (mode **2-3**).

	IZI $_{1\ Hz}$ **/ MΩ**						
$c([Fe(CN)_6]^{3-/4-})$ / mM	**e1**	**e2**	**e3**	**e4**	**e5**	**e6**	**mean ± SE**
0	0.772	0.795	0.795	0.796	0.758	0.772	0.781 ± 0.007
0.025	0.672	0.676	0.707	0.689	0.665	0.681	0.682 ± 0.006
0.05	0.651	0.649	0.699	0.667	0.648	0.661	0.663 ± 0.008
0.1	0.601	0.577	0.660	0.603	0.600	0.621	0.610 ± 0.011
0.2	0.493	0.439	0.567	0.462	0.504	0.528	0.499 ± 0.019
0.3	0.397	0.340	0.482	0.373	0.427	0.457	0.413 ± 0.022
0.4	0.328	0.274	0.414	0.306	0.373	0.401	0.349 ± 0.023
0.5	0.278	0.230	0.361	0.260	0.339	0.363	0.305 ± 0.023
1.0	0.155	0.125	0.210	0.142	0.211	0.225	0.178 ± 0.017

The presence of a redox active species in an AC circuit leads to an electron transfer from the electrode to the species in solution and vice versa at an appropriate potential. The electric equivalent circuit for this electrode-electrolyte interface contains the empirical faradaic impedance element (Z_f) in parallel to the constant phase element CPE (chapter 3.1.5, Fig. 3.4). The real part of Z_f is called charge-transfer resistance R_{ct} which is a kinetically controlled parameter. The second part of the faradaic impedance is called mass transfer impedance or Warburg impedance Z_W. The Warburg impedance consists of a real and an imaginary part of the same magnitude (diffusion controlled parameter). The influence of the Warburg element to the total impedance magnitude of a two-electrode system is strongly affected by the concentration of the redox active species (Fig. 3.4). An increased bulk concentration of the redox species causes a decrease in the magnitude of the Warburg coefficient σ (eq. 3.19) and the impedance contribution of the Warburg element to the total impedance of the system is decreased (eq. 3.20). Here, the redox couple concentration in the electrolyte is not sufficient (≤ 1 mM) to completely vanish the impedance contribution due to diffusion. However, R_{ct} is decreasing with increasing concentration of the redox couple. Thus, the total impedance magnitude of the system is strongly affected by R_{ct} in the lower frequency range.
However, the mathematical correlation between redox couple concentration and mean values of *IZI* at *f* = 1 Hz can be described by an exponential decay function (Fig. 6.4 C). Parameters of this function are listed in Tab. 6.3. The equation can be used to calculate time-dependent changes in redox tracer concentration within the basal compartments from the measured impedance raw data.

Tab. 6.3: Parameters of the exponential decay function ($c = A \cdot e^{(-IZI/t)} + c_0$, Origin8) which describe the relation between the added redox couple concentration ($c([Fe(CN)_6]^{3-/4-}$) and the detected impedance magnitude *IZI* at a frequency of 1 Hz (Fig. 6.4 C).

parameter / unit	**mean ± SE**
offset c_0 / mM	-0.05 ± 0.02
amplitude A / mM	2.44 ± 0.11
decay constant t / MΩ	0.21 ± 0.01
adj. R-Square	0.997

6.2.2 Detecting defects within confluent cell layers

For proof-of-concept studies, small defect areas were generated on purpose within a confluent cell monolayer grown on the porous filter membrane. In order to maintain the intactness of the supporting filter membrane, a small adhesive PDMS spacer was attached to the membrane prior to cell seeding. The spacer was present during the entire culture period to avoid cell growth into this area. It was detached directly before the measurement started. The filter insert was placed into the measurement chamber in a way that the existing defect area (~ 3 mm^2) was located directly above electrode no. 3. (Fig. 6.5 B). Transfilter mode (**1-2**) was neglected here and the impedance was recorded in a very narrow frequency window from 1 - 10 Hz which allows a time resolution of 1.2 min. After stable values of *IZI* at a frequency of 1 Hz were reached (0.8 MΩ), the redox couple (1 mM) was added to the apical filter compartment (Fig. 6.5 A). A rapid decrease of *IZI* is detectable for electrode 3 (e3) directly after redox couple addition. Stable values of *IZI* are reached again within 10 min (0.07 MΩ). e4 shows an impedance decrease which is delayed by around 10 min. 30 min after addition e2 and e6 show a decreasing signal. The signals of e1 and e5 show a minor impedance decrease.

The intentional defect is located above e3 and, hence, no cellular barrier hinders the diffusion of the redox tracer into the basal compartment. Since the cell-free region is more than four

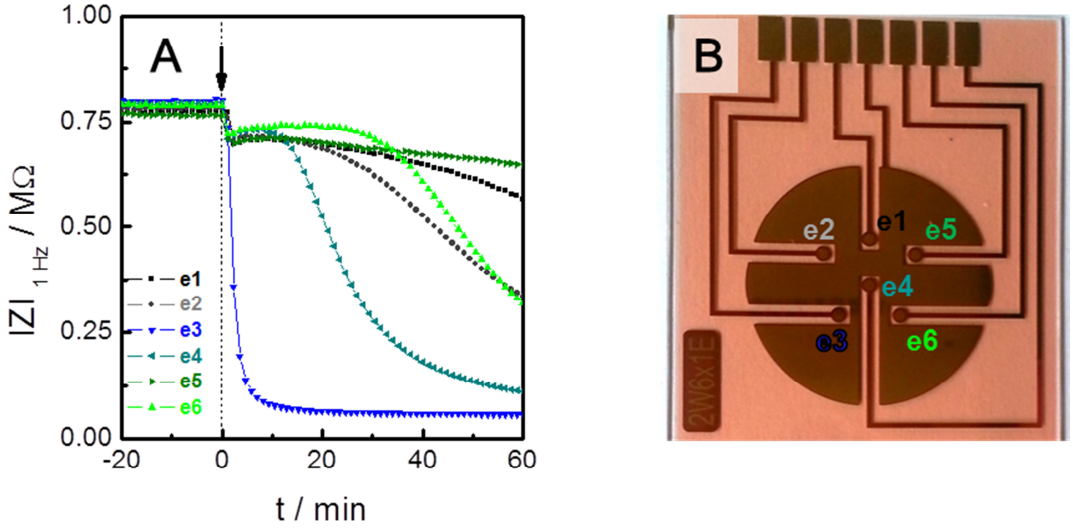

Fig. 6.5: A confluent monolayer of MDCK-Ir cells with an intentional defect area of ~ 3 mm^2 (placed above e3) is incubated at t = 0 with a 1 mM solution of $[Fe(CN)_6]^{3-/4-}$. The addition is performed to the apical filter compartment. The impedance magnitude *IZI* is followed at a frequency of 1 Hz in the basal compartment (co-planar mode **2-3**, **A**). A photograph of the electrode layout is displayed in **B** (diameter of e1-e6: 1 mm).

times bigger compared to surface area of electrode 3 (e3), a tracer leakage to the other electrodes underneath the filter membrane is observed. The redox couple diffuses from the detection site of e3 to the surrounding electrodes and spreads further with time. The defect area was then decreased in size to prevent spreading of the tracer substance. The experiment was repeated but reduced in duration (Fig. 6.6 A). Since the cell-free area is again located directly above e3, the impedance magnitude decreases by around 62 % within 15 min. All other electrodes show no significant signal change. The filter insert was washed twice with buffer, rotated 120° and the measurement was repeated (Fig. 6.6 B). Again, only the electrode which is directly located underneath the cell-free defect area shows a rapid impedance decrease (e1). After 15 min of incubation *IZI* is reduced by more than 77 %. The cell-covered insert was stained with carbol fuchsin solution and dried directly after the end of the measurement. Carbol fuchsin is used to enhance the contrast between filter membrane (white) and cell monolayer (pink color). Stereomicroscopic images of the whole filter membrane and phase contrast pictures of the defect area are shown in Fig. 6.7.

From these pictures it is obvious that no other defect is present within the cell layer after rotation. Moreover, the size of this cell-free area can be determined very accurately to A = 1.16 mm^2. TEER of this cell layer was determined to 77 Ωcm^2 prior to cell staining which is still acceptable according to values published in literature for this cell type (Tab. 5.5).

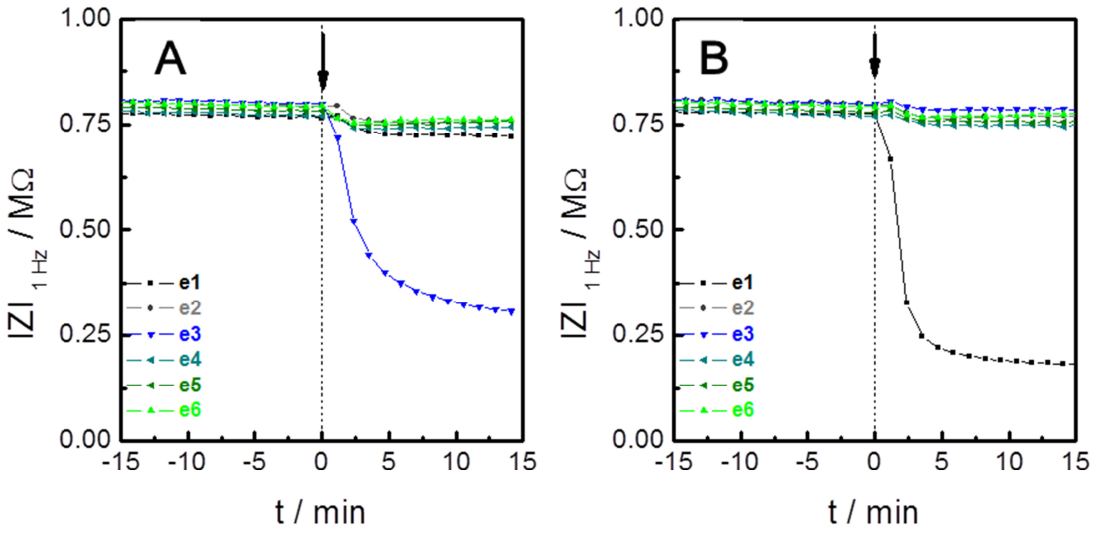

Fig. 6.6: A MDCK-Ir-covered filter insert with an intentional defect area of 1.16 mm^2 is incubated at t = 0 with a 1 mM solution of $[Fe(CN)_6]^{3-/4-}$. The addition is performed to the apical filter compartment. The impedance magnitude *IZI* is followed at a frequency of 1 Hz (co-planar mode **2-3**). **A** The defect area is located above e3. **B** The same insert was washed and rotated 120° before the measurement was repeated (defect above e1). TEER was measured to 77 Ωcm^2 after the measurement.

Hence, integral TEER values might lead to misinterpretation regarding the state of confluence of a cell layer whereas spatially resolved permeation recordings can be used to detect local defect area within an otherwise confluent cell layer.

However, the kinetics and final values of *IZI* differ in both experiments although the defect area remained constant. This effect is caused due to an experimental, but very reproducible manual error during the addition of the redox couple (appendix: Fig. 12.7 and Fig. 12.8). The data clearly show that the detection of defect areas is possible with the fabricated device. The time-dependent decrease in impedance magnitude *IZI* is dominated by the size of the defect area and can be detected in the co-planar measurement mode (**2-3**) at a frequency of 1 Hz.

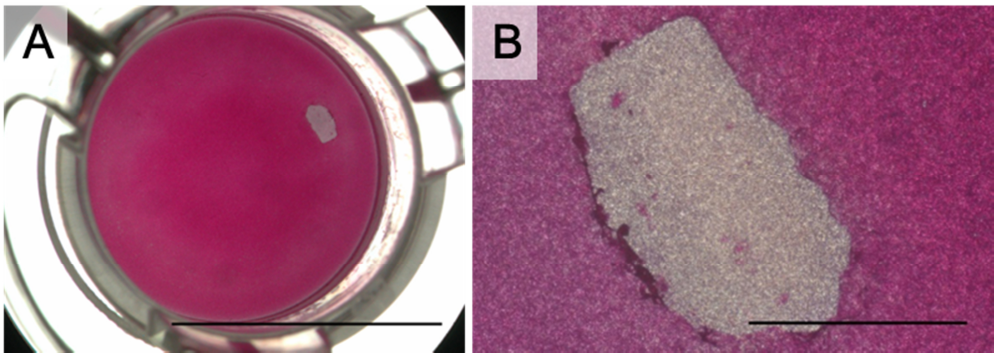

Fig. 6.7: Stereomicroscopic (**A**, scale bar: 10 mm) and phase contrast images (**B**, scale bar: 1 mm) of the cell-covered filter insert used for the experiments shown in Fig. 6.6. The cell-covered membrane was stained with pink carbol fuchsin solution for a better contrast. The defect area has a surface area of A = 1.16 mm^2.

6.2.3 Impedimetric monitoring of $[Fe(CN)_6]^{3-/4-}$ permeation across cell monolayers

Measurements on intact monolayers of different cell types were performed with the new device. The impedance of both measurement modes (**1-2**: transfilter mode for TEER determination, **2-3**: co-planar mode for basal tracer detection in six individual compartments) was recorded over a frequency window from 1 – 10^5 Hz. Control experiments showed that a buffer replacement without $[Fe(CN)_6]^{3-/4-}$ causes no change in impedance magnitude of the six individual co-planar detection electrodes at a frequency of 1 Hz (appendix: Fig. 12.9). Since the benefit of this approach does not only lie in the combination of two assays but in the individual monitoring of several permeation spots underneath a confluent cell layer, this chapter shows exemplary data of spatially resolved permeability recordings.

Simultaneous TEER and substrate diffusion measurements of highly permeable NRK cells are displayed in Fig. 6.8. The TEER remains stable (12.5 Ωcm^2) during the entire

measurement and it only slightly increases within the first 25 min after addition of the redox tracer (12.9 Ωcm^2). The permeation of $[Fe(CN)_6]^{3-/4-}$ across the confluent cell layer is detectable in the basal compartments directly after addition at t = 0 min. The impedance magnitude *IZI* drops for four of six electrodes from ~ 0.74 MΩ to final values of ~ 0.1 MΩ within eight minutes. Electrodes e1 and e2 show a delayed decrease.

The time course of TEER allows two conclusions: (i) the transcellular resistance fits exactly to data reported in literature for this cell type (Tab. 5.5) and (ii) the addition of the redox couple does not have any influence on the epithelial barrier function. TEER as well as the rapid impedance decrease show that a confluent monolayer of NRK cells is extremely leaky and, hence, does not act as effective diffusion barrier. However, heterogeneities within the diffusion kinetics of the tracer are not detectable for this leaky cell layer. Two of six individual electrodes (e1 and e2) show a delayed appearance of the redox couple only due to the measurement sequence.

The temporal resolution of the measurement is insufficient to detect differences in tracer permeation during the first five minutes. There are two options to improve the information content of impedance based permeability monitoring for leaky cell layers. Applying a reduced redox couple concentration would result in a lesser concentration gradient across the cell layer and, hence, the appearance of the tracer in the basal compartment will be retarded.

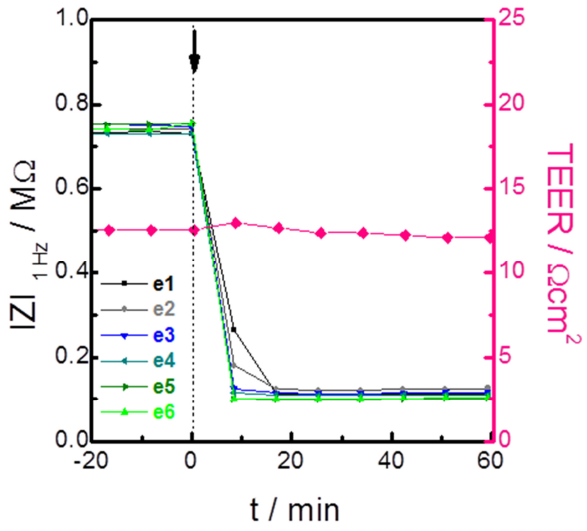

Fig. 6.8 NRK-covered filter insert is incubated at t = 0 with a 1 mM solution of $[Fe(CN)_6]^{3-/4-}$. The addition is performed to the apical filter compartment. The impedance magnitude *IZI* is followed at a frequency of 1 Hz (co-planar mode **2-3** for e1 - e6). The transfilter mode (**1-2**) is used to record TEER of the same insert simultaneously. The graph presents data of a typical experiment.

The alternative is an improvement of the temporal resolution of the measurement. So far it is necessary to record complete impedance spectra across the entire frequency window for all measurement modes which needs about 8 minutes. However, the software which controls the impedance analyzer can be reprogrammed. The resolution in time could be improved to around two minutes by recording only one complete impedance spectrum, which is needed for TEER determination, and detecting the tracer diffusion only at one fixed frequency (1 Hz). Although the experimental conditions need to be adapted for very leaky cell types, the electrochemical determination system for tracer permeation is suitable to detect substrate permeation and transcellular resistance simultaneously. Combined TEER and tracer permeation recordings were also performed with moderately tight MDCK-Ir cell layers (Fig. 6.9 A). Prior to redox tracer addition, the TEER was determined to 80.2 Ωcm^2. Transepithelial resistance is decreased at once after addition (- 5 Ωcm^2) and reaches a minimum of 71.8 Ωcm^2 (t = 42 min) thereafter. The recorded impedance magnitude *IZI* for all electrodes underneath the porous membrane is 0.75 MΩ except for e2. Upon addition of $[Fe(CN)_6]^{3-/4-}$, all co-planar electrodes detect different amounts of tracer substance in the basal compartments. e1, e2 and e3 show a slight increase in *IZI* directly after addition which is followed by a constant decrease during the experiment. This increase is not observed for the other tracer detecting electrodes. Final values of *IZI* are between 0.68 MΩ and 0.56 MΩ.

A minor TEER decrease after tracer addition was observed for MDCK-Ir cell layers before (Fig. 6.2). However, the magnitude of TEER still correlates favorably to the reported values (Tab. 5.5) and, hence, TEER values can be determined accurately with the new device. The permeation of the redox couple across the confluent MDCK-Ir cell layer shows varying time courses for all detection spots underneath the monolayer. This indicates a heterogeneous constitution of the MDCK-Ir epithelial barrier. The ability to hinder the passive diffusion of the redox tracer from the apical into the basal compartment differs in a way that only two electrodes show the same permeation time course. Furthermore, the final values of *IZI* for MDCK-Ir monolayers (~ 0.6 MΩ) differ significantly from those observed for highly leaky NRK cell layers (~ 0.1 MΩ). Hence, the new device is able to differentiate between epithelial barrier function not only via TEER recordings but also by substrate permeation measurements. In addition, the device can locally resolve the permeation of very small amounts of the tracer substance across the cell layer to the detecting electrodes.

The measurement was repeated with MDCK-Ir cell layers of the same population (Fig. 6.9 B).

Here, TEER is at a constant level during the entire measurement (~ 68 Ωcm^2). The tracer addition does not have any significant influence on the TEER. In contrast, the permeation of the redox compound is grouped into two time courses. Whereas e3, e4 and e5 show only minor alterations in *IZI*, e1, e2 and e6 decrease constantly after around 15 min to final values inbetween 0.48 MΩ – 0.35 MΩ. At t = 70 min, 5 μM cytochalasin D (cD) was added to the apical filter compartment. The transepithelial resistance decreases upon addition of this barrier disrupting drug to 4.5 Ωcm^2. The addition of cD also influences the kinetics of tracer diffusion. Hence, *IZI* recorded for all electrodes (e1 - e6) decreases rapidly to final values of ~ 0.05 MΩ.

The MDCK-Ir monolayer was prepared from the same population as the one studied in Fig. 6.9 A. Since both cell layers show similar TEER values but very different tracer profiles, it is obvious that this cell type forms very heterogeneous cellular barriers.

Moreover, the addition of cD causes a rapid loss of epithelial barrier function due to the disassembly of the actin cytoskeleton and the associated opening of cell-cell-contacts between adjacent cells. The permeation of ions across the cell layer is unhindered and the TEER decreases rapidly. Alterations in epithelial barrier function are also detectable underneath the filter support. Once tight cell-cell contacts are permeable, the redox couple diffuses directly through the porous filter membrane into the basal compartments. This

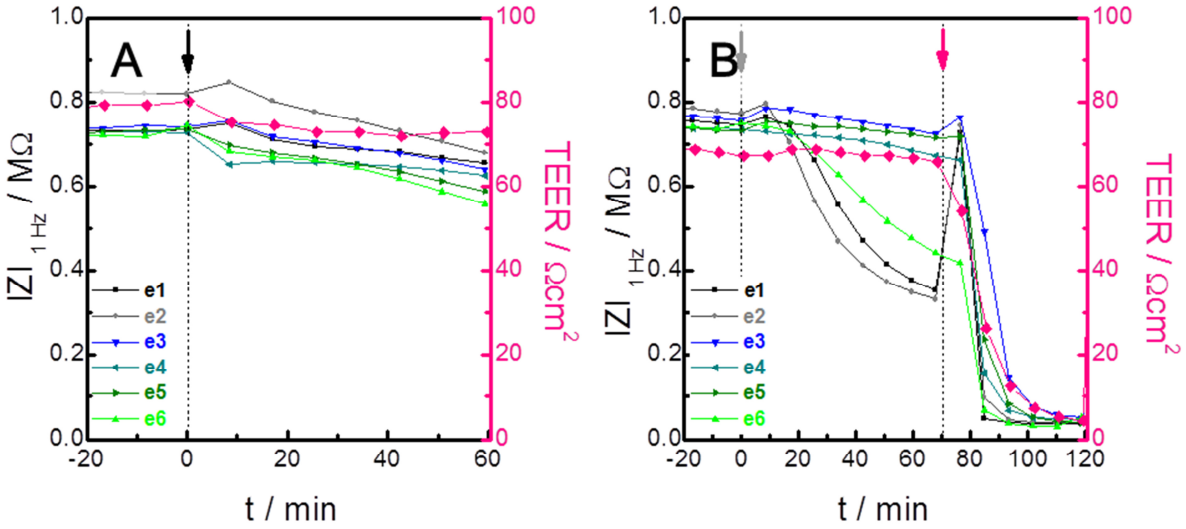

Fig. 6.9: The graphs present data of typical experiments with MDCK-Ir-covered filter inserts which are incubated at t = 0 with a 1 mM solution of $[Fe(CN)_6]^{3-/4-}$. The addition is performed to the apical filter compartment. The impedance magnitude *IZI* is followed at a frequency of 1 Hz underneath the cell layer (co-planar mode **2-3** for e1 - e6). The transfilter mode (**1-2**) is used to record TEER of the same insert simultaneously (**A**). The same experiment is repeated with a different insert (**B**). Additionally, at t = 70 min, cytochalasin D (5 μM) is added to the apical filter compartment.

unhindered diffusion is represented by the immediate decrease of *IZI*.

Besides highly permeable NRK cells and moderately tight epithelial barriers of MDCK-lr cells, MDCK-hr monolayers were investigated (Fig. 6.10 A). TEER of the MDCK-hr cell monolayer starts out at values of around 0.5 $k\Omega cm^2$. As seen before in Fig. 6.2, a transient resistance increase is observed during incubation with the redox couple and a TEER maximum of 1.2 $k\Omega cm^2$ is reached at t = 50 min. The appearance of $[Fe(CN)_6]^{3-/4-}$ is indicated in the basal compartments via e3, e5 and e6 and reaches final values of 0.55 – 0.44 MΩ. The other electrodes show no significant changes in *IZI* after the redox couple is added to the apical filter compartment.

Control measurements already showed, that $[Fe(CN)_6]^{3-/4-}$ can cause periodical changes in the transepithelial electrical resistance of MDCK-hr monolayers (Fig. 6.2). Nevertheless, the absolute TEER values determined here are within the variations commonly reported (Tab. 5.5). The variable time courses of tracer appearance detected at the six individual basal detection sites show similar trends as observed for MDCK-lr cell layers. Although TEER differs significantly for both subtypes, the ability to prevent the diffusion of $[Fe(CN)_6]^{3-/4-}$ is similar.

Another MDCK-hr-covered filter insert, prepared from the identical cell population, was studied (Fig. 6.10 B). TEER fluctuates during the first hour of the measurement between 0.9 $M\Omega cm^2$ and 1.3 $M\Omega cm^2$. Different time courses of *IZI* are observed in the co-planar detection mode upon addition of the redox couple to the apical filter compartment. Whereas e1 and e2 show no significant alteration in impedance magnitude, a decrease is detected for e3, e4 and e6. e5 shows a more rapid decreases to 0.4 MΩ at t = 60 min. At this time point, the drug cytochalasin D was added to the apical filter compartment which causes a decrease in TEER to final values of 146 Ωcm^2 and a continuous impedance decrease, monitored for all electrodes underneath the filter membrane. *IZI* reaches values in between 0.3 MΩ and 0.09 MΩ at the end of the measurement.

The measurement described above is another example for the heterogeneous nature of epithelial barrier function. Several detection spots show no or insignificant tracer permeation across the cell layer whereas other spots underneath the confluently covered membrane are less restrictive. In contrast, the barrier disrupting effect of cytochalasin D is visible as rapid TEER and impedance decrease in all measurement modes. The examples discussed here prove that recordings of transcellular resistance and substrate permeability for one individual

cell layer can be performed simultaneously. Moreover, several detection spots allow a spatial and time resolved permeation monitoring which is able to detect local heterogeneities in cellular barrier function towards substrate diffusion.

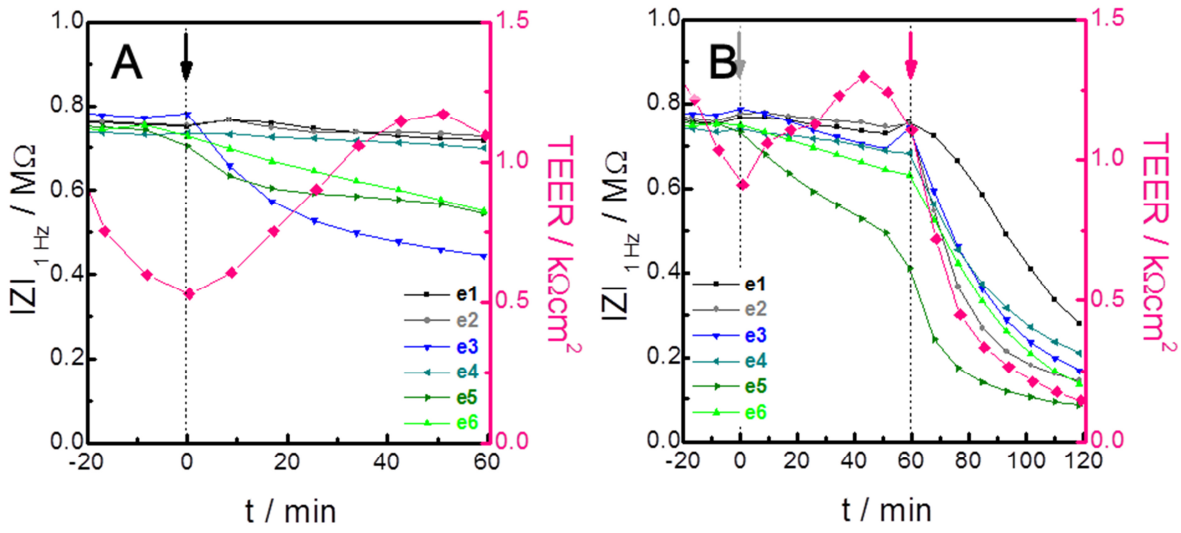

Fig. 6.10: MDCK-hr-covered filter inserts are incubated at t = 0 with a 1 mM solution of $[Fe(CN)_6]^{3-/4-}$. The addition is performed to the apical filter compartment. The impedance magnitude *IZI* is followed at a frequency of 1 Hz underneath the cell layer (co-planar mode **2-3** for e1 - e6). The transfilter mode (**1-2**) is used to record TEER of the same insert simultaneously (**A**). The same experiment is repeated with a different insert (**B**). At t = 70 min, cytochalasin D (10 μM) is added to the apical filter compartment. The graphs present data of typical experiments.

6.2.4 Permeability coefficients

Substrate and cell type specific permeability coefficients can be determined from permeation measurements (chapter 3.2.1). Therefore, the permeation of a tracer compound is usually analyzed over time by taking sequential samples from the receiver compartment. The rate by which the tracer passes the cellular barrier is entitled as apparent permeability coefficient P_{app} (eq. 3.27). This coefficient depends on the cross-sectional area of the filter membrane A, the initial tracer concentration in the donor compartment c_0 and the amount of substance detected in the receiver compartment over time ($\Delta n_R(t)/dt$). Only parameter A (filter area) needs to be adapted to calculate the apparent permeability of $[Fe(CN)_6]^{3-/4-}$ across confluent cell layers from impedance-based permeability measurements (A = 7.09E-3 cm^2). The recorded impedance magnitude *IZI* at a frequency of 1 Hz is used to calculate the concentration of the redox couple in the small receiver compartments above the electrodes. With the known volume of these compartments (V = 2.55E-04 cm^3), the amount of substance can be

calculated for every time point from the calibration curve (Fig. 6.4 C and Tab. 6.3). Furthermore, the calculation strictly followed the protocol described in the theoretical section (chapter 3.2.2). Only data which fulfilled the *sink-conditions* were used to calculate time dependent changes in n_R (eq. 3.30). In addition, only the linear phase within the permeation profile was used (Fig. 3.5). The experimental data for this period were analyzed by a linear regression to obtain the parameter $\Delta n_R(t)/dt$. The obtained parameters (slope and error of slope) were used, if the adjusted coefficient of determination (adj. R^2) of the linear regression was ≥ 0.9. A graphical illustration of the calculation process is given in the supplementary information section (appendix: Fig. 12.10).

Individual permeability coefficients were determined for both MDCK cell strains only, since the applied concentration of 1 mM $[Fe(CN)_6]^{3-/4-}$ was too high for experiments performed with NRK cell layers to meet all assumptions of the calculation protocol. The P_{app} values determined for three cell-covered filter inserts of each MDCK cell type are presented in Tab. 6.4. The range of P_{app} values and their mean, integrated over all electrodes are listed for each filter insert. 75 % of all electrodes provided evaluable impedance data. Electrodes which were not used for P_{app} calculations showed very rapid tracer permeation indicating defects. Hence, *sink-conditions* were not fulfilled. P_{app} varies in a range from ~ $0.1 \cdot 10^{-6}$ cm/s to ~ $1.0 \cdot 10^{-6}$ cm/s for MDCK-hr cell layers and is determined to values up to ~ $1.7 \cdot 10^{-6}$ cm/s for the low resistance type (MDCK-lr). Since permeability coefficients are not reported for this redox probe, the obtained results can only be compared to other tracer compounds (Tab. 6.5). Although the redox probe is of lower molecular mass and holds a smaller hydrodynamic radius than reported for fluorescein, P_{app} for $[Fe(CN)_6]^{3-/4-}$ is significantly smaller. The additional negative charges might restrict these cyanide complexes from passing the cellular

Tab. 6.4: Apparent permeability coefficients (P_{app} in 10^{-6} cm/s) calculated for three individual MDCK-lr and MDCK-hr monolayers (filter inserts 1 - 3). The number of electrodes per insert, which are used to calculate P_{app} is given in the table. The range of P_{app} values and the mean values determined for each filter insert are listed.

		P_{app} ($[Fe(CN)_6]^{3-/4-}$) / 10^{-6} cm/s	
cell line	**electrodes**	**individual value ± SD**	**mean ± SDM**
MDCK-lr (1)	6/6	(0.31 ± 0.03) – (0.60 ± 0.02)	0.49 ± 0.04
MDCK-lr (2)	6/6	(0.16 ± 0.02) – (1.1 ± 0.1)	0.43 ± 0.03
MDCK-lr (3)	4/6	(0.12 ± 0.01) – (1.7 ± 0.2)	0.56 ± 0.07
MDCK-hr (1)	3/6	(0.54 ± 0.01) – (1.00 ± 0.07)	0.77 ± 0.04
MDCK-hr (2)	5/6	(0.13 ± 0.01) – (0.56 ± 0.01)	0.31 ± 0.01
MDCK-hr (3)	3/6	(0.14 ± 0.01) – (0.91 ± 0.01)	0.42 ± 0.01

barrier predominantly via the paracellular pathway across bicellular tight junctions between two adjacent cells (bTJ, pore-Ø: ~ 0.8 nm, Van Itallie et al. 2009) as it is reported for fluorescein (Krug et al. 2009a). The apparent permeability coefficient determined here of the redox couple $[Fe(CN)_6]^{3-/4-}$ is in the same order of magnitude as reported for 4kDa-FITC dextran, although both substances differ in mass, charge and hydrodynamic radius r_h. Krug and colleagues reported that macromolecular passage (> 3000 g/mol) across MDCK monolayers (low resistance type) is mainly provided via very rare but large tricellular tight junctions (tTJ: tube-Ø: ~ 10 nm, Staehelin 1973). Hence, it could be assumed that also the permeation of cyanide complexes is provided by central tubes which are located only at the contact points of three cells.

Tab. 6.5: Examples of apparent permeability coefficients (P_{app} in 10^{-6} cm/s), determined for MDCK-lr monolayers, are compared to the hydrodynamic radius (r_h), molecular mass *M* and charge of the substrates.

substrate	*M / g/mol*	*charge*	r_h / nm	P_{app} / 10^{-6} cm/s	reference
sucrose	342	-	0.5[2]	0.09 ± 0.02	Lohmann et al. 2002
10kDa-FITC dextran	10000	-	1.86[3]	0.13 ± 0.03	Krug et al. 2009a
4kDa-FITC dextran	4400	-	1.3[4]	0.48 ± 0.10	Krug et al. 2009a
$[Fe(CN)_6]^{3-/4-}$	212	-3 / -4	0.475[5] / 0.422[6]	0.49 ± 0.02	this work
fluorescein	332	-2	0.5[4]	4.80 ± 1.21	Krug et al. 2009a

Apparent permeability coefficients P_{app} reflect the permeation rate of a marker molecule for a cell-covered filter insert. Hence, P_{app} should be corrected by the value for a cell-free filter insert in order to calculate the cell-related permeability coefficient P_E (eq.3.29). Experimental data recorded for cell-free inserts however, cannot be used to calculate the filters' permeability coefficients (appendix: Fig. 12.11). Similar to the time course of *IZI* observed for highly permeable NRK monolayers, the diffusion of the redox couple (1 mM) into the very small basal compartments is too fast with respect to the time resolution of the measurement.

Apparent permeability coefficients, as derived from impedance-based permeability assays, show that barrier function of cell monolayers is of heterogeneous nature. As the time courses of *IZI* at 1 Hz already indicated, local alterations within a confluent cell layer can be monitored in an automated way with a moderate time resolution (further optimization is possible).

[2] Schultz and Solomon 1961
[3] Armstrong et al. 2004
[4] Ambati et al. 2000
[5] Fornasiero et al. 2008
[6] Nightingale 1959

Variations of passive trancellular diffusion of redox mediators were imaged before via scanning electrochemical microscopy (Bergner et al. 2012) or via fluorescence live-cell imaging for dextrans (Krug et al. 2009a). However, the approach presented here offers the possibility to quantify these minor variations in cellular transport behavior.

6.3 Optical analysis of $[Fe(CN)_6]^{3-/4-}$ permeation

Since $[Fe(CN)_6]^{3-}$ absorbs light at a wavelength of 405 nm in a concentration dependent manner (appendix: Fig. 12.12), permeation measurements of the redox couple across confluent cell layers can be performed with an optical readout. Cells were cultured on permeable filter inserts under identical conditions as used for the impedimetric approach. 1 mM solution of $[Fe(CN)_6]^{3-/4-}$ was added to the apical filter compartment. Samples were collected from the basal compartment over time and analyzed via absorbance spectroscopy. However, tracer concentration in the basal compartment was found to be below the detection limit when cell-covered filter inserts were studied. Hence, the redox tracer concentration was increased by a factor of four to guarantee reliable optical analysis of tracer substance in the receiver compartments. Time-dependent concentration of $[Fe(CN)_6]^{3-/4-}$ in these compartments is displayed for cell-free and cell-covered filter inserts in Fig. 6.11. The tracer permeation across cell-free filter membranes results in a rapid concentration increase in the receiver compartment. A linear concentration profile is detectable up to t = 24 min before the

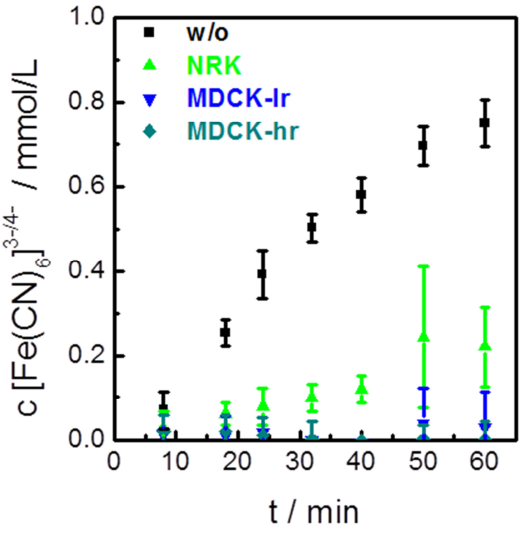

Fig. 6.11: Cell-free (■ w/o) and cell-covered filter inserts (▲ NRK, ▼ MDCK-lr, ♦ MDCK-hr) are incubated at t = 0 with a 4 mM solution of $[Fe(CN)_6]^{3-/4-}$. The addition is performed to the apical filter compartment. 100 µL samples are taken from the basal filter compartments to determine the permeation of the tracer compound across the filter inserts (mean ± SDM, n = 3).

time course saturates with a final value of (0.75 ± 0.06) mmol/L. A concentration increase is also clearly detectable for highly permeable NRK cell layers. Due to the reduced slope of the time profile, c($[Fe(CN)_6]^{3-/4-}$) reaches a value of (0.12 ± 0.03) mmol/L at t = 40 min. The concentration in the receiver compartments further increases afterwards and reaches an end value of (0.22 ± 0.09) mmol/L. For both types of MDCK cell layers, the concentration of the tracer compound is hardly detectable. Best estimates for marker concentrations are (0.04 ± 0.08) mmol/L for MDCK-lr cell layers at t = 50 min and to (0.02 ± 0.04) mmol/L for MDCK-hr monolayers at t = 18 min.

These data serve as basis for the calculation of cell-specific apparent permeability coefficients according to eq. 3.27 (theoretical section). As mentioned in the previous section, P_{app} calculation strictly followed all requirements of the theoretical protocol (e.g. *sink-conditions*, see chapter 3.2.2). The apparent permeability coefficient of cell-free filter membranes is calculated to (76 ± 10)·10^{-6} cm/s. In presence of a confluent monolayer of NRK cells, P_{app} is (19 ± 8)·10^{-6} cm/s. A value of (1 ± 3)·10^{-6} cm/s is calculated for both MDCK subtypes. Permeable NRK monolayers form very weak barriers (high P_{app}) whereas monolayers of MDCK cells are regarded as moderately (MDCK-lr) or tight epithelium (MDCK-hr, low P_{app}).

A comparison between optically and electrochemically derived P_{app} values for MDCK cells shows that optically determined values are in the same order of magnitude but show a high variance. Although the concentration of the probe is four times higher in the optical approach, the sensitivity of the absorbance measurement is not good enough to resolve very small amounts of tracer substance sufficiently well. In addition, optical determination of permeability coefficients results in integrated values and, hence, can not resolve local heterogeneities in transcellular tracer permeation. Another major drawback is obvious when comparing the experimental procedure of both assays. Whereas the impedance-based readout is automated and can be fine-tuned in its temporal resolution, the optical measurement is time-consuming and needs manual operation.

Tab. 6.6: Apparent permeability coefficients (P_{app} in 10^{-6} cm/s) calculated for cell-free (w/o) and cell-covered (NRK, MDCK-lr and MDCK-hr) filter inserts (mean ± SDM, n = 3).

cell line	P_{app} / 10^{-6} cm/s
cell-free	76 ± 10
NRK	19 ± 8
MDCK-lr	1 ± 3
MDCK-hr	1 ± 3

6.4 Summary and outlook

The transepithelial electrical resistance (TEER) is often determined to ensure cellular barrier integrity prior to *in vitro* permeability assays (parameter: P_{app}). The second project in this thesis introduced an impedance-based approach for combined recordings of substrate and ion permeation across confluent epithelial barriers. A simultaneous and automated permeability monitoring of monolayer resistance towards ions (TEER) and tracer substance (P_{app}) was enabled by using a redox active compound ($[Fe(CN)_6]^{3-/4-}$). Additionally, the new device offers the possibility to extract spatially resolved permeability coefficients (P_{app}) from the time courses of individual electrodes spread on the bottom of the basal compartment. Several sensing electrodes are arranged underneath the cell-covered filter support to detect local heterogeneities in epithelial barrier function or even defect areas within the confluent cell layer.

So far, the impedance-based detection set-up relies on the application of redox mediators as tracer compounds. Ferrocene, $[Ru(bpy)_3]^{3+/2+}$ or even NAD^+/NADH are possible tracer candidates besides $[Fe(CN)_6]^{3-/4-}$, when used in cytocompatible concentrations. Temporal and spatial resolution of the device can be further improved by modifying the software which controls the impedance analyzer and the integration of additional detection electrodes. Furthermore, the new device might be a useful tool to discriminate between transcellular and paracellular resistance similar to the two-path impedance spectroscopy technique (Krug et al. 2009b) but without the necessity of sample collection and coupled tracer detection.

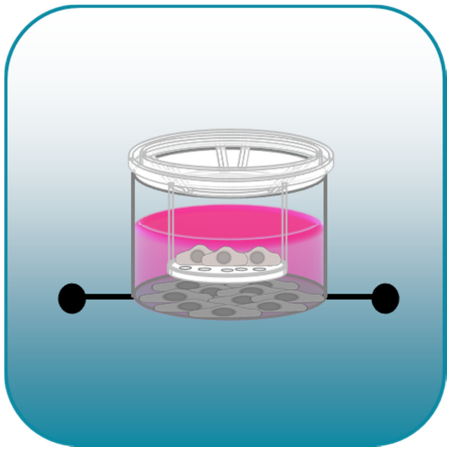

7 Monitoring the permeation of endogenous molecules via whole-cell impedance-based biosensors

So far, standardized *in vitro* transcellular permeability assays require a labeled tracer molecule. Fluorescent probes are often preferred over radiolabeled marker compounds to reduce technical efforts and safety precautions. However, results obtained *in vitro* must be interpreted with caution since the covalently coupled fluorescent label might alter the physicochemical properties of the tracer. The use of unlabeled compounds is preferable but its permeation across a cell layer can only be analyzed by using complex detection techniques like liquid chromatography. It was the aim of the project described in this section to overcome the limitations imposed by the need of labeled compounds and/or subsequent detection steps.

The assay format described here utilizes an impedance-based readout to detect the permeation of endogenous tracers across confluent cell layers without any need for chemical analysis. A sensor cell layer was cultured in a measurement chamber, which includes integrated and optically transparent ITO electrodes on the bottom. A porous filter insert, which serves as growth substrate for the barrier-froming cell layer, was mounted above the sensor cell layer. Label-free detection of different unlabeled ligands (tracers), penetrating through intact cellular barriers, was enabled by using adherently growing cell types as sensor cells which endogenously express G-protein coupled receptors (GPCRs) on the cell surface. Since

this qualitative detection principle is based on fast ligand-receptor interactions at the sensor cell surface, the GPCR superfamily represents ideal target candidates (Katritch et al. 2013, Stevens et al. 2013). Membrane-bound GPCRs respond to a variety of extracellular messengers like biogenic amines, lipids as well as peptides and nucleic acid derivatives (Jacoby et al. 2006), thereby transmitting signals across the cell membrane. Moreover, extracellular stimulation of GPCRs can lead to alterations of the actin cytoskeleton which results in cell shape changes or modified cell adhesion (Cotton and Claing 2009). Impedance-based transducers are sensitive to these morphological changes and were used before to study GPCR activation (Ciambrone et al. 2004, Yu et al. 2006, Scott and Peters 2010, Lieb et al. 2016).

7.1 U-373 MG cells as sensory element

Human U-373 MG glioblastoma cells endogenously express the histamine sensitive H_1 receptor (H_1R) which belongs to the class A (rhodopsin-like family) of GPCRs (Horn et al. 2003). Histamine is a biogenic amine, which is derived in the humane body by decarboxylation of L-histidine. Under physiological conditions, the amine is present as monocation and exists in two tautomeric forms. H_1R activation of U-373 MG cells caused by exposure to the agonist histamine results in an increase of intracellular calcium and inositol-1,4,5-triphosphate concentration (Young et al. 1998, Barajas et al. 2008, Seifert et al. 2013). Impedance measurements on U-373 MG cells resolved a characteristic and concentration-dependent response pattern for histamine induced GPCR activation (Lieb et al. 2016).

7.1.1 Impact of histamine on epithelial barrier function

Histamine diffusion across confluent cell layers can be monitored via impedance measurements on U-373 MG cells. Here, the receptor activation serves as detection system only. The focus lies on the transcellular permeation of the receptor ligand. The impedance-based readout of the sensor cell layer is used to receive qualitative information about the permeability of the tracer compound and to characterize the cellular barrier with respect to its tightness towards the tracer. In order to use the histamine-H_1R-system as detection method, potential barrier altering effects of the tracer / receptor agonist histamine need to be considered for each barrier-forming cell monolayer.

TEER measurements were performed to guarantee barrier integrity of different cell types during exposure to high histamine concentrations (Fig. 7.1). High agonist concentrations are experimentally needed here, since the ligand gets diluted by a factor of five due to the large basal compartment volume in which the sensor cells are cultured (V_{apical} = 0.5 mL, V_{basal} = 2.0 mL). The TEER of highly permeable NRK monolayers increases about 29 % from (6.8 ± 0.4) Ωcm^2 to (8.8 ± 0.3) Ωcm^2 after the addition of a solution including 100 µM histamine to the apical filter compartment. A minor and transient resistance decrease form (63.3 ± 2.4) Ωcm^2 to (56.3 ± 4.8) Ωcm^2 is observed for MDCK-lr cells directly after histamine addition. Tight epithelial barriers (MDCK-hr) show a transient decrease in resistance that recovers and eventually overshoots baseline levels of (1377 ± 31) Ωcm^2 (t = 0 min) at the end of the measurement period ((1688 ± 11) Ωcm^2 at t = 48 min).

During histamine exposure, the transcellular resistance monitored here agrees very well with the reported order of magnitude for all three cell types (Tab. 5.5). Effects of histamine exposure to confluent layers of NRK or MDCK cells have not been described so far. However, histamine is reported to act as mediator for barrier function of other epithelia, like human airway epithelia or nasal epithelial cells (Takeuchi et al. 2001, Zabner et al. 2003, Jutel et al. 2009). Since addition of histamine to the apical cell compartment causes minimal and insignificant alterations in barrier function, histamine is regarded as a suitable penetration marker for further experiments.

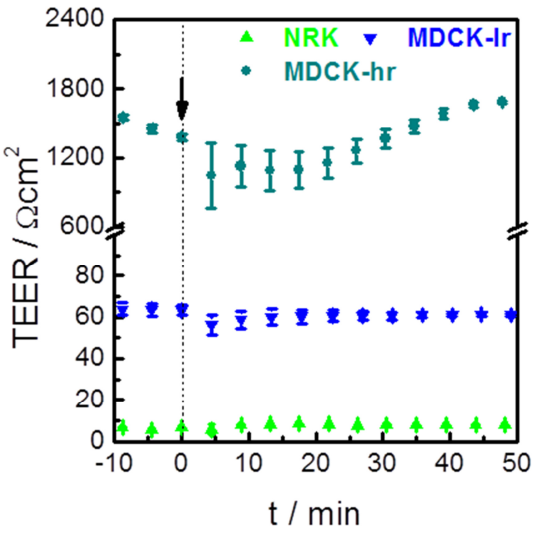

Fig. 7.1: Time course of the transepithelial electrical resistance (TEER) after apical addition of 100 µM histamine to confluent monolayers of different cell types (▲ NRK, ▼ MDCK-lr; ● MDCK-hr; mean ± SE, n = 3).

7.1.2 Monitoring histamine diffusion across barrier forming cell layers

U-373 MG sensor cells were cultured directly on optically transparent ITO electrodes on the bottom of the measurement chamber which includes a small circular working electrode and a large counter electrode (Fig. 4.5). ITO was preferred over gold as electrode material since the oxide can be deposited as conducting film which is optically transparent and hence, best suited for microscopic observation of the cultured cell layers. By comparing impedance spectra of cell-free and cell-covered ITO-electrodes (appendix: Fig. 12.13) a sampling frequency of 25 kHz was selected for all measurements. Different cell monolayers were grown to confluence on permeable filter inserts and placed above the sensor cell layer. Control experiments were performed by replacing the buffer in the apical filter compartment (Fig. 7.2 A). Normalized impedance time courses, recorded for U-373 MG-covered electrodes in the basolateral filter compartment, show no significant response under control conditions. Regardless whether a confluent cell layer is present above the sensor cells or not, a minor impedance increase of less than 4 % is detectable directly after buffer replacement. The signals decrease with time and reaches stable values after around 15 min. Hence, the replacement of the agonist-free apical filter volume causes no significant signal of the sensor cell layer in the basolateral filter compartment.

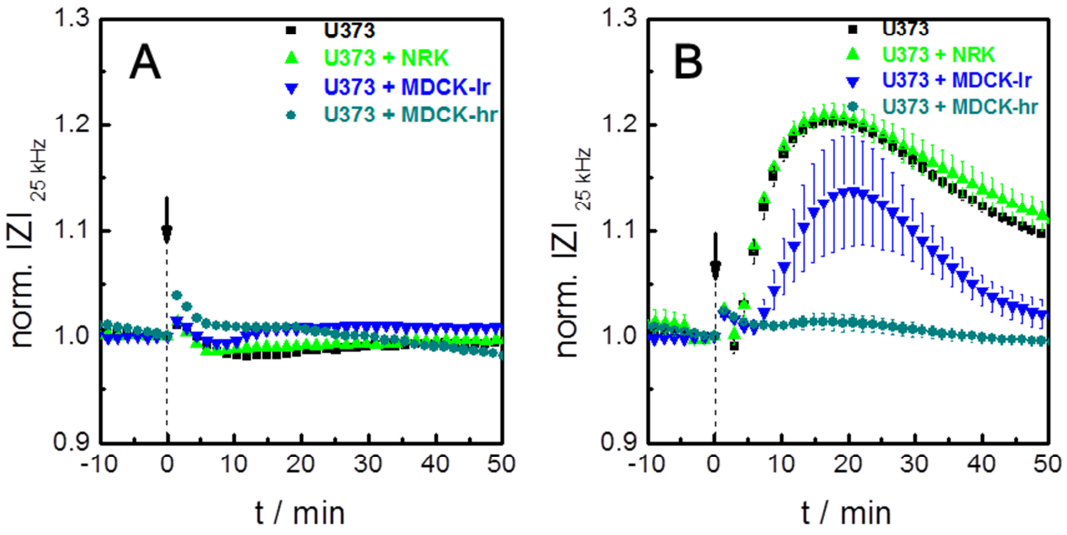

Fig. 7.2: Time course of the normalized impedance magnitude (norm. *IZI*) recorded at a frequency of 25 kHz for U-373 MG cells cultured on ITO-electrodes. The filter inserts which were mounted above the sensor cell layers were either kept cell-free or covered by a confluent cell layer of different types (▲ + NRK, ▼ + MDCK-lr; ● + MDCK-hr). **A** Histamine-free buffer was added at t = 0 min to the apical filter compartment. **B** The buffer in the apical filter compartment is replaced by a second buffer containing 100 µM histamine (mean ± SE, n = 4).

Fig. 7.2 B shows the time course of norm. *IZI* when histamine containing solutions (100 μM) were added to the apical filter compartments. U-373 MG cells respond directly after agonist addition to cell-free or NRK-covered filter inserts. Almost identical impedance patterns are observed. A minimal increase of (103.6 ± 0.1) % is monitored at t = 1.5 min. 90 seconds later, the impedance drops to a value of (100.2 ± 0.1) % for NRK-covered membranes and to (99.0 ± 0.6) % for cell-free filter devices.

For both conditions, the initial impedance dip is followed by a fast increase until a maximum value of (121 ± 1) % is reached at t = 18 min after histamine is added to the apical compartment. At the end of the measurement, normalized impedance values between (109.3 ± 0.01) % and (111.0 ± 0.01) % are obtained. No impedance decrease is monitored for MDCK-covered filter inserts at the beginning of the experiments. U-373 MG cells respond to agonist addition to the apical compartment after 7 min when MDCK-lr cells are present on the filter membrane. The signal rise is less pronounced than observed for cell-free and NRK-covered filter inserts and reaches a maximum of (114 ± 5) % at t = 20 min. The impedance decreases to final values of (102 ± 1) % at the end of the experiment. When MDCK-hr cell layers are placed above the sensor cell layer, only unspecific changes of the impedance signal are monitored, similar to the time course observed during control experiments (Fig. 7.2 A).

Similar and concentration-dependent impedance patterns were reported by Lieb et al. (2016). The authors found initial impedance dips for agonist concentrations ≥ 0.3 μM and a pronounced peak after around 15 min of U-373 MG stimulation with histamine. In addition, impedance values stayed significantly increased at the end of the measurement in comparison to baseline levels. The impedance patterns presented here are similar. Peak appearance is delayed here for around 3 - 5 min compared to reported data since the agonist is not added directly to the sensor cells. After histamine addition to the upper filter compartment, agonist diffusion towards the sensor cell layer is hindered by confluent cell monolayers. The impedance patterns allow a rough estimate of cellular barrier function of the monolayers under study. Leaky NRK cells do not act as effective diffusion barrier and hence, no differentiation between cell-free and NRK-covered filter conditions is possible within the first 30 min of stimulation. Apparently, the initial impedance dip found here is related to the amount of agonist since it is only found for sudden and high histamine concentrations (Lieb et al. 2016). MDCK-lr cell layers form moderate tight cell-cell contacts which hinder the diffusion

of the receptor agonist into the lower filter compartment. Thus, a retarded and less pronounced impedance maximum is detectable. The fact that no response to histamine addition to the upper compartment was found in presence of MDCK-hr monolayers is related to the tightness of this epithelium. Confluent monolayers of MDCK-hr act as highly effective diffusion barrier to histamine and prohibit agonist diffusion to the detection side.

In order to confirm that the observed signal is indeed related to H_1R activation by stimulation with its agonist histamine, the above described experiments were repeated in presence of an

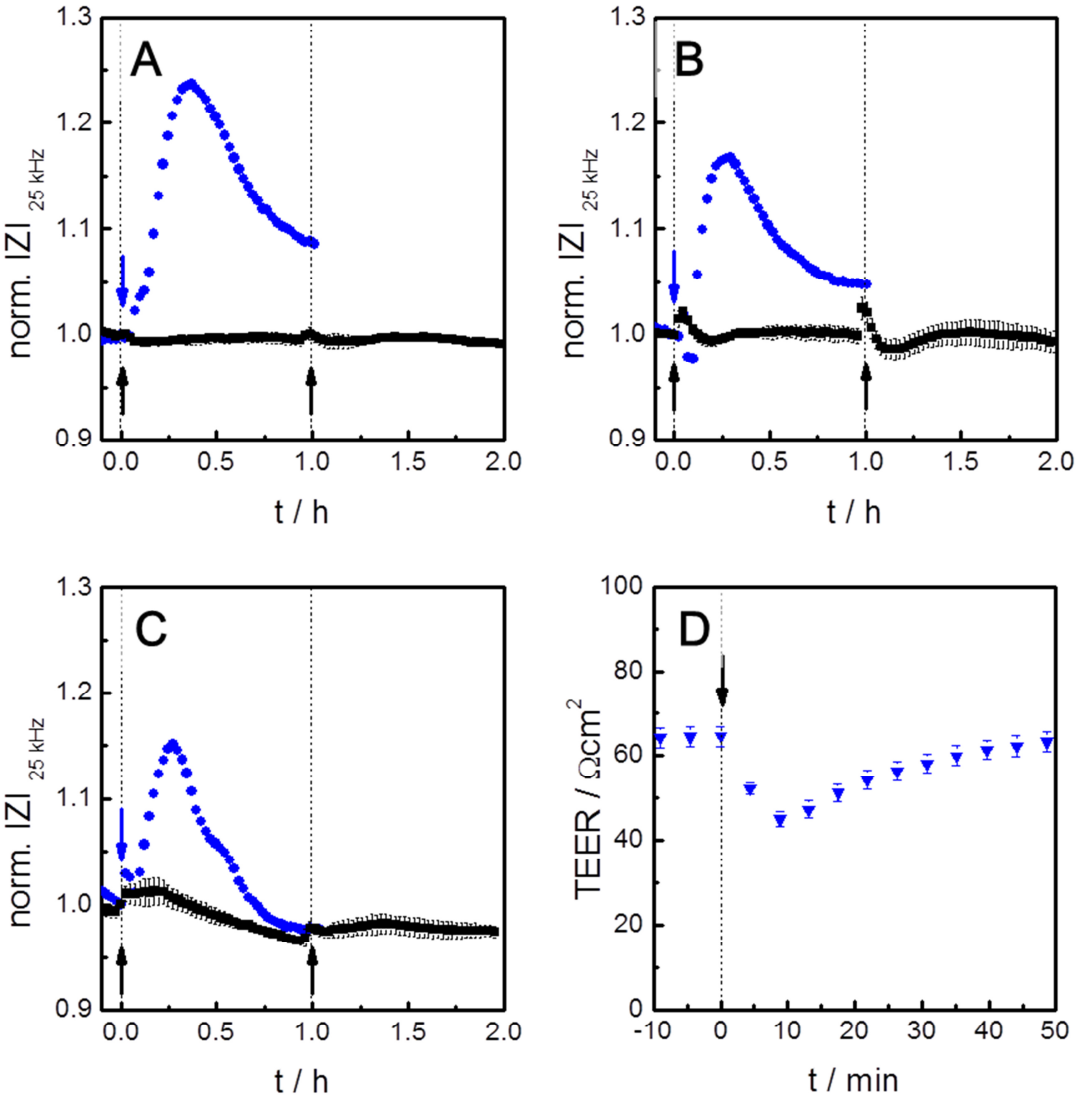

Fig. 7.3: Typical time course of the normalized impedance magnitude at a frequency of 25 kHz for U-373 MG cells cultured on ITO-electrodes. At t = 0 h, either histamine (100 µM, ↓, ●) or mepyramine (5 µM, ↑, ■) was added to the upper filter compartment. At t = 1 h, 100 µM histamine was added to the mepyramine preincubated cells (↑, ■, mean ± SE, n = 3). The filter membranes were cell-free (**A**) or covered by a confluent layer of NRK cells (**B**) and MDCK-Ir cells (**C**). **D** TEER progression for MDCK-Ir cells upon addition of 5 µM mepyramine to the apical membrane side (mean ± SE, n = 4).

H_1R antagonist. For this purpose, the competitive H_1R antagonist mepyramine (Pyrrilamin®) was used (Hill 1990, van der Goot and Timmerman 2000). Antagonist addition (5 μM) was performed via the apical filter compartments one hour prior to histamine stimulation since TEER measurements showed only a transient and minor resistance decrease (Fig. 7.3 D). Mepyramine-free control experiments were performed simultaneously to confirm the activity of the target receptor (Fig. 7.3 A - C: ● blue symbols). The addition of mepyramine (t = 0 h) and the subsequent stimulation with histamine (t = 1 h) cause no significant alteration in the observed impedance signal for set-ups including cell-free filter inserts (Fig. 7.3 A). In case NRK-covered filter membranes are located above the sensor cells, exposure to mepyramine leads to a minor impedance increase (~ 2 %) before baseline levels are again reached at t = 20 min (Fig. 7.3 B). The subsequent addition of histamine to the mepyramine containing buffer at t = 1 h shows a similar signal pattern. Experiments performed in presence of confluent MDCK-lr cell layers are displayed in Fig. 7.3 C. U-373 MG response to mepyramine shows an impedance increase of around 1 % (t = 0 h). The signal stays stable until t = 15 min before a constant decrease to (96.6 ± 0.4) % is observed. The addition of histamine one hour after antagonist exposure causes a minor signal increase to (97.7 ± 0.5) % which stays constant in the following 60 min. Measurements including MDCK-hr monolayers were not performed, since no response of U-373 MG cells upon exposure to histamine was detected before (Fig. 7.2 B).

Whereas all control experiments proved that the endogenous histamine H_1 receptor is active, the characteristic signal pattern in the impedance time course was absent when mepyramine was added to the apical filter compartment first. Hence, it is likely that mepyramine can penetrate across confluent layers of NRK and MDCK cells to serve as H_1 receptor antagonist at the surface of the sensor cells. These findings confirm that the sensor cell layer response is caused by the presence of the specific receptor agonist in the basal compartment only. Detection time as well as peak height of the characteristic impedance pattern are influenced by the cellular diffusion barrier which is located above the sensor cells. The retarded occurrence of the impedance signal can be directly related to an increase of cellular barrier function from NRK to MDCK monolayers.

7.1.3 Permeability coefficients of H_1R ligands

Substrate (H_1R ligands) and cell type specific permeability coefficients can be determined by permeation measurements (chapter 3.2.1) to obtain time-dependent concentration profiles. The permeation of radiolabeled histamine or mepyramine across cell-covered filter inserts is therefore measured over time by taking several buffer samples from the receiver compartment.

The diffusion of radiolabeled histamine across cell-free and cell-covered filter inserts was followed over a period of 60 min. The time-dependent increase of histamine in the receiver compartment is shown in Fig. 7.4 A. A rapid and linear increase in tracer concentration is detectable within the first ten minutes for cell-free filter inserts. Subsequently, the slope of the concentration profile decreases with time. A histamine concentration of (15.5 ± 0.5) μM is reached at the end of the measurement period. Histamine accumulation in the receiver compartment is significantly decreased in presence of NRK-covered filter inserts. A linear increase is measured over the entire time scale. At t = 60 min, histamine concentration is determined to (6.1 ± 0.2) μM in the basal receiver compartment.

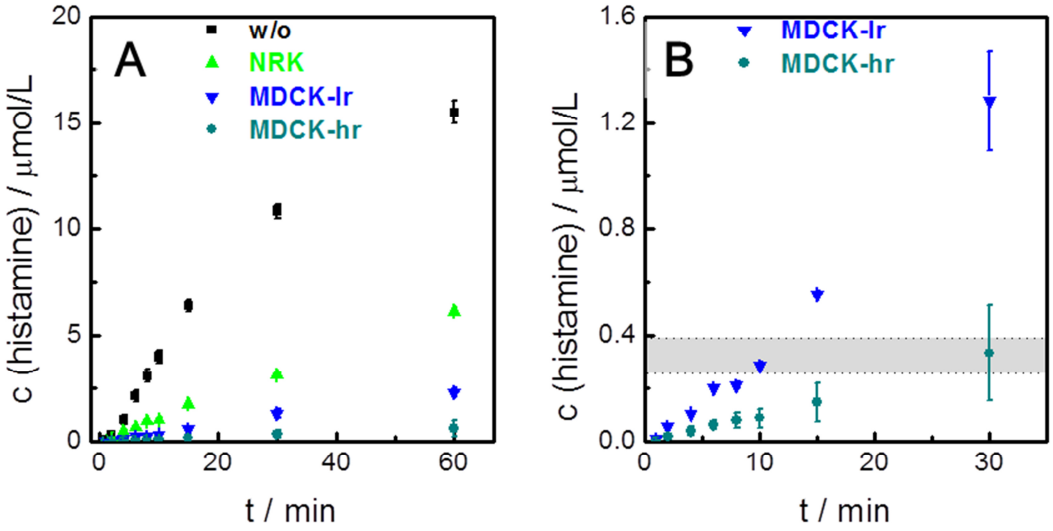

Fig. 7.4: A: Cell-free (■ w/o) and cell-covered filter insert (▲ NRK, ▼ MDCK-lr, ● MDCK-hr) are incubated at t = 0 with a 100 μM solution of radiolabeled histamine (mean ± SDM, n = 3*). The addition is performed to the apical filter compartment. 100 μL samples are taken from the basal filter compartments to determine the tracer concentration over time. **B** Same set of data as shown in **A** focused on MDCK experiments. The grey area visualizes the EC_{50} value for U-373 MG stimulation with histamine determined by Lieb et al. (2016, EC_{50} = 0.31 ± 0.06 μM).

* MDCK-lr (n = 2): Although equal TEER values were determined prior to the permeability assay, one of three individual filter insert showed significantly increased but highly variable basal tracer concentrations which were up to 18 time higher compared to the other inserts. Therefore, data from this insert were neglected here. Graphs including all MDCK-lr inserts are displayed in the supporting information (appendix: Fig. 12.14).

A linear increase of histamine is also visible when MDCK cells are cultured on the porous filter membrane (Fig. 7.4 B). 60 minutes after addition of the radiolabeled compound to the apical filter compartment, a concentration of (2.3 ± 0.2) μM is detected in the compartment underneath MDCK-lr monolayers. The concentration of histamine is reduced to (0.6 ± 0.4) μM at t = 60 min for MDCK-hr cells.

The time-dependent histamine increase in the receiver compartment correlates to the reported properties in cellular barrier function for the three cell types. Histamine diffusion decreases with the increase in barrier function from highly permeable NRK cells over leaky (moderately tight) MDCK-lr monolayers to tight epithelial sheets formed by MDCK-hr cells. Moreover, the concentration of histamine is found to be below the reported EC_{50} value of (0.31 ± 0.06) μM for U-373 MG stimulation within the first 5 to 10 min only for confluent MDCK cell layers (grey area in Fig. 7.4 B, Lieb et al. 2016). These findings explain the delayed U-373 MG response to histamine which was observed in the impedance-based permeation studies on MDCK-lr cells (Fig. 7.2 B). In addition, the insignificant response of U-373 MG sensor cells to histamine exposure on the apical membrane side of MDCK-hr monolayers is explainable by the histamine diffusion profile. Since ligand concentrations above EC_{50} values are reached only after an incubation time of more than 30 min (Fig. 7.4 B), the sensor cells in the impedance-based assays were exposed to very small amounts of histamine during the entire measurement. The persistent exposure to low ligand concentrations is reported to cause receptor desensitization and internalization. Agonist-induced internalization is then followed by either receptor resensitization (recycling process) or by a down regulation of the receptor expression level (Hishinuma and Ogura 2000, Luttrell and Gesty-Palmer 2010, Hishinuma et al. 2012). Hence, receptor desensitization/resensitization due to the sustained exposure to low histamine concentrations might cause the detected lack in U-373 MG response upon H_1R stimulation when MDCK-hr monolayers are used as diffusion barrier.

As mentioned in the theoretical section, the rate by which a tracer compound passes cellular barriers is entitled as apparent permeability coefficient P_{app} (eq. 3.27). The concentration detected in the receiver compartment (Fig. 7.4) is used to calculate the amount of substance diffusing across the cell layer over time ($\Delta n_R(t)/dt$). The calculation of P_{app} strictly followed the protocol described in the theoretical section (chapter 3.2.2). Data which met *sink-conditions* were used to calculate time-dependent changes in n_R (eq. 3.30) using only the linear phase in

the permeation profile (Fig. 3.5). The experimental data of this linear phase were analyzed by a linear regression to obtain the parameter $\Delta n_R(t)/dt$. The obtained parameters (slope and error of slope) were used if the adjusted coefficient of determination (adj. R^2) of the linear regression was beyond 0.9. Furthermore, tracer retention (due to adsorption to the cell membranes, filter insert or plastics) was taken into account (Youdim et al. 2003) by measuring the amount of substance in both compartments at the end of the experiment to quantify the loss of mass ($n_{ret.}$) and to use equation 3.28 (theoretical section) to calculate P_{app}. In addition, the permeability coefficient for a cell-covered filter insert ($P_{app,exp}$) was corrected by the value for cell-free filter inserts ($P_{app,filter}$) according to eq.3.29 to calculate the permeability coefficient P_E.

P_{app} and P_E values are listed in Tab. 7.1 for all conditions. For leaky NRK cell layers, P_E values of $(0.7 \pm 0.3) \cdot 10^{-6}$ cm/s are obtained. Permeability of MDCK-lr monolayers towards histamine is determined to $(0.2 \pm 0.3) \cdot 10^{-6}$ cm/s and to $(0.1 \pm 0.3) \cdot 10^{-6}$ cm/s for MDCK-hr cell layers.

Tab. 7.1: Apparent permeability coefficients of histamine (P_{app} in 10^{-6} cm/s) determined for cell-free and cell-covered filter inserts (mean ± SDM, n = 3). P_{app} values are corrected for histamine permeability across cell-free filter membranes to obtain the permeability coefficient P_E (in 10^{-6} cm/s).

cell line	P_{app} / 10^{-6} cm/s	P_E / 10^{-6} cm/s
cell-free	2.5 ± 0.3	
NRK	0.54 ± 0.01	0.7 ± 0.3
MDCK-lr	0.184 ± 0.005	0.2 ± 0.3
MDCK-hr	0.06 ± 0.02	0.1 ± 0.3

A variety of permeability coefficients was reported for MDCK cells by Irvine et al. in 1999. However, histamine is not among the tracer compounds. The focus of ongoing research is adressed on the effect of histamine towards different cellular barrier systems but not on its permeation (Abbott 2000, Takeuchi et al. 2001, Zabner et al. 2003, Booth and Kim 2012, Bischoff et al. 2016). Although there is a lack of comparable data, the trends in histamine permeability reflect the properties of the cell layers under study to act as diffusion barrier. The P_E values decrease with increasing barrier function from permeable NRK monolayers to highly resistive MDCK-hr cells.

Similar permeation experiments were also performed with the H_1R antagonist mepyramine for cell-free filter inserts as well as for NRK- and MDCK-lr-covered filters (Fig. 7.5). A linear

increase of mepyramine concentration in the receiver compartment is detectable for all inserts after a lag phase of four minutes. The linear increase of mepyramine concentration in the basal compartments is completed after 15 min. At t = 60 min, an antagonist concentration of (0.74 ± 0.01) μM is found underneath cell-free filter membranes. The detectable concentration of mepyramine is decreased to a value of (0.53 ± 0.03) μM after permeation through NRK cells and to (0.47 ± 0.02) μM in case of MDCK-Ir cell monolayers cultured on the filter membrane.

The time-dependent tracer concentration in the receiver compartment shows rapid mepyramine diffusion across NRK and MDCK-Ir cell layers. TEER measurements indicated a minor decrease in MDCK-Ir barrier function upon addition of mepyramine (Fig. 7.3 D) which probably influences tracer accumulation in the first 30 min of the experiment.

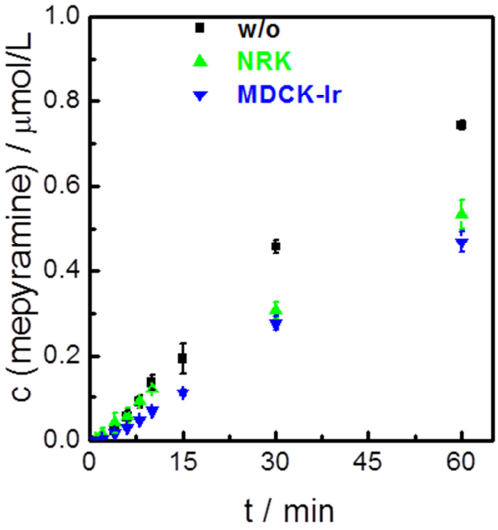

Fig. 7.5: Cell-free (■ w/o) and cell-covered filter inserts (▲ NRK, ▼ MDCK-Ir) are incubated at t = 0 with a 5 μM solution of radiolabeled mepyramine (mean ± SDM, n = 3). The addition is performed to the apical filter compartment. 100 μL samples are taken from the basal filter compartments to determine the tracer concentration over time.

However, data obtained in the linear concentration range (4 – 15 min) were used to calculate the (apparent) permeability coefficients of mepyramine. Values of P_{app} and P_E are listed in Tab. 7.2. Leaky NRK cell layers show a very high P_{app} value of (102 ± 22)·10^{-6} cm/s which is similar to cell-free conditions ((104 ± 13)·10^{-6} cm/s). Permeability of MDCK-Ir monolayers towards mepyramine is determined to (74 ± 6)·10^{-6} cm/s. P_E values are determined according to equation 3.29 but the here presented permeability coefficients for mepyramine are

extremely increased compared to values obtained for histamine (Tab. 7.1). So far, P_{app} or P_E values for mepyramine have not been reported for NRK or MDCK cells but the findings obtained here are in the same order of magnitude as reported for other cell types (Tsinman et al. 2011).

The high rates by which mepyramine passes cellular barriers of NRK or MDCK-Ir monolayers supports the results presented above. Fast mepyramine diffusion into the receiver compartment blocks U-373 MG response to histamine and, hence, the impedance-based readout of H_1 receptor stimulation shows no significant signal pattern (Fig. 7.3 A - C).

Tab. 7.2: Apparent permeability coefficients of mepyramine (P_{app} in 10^{-6} cm/s) determined for cell-free and cell-covered filter inserts (mean ± SDM, n = 3). P_{app} values are corrected for mepyramine permeability across cell-free filter membranes to obtain the permeability coefficient P_E (in 10^{-6} cm/s).

cell line	P_{app} / 10^{-6} cm/s	P_E / 10^{-6} cm/s
cell-free	104 ± 13	
NRK	102 ± 22	5304 ± 25
MDCK-Ir	74 ± 6	257 ± 14

7.2 BAECs as sensory element

In order to prove that a qualitative permeation assay can be performed by the use of an impedance-based detection system, other ligand-receptor couples were investigated. Bovine aortic endothelial cells (BAEC) endogenously express the β_2-adrenergic receptor (β_2AR, class A of GPCRs). Activation of BAEC β_2AR with the synthetic agonist isoprenaline (isoproterenol) leads to adenylyl cyclase stimulation which is accompanied by a subsequent increase in the concentration of the second messenger cAMP (Zink et al. 1993). Impedance measurements on BAECs already illustrated a characteristic response pattern upon exposure to isoprenaline (Wegener et al. 1999) and, hence, BAECs are suited to act as sensor cell layer for the impedance-based monitoring of β_2-agonist diffusion.

Confluent cell layers were cultured similar to U-373 MG cells directly on optically transparent ITO electrodes (Fig. 4.5). Normalized impedance spectra peaked at a frequency of 16 kHz (appendix: Fig. 12.15) which was selected as sampling frequency for all measurements. Different cell monolayers were grown to confluence on permeable filter inserts and placed above the BAEC sensor cell layer prior to agonist addition.

Control experiments were performed by adding isoprenaline-free buffer to the apical filter

compartment (Fig. 7.6 A). As the normalized impedance time courses show, agonist-free buffer caused no significant BAEC response in the basolateral filter compartment. Minor fluctuations were monitored which are in a range of ± 5 % of baseline impedance values. To obtain significant impedance signals in response to β_2AR activation of BAECs, high receptor agonist concentrations are needed for further experiments. For proof-of-concept studies, the applied isoprenaline concentration was set to 100 μM (equilibrium concentration: 20 μM) although EC_{50} values are reported to be around (0.3 ± 0.1) μM (Zink et al. 1993, Wegener et al. 1999, Lieb et al. 2016).

Time courses of the normalized impedance magnitude (norm. *IZI*) after addition of isoprenaline containing buffer to the apical filter side (100 μM) is illustrated in Fig. 7.6 B. Directly after addition of isoprenaline, the normalized impedance signal of BAEC-covered ITO electrodes increases for cell-free and NRK-covered filter inserts to a maximum response of (114.4 ± 0.3) % at t = 10 min. Later the signal slightly decreases to (111.8 ± 0.9) % for cell-free inserts, to (110.2 ± 1.6) % for NRK-covered membranes, and stays at these levels until the end of the observation time. In case MDCK-lr cells were located above the sensor cell layer, the impedance signal shows two maxima. The first peak is recorded at t = 1.5 min which reaches a value of (102.6 ± 0.2) %. This peak is followed by a second increase in the impedance and reaches a maximum of (111.5 ± 1.1) % 13 min after agonist addition. Minor fluctuations are monitored in the following 40 min. Such impedance patterns are not obtained with a confluent monolayer of MDCK-hr cells above the sensor cell layer. 90 s after isoprenaline addition, the normalized impedance peaks at a value of (103.6 ± 0.4) %. This small increase is followed by a decrease back to baseline levels and stays almost constant during the entire measurement period.

Comparing control experiments to the impedance pattern obtained in presence of isoprenaline, the first impedance increase is probably related to the buffer replacement in the apical filter compartment. A rapid onset in the impedance signal to a significant and constant maximum was also reported by Wegener et al. (1999) for the direct exposure of BAECs to isoprenaline. Recent studies performed on BAECs showed a more retarded impedance increase upon addition of isoprenaline (t = 10 min) which is followed by a slight signal decrease (Lieb et al. 2016). However, the time profile of the signal as well as the maximum peak height is influenced by the cellular barrier located above the sensor cells. The retarded appearance of the impedance signal can be directly related to an increase of cellular barrier

function from NRK to MDCK monolayers. Furthermore, no characteristic impedance increase upon agonist stimulation was detected for BAECs in presence of tight MDCK-hr cell layers. Hence, the agonist-receptor system in BAECs (isoprenaline-β_2AR) is suited to serve as qualitative permeation sensor similar to the histamine induced H_1R stimulation in U-373 MG cells.

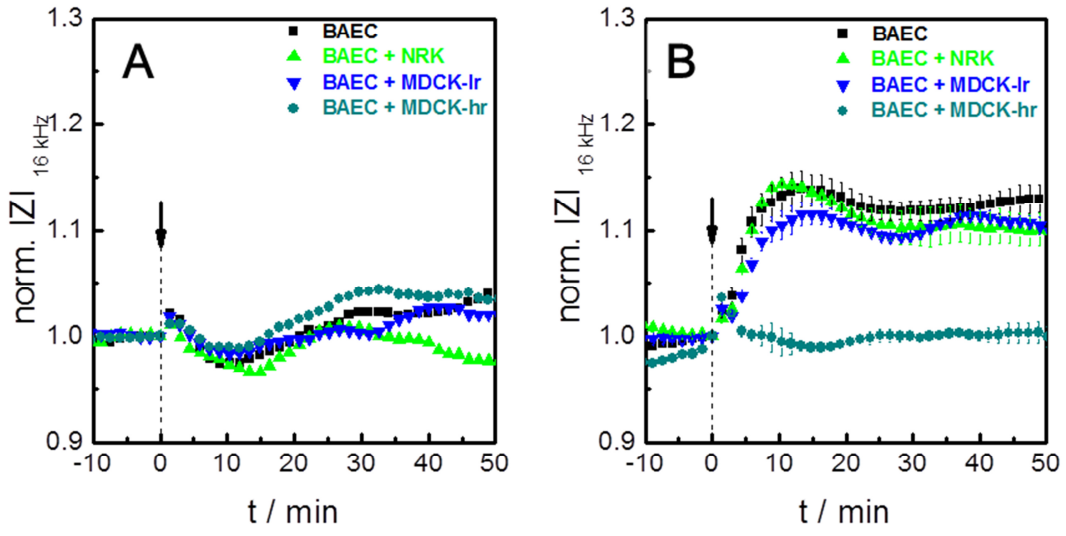

Fig. 7.6: Time course of the normalized impedance magnitude (norm. *IZI*) recorded at a frequency of 16 kHz for BAECs cultured on ITO-electrodes. The filter inserts which were mounted above the sensor cell layers were either kept cell-free or covered by a confluent cell layers of different types (▲ + NRK, ▼ + MDCK-lr; ● + MDCK-hr). **A** Isoprenaline-free buffer was added at t = 0 min to the apical filter compartment. **B** The buffer in the apical filter compartment was replaced by a second buffer containing 100 µM isoprenaline (mean ± SE, n = 3).

7.3 Summary, conclusion and outlook

The assay described here utilizes an impedance-based readout to detect the permeation of unlabeled, endogenous tracers across confluent cell layers without any chemical analysis. Therefore, a sensor cell layer was cultured directly upon transparent ITO electrodes which are integrated into the measurement chamber. Porous filter inserts serve as growth substrates for the cell layer whose barrier function is addressed and were mounted above the sensor cell layer. A label-free and indirect detection of the diffusion of different tracers (ligands) was enabled by using adherently growing cell types as sensor cells which endogenously express G-protein coupled receptors (GPCRs). GPCR agonists were added to the apical filter compartment. Ligand permeation through cellular barriers could be detected in a

semi-quantitative manner due to specific agonist-receptor interactions of the sensor cell layers. The time-dependent impedance pattern upon addition of a certain receptor ligand is directly related to the amount of substance which passes the cellular barrier and, hence, gives information about the permeability of the specific ligand across the cell layers under study.

The assay format presented here can be used to detect the permeation of a variety of other substances (lipids, peptides, nucleic acid derivatives) since endogenous ligands for GPCRs are highly diverse (Jacoby et al. 2006, Katritch et al. 2013). So far, around 40 % of the marketed drugs target the GPCR superfamily (Garland 2013, Stevens et al. 2013). With GPCRs being in the focus of pharmacological research and drug development, also receptor agonist/antagonist uptake and permeability studies are of major interest (Avdeef 2012). The label-free impedance-based permeation assay combines GPCR target screening assays with ligand permeability studies. The permeation monitoring via whole-cell impedance-based biosensors is suitable to serve as a high throughput screening tool since miniaturization, automatization and profiling for characteristic signal patterns is already possible (Fang et al. 2008, Scott and Peters 2010). In addition, TEER measurements of the barrier-forming cell layers could be achieved by integrating a third electrode into the apical filter compartment of the set-up analog to the device described in chapter 5.

8 Impedimetric monitoring of epithelial barrier function: relevance and perspectives

Impedance-based measurements are the most versatile tool to study epithelial or endothelial barrier function *in vitro*. The measurement principle is based on a label-free and non-invasive readout and allows a detailed analysis of adherently growing cells. Solid or porous electrodes or even permeable filter membranes serve as growth substrate for the cell layer under study. Since impedimetric techniques (transfilter resistance measurements, ECIS technique, two-path impedance spectroscopy) provide an outstanding sensitivity to functional changes of cellular barriers, integrated whole-cell measurements offer a high content of information. Among the experimental parameters, the sampling frequency is of major importance. Furthermore, equivalent circuit modelling is used to quantify cell-related parameters like the transepithelial electrical resistance of an epithelium. Impedimetric measurements can be performed in a time-resolved and automated manner which offers the possibility to serve as high throughput screening tool and, hence, are not only applied in basic research but also in pharmaceutical industry. Furthermore, impedance spectroscopy can be combined with other label-free techniques, such as the quartz crystal microbalance (Janshoff et al. 1996) or surface plasmon resonance spectroscopy (Michaelis et al. 2013) to enable a multiparametric assay format. As the technique is label-free, subsequent invasive assays (fluorescence microscopy, Grieshaber et al. 2008) are applicable.

Due to all of these benefits, impedance-based assay techniques already became a potent method to study cell-type specific properties. These assays are used as a simple indicator for the state of confluency of a cell layer or for the quantification of cell-cell and cell-substrate contacts (Wegener et al. 1996a, Wegener et al. 2000, Wegener 2006). Cytotoxicity (Sperber et al. 2016), migration behavior (Keese et al. 2004) or even cellular micromotion (Giaever and Keese 1991, Giaever and Keese 1993) are detectable. In addition, cell differentiation monitoring (Bagnaninchi and Drummond 2011) or cellular response monitoring upon exposure to a variety of different ions, metabolites, second messengers or drug candidates (Wegener et al. 1999, Yu et al. 2006) are routinely performed.

All these aspects are especially important for interfacial tissues. Epithelial or endothelial tissues play a critical role in the maintenance of specific organ functions and homeostasis

(Fink and Delude 2005) and therefore capture an exceptional research interest. Since transport processes across intact barrier-forming cell layers are strictly regulated under physiological conditions (Hillgren et al. 1995, Anderson 2001, Wise 2002, Balimane et al. 2006, Komarova and Malik 2010), alterations in the cellular junctions and the resulting effects upon the permeability properties of interfacial tissues can induce pathological conditions (Davignon and Ganz 2004, Abbott et al. 2006, Davignon and Ganz 2004, Holgate 2007).

The impedance-based assays developed in this thesis enhance the information content of already established measurements not only for separately cultured epithelial monolayers but also for co-cultured cellular barrier systems (chapter 5). Specific electrode designs and assay combinations allow a simultaneous detection of transcellular resistance and tracer permeability of an electrochemically active compound across intact monolayers (chapter 6). Cellular heterogeneities in barrier function can be spatially resolved with a high resolution in time in an automated manner. Moreover, a new assay technique was presented here which is a useful tool to detect the permeation of unlabeled endogenous substrates in a semi-quantitative and label-free manner (chapter 7).

As these assays are based on impedance spectroscopy measurements only, all approaches offer the above mentioned benefits of this label-free technique. Automated and time-resolved analysis of cellular barrier function as well miniaturization are possible.

Impedance-based analysis of different cell types will keep their outstanding position in basic research and expand their impact as highly potent screening tools (Fang et al. 2008, Scott and Peters 2010).

9 Summary

Dynamics and alterations of cellular barriers (epithelial or endothelial tissue) are studied in detail under physiological and pathological conditions *in vitro*. In order to do so, interfacial tissue is commonly cultured on permeable growth substrates to mimic *in vivo* like conditions. Impedimetric techniques (transfilter resistance measurements, electric cell-substrate impedance sensing: ECIS) serve as frequently used tool to monitor cellular barrier function since the readout can be performed in a label-free and time-resolved manner without any harmful side effects. The present study was focused on the development of new impedance-based assay techniques to enhance the information content of measurements performed on epithelial cell monolayers.

One of the projects presented here was targeted on standardized TEER measurements (transepithelial or –endothelial electrical resistance). Usually, TEER serves as a measure for barrier function of filter grown cell monolayers. Since co-cultured *in vitro* models mimic physiological situations far better than experiments on single cell layers, TEER is determined for co-cultured cell layers too. However until today, only integrated signals, recorded for both cell layers cultured on either side of the porous growth substrate, are obtained. Alterations in cellular barrier function can not be attributed to one of both cell populations. In order to overcome these limitations, permeable electrodes were prepared from commercially available filter inserts.by depositing a thin gold film on the back side of the filter membrane. Integrated into the standard two-electrode set-up, the modified device offered the possibility to monitor both co-cultured monolayers separately. As the normal transfilter measurement was still accessible, individual contributions of each cell type could be compared with the integrated signal. The new device was evaluated in cell attachment and spreading studies performed with homogeneous and heterogeneous co-culture models. Additional proof-of-concept studies illustrated that the porous electrodes were capable of monitoring alterations in cellular barrier function for both populations separately. Independent TEER profiles were obtained for co-cultured cell layers in cytoskeleton disassembly/reassembly assays. Furthermore, the electrode design of the device was modified. Dividing the bottom electrode into a small working electrode and a large counter electrode offered the possibility to apply the ECIS principle for cells cultured directly on the bottom of the chamber underneath an epithelial barrier. The extended four-electrode set-up was used to record impedance spectra and to determine all cell-related parameters (TEER, C_{cl}) of co-cultured cell layers on both sides of

the porous electrode and an additional third cell layer simultaneously.

TEER is often determined to ensure cellular barrier integrity prior to other assay techniques like *in vitro* permeability assays. Permeability assays are routinely performed to characterize interfacial tissue by detecting the diffusion of a radio- or fluorescently labeled tracer compound across cell monolayers. The aim of the second project presented here was to design an impedance-based device for combined recordings of substrate and ion permeation across confluent epithelial barriers. The simultaneous and automated permeability monitoring of monolayer resistance towards ions (TEER) and a permeability of a probe (P_{app}) was enabled by using a special electrode layout and a redox active tracer compound ($[Fe(CN)_6]^{3-/4-}$). Two electrodes sandwiching the epithelial cell layer were used to record transcellular resistance while tracer diffusion across different cell monolayers was detected simultaneously by several electrodes, located underneath the filter membrane. The new device was used to calculate individual apparent permeability coefficients (P_{app}) which reflected local heterogeneities in cellular barrier function or defect areas within confluent cell layers. Compared to optical measurements which allow only for integrated permeability determination, the new automated assay technique was found to be superior regarding sensitivity, accuracy and handling.

Standardized *in vitro* cellular permeability assays still require a labeled tracer molecule. Fluorescent-labeling of certain compounds is preferred over radiolabeled markers to reduce safety precautions. However, covalently coupled probes might alter the physicochemical properties of the tracer. Using unlabeled compounds is currently the best strategy for permeability assays but technical efforts are high since subsequent detection by chemical analysis is needed (e.g. liquid chromatography). The third project within this thesis aimed for the development of a new assay strategy which utilizes an impedance-based readout to detect the permeation of unlabeled tracers across confluent cell layers without the need for chemical analysis. Therefore, a culture well with integrated and transparent ITO electrodes was fabricated. With these electrodes, ECIS like measurements were performed on adherently growing cell types (sensor cells) which endogenously express G-protein coupled receptors (GPCRs). GPCR activation in response to the presence of an agonist used as permeability probe was followed via impedance monitoring. Unlabeled agonist permeation through intact cellular barriers was detected in a semi-quantitative manner by specific agonist-receptor interactions on the sensor cell layers in the basal compartment of the

assembled device. For proof-of-concept studies, two agonist-receptor systems were tested here. Characteristic impedance patterns were observed depending on the sensor cell layer and the epithelial barrier under study. The sensor cell response was found to be related to the amount of substance which permeates across the epithelial barrier. The new impedance-based readout detected the permeation of unlabeled endogenous receptor ligands in a reproducible manner. Semi-quantitative information about the permeability of the ligands under study was obtained without any coupled detection step.

10 Zusammenfassung

Zahlreiche Studien befassen sich mit der Charakterisierung und der Dynamik Barriere-bildender Zellschichten (Zellen der Haut, der Darm- oder Gefäßauskleidung). *In vitro* Modelle dienen dabei der detaillierten Untersuchung diverser Grenzflächengeweben unter physiologischen sowie pathologischen Bedingungen. In der Regel werden dafür immortalisierte Zelllinien, seltener auch primär isolierte Zellen, auf permeablen Substraten kultiviert, um deren biologische Anordnung als Grenzfläche zwischen zwei Kompartimenten unterschiedlicher Zusammensetzung nachzuempfinden. Als nicht-invasive Techniken eignen sich impedanzspektroskopische Messmethoden besonders gut zur Untersuchung solcher Zellbarrieren. Widerstandsmessungen an zellbedeckten Filtermembranen können zeitliche Veränderungen der Barrierefunktion wiederspiegeln. Ebenso ist es möglich, adhärente Zellen direkt auf Filmelektroden zu kultivieren und deren Verhalten impedanzespektroskopisch zu analysieren (*electric cell-substrate impedance sensing: ECIS*). Die hier vorliegende Studie widmete sich der Entwicklung neuer impedanzbasierter Testverfahren zur Untersuchung von Epithel- und Endothelzellen.

Eines der hier vorgestellten Projekte befasste sich mit der nicht-invasiven Quantifizierung der Permeabilität Barriere-bildender Zellschichten gegenüber Ionen. Der transepitheliale / transendotheliale elektrische Widerstand (engl.: TEER) wird vorwiegend von zweidimensionalen Zellschichten bestimmt. TEER-Messungen an kokultivierten Zellschichten werden ebenfalls vermehrt durchgeführt, da derartige Modelle den *in vivo* Begebenheiten ähnlicher sind. Jedoch resultieren Widerstandmessungen an Kokulturen lediglich in der Detektion eines integrierten Messsignals. Durch das einseitige Aufbringen eines Goldfilmes auf Filtermembranen wurden hochpermeable Wachstumssubstrate dahingehend funktionalisiert, dass diese selbst als Elektrode dienen. Dadurch wurde es ermöglicht, Zellschichten auf beiden Seiten der Membran unabhängig voneinander impedimetrisch zu beobachten und einer quantitativen Analyse zugänglich zu machen. Davon uneingeschränkt konnten simultan auch klassische Transfiltermessungen durchgeführt werden. Das Konzept der Verwendung von porösen Elektroden als *Transducer* in impedimetrischen und zellbasierten Assays wurde durch Studien zum Adhäsions- und Spreitverhalten von mono- und kokultivierten Zellschichten validiert. Zusätzlich wurde gezeigt, dass permeable Elektroden eine detaillierte Effektanalytik kokultivierter Zellschichten auch unter dem Einfluss

von Modeltoxinen ermöglichen. Für eine darauf aufbauende Anwendung wurde die Messkammer modifiziert. Durch die Separation der in die Messeinheit integrierten Bodenelektrode in zwei Elektroden unterschiedlicher Fläche wurde ein weitere Messmodus im unteren Filterkompartiment generiert (ECIS Modus). Die Verwendung permeabler Filterelektroden ermöglichte bei gleichzeitiger Anwendung des ECIS-Prinzips die simultane, impedimetische Beobachtung und Quantifizierung der Kokultur auf der porösen Filtermembran und einer dritten Zellschicht am Boden der Messkammer.

TEER-Bestimmungen werden routinemäßig durchgeführt um die Integrität diverser Zellschichten für nachgeschaltete Testverfahren zu garantieren. Dabei handelt es sich häufig um Diffusionsmessungen. Grenzflächengewebe wie Epithel- und Endothelzellen kontrollieren die passive Diffusion bestimmter Komponenten. Bei Diffusionsmessungen werden sowohl radiomarkierte als auch fluoreszierende Sondenmoleküle eingesetzt, welche die technischen Anforderungen solcher Methoden enorm erhöhen. Das zweite hier beschriebene Projekt befasste sich mit der kombinierten Detektion des transzellulären elektrischen Widerstandes einer Zellschicht und der Verfolgung der transzellulären Diffusion spezieller, redox-aktiver Sonden. Eine besondere Elektrodenanordnung ermöglichte die TEER-Bestimmung während gleichzeitig die Permeation der Sonden durch Elektroden unterhalb des porösen Wachstumssubstrates aufgezeichnet wurde. Durch die Integration mehrerer kleiner Detektionspunkte konnte gezeigt werden, dass der Nachweis kleiner Defektstellen innerhalb der Zellschicht möglich ist. Die automatisierte und zeitaufgelöste Detektion der Sonden ermöglichte die Berechnung lokaler, apparenter Permeabilitätskoeffizienten. Dadurch gelang es lokale Schwankungen der Barrierefunktion konfluenter Zellschichten zu quantifizieren. Ein Vergleich mit optischen Detektionsmethoden verdeutlichte die Vorteile impedanzbasierter Permeabilitätsmessungen hinsichtlich Sensitivität, lokaler und zeitlicher Auflösung sowie experimenteller Durchführung.

Die Notwendigkeit markierter Sondenmoleküle lässt sich bei Permeabilitätsstudien nur durch nachgeschaltete Detektionsverfahren umgehen. Um die physikochemischen Eigenschaften diverser Verbindungen nicht durch die kovalente Kopplung an eine Fluorsezenssonde zu beeinflussen können unmarkierte Substanzen beispielsweise durch chromatographische Verfahren nachgewiesen werden. Um den technischen Aufwand solcher Tests zu verringern wurde im dritten hier beschriebenen Projekt eine impedanzbasierte Technik entwickelt, die es erlaubt das Permeationsverhalten unmarkierter Substanzen zu untersuchen. Auf der

Grundlage des ECIS-Prinzips wurden transparente Elektroden angefertigt. Als Elektrodenmaterial wurde dabei Indiumzinnoxid (ITO) verwendet. Derartige Elektroden wurden in Kulturgefäße integriert und dienten so als Substrat für adhärent wachsende Zellen. Für diesen impedanzbasierten Assay wurden beispielhaft Sensorzellen verwendet, welche G-Protein-gekoppelte Rezeptoren (GPCRs) endogen exprimieren. Über den Sensorzellen wurden permeable Filtermembranen platziert, auf welchen unterschiedliche, Barriere-bildende Zellschichten kultiviert wurden. Der Messaufbau bestand somit aus einem 2-Kammern-System. Die Diffusion unmarkierter Rezeptor-Agonisten von der oberen Kammer in das nachgeschaltete Kompartiment hin zur Sensorzellschicht wurde daher durch eine zelluläre Barriere beeinflusst. Es konnte erfolgreich gezeigt werden dass sowohl das Ansprechverhalten der verwendeten Sensorzellen, als auch die Intensität charakteristischer Signalmuster in den hier untersuchten Ligand-Rezeptor-Systemen mit der Agonistkonzentration im unteren Kompartiment korrelierte. Anhand dieser Impedanzmuster konnten die Barriereeigenschaften der getesteten Grenzflächengewebe semi-quantitativ eingeordnet werden. Der hier vorgestellte impedanzbasierte Assay ermöglicht daher die Untersuchung unmarkierter, endogener Substanzen im Hinblick auf ihr Permeabilitätsverhalten.

11 References

A

Abbott, NJ, (2000) Inflammatory Mediators and Modulation of Blood–Brain Barrier Permeability. *Cellular and Molecular Neurobiology* **20** (2): 131-147.

Abbott, NJ, Ronnback, L and Hansson, E, (2006) Astrocyte-endothelial interactions at the blood-brain barrier. *Nat Rev Neurosci* **7** (1): 41-53.

Al-Amoudi, A, Díez, DC, Betts, MJ and Frangakis, AS, (2007) The molecular architecture of cadherins in native epidermal desmosomes. *Nature* **450** (7171): 832-837.

Alberts, B, Johnson, A, Lewis, J, Morgan, D, Raff, M, Roberts, K and Walter, P, (2015) Molecular Biology of the Cell, Garland Science.

Alpha, YS, Brieher, WM and Gumbiner, BM, (1997) Molecular and functional analysis of cadherin-based adherens junctions. *Annual review of cell and developmental biology* **13** (1): 119-146.

Ambati, J, Canakis, CS, Miller, JW, Gragoudas, ES, Edwards, Al, Weissgold, DJ, Kim, I, Delori, FoC and Adamis, AP, (2000) Diffusion of High Molecular Weight Compounds through Sclera. *Investigative Ophthalmology & Visual Science* **41** (5): 1181-1185.

Anderson, JM, (2001) Molecular structure of tight junctions and their role in epithelial transport. *Physiology* **16** (3): 126-130.

Armstrong, JK, Wenby, RB, Meiselman, HJ and Fisher, TC, (2004) The Hydrodynamic Radii of Macromolecules and Their Effect on Red Blood Cell Aggregation. *Biophysical Journal* **87** (6): 4259-4270.

Avdeef, A, (2012) Absorption and drug development: solubility, permeability, and charge state, John Wiley & Sons.

B

Bagnaninchi, PO and Drummond, N, (2011) Real-time label-free monitoring of adipose-derived stem cell differentiation with electric cell-substrate impedance sensing. *Proceedings of the National Academy of Sciences* **108** (16): 6462-6467.

Balcarova-Staender, J, Pfeiffer, SE, Fuller, SD and Simons, K, (1984) Development of Cell-Surface Polarity in the Epithelial Madin-Darby Canine Kidney (Mdck) Cell-Line. *Embo Journal* **3** (11): 2687-2694.

Balimane, PV, Han, Y-H and Chong, S, (2006) Current industrial practices of assessing permeability and P-glycoprotein interaction. *The AAPS journal* **8** (1): E1-E13.

Ballard, ST, Hunter, JH and Taylor, AE, (1995) Regulation of Tight-Junction Permeability During Nutrient Absorption Across the Intestinal Epithelium. *Annual Review of Nutrition* **15** (1): 35-55.

Barajas, M, Andrade, A, Hernandez-Hernandez, O, Felix, R and Arias-Montaño, J-A, (2008) Histamine-induced Ca2+ entry in human astrocytoma U373 MG cells: Evidence for involvement of store-operated channels. *Journal of Neuroscience Research* **86** (15): 3456-3468.

Bard, AJ and Faulkner, LR, (2001) Electrochemical Methods: Fundamentals and Applications, John Wiley & Sons, Inc.

Baumgarten, C and Feher, J, (2001) Osmosis and the regulation of cell volume. *Cell Physiology Sourcebook: A Molecular Approach* **3**

Benson, K, Cramer, S and Galla, H-J, (2013) Impedance-based cell monitoring: barrier properties and beyond. *Fluids and Barriers of the CNS* **10** (1): 5.

Bergner, S, Wegener, J and Matysik, F-M, (2012) Monitoring passive transport of redox mediators across a confluent cell monolayer with single-cell resolution by means of scanning electrochemical microscopy. *Analytical Methods* **4** (3): 623-629.

Bevington, P and Robinson, DK, (1969) Data reduction and error analysis for the physical sciences, Kent A. Peterson.

Beyer, EC, Paul, DL and Goodenough, DA, (1990) Connexin family of gap junction proteins. *Journal of Membrane Biology* **116** (3): 187-194.

Bigner, DD, Bigner, SH, Ponten, J, Westermark, B, Mahaley, MS, Ruoslahti, E, Herschman, H, Eng, LF and Wikstrand, CJ, (1981) Heterogeneity of Genotypic and Phenotypic Characteristics of 15 Permanent Cell-Lines Derived from Human Gliomas. *Journal of Neuropathology and Experimental Neurology* **40** (3): 201-229.

Bijvelds, M, Kolar, Z, Bonga, S and Flik, G, (1997) Mg2+ transport in plasma membrane vesicles of renal epithelium of the Mozambique tilapia (Oreochromis mossambicus). *Journal of experimental biology* **200** (13): 1931-1939.

Bischoff, I, Hornburger, MC, Mayer, BA, Beyerle, A, Wegener, J and Fürst, R, (2016) Pitfalls in assessing microvascular endothelial barrier function: impedance-based devices versus the classic macromolecular tracer assay. *Scientific Reports* **6** 23671.

Booth, R and Kim, H, (2012) Characterization of a microfluidic in vitro model of the blood-brain barrier (muBBB). *Lab Chip* **12** (10): 1784-92.

Borradori, L and Sonnenberg, A, (1996) Hemidesmosomes: roles in adhesion, signaling and human diseases. *Current opinion in cell biology* **8** (5): 647-656.

Burridge, K, Fath, K, Kelly, T, Nuckolls, G and Turner, C, (1988) Focal adhesions: transmembrane junctions between the extracellular matrix and the cytoskeleton. *Annual review of cell biology* **4** (1): 487-525.

Butor, C and Davoust, J, (1992) Apical to basolateral surface area ratio and polarity of MDCK cells grown on different supports. *Experimental Cell Research* **203** (1): 115-127.

C

Carpi-Medina, P and Whittembury, G, (1988) Comparison of transcellular and transepithelial water osmotic permeabilities (Pos) in the isolated proximal straight tubule (PST) of the rabbit kidney. *Pflügers Archiv* **412** (1): 66-74.

Carr, G, Wright, JA and Simmons, NL, (2010) Epithelial barrier resistance is increased by the divalent cation zinc in cultured MDCKII epithelial monolayers. *J Membr Biol* **237** (2-3): 115-23.

Chen, X and Macara, IG, (2005) Par-3 controls tight junction assembly through the Rac exchange factor Tiam1. *Nat Cell Biol* **7** (3): 262-269.

Ciambrone, GJ, Liu, VF, Lin, DC, McGuinness, RP, Leung, GK and Pitchford, S, (2004) Cellular dielectric spectroscopy: a powerful new approach to label-free cellular analysis. *Journal of biomolecular screening* **9** (6): 467-480.

Citi, S, Sabanay, H, Jakes, R, Geiger, B and Kendrick-Jones, J, (1988) Cingulin, a new peripheral component of tight junctions. *Nature* **333** (6170): 272-276.

Claude, P, (1978) Morphological factors influencing transepithelial permeability: A model for the resistance of thezonula occludens. *J Membr Biol* **39** (2-3): 219-232.

Cohen, AW, Carbajal, JM and Schaeffer, RC, (1999) VEGF stimulates tyrosine phosphorylation of β-catenin and small-pore endothelial barrier dysfunction. *American Journal of Physiology-Heart and Circulatory Physiology* **277** (5): H2038-H2049.

Cole, KS, (1972) Membranes, ions, and impulses: a chapter of classical biophysics, Univ of California Press.

Cotton, M and Claing, A, (2009) G protein-coupled receptors stimulation and the control of cell migration. *Cellular signalling* **21** (7): 1045-1053.

Curry, FR, (1985) Effect of albumin on the structure of the molecular filter at the capillary wall. *Federation Proceedings* **44** (10): 2610-2613.

D

Daniels, JS and Pourmand, N, (2007) Label-Free Impedance Biosensors: Opportunities and Challenges. *Electroanalysis* **19** (12): 1239-1257.

Davignon, J and Ganz, P, (2004) Role of Endothelial Dysfunction in Atherosclerosis. *Circulation* **109** (23 suppl 1): III-27-III-32.

Delarco, JE and Todaro, GJ, (1978) Epithelioid and Fibroblastic Rat-Kidney Cell Clones - Epidermal Growth-Factor (Egf) Receptors and Effect of Mouse Sarcoma-Virus Transformation. *Journal of Cellular Physiology* **94** (3): 335-342.

Dubrovskyi, O, Birukova, AA and Birukov, KG, (2013) Measurement of local permeability at subcellular level in cell models of agonist-and ventilator-induced lung injury. *Laboratory investigation* **93** (2): 254-263.

Dukes, J, Whitley, P and Chalmers, A, (2011) The MDCK variety pack: choosing the right strain. *BMC Cell Biology* **12** (1): 43.

F

Fang, Y, Frutos, AG and Verklereen, R, (2008) Label-free cell-based assays for GPCR screening. *Combinatorial chemistry & high throughput screening* **11** (5): 357-369.

Fanning, AS and Anderson, JM, (2009) Zonula Occludens-1 and -2 Are Cytosolic Scaffolds That Regulate the Assembly of Cellular Junctions. *Annals of the New York Academy of Sciences* **1165** (1): 113-120.

Fink, MP and Delude, RL, (2005) Epithelial Barrier Dysfunction: A Unifying Theme to Explain the Pathogenesis of Multiple Organ Dysfunction at the Cellular Level. *Critical Care Clinics* **21** (2): 177-196.

Fornasiero, F, Park, HG, Holt, JK, Stadermann, M, Grigoropoulos, CP, Noy, A and Bakajin, O, (2008) Ion exclusion by sub-2-nm carbon nanotube pores. *Proceedings of the National Academy of Sciences* **105** (45): 17250-17255.

Freshney, RI, (2005)**,**Cryopreservation, Culture of Animal Cells, John Wiley & Sons, Inc., (2005).

Fuller, Sv, Von Bonsdorff, C-H and Simons, K, (1984) Vesicular stomatitis virus infects and matures only through the basolateral surface of the polarized epithelial cell line, MDCK. *Cell* **38** (1): 65-77.

Furuse, M, (2010)**,**Chapter 1 - Introduction: Claudins, Tight Junctions, and the Paracellular Barrier, in: Alan SLY (Ed.), Current Topics in Membranes, Academic Press, (2010), Vol. Volume 65, pp. 1-19.

Furuse, M, Fujita, K, Hiiragi, T, Fujimoto, K and Tsukita, S, (1998) Claudin-1 and-2: novel integral membrane proteins localizing at tight junctions with no sequence similarity to occludin. *The Journal of cell biology* **141** (7): 1539-1550.

Furuse, M, Furuse, K, Sasaki, H and Tsukita, S, (2001) Conversion of zonulae occludentes from tight to leaky strand type by introducing claudin-2 into Madin-Darby canine kidney I cells. *Journal of Cell Biology* **153** (2): 263 - 272.

Furuse, M, Hirase, T, Itoh, M, Nagafuchi, A, Yonemura, S and Tsukita, S, (1993) Occludin: a novel integral membrane protein localizing at tight junctions. *The Journal of cell biology* **123** (6): 1777-1788.

G

Gallicano, GI, Kouklis, P, Bauer, C, Yin, M, Vasioukhin, V, Degenstein, L and Fuchs, E, (1998) Desmoplakin is required early in development for assembly of desmosomes and cytoskeletal linkage. *The Journal of cell biology* **143** (7): 2009-2022.

Gao, L, Joberty, G and Macara, IG, (2002) Assembly of Epithelial Tight Junctions Is Negatively Regulated by Par6. *Current Biology* **12** (3): 221-225.

Garland, SL, (2013) Are GPCRs Still a Source of New Targets? *Journal of biomolecular screening*

Gekle, M, Wünsch, S, Oberleithner, H and Silbernagl, S, (1994) Characterization of two MDCK-cell subtypes as a model system to study principal cell and intercalated cell properties. *Pflügers Archiv* **428** (2): 157-162.
Ghandehari, H, Smith, PL, Ellens, H, Yeh, P-Y and Kopeček, J, (1997) Size-Dependent Permeability of Hydrophilic Probes Across Rabbit Colonic Epithelium. *Journal of Pharmacology and Experimental Therapeutics* **280** (2): 747-753.
Giaever, I and Keese, C, (1993) Correction: Micromotion of mammalian cells measured electrically. *Proceedings of the National Academy of Sciences of the United States of America* **90** (4): 1634-1634.
Giaever, I and Keese, CR, (1984) Monitoring fibroblast behavior in tissue culture with an applied electric field. *Proceedings of the National Academy of Sciences* **81** (12): 3761-3764.
Giaever, I and Keese, CR, (1991) Micromotion of mammalian cells measured electrically. *Proceedings of the National Academy of Sciences* **88** (17): 7896-7900.
Gitter, A, Bertog, M, Schulzke, J-D and Fromm, M, (1997) Measurement of paracellular epithelial conductivity by conductance scanning. *Pflügers Archiv* **434** (6): 830-840.
Gitter, AH, Wullstein, F, Fromm, M and Schulzke, JD, (2001) Epithelial barrier defects in ulcerative colitis: characterization and quantification by electrophysiological imaging. *Gastroenterology* **121** (6): 1320-1328.
Goldstein, B, (2007) The PAR proteins : fundamental players in animal cell polarization. *Dev. Cell* **13** 609-622.
González-Mariscal, L, Betanzos, A and Ávila-Flores, A, (2000) MAGUK proteins: structure and role in the tight junction. *Seminars in Cell & Developmental Biology* **11** (4): 315-324.
Grieshaber, D, MacKenzie, R, Vörös, J and Reimhult, E, (2008) Electrochemical Biosensors - Sensor Principles and Architectures. *Sensors* **8** (3): 1400.
Gumbiner, B and Simons, K, (1986) A functional assay for proteins involved in establishing an epithelial occluding barrier: identification of a uvomorulin-like polypeptide. *Journal of Cell Biology* **102** (2): 457-68.
Gumbiner, BM, (1996) Cell adhesion: the molecular basis of tissue architecture and morphogenesis. *Cell* **84** (3): 345-357.
Günzel, D, Krug, SM, Rosenthal, R and Fromm, M, (2010)**,**Biophysical Methods to Study Tight Junction Permeability, in: Alan SLY (Ed.), Current Topics in Membranes, Academic Press, (2010), Vol. Volume 65, pp. 39-78.
Günzel, D, Zakrzewski, SS, Schmid, T, Pangalos, M, Wiedenhoeft, J, Blasse, C, Ozboda, C and Krug, SM, (2012) From TER to trans-and paracellular resistance: lessons from impedance spectroscopy. *Annals of the New York Academy of Sciences* **1257** (1): 142-151.

H

Hamilton, KL and Devor, DC, (2016) Ion Channels and Transporters of Epithelia in Health and Disease, Springer.
Harris, TJ and Tepass, U, (2010) Adherens junctions: from molecules to morphogenesis. *Nature reviews Molecular cell biology* **11** (7): 502-514.
Hartmann, C, Zozulya, A, Wegener, J and Galla, H-J, (2007) The impact of glia-derived extracellular matrices on the barrier function of cerebral endothelial cells: An in vitro study. *Experimental Cell Research* **313** (7): 1318-1325.
Heiskanen, A and Emnéus, J, (2011)**,**Monitoring of Cellular Dynamics with Electrochemical Detection Techniques, in: Eliaz N (Ed.), Applications of Electrochemistry and Nanotechnology in Biology and Medicine I, Springer New York, New York, NY, (2011), pp. 1-104.
Hill, SJ, (1990) Distribution, properties, and functional characteristics of three classes of histamine receptor. *Pharmacological reviews* **42** (1): 45-83.
Hillgren, KM, Kato, A and Borchardt, RT, (1995) In vitro systems for studying intestinal drug absorption. *Medicinal research reviews* **15** (2): 83-109.
Hishinuma, S and Ogura, K, (2000) Ca2+/Calmodulin-Mediated Regulation of the Desensitizing Process in Gq Protein-Coupled Histamine H1 Receptor-Mediated Ca2+ Responses in Human U373 MG Astrocytoma Cells. *Journal of Neurochemistry* **75** (2): 772-781.
Hishinuma, S, Sato, Y, Akatsu, C and Shoji, M, (2012) The Affinity of Histamine for Gq Protein-Coupled Histamine H₁-Receptors Is Predominantly Regulated by Their Internalization in Human Astrocytoma Cells. *Journal of Pharmacological Sciences* **119** (3): 233-242.
Holgate, ST, (2007) Epithelium dysfunction in asthma. *Journal of Allergy and Clinical Immunology* **120** (6): 1233-1244.
Horn, F, Bettler, E, Oliveira, L, Campagne, F, Cohen, FE and Vriend, G, (2003) GPCRDB information system for G protein-coupled receptors. *Nucleic Acids Res* **31** (1): 294-297.
Hua, SZ and Pennell, T, (2009) A microfluidic chip for real-time studies of the volume of single cells. *Lab on a Chip* **9** (2): 251-256.
Hynes, RO, (2002) Integrins: Bidirectional, Allosteric Signaling Machines. *Cell* **110** (6): 673-687.

I

Ikenouchi, J, Furuse, M, Furuse, K, Sasaki, H, Tsukita, S and Tsukita, S, (2005) Tricellulin constitutes a novel barrier at tricellular contacts of epithelial cells. *The Journal of cell biology* **171** (6): 939-945.
Irvine, JD, Takahashi, L, Lockhart, K, Cheong, J, Tolan, JW, Selick, HE and Grove, JR, (1999) MDCK (Madin–Darby canine kidney) cells: A tool for membrane permeability screening. *Journal of Pharmaceutical Sciences* **88** (1): 28-33.

J

Jacoby, E, Bouhelal, R, Gerspacher, M and Seuwen, K, (2006) The 7 TM G-protein-coupled receptor target family. *ChemMedChem* **1** (8): 760-782.

Janshoff, A, Wegener, J, Sieber, M and Galla, H-J, (1996) Double-mode impedance analysis of epithelial cell monolayers cultured on shear wave resonators. *European Biophysics Journal* **25** (2): 93-103.

Jovov, B, Wills, NK and Lewis, SA, (1991) A spectroscopic method for assessing confluence of epithelial cell cultures. *American Journal of Physiology - Cell Physiology* **261** (6): C1196-C1203.

Jutel, M, Akdis, M and Akdis, C, (2009) Histamine, histamine receptors and their role in immune pathology. *Clinical & Experimental Allergy* **39** (12): 1786-1800.

K

K'Owino, IO and Sadik, OA, (2005) Impedance Spectroscopy: A Powerful Tool for Rapid Biomolecular Screening and Cell Culture Monitoring. *Electroanalysis* **17** (23): 2101-2113.

Katritch, V, Cherezov, V and Stevens, RC, (2013) Structure-Function of the G-protein-Coupled Receptor Superfamily. *Annual review of pharmacology and toxicology* **53** 531-556.

Keese, CR, Wegener, J, Walker, SR and Giaever, I, (2004) Electrical wound-healing assay for cells in vitro. *Proc Natl Acad Sci U S A* **101** (6): 1554-1559.

Kimelberg, HK, O'Connor, ER, Sankar, P and Keese, C, (1992) Methods for determination of cell volume in tissue culture. *Canadian Journal of Physiology and Pharmacology* **70** (S1): S323-S333.

Kleinhans, FW, (1998) Membrane Permeability Modeling: Kedem–Katchalsky vs a Two-Parameter Formalism. *Cryobiology* **37** (4): 271-289.

Knepper, MA, (1994) The aquaporin family of molecular water channels. *Proceedings of the National Academy of Sciences* **91** (14): 6255-6258.

Komarova, Y and Malik, AB, (2010) Regulation of endothelial permeability via paracellular and transcellular transport pathways. *Annual review of physiology* **72** 463-493.

Korjamo, T, Heikkinen, AT and Mönkkönen, J, (2009) Analysis of unstirred water layer in in vitro permeability experiments. *Journal of Pharmaceutical Sciences* **98** (12): 4469-4479.

Koster, J, Geerts, D, Favre, B, Borradori, L and Sonnenberg, A, (2003) Analysis of the interactions between BP180, BP230, plectin and the integrin α6β4 important for hemidesmosome assembly. *Journal of cell science* **116** (2): 387-399.

Kottra, G, Weber, G and Fromter, E, (1989) A method to quantify and correct for edge leaks in Ussing chambers. *Pflugers Arch* **415** (2): 235-40.

Krug, SM, Amasheh, S, Richter, JF, Milatz, S, Gunzel, D, Westphal, JK, Huber, O, Schulzke, JD and Fromm, M, (2009a) Tricellulin Forms a Barrier to Macromolecules in Tricellular Tight Junctions without Affecting Ion Permeability. *Molecular Biology of the Cell* **20** (16): 3713-3724.

Krug, SM, Fromm, M and Günzel, D, (2009b) Two-Path Impedance Spectroscopy for Measuring Paracellular and Transcellular Epithelial Resistance. *Biophysical Journal* **97** (8): 2202-2211.

Krug, SM, Schulzke, JD and Fromm, M, (2014)**,**Tight junction, selective permeability, and related diseases, Seminars in Cell & Developmental Biology, Elsevier, (2014), Vol. 36, pp. 166-176.

L

Lasia, A, (2002)**,**Electrochemical Impedance Spectroscopy and its Applications, in: Conway BE, Bockris JOM and White RE (Eds.), Modern Aspects of Electrochemistry, Springer US, Boston, MA, (2002), pp. 143-248.

Lieb, S, Michaelis, S, Plank, N, Bernhardt, G, Buschauer, A and Wegener, J, (2016) Label-free analysis of GPCR-stimulation: The critical impact of cell adhesion. *Pharmacological Research* **108** 65-74.

Limonciel, A, Wilmes, A, Aschauer, L, Radford, R, Bloch, KM, McMorrow, T, Pfaller, W, van Delft, JH, Slattery, C, Ryan, MP, Lock, EA and Jennings, P, (2012) Oxidative stress induced by potassium bromate exposure results in altered tight junction protein expression in renal proximal tubule cells. *Archives of Toxicology* **86** (11): 1741-1751.

Lipschutz, JH, Li, S, Arisco, A and Balkovetz, DF, (2005) Extracellular signal-regulated kinases 1/2 control claudin-2 expression in Madin-Darby canine kidney strain I and II cells. *Journal of Biological Chemistry* **280** (5): 3780-3788.

Litjens, SH, de Pereda, JM and Sonnenberg, A, (2006) Current insights into the formation and breakdown of hemidesmosomes. *Trends in cell biology* **16** (7): 376-383.

Lo, C-M, Keese, CR and Giaever, I, (1999) Cell–Substrate Contact: Another Factor May Influence Transepithelial Electrical Resistance of Cell Layers Cultured on Permeable Filters. *Exp Cell Res* **250** (2): 576-580.

Lo, CM, Keese, CR and Giaever, I, (1995) Impedance analysis of MDCK cells measured by electric cell-substrate impedance sensing. *Biophys J* **69** (6): 2800-2807.

Loeschke, K and Bentzel, CJ, (1994) Osmotic water flow pathways across Necturus gallbladder: role of the tight junction. *American Journal of Physiology-Gastrointestinal and Liver Physiology* **266** (4): G722-G730.

Lohmann, C, Hüwel, S and Galla, H-J, (2002) Predicting Blood-Brain Barrier Permeability of Drugs: Evaluation of Different In Vitro Assays. *Journal of Drug Targeting* **10** (4): 263-276.

Luttrell, LM and Gesty-Palmer, D, (2010) Beyond Desensitization: Physiological Relevance of Arrestin-Dependent Signaling. *Pharmacological reviews* **62** (2): 305-330.

M

Macdonald, JR, (1992) Impedance spectroscopy. *Annals of Biomedical Engineering* **20** (3): 289-305.

Macdonald, JR and Johnson, WB, (2005)**,**Fundamentals of Impedance Spectroscopy, Impedance Spectroscopy, John Wiley & Sons, Inc., (2005), pp. 1-26.

Madsen, KM and Tisher, CC, (1986) Structural-functional relationships along the distal nephron. *American Journal of Physiology - Renal Physiology* **250** (1): F1-F15.

Maeda, S, Nakagawa, S, Suga, M, Yamashita, E, Oshima, A, Fujiyoshi, Y and Tsukihara, T, (2009) Structure of the connexin 26 gap junction channel at 3.5 Å resolution. *Nature* **458** (7238): 597-602.

Mandell, KJ and Parkos, CA, (2005) The JAM family of proteins. *Advanced drug delivery reviews* **57** (6): 857-867.

Matter, K and Balda, MS, (2003) Functional analysis of tight junctions. *Methods* **30** (3): 228-234.

Maurel, C, (1997) Aquaporins and water permeability of plant membranes. *Annual review of plant biology* **48** (1): 399-429.

McNeil, E, Capaldo, CT and Macara, IG, (2006) Zonula Occludens-1 Function in the Assembly of Tight Junctions in Madin-Darby Canine Kidney Epithelial Cells. *Molecular Biology of the Cell* **17** (4): 1922-1932.

Michaelis, S, Rommel, CE, Endell, J, Göring, P, Wehrspohn, R, Steinem, C, Janshoff, A, Galla, H-J and Wegener, J, (2012) Macroporous silicon chips for laterally resolved, multi-parametric analysis of epithelial barrier function. *Lab on a Chip* **12** (13): 2329-2336.

Michaelis, S, Wegener, J and Robelek, R, (2013) Label-free monitoring of cell-based assays: Combining impedance analysis with SPR for multiparametric cell profiling. *Biosensors & Bioelectronics* **49** 63-70.

Murata, K, Mitsuoka, K, Hirai, T, Walz, T, Agre, P, Heymann, JB, Engel, A and Fujiyoshi, Y, (2000) Structural determinants of water permeation through aquaporin-1. *Nature* **407** (6804): 599-605.

N

Nakagawa, S, Maeda, S and Tsukihara, T, (2010) Structural and functional studies of gap junction channels. *Current opinion in structural biology* **20** (4): 423-430.

Neuhaus, W, Bogner, E, Wirth, M, Trzeciak, J, Lachmann, B, Gabor, F and Noe, CR, (2006) A novel tool to characterize paracellular transport: the APTS–dextran ladder. *Pharmaceutical research* **23** (7): 1491-1501.

Niessen, CM, (2007) Tight Junctions/Adherens Junctions: Basic Structure and Function. *Journal of Investigative Dermatology* **127** 2525-2532.

Nightingale, ER, (1959) Phenomenological Theory of Ion Solvation. Effective Radii of Hydrated Ions. *The Journal of Physical Chemistry* **63** (9): 1381-1387.

P

Pajkossy, T, (1994) Impedance of rough capacitive electrodes. *Journal of Electroanalytical Chemistry* **364** (1–2): 111-125.

Patton, KT, (2015) Anatomy & Physiology, Elsevier Science Health Science.

Phelps, JE and DePaola, N, (2000) Spatial variations in endothelial barrier function in disturbed flows in vitro. *American Journal of Physiology-Heart and Circulatory Physiology* **278** (2): H469-H476.

Poler, S and Reuss, L, (1987) Protamine alters apical membrane K+ and Cl-permeability in gallbladder epithelium. *American Journal of Physiology-Cell Physiology* **253** (5): C662-C671.

Powell, DW, (1981) Barrier function of epithelia. *American Journal of Physiology - Gastrointestinal and Liver Physiology* **241** (4): G275-G288.

Preston, GM and Agre, P, (1991) Isolation of the cDNA for erythrocyte integral membrane protein of 28 kilodaltons: member of an ancient channel family. *Proceedings of the National Academy of Sciences* **88** (24): 11110-11114.

Primiceri, E, Chiriaco, MS, Dioguardi, F, Monteduro, AG, D'Amone, E, Rinaldi, R, Giannelli, G and Maruccio, G, (2011) Automatic transwell assay by an EIS cell chip to monitor cell migration. *Lab on a Chip* **11** (23): 4081-4086.

Prozialeck, WC, Edwards, JR, Lamar, PC and Smith, CS, (2006) Epithelial barrier characteristics and expression of cell adhesion molecules in proximal tubule-derived cell lines commonly used for in vitro toxicity studies. *Toxicology in Vitro* **20** (6): 942-953.

R

Raistrick, ID and Macdonald, JR, (2005)**,**Theory, Experiments and Applications, Impedance Spectroscopy, John Wiley & Sons, Inc., (2005), pp. 27-128.

Randles, JEB, (1947) Kinetics of rapid electrode reactions. *Discussions of the Faraday Society* **1** (0): 11-19.

Rehder, D, Iden, S, Nasdala, I, Wegener, J, Zu Brickwedde, M-KM, Vestweber, D and Ebnet, K, (2006) Junctional adhesion molecule-a participates in the formation of apico-basal polarity through different domains. *Experimental Cell Research* **312** (17): 3389-3403.

Reichel, A, Begley, DJ and Abbott, NJ, (2003) An overview of in vitro techniques for blood-brain barrier studies. *The Blood-Brain Barrier: Biology and Research Protocols* 307-324.

Reiß, B, (2004) Mikrogravimetrische Untersuchung des Adhäsionskontakts tierischer Zellen: Eine biophysikalische Studie. Westfälischen Wilhelms-Universität Münster

Reiß, B and Wegener, J, (2015)**,**Impedance analysis of different cell monolayers grown on gold-film electrodes, 2015 37th Annual International Conference of the IEEE Engineering in Medicine and Biology Society (EMBC), (2015), pp. 7079-7082.

Richardson, JCW, Scalera, V and Simmons, NL, (1981) Identification of 2 Strains of Mdck Cells Which Resemble Separate Nephron Tubule Segments. *Biochimica Et Biophysica Acta* **673** (1): 26-36.

Robelek, R and Wegener, J, (2010) Label-free and time-resolved measurements of cell volume changes by surface plasmon resonance (SPR) spectroscopy. *Biosensors and Bioelectronics* **25** (5): 1221-1224.

Roignot, J, Peng, X and Mostov, K, (2013) Polarity in mammalian epithelial morphogenesis. *Cold Spring Harbor perspectives in biology* **5** (2): a013789.

Rommel, C, (2007) Tierische Zellen auf nanoporösen Oberflächen: Grundlagen und bioanalytische Anwendungen. Westfälischen Wilhelms-Universität Münster

Rosenthal, R, Milatz, S, Krug, SM, Oelrich, B, Schulzke, J-D, Amasheh, S, Günzel, D and Fromm, M, (2010) Claudin-2, a component of the tight junction, forms a paracellular water channel. *Journal of cell science* **123** (11): 1913-1921.

S

Sadik, OA, Aluoch, AO and Zhou, A, (2009) Status of biomolecular recognition using electrochemical techniques. *Biosensors and Bioelectronics* **24** (9): 2749-2765.

Sanders, S, Madara, J, McGuirk, D, Gelman, D and Colgan, S, (1995) Assessment of Inflammatory Events in Epithelial Permeability: A Rapid Screening Method using Fluorescein Dextrans.

Schafer, JA, Patlak, CS, Troutman, SL and Andreoli, TE, (1978) Volume absorption in the pars recta. II. Hydraulic conductivity coefficient. *American Journal of Physiology-Renal Physiology* **234** (4): F340-F348.

Schultz, SG and Solomon, AK, (1961) Determination of the Effective Hydrodynamic Radii of Small Molecules by Viscometry. *The Journal of General Physiology* **44** (6): 1189-1199.

Scott, CW and Peters, MF, (2010) Label-free whole-cell assays: expanding the scope of GPCR screening. *Drug Discov Today* **15** (17-18): 704-16.

Seifert, R, Strasser, A, Schneider, EH, Neumann, D, Dove, S and Buschauer, A, (2013) Molecular and cellular analysis of human histamine receptor subtypes. *Trends in Pharmacological Sciences* **34** (1): 33-58.

Shapiro, L, Fannon, AM, Kwong, PD, Thompson, A, Lehmann, MS, Grübel, G, Legrand, J-F, Als-Nielsen, J, Colman, DR and Hendrickson, WA, (1995) Structural basis of cell-cell adhesion by cadherins. *Nature* **374** (6520): 327-337.

Shin, K, Fogg, V and Margolis, B, (2006) Tight junctions and cell polarity. *Annu Rev Cell Dev Biol* **22** 207 - 235.

Sill, HW, Butler, C, Hollis, TM and Tarbell, JM, (1992) Albumin permeability and electrical resistance as means of assessing endothelial monolayer integrity in vitro. *Journal of tissue culture methods* **14** (4): 253-257.

Solomon, AK, (1989),Water channels across the red blood cell and other biological membranes, Methods in Enzymology, Academic Press, (1989), Vol. Volume 173, pp. 192-222.

Sperber, M, (2016) Impedance-Based Analysis of the Cellular Response to Microparticles: Theory, Assay Development and Model Study. Regensburg

Sperber, M, Hupf, C, Lemberger, M-M, Goricnik, B, Hinterreiter, N, Lukic, S, Oberleitner, M, Stolwijk, JA and Wegener, J, (2016),Monitoring the Impact of Nanomaterials on Animal Cells by Impedance Analysis: A Noninvasive, Label-Free, and Multimodal Approach, in: Wegener J (Ed.), Measuring Biological Impacts of Nanomaterials, Springer International Publishing, Cham, (2016), pp. 45-108.

Spring, KR, (1998) Routes and mechanism of fluid transport by epithelia. *Annual review of physiology* **60** (1): 105-119.

Staehelin, L, (1973) Further observations on the fine structure of freeze-cleaved tight junctions. *Journal of cell science* **13** (3): 763-786.

Stevens, RC, Cherezov, V, Katritch, V, Abagyan, R, Kuhn, P, Rosen, H and Wuthrich, K, (2013) The GPCR Network: a large-scale collaboration to determine human GPCR structure and function. *Nat Rev Drug Discov* **12** (1): 25-34.

Stevenson, BR, Anderson, JM, Goodenough, DA and Mooseker, MS, (1988) Tight junction structure and ZO-1 content are identical in two strains of Madin-Darby canine kidney cells which differ in transepithelial resistance. *The Journal of Cell Biology* **107** (6): 2401-2408.

Stevenson, BR and Begg, DA, (1994) Concentration-dependent effects of cytochalasin D on tight junctions and actin filaments in MDCK epithelial cells. *J Cell Sci* **107** (3): 367-375.

Stevenson, BR, Siliciano, JD, Mooseker, MS and Goodenough, DA, (1986) Identification of ZO-1: a high molecular weight polypeptide associated with the tight junction (zonula occludens) in a variety of epithelia. *The Journal of Cell Biology* **103** (3): 755-766.

Stolwijk, JA, Hartmann, C, Balani, P, Albermann, S, Keese, CR, Giaever, I and Wegener, J, (2011) Impedance analysis of adherent cells after in situ electroporation: Non-invasive monitoring during intracellular manipulations. *Biosensors and Bioelectronics* **26** (12): 4720-4727.

Sugiharto, S, Lewis, TM, Moorhouse, AJ, Schofield, PR and Barry, PH, (2008) Anion-cation permeability correlates with hydrated counterion size in glycine receptor channels. *Biophysical Journal* **95** (10): 4698-4715.

T/U

Takeuchi, K, Kishioka, C, Ishinaga, H, Sakakura, Y and Majima, Y, (2001) Histamine alters gene expression in cultured human nasal epithelial cells. *Journal of Allergy and Clinical Immunology* **107** (2): 310-314.

Tsinman, O, Tsinman, K, Sun, N and Avdeef, A, (2011) Physicochemical Selectivity of the BBB Microenvironment Governing Passive Diffusion—Matching with a Porcine Brain Lipid Extract Artificial Membrane Permeability Model. *Pharmaceutical research* **28** (2): 337-363.

Ussing, HH, (1949) The distinction by means of tracers between active transport and diffusion. *Acta physiologica scandinavica* **19** (1): 43-56.

V

van der Goot, H and Timmerman, H, (2000) Selective ligands as tools to study histamine receptors. *European Journal of Medicinal Chemistry* **35** (1): 5-20.

Van Itallie, CM and Anderson, JM, (2006) Claudins and epithelial paracellular transport. *Annu. Rev. Physiol.* **68** 403-429.

Van Itallie, CM, Holmes, J, Bridges, A and Anderson, JM, (2009) Claudin-2-dependent Changes in Noncharged Solute Flux Are Mediated by the Extracellular Domains and Require Attachment to the PDZ-scaffold. *Annals of the New York Academy of Sciences* **1165** (1): 82-87.

Van Itallie, CM, Holmes, J, Bridges, A, Gookin, JL, Coccaro, MR, Proctor, W, Colegio, OR and Anderson, JM, (2008) The density of small tight junction pores varies among cell types and is increased by expression of claudin-2. *Journal of cell science* **121** (3): 298-305.

Verkman, A, (1995) Optical methods to measure membrane transport processes. *J Membr Biol* **148** (2): 99-110.

Verkman, A and Mitra, AK, (2000) Structure and function of aquaporin water channels. *American Journal of Physiology-Renal Physiology* **278** (1): F13-F28.

Verkman, A, Van Hoek, AN, Ma, T, Frigeri, A, Skach, W, Mitra, A, Tamarappoo, BK and Farinas, J, (1996) Water transport across mammalian cell membranes. *American Journal of Physiology-Cell Physiology* **270** (1): C12-C30.

Verkman, AS, (2000) Water Permeability Measurement in Living Cells and Complex Tissues. *J Membr Biol* **173** (2): 73-87.

W

Wang, AZ, Ojakian, GK and Nelson, WJ, (1990) Steps in the morphogenesis of a polarized epithelium. I. Uncoupling the roles of cell-cell and cell-substratum contact in establishing plasma membrane polarity in multicellular epithelial (MDCK) cysts. *Journal of cell science* **95** (1): 137-151.

Watson, CJ, Rowland, M and Warhurst, G, (2001) Functional modeling of tight junctions in intestinal cell monolayers using polyethylene glycol oligomers. *American Journal of Physiology - Cell Physiology* **281** (2): C388-C397.

Wegener, J, (1998) Impedanzspektroskopische und mikrogravimetrische Untersuchungen an barrierebildenden Zellen auf planaren Goldelektroden. Westfälischen Wilhelms-Universität Münster

Wegener, J, (2006) Cell surface interactions. *Wiley Encyclopedia of Biomedical Engineering*

Wegener, J, Abrams, D, Willenbrink, W, Galla, HJ and Janshoff, A, (2004) Automated multi-well device to measure transepithelial electrical resistances under physiological conditions. *Biotechniques* **37** (4): 590, 592-4, 596-7.

Wegener, J, Franke, H, Decker, S, Erben, M and Galla, H-J, (1996a)**,**New Techniques to Study Transepithelial and Transendothelial Resistances of Cultured Cells, in: Couraud P-O and Scherman D (Eds.), Biology and Physiology of the Blood-Brain Barrier: Transport, Cellular Interactions, and Brain Pathologies, Springer US, Boston, MA, (1996a), pp. 147-152.

Wegener, J, Keese, CR and Giaever, I, (2000) Electric Cell–Substrate Impedance Sensing (ECIS) as a Noninvasive Means to Monitor the Kinetics of Cell Spreading to Artificial Surfaces. *Exp Cell Res* **259** (1): 158-166.

Wegener, J and Seebach, J, (2014) Experimental tools to monitor the dynamics of endothelial barrier function: a survey of in vitro approaches. *Cell and Tissue Research* **355** (3): 485-514.

Wegener, J, Sieber, M and Galla, H-J, (1996b) Impedance analysis of epithelial and endothelial cell monolayers cultured on gold surfaces. *Journal of Biochemical and Biophysical Methods* **32** (3): 151-170.

Wegener, J, Zink, S, Rosen, P and Galla, HJ, (1999) Use of electrochemical impedance measurements to monitor beta-adrenergic stimulation of bovine aortic endothelial cells. *Pflugers Archiv-European Journal of Physiology* **437** (6): 925-934.

Weis, R and Fromherz, P, (1997) Frequency dependent signal transfer in neuron transistors. *Physical Review E* **55** (1): 877-889.

Weiss, N, Miller, F, Cazaubon, S and Couraud, P-O, (2009) The blood-brain barrier in brain homeostasis and neurological diseases. *Biochimica et Biophysica Acta (BBA) - Biomembranes* **1788** (4): 842-857.

Whittembury, G and Reuss, L, (1992) Mechanisms of coupling of solute and solvent transport in epithelia. *The Kidney: Physiology and Pathophysiology* **2** 317-360.

Wills, NK, Reuss, L and Lewis, S, (2012) Epithelial Transport: A guide to methods and experimental analysis, Springer Netherlands.

Wise, C, (2002) Epithelial Cell Culture Protocols, Humana Press.

Y

Ye, R and Verkman, AS, (1989) Simultaneous optical measurement of osmotic and diffusional water permeability in cells and liposomes. *Biochemistry* **28** (2): 824-829.

Youdim, KA, Avdeef, A and Abbott, NJ, (2003) In vitro trans-monolayer permeability calculations: often forgotten assumptions. *Drug Discovery Today* **8** (21): 997-1003.

Young, KW, Pinnock, RD and Nahorski, SR, (1998) Determination of the inositol (1,4,5) trisphosphate requirement for histamine- and substance P-induced Ca2+ mobilisation in human U373 MG astrocytoma cells. *Cell Calcium* **24** (1): 59-70.

Yu, ASL, McCarthy, KM, Francis, SA, McCormack, JM, Lai, J, Rogers, RA, Lynch, RD and Schneeberger, EE, (2005) Knockdown of occludin expression leads to diverse phenotypic alterations in epithelial cells. *American Journal of Physiology - Cell Physiology* **288** (6): C1231-C1241.

Yu, N, Atienza, JM, Bernard, J, Blanc, S, Zhu, J, Wang, X, Xu, X and Abassi, YA, (2006) Real-time monitoring of morphological changes in living cells by electronic cell sensor arrays: an approach to study G protein-coupled receptors. *Analytical Chemistry* **78** (1): 35-43.

Z

Zabner, J, Winter, M, Excoffon, KJA, Stoltz, D, Ries, D, Shasby, S and Shasby, M, (2003) Histamine alters E-cadherin cell adhesion to increase human airway epithelial permeability. *Journal of Applied Physiology* **95** (1): 394-401.

Zahraoui, A, Joberty, G, Arpin, M, Fontaine, JJ, Hellio, R, Tavitian, A and Louvard, D, (1994) A small rab GTPase is distributed in cytoplasmic vesicles in non polarized cells but colocalizes with the tight junction marker ZO-1 in polarized epithelial cells. *The Journal of cell biology* **124** (1): 101-115.

Zaidel-Bar, R, Itzkovitz, S, Ma'ayan, A, Iyengar, R and Geiger, B, (2007) Functional atlas of the integrin adhesome. *Nat Cell Biol* **9** (8): 858-867.

Zhang, S, Wang, N, Yu, H, Niu, Y and Sun, C, (2005) Covalent attachment of glucose oxidase to an Au electrode modified with gold nanoparticles for use as glucose biosensor. *Bioelectrochemistry* **67** (1): 15-22.

Zhao, L, Li, X, Lin, Y, Yang, L, Yu, P and Mao, L, (2012) Electrochemical impedance spectroscopic measurements of FCCP-induced change in membrane permeability of MDCK cells. *Analyst* **137** (9): 2199-2204.

Zink, S, Rösen, P, Sackmann, B and Lemoine, H, (1993) Regulation of endothelial permeability by β-adrenoceptor agonists: Contribution of β1- and β2-adrenoceptors. *Biochimica et Biophysica Acta (BBA) - Molecular Cell Research* **1178** (3): 286-298.

12 Appendix

12.1 Supplementary information

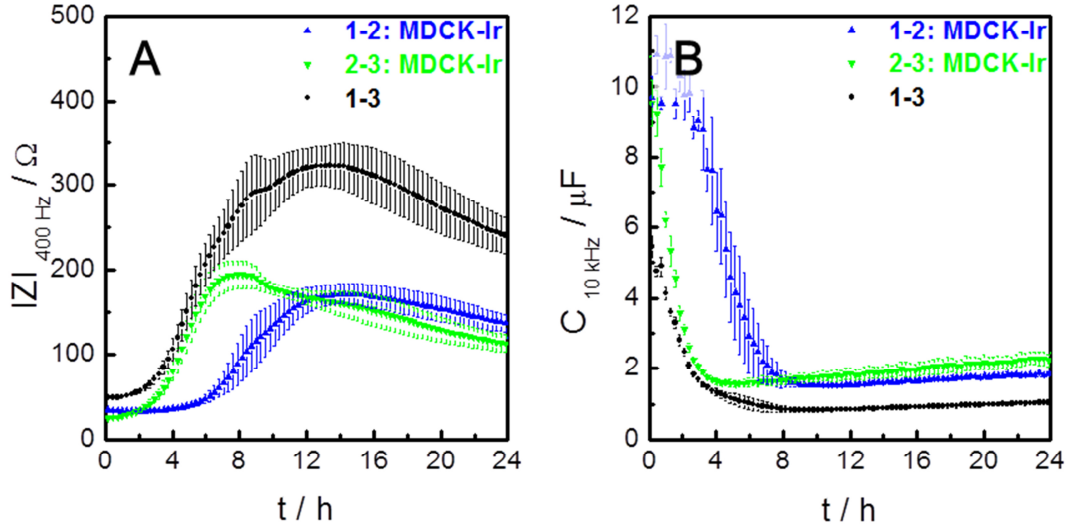

Fig. 12.1: Time course of the impedance magnitude *IZI* at 400 Hz (**A**) and capacitance *C* measured at 10 kHz (**B**) for all three possible measurement modes (mean ± SE, n = 3). Co-cultured MDCK-Ir cells were seeded four hours before t = 0 h on the back side of the filter membrane (▼ **2-3**) and at t = 0 h on the upper side of the porous membrane (▲ **1-2**). Values for the entire system are shown in black (● **1-3**).

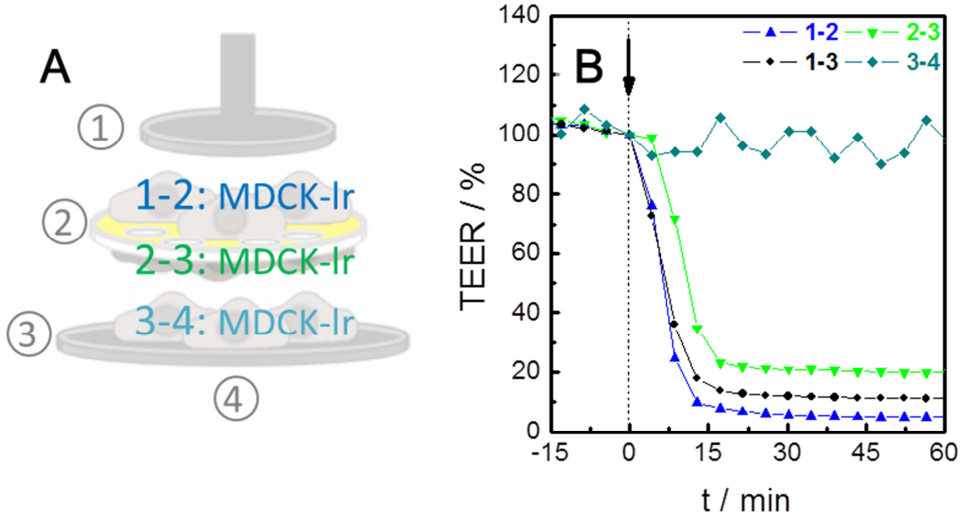

Fig. 12.2: A: The scheme presents the experimental setup for the simultaneous measurement of the transepithelial electrical resistance of both cell layers cultured on the membrane of a filter device and an additional third cell layer on the bottom of the measurement chamber in one experiment. **B** Exemplary data for the time course of the relative TEER of three MDCK-Ir cell layers (▲ **1-2** upper membrane side, ▼ **2-3** lower membrane side, ♦ **3-4** ECIS-mode: chamber bottom) and the transfilter measurement mode (● **1-3**) after addition of 3 μM cytochalasin D (cD) at t = 0h to the upper chamber compartment.

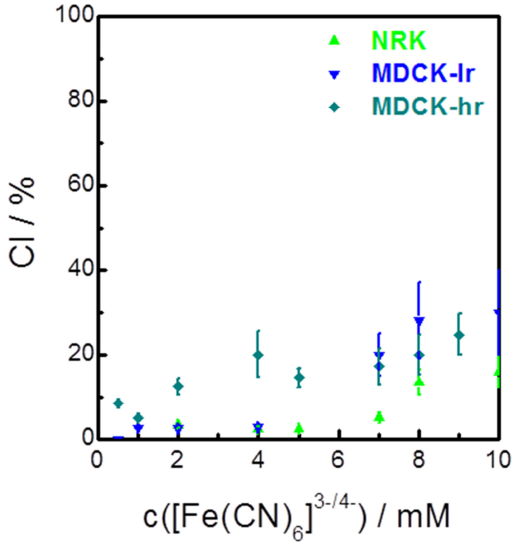

Fig. 12.3: PrestoBlue® assay (performed in a 96-well plate) to analyze cell viability of adherently growing cell types (▲ NRK, ▼ MDCK-lr, ♦ MDCK-hr) in presence of different concentrations of $[Fe(CN)_6]^{3-4-}$. The cytotoxicity index (CI) is determined after 3 h incubation time (mean ± SDM, n = 8; PrestoBlue®: Invitrogen, Life technologies, Darmstadt, Germany; fluorescence detection: λ_{ex} = 532 nm, λ_{em} = 600 nm, equipment: Genios, Tecan, Maennedorf, Switzerland: bottom readout).

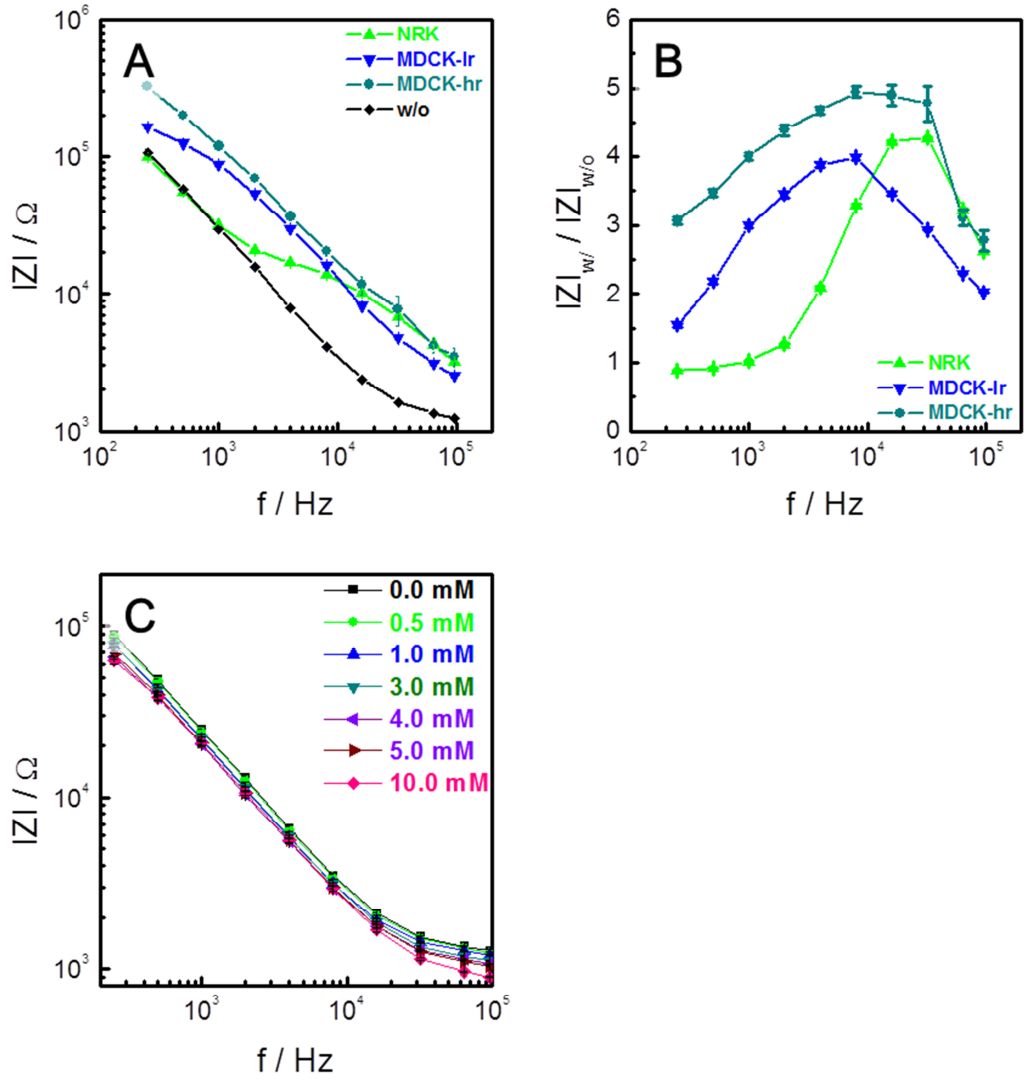

Fig. 12.4: 96-well ECIS measurements. **A** Frequency spectra of the impedance magnitude *|Z|* of cell-covered (▲ NRK, ▼ MDCK-lr, ● MDCK-hr) and cell-free (♦ **w/o**) electrodes (mean ± SE, n ≥ 25). **B** Normalization of the impedance spectra shown in graph A. Frequency spectra of impedance magnitude *|Z|* of cell-free 96-well ECIS electrodes in presence of variable concentrations of redox couple $[Fe(CN)_6]^{3-/4-}$ (**C**).

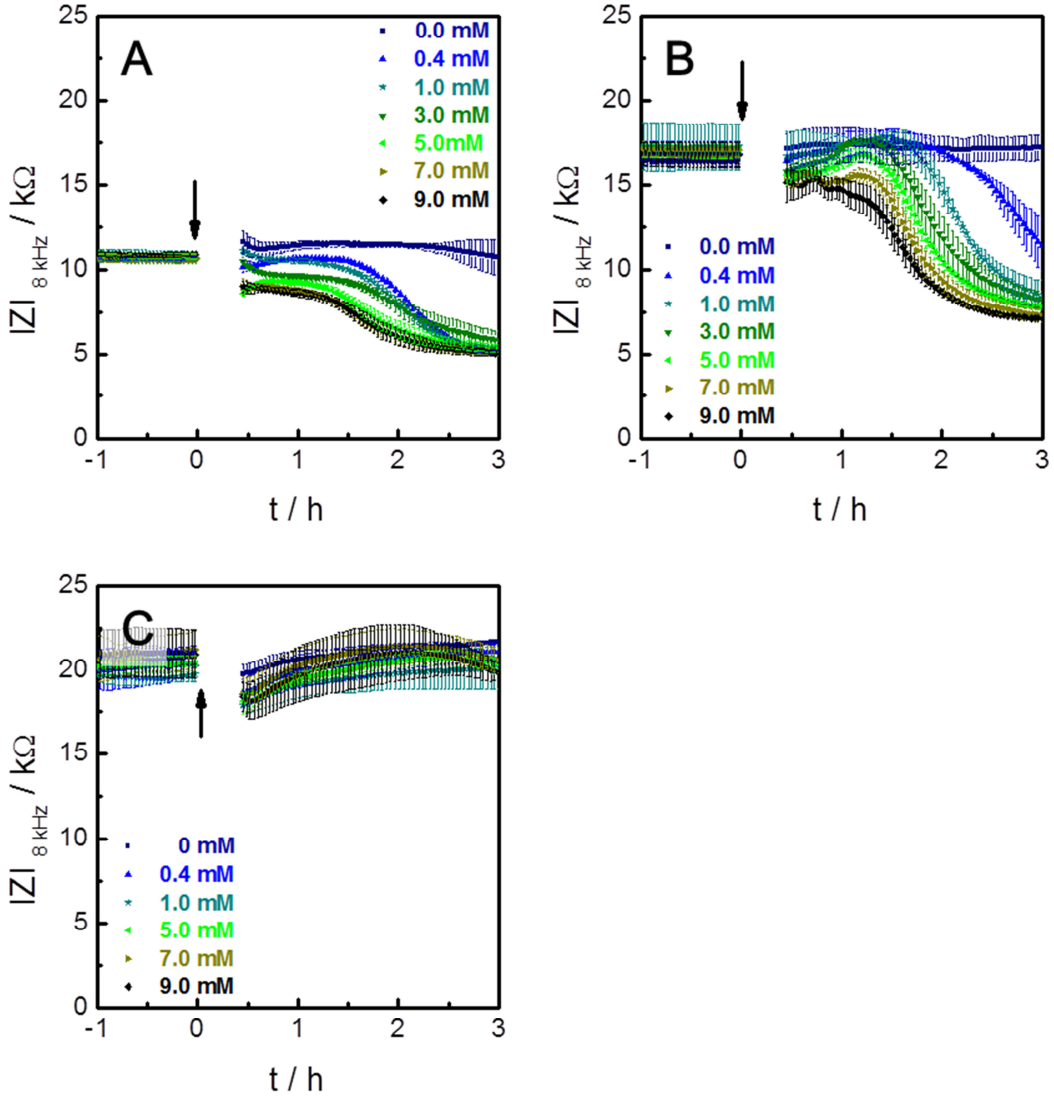

Fig. 12.5: 96-well ECIS measurements on confluent monolayers of NRK cells (**A**), MDCK-lr cells (**B**) and MDCK-hr cells (**C**). Time course impedance magnitude *IZI* at a frequency of 8 kHz in presence (addition at t = 0 h) of different concentrations of $[Fe(CN)_6]^{3-4-}$ (mean ± SDM, n = 3).

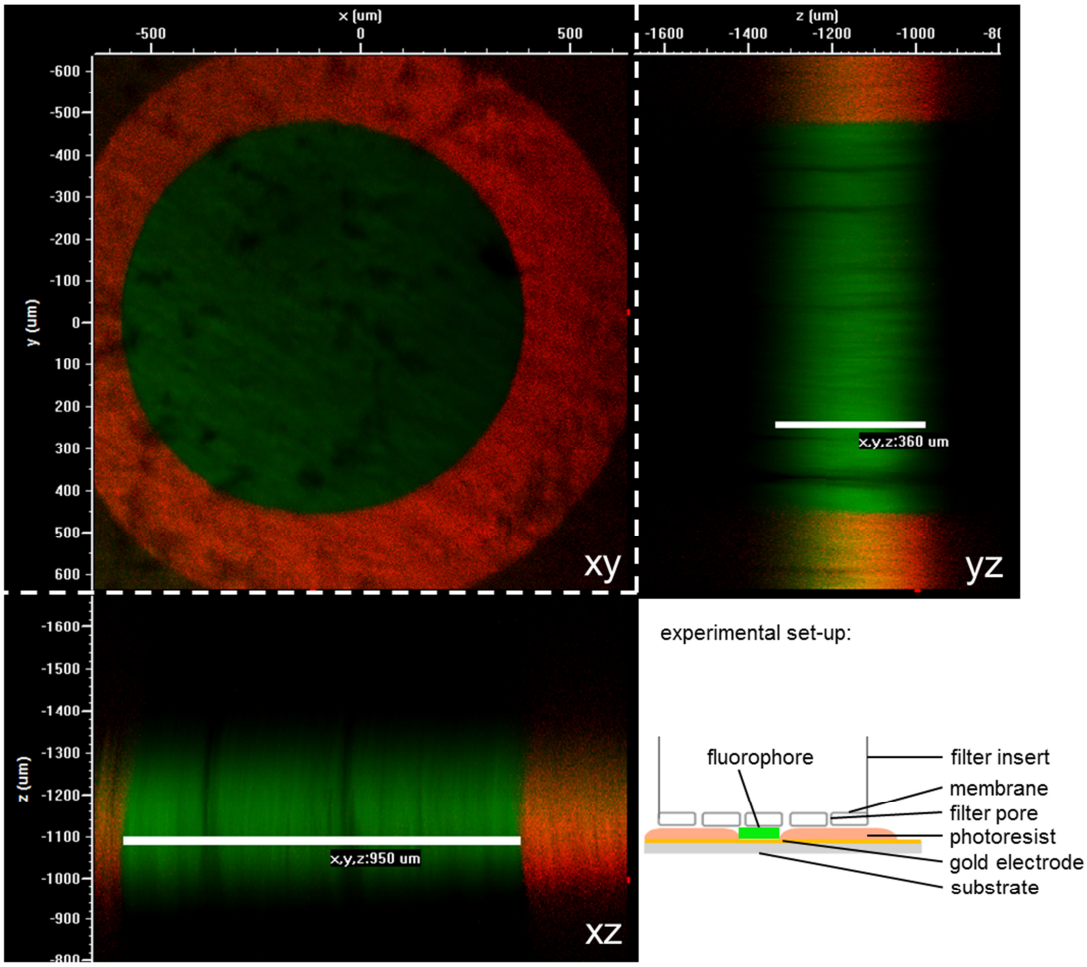

Fig. 12.6: Confocal scanning microscopy: Optical sections and scheme of the experimental set-up for the determination of the basal filter compartment volume. A green emitting fluorophore was added to the buffer (2 mg/mL 4-kDa FITC-dextran) and optical sections of the device were recorded by confocal scanning microscopy. The x-y-cross section shows the intrinsic red fluorescence of the insulting photopolymer which delineates the active electrode area (lower panel, left: Ø = 950 μm, A_{el} = 7.09E-03 cm^2). The height of the compartment is displayed in the y-z-cross section. The green fluorophore is clearly detectable up to 360 μm above the electrode surface (upper panel, right). The volume underneath the filter membrane is calculated to 2.55E-04 cm^3.
Measurement details: type: Nikon Eclipse 90i (Nikon Instruments Europe, Amstelveen, Netherlands); pinhole: L; step size: 10 μm, average: n = 2; laser 1: λ_{ex} = 488 nm; detector 1: 515/30 nm (gain 105); laser 2: λ_{ex} = 543 nm; detector 2: 650 nm LP (gain 179).

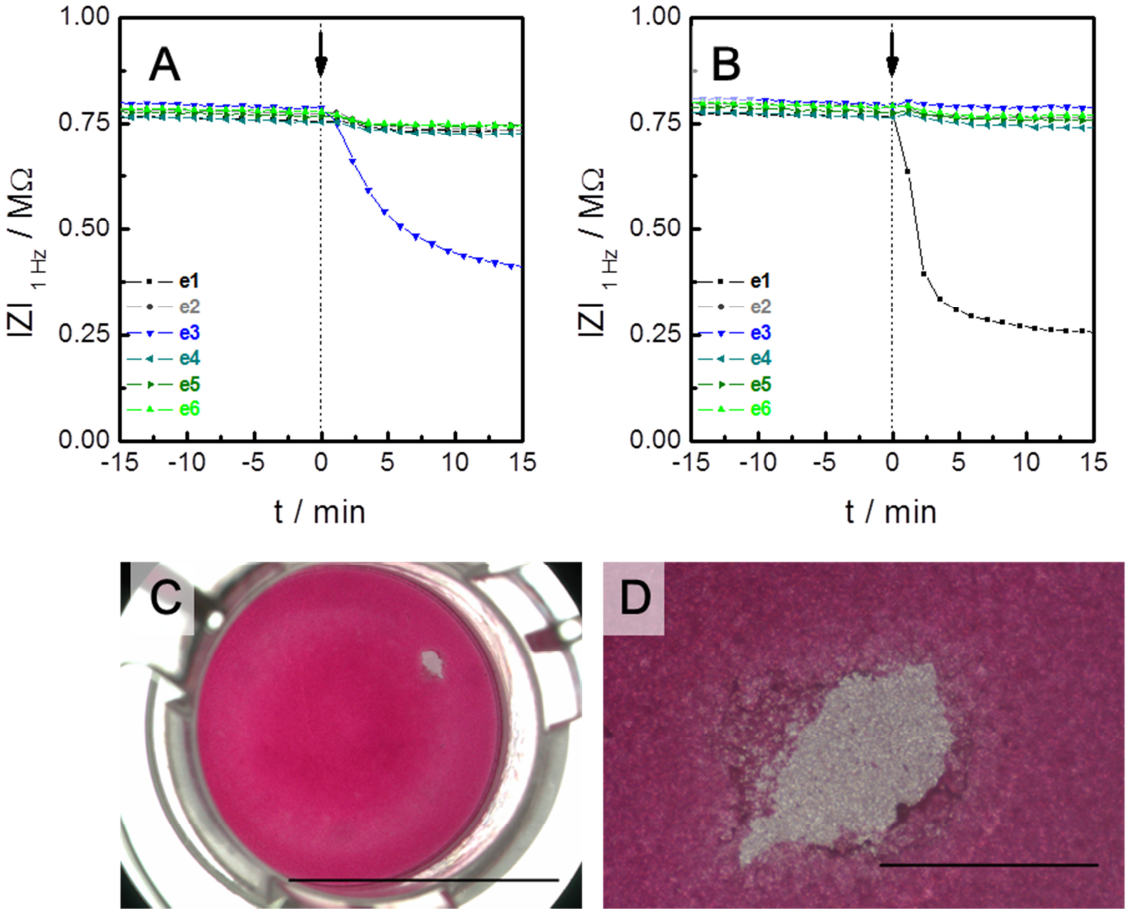

Fig. 12.7: A MDCK-II-covered filter insert with an intentional defect area was incubated at t = 0 with a 1 mM solution of $[Fe(CN)_6]^{3-/4-}$. The addition was performed to the apical filter compartment. The impedance magnitude *IZI* is followed at a frequency of 1 Hz (co-planar mode **2-3**). **A** The defect area is located above e3. **B** The same insert was washed and rotated 120° before the measurement was repeated (defect above e1). TEER was measured to 79 Ωcm^2 after the measurement. Stereomicroscopic (**C**, scale bar: 10 mm) and phase contrast images (**D**, scale bar: 1 mm) of the cell-covered filter insert used for the experiments shown in **A** and **B**. The cell-covered membrane was stained with carbol fuchsin solution for a better contrast. The defect area has a surface area of A = 0.49 mm^2.

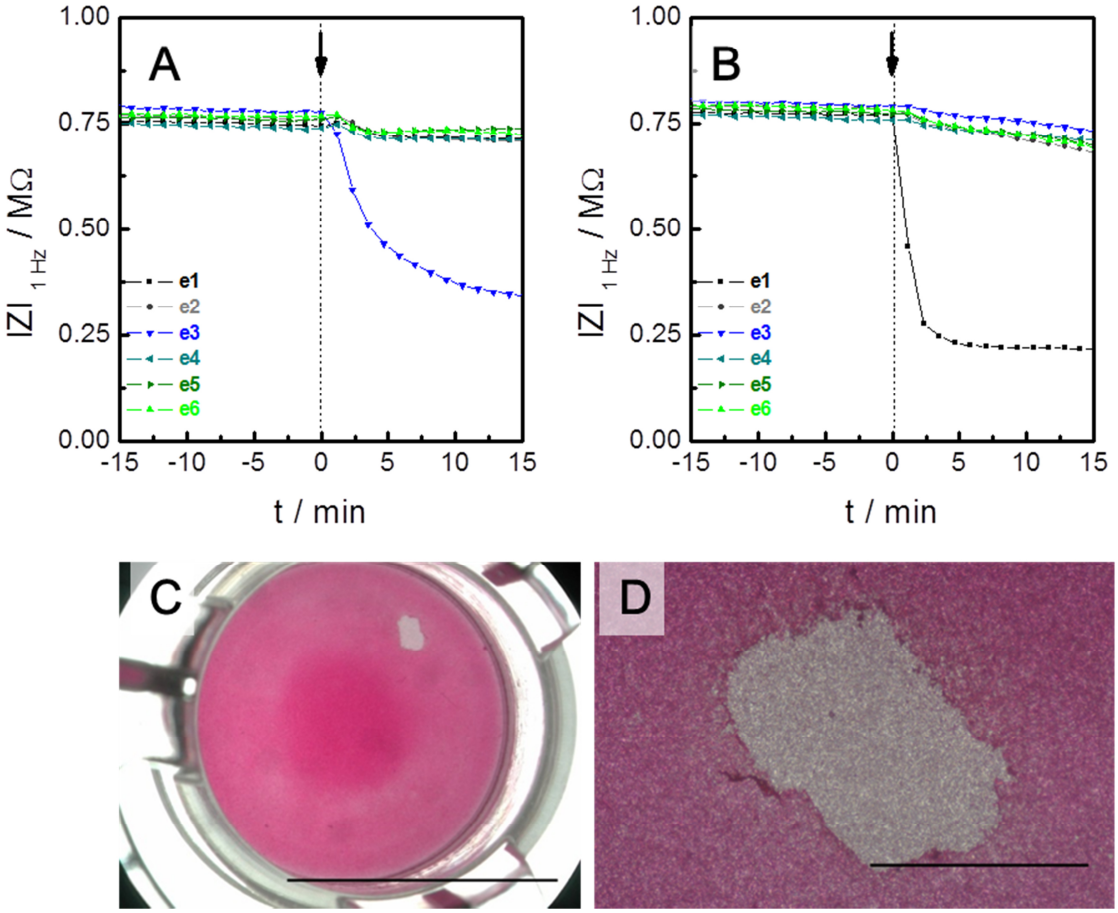

Fig. 12.8: A MDCK-lr-covered filter insert with an intentional defect area was incubated at t = 0 with a 1 mM solution of $[Fe(CN)_6]^{3-/4-}$. The addition was performed to the apical filter compartment. The impedance magnitude *IZI* is followed at a frequency of 1 Hz (co-planar mode **2-3**) **A** The defect area was located above e3. **B** The same insert was washed and rotated 120° before the measurement was repeated (defect above e1). TEER was measured to 70 Ωcm^2 after the measurement. Stereomicroscopic (**C**, scale bar: 10 mm) and phase contrast images (**D**, scale bar: 1 mm) of the cell-covered filter insert used for the experiments shown in **A** and **B**. The cell-covered membrane was stained with carbol fuchsin solution for a better contrast. The defect area has a surface area of A = 0.95 mm^2.

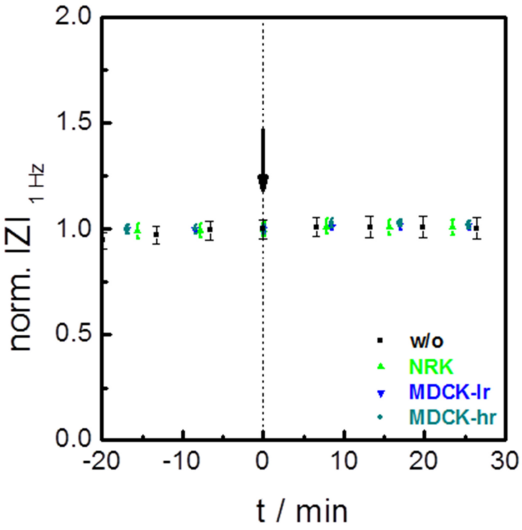

Fig. 12.9: Noralized impedance magnitude *IZI* at a frequency of 1 Hz is recorded in the co-planar detection mode **2-3** in the basal compartment. For control experiments, the buffer was replaced by fresh buffer solution in the apical compartment of cell-free (w/o) or cell-covered (▲ NRK, ▼ MDCK-lr, ● MDCK-hr) filter inserts (mean ± SE, n = 6) at t = 0 min.

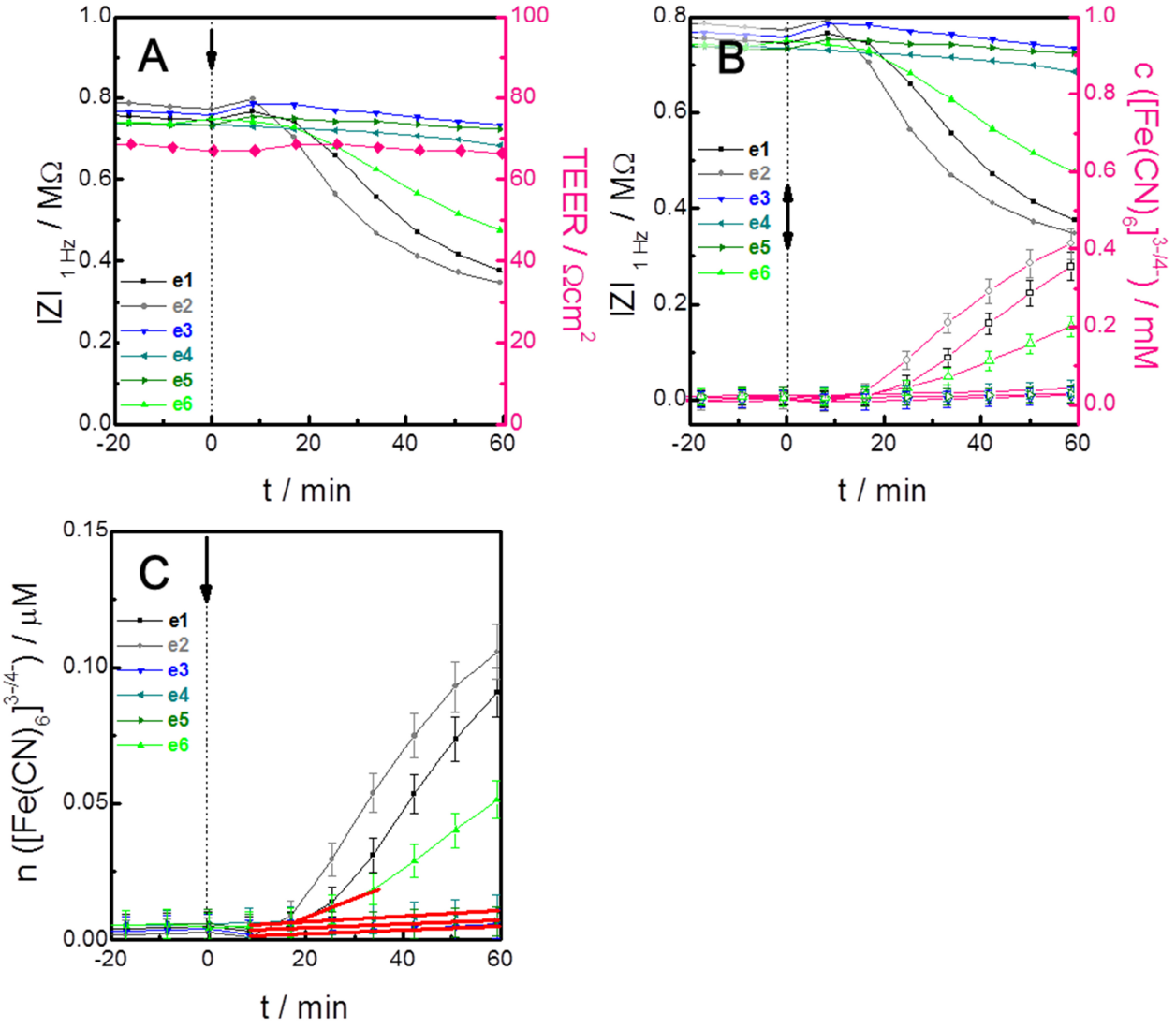

Fig. 12.10: Graphical illustration of the protocol to calculate apparent permeability coefficients derived from impedance measurements. **A** The alterations of *IZI* upon the addition of the tracer substance are recorded at a frequency of 1 Hz. **B** Due to the calibration of the set-up, the time-dependent decrease in *IZI* can be transferred into the corresponding tracer concentration ($c[Fe(CN)_6]^{3-/4-}$, empty symbols). **C** The amount of substance ($n[Fe(CN)_6]^{3-/4-}$) is calculated by multiplication with the receiver compartment volume (2.55E-04 cm3). The slope $dn_R(t)/dt$ of a linear regression (red solid line) was only used for the calculation of P_{app} when *sink-conditions* are met and adj. R^2 was ≥ 0.90 (**C**). Here, data from four of six electrodes can be used for the calculation.

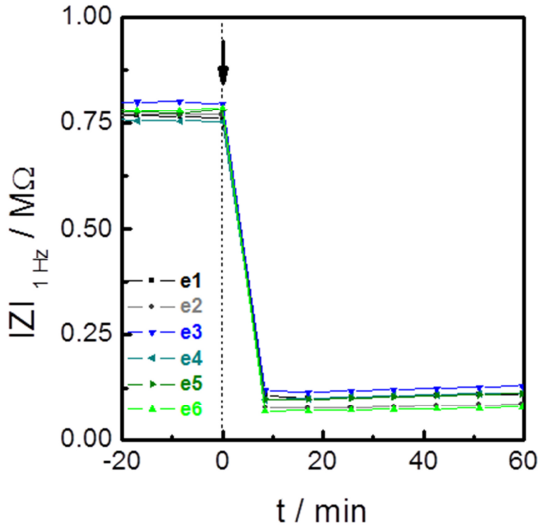

Fig. 12.11: At t = 0, a 1 mM solution of $[Fe(CN)_6]^{3-/4-}$ was added to the apical filter compartment of a cell-free insert. The impedance magnitude *IZI* is followed at a frequency of 1 Hz (co-planar mode **2-3** for e1 - e6).

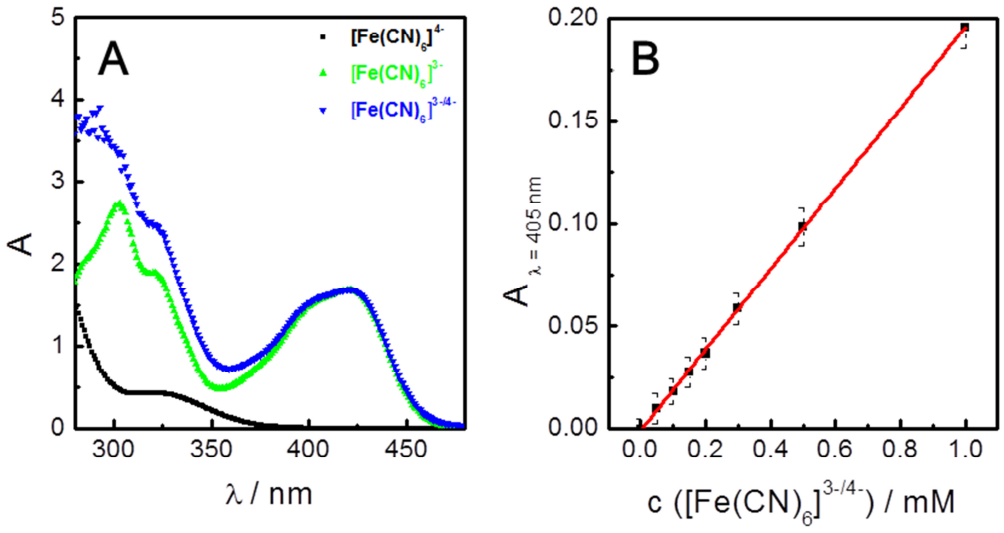

Fig. 12.12: A Absorbance spectra for $[Fe(CN)_6]^{3-}$ and $[Fe(CN)_6]^{4-}$ ions, as well as for a 1:1 mixture of both complexes (1 mM in PBS^{++} buffer) performed in quartz cuvettes (Hemma Analytics, Muellheim, Germany). Absorbance was measured via a UV-VIS-Photometer (Sunrise, Tecan, Maennedorf, Switzerland). **B** Linear regression analysis for the relation between concentration and absorbance of $[Fe(CN)_6]^{3-/4-}$ mixtures measured at λ = 405 nm (mean ± SDM, n = 9). Fit function: A_{405nm} = -(0.001 ± 0.003) + x(0.20 ± 0.01), adj. R-Square: 0.999.

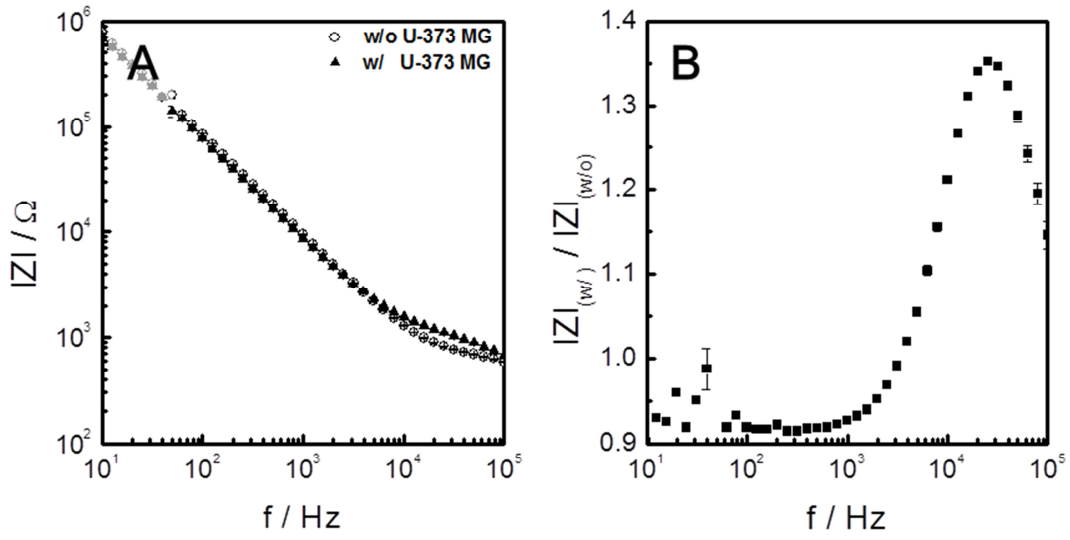

Fig. 12.13: A Frequency spectra of the impedance magnitude *IZI* with (▲ w/) or without (○ w/o) U-373 MG cell layers cultured on ITO electrodes (mean ± SE, n = 3). **B** Normalization of the impedance spectra displayed in **A** reveal a sensitive frequency at 25 kHz (peak maximum).

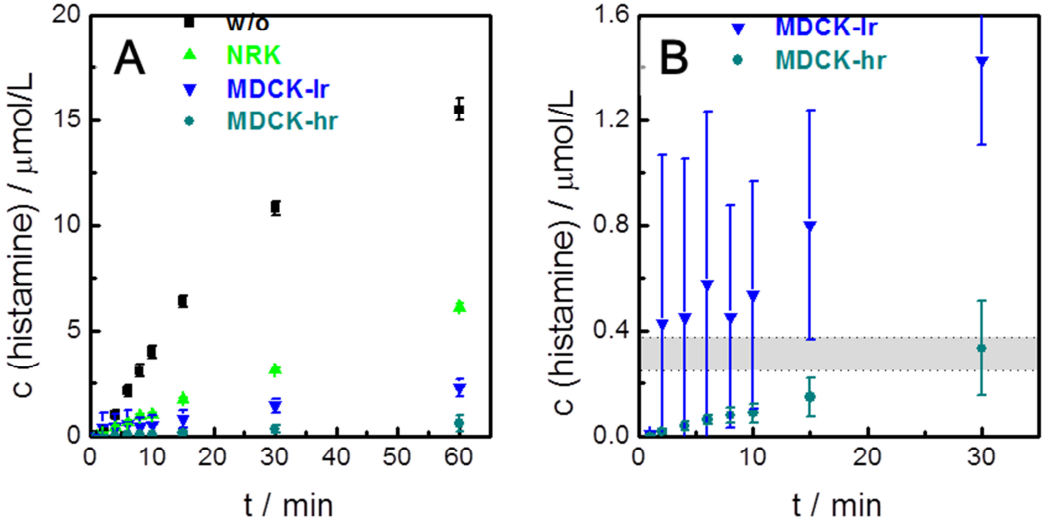

Fig. 12.14: A Cell-free (■ w/o) and cell-covered filter insert (▲ NRK, ▼ MDCK-lr, ♦ MDCK-hr) are incubated at t = 0 with a 100 µM solution of radiolabeled histamine (mean ± SDM, n = 3). The addition is performed to the apical filter compartment. 100 µL samples are taken from the basal filter compartments to determine the tracer concentration over time. **B** Same set of data as shown in (**A**) focused on MDCK experiments. The grey area visualized the EC_{50} value for histamine stimulation of U-373 MG cells (determined by Lieb et al. 2016, EC_{50} = 0.30 ± 0.08 µM).

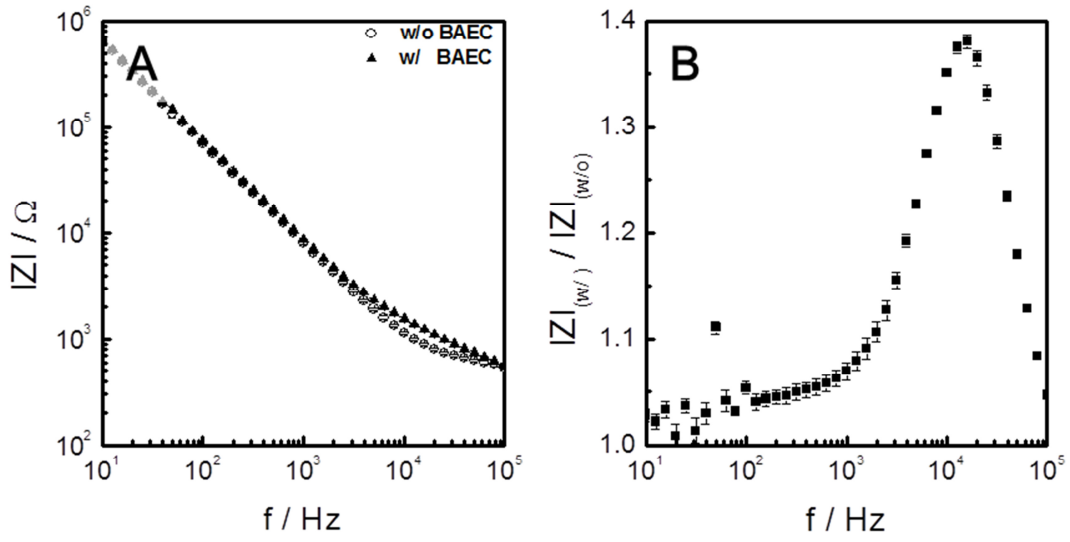

Fig. 12.15: A Frequency spectra of the impedance magnitude *IZI* with (▲ w/) or without (○ w/o) BAEC monolayers cultured on ITO electrodes (mean ± SE, n = 3). **B** Normalization of the impedance spectra shown in **A** reveal a sensitive frequency at 16 kHz (peak maximum).

12.2 Abbreviations and symbols

°C	degree Celsius
2PI	two-path impedance spectroscopy
A, A	area, Ampere
α	subcellular impedance (ECIS model)
Å	angstrom
AC	alternating current
A_{CPE}	parameter of CPE
A_{mem}	membrane area
AQP	aquaporin
β_2AR	β_2-adrenergic receptor
BAEC	bovine aortic endothelila cells
BP230	bullous pemphigoid antigen 230
bpy	bipyridine
C	capacitor / capacitance
c	concentration
*c**	bulk concentration
C_{cl}	cell layer capacitance
cD	cytochalasin D
$C_{paras.}$	parasitic capacitance
Ci	Curie
CI	cytotoxic index
CLSM	confocal laser scanning microscopy
cm	centimeter
C_{mem}	membrane capacitance
CPE	constant phase element
c_w	water concentration
d	thickness, distance
D, D	diffusion coefficient, Dalton
DC	direct current
DDZ	Deutsches Disbetes-Zentrum
DMSO	dimethyl sulfoxide
DSMZ	Deutsche Sammlung von Mikroorganismen und Zellkulturen
d_{sub}	cell-substrate distance
D_w	diffusion coefficient of water
EC_{50}	half maximal effective concentration
ECIS	electric cell-substrate impedance sensing
ECM	extracellular matrix
EDTA	ethylenediamintetraacetic acid
f	frequency
F, *F*	Farad, Faraday constant, dilution factor

FBS	fetal bovine serum
FITC	fluorescein isothiocyanate
g	gram, gravity
GPCR	G-protein coupled receptor
h, *h*	hour, height / thickness
H_1R	histamine 1 receptor
hr	high resistance
Hz	Hertz
I	current
I_0, I_1	modified Bessel functions of the first kind (order 0,1)
IS	impedance spectroscopy
ITO	indium tin oxide
IZI	impedance magnitude
j	phase shift
J_{volume}	volume flux
J_w	diffusive water flux
K	distribution coefficient
k	kilo
L, *L*	Liter, inductor
λ	wavelength
L_p	hydraulic permeability
LP	Longpass filter
lr	low resistance
m	Micro, meter
M	molarity (mol/L), Mega
MDCK	Madin Darby canine kidney
min	minute
n, n	amount of substance, stoichiometric number of electrons, nano
$NAD^+/NADH$	nicotinamide adenine dinucleotide
n_{CPE}	parameter of CPE
NMR	nuclear magnetic resonance
NRK-52E	normal rat kidney (clone 52E)
Ø	diameter
p	relative error
P	hydrostatic pressure
π	osmotic pressure
P_{app}	apparent permeability coefficient
P_d	diffusional permeability coefficient of water
PDMS	polydimethylsiloxane
P_E	molecular permeability coefficient
PET	polyethylene
P_f	osmotic permeability coefficient

R	resistor /resistance, gas constant
ρ	resistivity
R_b	barrier resistance (ECIS model)
R_{bulk}	bulk resistance
r_c	cell radius
R_{cl}	cell layer resistance
R_{ct}	charge-transfer resistance
$R_{paras.}$	parasitic resistance
rms	root mean square
R_{para}	paracellular resistance
rpm	rounds per minute
r_{pore}	pore radius
R_{sub}	subepithelial resistance
ρ_{sub}	solution resistivity
R_{trans}	transcellular resistance
s	second
S, S	Siemens, weighted sum of squares
σ	Warburg coefficient, conductivity
SDM	standard deviation of mean
SE	standard error
SECM	scanning electrochemical microscopy
σ_s	solute reflection coefficient
t	time
T	absolute temperature
TEER	transepithelial / -endpthelial electrical resistance
U	voltage
U-373 MG	human glioma cell line
UV	ultraviolet
UV-VIS	ultraviolet-visible
V	volume
V_w	partial molar volume of water
Ω	Ohm
w	angular frequency
ω_i	proportional weighting factor
Z	complex impedance
Z_f	faradaic impedance element
Z_W	Warburg impedance

Curriculum Vitae

Personal Information:

Name	Kathrin Hajek
Date of Birth	August, 18th 1987
Place of Birth	Freilassing, Germany
Nationality	German

University Studies and School Education:

since 10/2012	Doctoral Student for a PhD in science (Dr. rer. nat.) Working Group Bioanalytics und Biosensors, Prof. Dr. J. Wegener Institute of Analytical Chemistry, Chemo- und Biosensors, University of Regensburg, Germany
10/2010 - 09/2012	Master of Science in Chemistry, University of Regensburg Master Thesis: *"Entwicklung labelfreier analytischer Methoden zur zeitaufgelösten Untersuchung der Zelldifferenzierung".* Working Group of Prof. Dr. J. Wegener Institute of Analytical Chemistry, Chemo- und Biosensors, University of Regensburg, Germany
10/2007 – 11/2010	Bachelor of Science in Chemistry, University of Regensburg, Bachelor Thesis: *"Intramolekulare Zyklisierungen von Indolen und Pyrrolen mit sichtbarem Licht und TiO_2".* Working Group of Prof. Dr. B. König Institute of Organic Chemistry, University of Regensburg, Germany
06/2007	University-entrance Diploma (Abitur) Karlsgymnasium, Bad Reichenhall

Danksagung

Viele Menschen haben mich während der letzten Jahre in jeder Hinsicht unterstützt, gefördert und auch gefordert.

Mein größter Dank gilt Herrn Prof. Dr. Joachim Wegener!

Ich möchte mich ebenfalls bedanken bei Herrn Prof. Dr. Günther Bernhardt für die freundliche Übernahme des Zweitgutachtens und für seine tatkräftige Unterstützung bei diversen Problemstellungen.

Ein besonderer Dank gilt auch PD Dr. Miriam Breunig für die spontane Übernahme des Amtes des Drittprüfers! Vielen Dank!

Dr. Stefanie Michaelis möchte ich besonders hervorheben. Ich danke dir Steffi für die letzten vier Jahre. Du hattest immer ein offenes Ohr für mich und nie zu viel zu tun um nicht doch noch schnell jede meiner Fragen zu beantworten. Ich hab sehr viel von Dir gelernt und werde mich immer gern an unsere gemeinsame Zeit im Labor erinnern.

Unterstützt wurde ich außerdem von Dr. Judith Stolwijk, Barbara Goricnik, Nadja Hinterreiter und von Maria Beer-Krön. Vielen Dank Mädls!

Ein großer Dank auch an alle weiteren und ehemaligen Mitstreiter des AK Wegener.
Dr. Lem, Götzfried, Romy, Carina, Christina, Sonja und besonders dir Flo: DANKE!

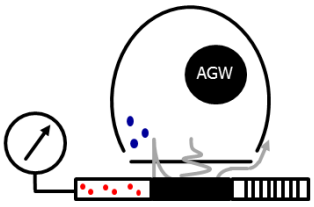

Zudem waren Marina Schmid, Dr. Thea Hering und Dr. Alexander Zöpfl maßgeblich am Gelingen dieser Arbeit beteiligt. Ohne euch hätt ichs nicht bis hierher geschafft!

Meine Familie möchte ich besonders danken. Ihr habt mich während Studium und Promotion immer unterstützt, ermutigt und aufgebaut. Diese Arbeit ist euch gewidmet.